CONSTRAINED CONTROL OF COMPLEX HELICOPTER MODELS

Tugrul Oktay

Dissertation submitted to the faculty of the Virginia Polytechnic Institute and State University in partial fulfillment of the requirements for the degree of

Doctor of Philosophy
In
Aerospace Engineering

Cornel Sultan, Chair
Craig Woolsey
Mazen Farhood
Michael Philen

March 19, 2012
Blacksburg, VA

CONSTRAINED CONTROL OF COMPLEX HELICOPTER MODELS

Tugrul Oktay

ABSTRACT

Complex helicopter models that include effects typically ignored in control models, such as an analytical formulation for fuselage aerodynamics, blade lead-lagging and flexibility, and tail rotor aerodynamics, are derived. The landing gear, horizontal tailplane, a fully articulated main rotor, main rotor downwash, and blade flapping are also modeled. The modeling process is motivated by the desire to build control oriented, physics based models that directly result in ordinary differential equations (ODE) models which are sufficiently rich in dynamics information.

A physics based model simplification procedure, which is called new ordering scheme, is developed to reduce the number of terms in these large nonlinear ODE models, while retaining the same number of governing equations of motion. The resulting equations are trimmed and linearized around several flight conditions (i.e. straight level flight, level banked turn, and helical turn) using Maple and Matlab. The resulting trims and model modes are validated against available literature data.

The linearized models are first used for the design of variance constrained controllers with inequality constraints on outputs or inputs, output variance constrained controllers (OVC) and input variance constrained controllers (IVC), respectively. The linearized helicopter models are also used for the design of online controllers which exploit the constrained model predictive control (MPC) theory. The ability of MPC to track highly constrained, heterogeneous discontinuous trajectories is examined. The performance and robustness of all these controllers (e.g. OVC, IVC, MPC) are thoroughly investigated with respect to several modeling uncertainties. Specifically, for robustness studies, variations in the flight conditions and helicopter inertial properties, as well as blade flexibility effects, are considered.

Furthermore, the effectiveness of adaptive switching between controllers for the management of sensor failure during helicopter operations is studied using variance constrained controllers. Finally, the simultaneous design of the helicopter and control system is examined using simultaneous perturbation stochastic approximation in order to save active control energy.

ACKNOWLEDGEMENT

TABLE OF CONTENTS

LIST OF TABLES

LIST OF FIGURES

NOMENCLATURE

Roman Symbols

a	Blade lift curve slope
a	SPSA (Singular Perturbation Stochastic Approximation) parameter
b	Blade thickness, [m]
c	Blade chord length, [m]
c_d	Blade drag coefficient
c_{d_f}, c_{d_p}	Fuselage skin friction and pressure drag coefficients
$c_{d_{h\&s}}$	Tail rotor hub and shaft (h&s) drag coefficient
$c_{d_{lg}}$	Landing gear (lg) drag coefficient
c_l	Blade section lift coefficient
C_ζ	Lagging damper damping coefficient, [Nms/rad]
d	Fuselage diameter, [m]
d	SPSA parameter
e	Blade hinge offset, [m]
E_∞	Expected value operator
g	Gravitational acceleration, [m/s^2]
h	Vertical distance from helicopter's center of gravity (cg) to main rotor hub, [m]
I	Helicopter inertia matrix
I_b	Blade moment of inertia, [kg m^2]
I_{xx}, I_{yy}, I_{zz}	Helicopter's main moments of inertia, [kg m^2]
I_{xy}, I_{xz}, I_{yz}	Helicopter's product moments of inertia, [kg m^2]
J	Control effort
K_T	Tail rotor thrust coefficient, [N/rad]
K_β	Flapping spring stiffness coefficient, [Nm/rad]
K_ζ	Lagging spring stiffness coefficient, [Nm/rad]
l	Fuselage length, [m]

m	Linear mass density of blade, [kg/m]
L, M, N	Helicopter external moments, [Nm]
M_a	Helicopter's mass, [kg]
$\dot{m}_q$	Mass flow emerged by control volume, [kg/s]
p_3	Final wake pressure, $[N/m^2]$
p_∞	Pressure of undisturbed air, $[N/m^2]$
r	Blade strip distance from flapping&lead-lagging hinge, [m]
R	Main rotor radius, [m]
S	SPSA parameter
t	Time, [s]
T	Rotor thrust, [N]
V_A	Forward flight velocity, [m/s]
v_3	Final wake velocity, [m/s]
v_c	Climb velocity, [m/s]
v_i	Main rotor inflow, [m/s]
X, Y, Z	Helicopter external forces
x	State vector of nonlinear model
x	Nondimensional position of blade element from the blade hinge
x	Set of optimization parameters
x_A, y_A, z_A	Aircraft frame unit vectors
x_F, y_F, z_F	Flapping frame unit vectors
x_{FL}, y_{FL}, z_{FL}	Flapping&lead-lagging frame unit vectors
x_R, y_R, z_R	Rotating frame unit vectors
x_L, y_L, z_L	Lagging frame unit vectors
x_p	State vector of linearized model
x_F, z_F	Horizontal and vertical distances cg to nose, [m]
x_{lg}, z_{lg}	Horizontal and vertical distances cg to landing gear (lg), [m]
x_T, z_T	Horizontal and vertical distances cg to tail rotor, [m]

u, v, w	Helicopter linear velocities in aircraft frame, [m/s]
υ	Control vector of nonlinear model
u	Control vector of linearized model
p, q, r	Helicopter angular velocities in aircraft frame, [rad/s]

Greek Symbols

α	Blade element angle of attack, [rad]
α_F	Fuselage angle of attack, [rad]
β	Single blade flapping angle, [rad]
β_0, β_c, β_s, β_d	Collective, two cyclic, and differential blade flapping angles, [rad]
β_F	Fuselage sideslip angle, [rad]
γ	Lock number
γ_{FP}	Flight path angle
δ_0, δ_2	Parasite and induced blade drag coefficients
ζ	Single blade lagging angle, [rad]
ζ_0, ζ_c, ζ_s, ζ_d	Collective, two cyclic, and differential blade lagging angles, [rad]
θ	Single blade flapping angle, [rad]
θ_0, θ_c, θ_s	Collective and two cyclic blade pitch angles, [rad]
θ_{tw}	Blade twist, [rad]
Θ	SPSA parameter
λ_0, λ_c, λ_s	Uniform and two cyclic rotor main inflow components
λ	SPSA parameter
Ω	Main rotor constant angular velocity, [rad/s]
ρ	Air density, [$\mathrm{kg/m}^3$]
χ	Wake skew angle, [rad]
ψ	Blade azimuth angle, [rad]
ϕ_A, θ_A, ψ_A	Helicopter orientation angles in aircraft frame, [rad]

Sub and Superscripts and Conventions

$\otimes$	Vector product
^	Nondimensionalized quantity and predicted quantity
T	Transpose

CHAPTER 1:

Introduction

1.1 Literature Review and Summary

Historically, aerospace vehicles control was approached using a decoupling principle: a single rigid body model was considered sufficient and the equations of motion were assumed to decouple. This led to tremendous simplification, resulting in low order controllers. However, when inertial roll coupling was first analyzed [1], the decoupling approximation was soon found inadequate even for fixed wing aircraft. Nevertheless, decoupling continued to be used because technological limitations placed severe restrictions on the dimension of controllers that could be implemented.

For rotorcraft, the single rigid body and decoupling assumptions are crude approximations. Their relative success in helicopter control was due to very conservative designs, which are not suitable for multi-objective missions with conflicting requirements. Several publications actually advocate for the use of coupled, multibody models for rotorcraft control design. For example in [2-4] rotor and control system optimization was performed over flap stiffness, flap-lag elastic coupling factor, and control parameters. In [2] a coupled rotor-fuselage model with rigid blades [5,6] was used for integrated design, leading to the conclusion that lower control effort is achieved if the rotor and control system are designed simultaneously. Moreover, rotor dynamics and handling qualities cannot be treated independently [7].

For control design the ideal situation is when the model used for control is physics-based and it captures the essential dynamics of interest through a process called "control oriented modeling". The main advantage of physics versus data based (e.g. identified)

1

models is that the former are more robust and versatile than the latter. In the first part of this dissertation the development of such models for helicopters is presented. The models include a fully articulated main rotor, linear main rotor downwash, blade flexibility, an analytical formulation for fuselage aerodynamics using slender body theory, a tail rotor aerodynamic model, horizontal tailplane, and landing gear. For control oriented modeling, lumped system modeling [8] is used for blade flexibility instead of solving nonlinear partial differential equations (PDEs) [9,10] or using finite element methods [11]. The control oriented modeling approach, which involves application of the physics principles, leads directly to dynamic models composed of finite sets of ordinary differential equations (ODEs). This is a tremendous advantage for control design because it facilitates the direct use of modern, multivariable control theory tools. Modern control system design relies heavily on state space representations of the system's dynamics, which are readily obtained from ODEs. However, the situation is different, if application of the physics principles leads to models composed of PDEs. To obtain a finite set of ODEs from the infinite dimensional set of PDEs, tremendous work is required to find and retain a finite number of modes for control design. Thus only several ODEs are retained, usually selected to capture the modes that are considered relevant for the control design problem of interest, amounting to qualitative and quantitative alteration of the original PDEs based mathematical model. Moreover, this procedure complicates the verification and validation of the control system.

The models obtained using the control oriented approach consist indeed of nonlinear ODEs, but have too many terms, making their use in fast computation impossible. Therefore, a systematic simplification method, which is called "new ordering scheme", is

applied to reduce the number of terms. The resulting models are validated by comparing their features, specifically trim values and eigenvalues of linearized models, with results in the literature.

In the second part of the dissertation the feasibility of these models in modern control design is studied. Since helicopters are subject to output and input limitations and a key requirement is minimization of control energy, the performances of output variance constrained controllers (OVC) and input variance constrained controllers (IVC) [12-19] were investigated. Such controllers were designed for linearized models and several flight conditions, monitoring: a) speed of convergence of solution algorithms, b) stability of the closed loop systems, c) satisfaction of constraints. Furthermore, since systems are subject to modeling uncertainties, closed loop stability robustness is thoroughly evaluated, first by varying helicopter's speed. Secondly, the effect of modeling uncertainties was evaluated by using controllers designed for rigid blade models on flexible blade models and finally using controllers designed for flexible blade models with uncertain inertial properties.

One deficiency of the previously discussed variance constrained controllers is that they do not consider output and input constraints simultaneously. Due to this reason, model predictive control (MPC), which accounts simultaneously for output and input constraints, was examined. Past research in MPC for helicopters focused predominantly on simple [20-25] or identified models such as those obtained using neural networks [26-31]. On the other hand, the models created in this dissertation are physics based, control oriented, and sufficiently complex to account for important effects in helicopter dynamics. MPCs were designed for control oriented models evaluating: a) ability to track

discontinuous trajectories, b) satisfaction of heterogeneous constraints, c) computation time, d) robustness to modeling uncertainties.

For maneuvering flight, control design is critical for safe and performant helicopter operation. In particular, helical turns and banked turns are of major interest. For example, they enable transitioning between two straight level flight conditions and monitoring an area of interest. They also allow armed helicopters to avoid ground attack, to possibly engage in air to air combat, etc. In this study the design of modern controllers are analyzed for such maneuvers. Since these maneuvers are highly constrained, any control design should account for constraints on outputs and inputs. Due to these requirements, variance constrained controllers with inequality constraints on outputs or inputs and model predictive control (MPC), which explicitly accounts for many constraints, are analyzed.

Another important issue in helicopter control is management of sensor failure. Physical (direct) redundancy, which means adding duplicate or even multiple sensors, is sometimes used for aerospace vehicles. This approach has many limitations [32,33]. For example, some sensors can be very expensive, and there are stringent space limitations on board helicopters which limit the number of sensors that can be carried. Moreover, placement of specific sensors is predetermined due to physical and operational conditions. For example, if all sensors measuring the same quantity are placed in a certain region of the helicopter, a physical phenomenon, such as regional stall and flow separation, may cause failure of these sensors all together. Therefore, different approaches, in which mathematical relations are used to obtain redundant measurements, are recently being developed [33-37].

In this dissertation an alternative approach, namely adaptive switching between controllers which are adequate for different sets of sensors, but provide the same prespecified performance, is proposed. This approach has nowadays become possible due to recent advances in control theory, signal processing, microelectronics, power electronics, and microprocessors. Switching between controllers can then be easily and reliably implemented electronically, thus not requiring addition of mass. The idea investigated is if one can adaptively change the controller in flight to satisfy the same constraints when the set of measurements changes due to sensor failure. Therefore, variance constrained controllers and MPC with different sets of measurements are also studied.

Traditionally, the plant to be controlled is given a priori to the control engineer who has no influence on the plant design process. However, it is well-known that the plant and control system design problems are not independent [38,39]. Simple changes in plant parameters may improve performance significantly. The traditional sequential approach: 1) design the plant, and 2) design the control system, does not usually provide the best overall design [38,39]. Ideally, the plant and control system should be simultaneously designed to optimize a given objective (e.g. cost function). This is definitely a much more difficult problem. In this dissertation we pursue this idea and simultaneously design helicopter plant (blade and operation parameters) and control system to minimize the active control effort while obeying constraints on the physical parameters of the helicopter and control system.

Previous work in helicopter redesign was limited to passive design -- control system parameters were never included. For example, in [7] a redesign optimization study is

performed in which rotor dynamics and flight dynamics are simultaneously taken into account to maximize the damping of a rotor lag mode with respect to certain design parameters (e.g. blade torsion stiffness, blade chord length). In another study [40], vibratory loads at the rotor hub, which are the main sources of helicopter vibration, are reduced by redesigning the helicopter using certain variables (e.g. blade lag and torsion stiffness). Several other papers also report helicopter redesign studies [41,42].

For our simultaneous design study complex physics based control oriented helicopter models are used. However, the resulting constrained optimization problem is very complex and does not allow analytical computation of derivatives such as gradients and Hessians. Since numerical approximation of these derivatives for such complex (large) problems is prohibitive and possibly numerically unstable, we selected a fast stochastic optimization method, called SPSA (simultaneous perturbation stochastic approximation), to solve these problems [43,44]. An algorithm, which illustrates the effectiveness of combining SPSA and simultaneous helicopter plant and control system design to minimize control effort, is developed. A novel adaptive SPSA that accounts for the constraints that the optimization variables must be between lower and upper limits is also developed to solve related problems.

1.2 Main Contributions

One of the major contributions of this dissertation is in showing a complete process of control oriented, physics based model development for helicopters followed by modern control design. The modeling process is specifically designed to result in ODEs which are sufficiently rich in dynamics information for modern control design.

For this dissertation, in order to simplify the nonlinear ODEs, firstly the classical ordering scheme (see Celi [45]) was used. However, it was quickly ascertained that strict application of this classical ordering scheme leads to erroneous results (for example, unrealistic modes were obtained). This led to the development of a novel model simplification procedure, called the "new ordering scheme", which resulted in realistic trim conditions and modes which were also validated against available literature data.

Another important contribution of this dissertation is that it shows that modern constrained controllers can be applied to the helicopter models developed herein, which are beyond the typical complexity used for helicopter control design. This is the first study to apply variance constrained controllers to helicopters, while also thoroughly investigating their stability robustness properties. This is also the first advanced study which shows that constrained MPC can be used and implemented online to robustly track discontinuous helicopter trajectories, even when the models are sophisticated and physics based.

The simultaneous helicopter plant and control system design idea is also investigated with advanced constrained control techniques and highly complex helicopter models. This is the first study which shows a complete process of simultaneous helicopter plant and control system design. This is also the first study examining simultaneous helicopter plant and control system design using variance constrained controllers. A stochastic optimization technique, specifically SPSA, is used for the first time for this purpose. A novel adaptive SPSA accounting for the constraints that the optimization variables must be between lower and upper limits is also developed.

Finally, the idea to switch adaptively between controllers for the management of

sensor failure during helicopter operations is investigated, also for the first time. Specifically, output variance constrained controllers (OVC) and input variance constrained controllers (IVC) are considered.

CHAPTER 2:

Modeling and Model Simplification

2.1 Newton-Euler (Dynamic) and Kinematic Equations of a Generic Helicopter

Throughout this dissertation the following general key assumptions are made to derive Newton-Euler and kinematic equations of a generic helicopter:

Key Assumptions:

- The helicopter has a plane of symmetry.

- The gravitational force and moment acting on the blade is ignored.

- Each blade is composed of individual blade segments that are considered rigid.

In order to derive Newton-Euler equations of the helicopter, forces and moments due to the blade motion should be found. To obtain these forces and moments, the position, velocity and acceleration of any generic blade point are needed. For the simplified blade model depicted in Fig. 2.1 these vectors can be easily obtained as showed next.
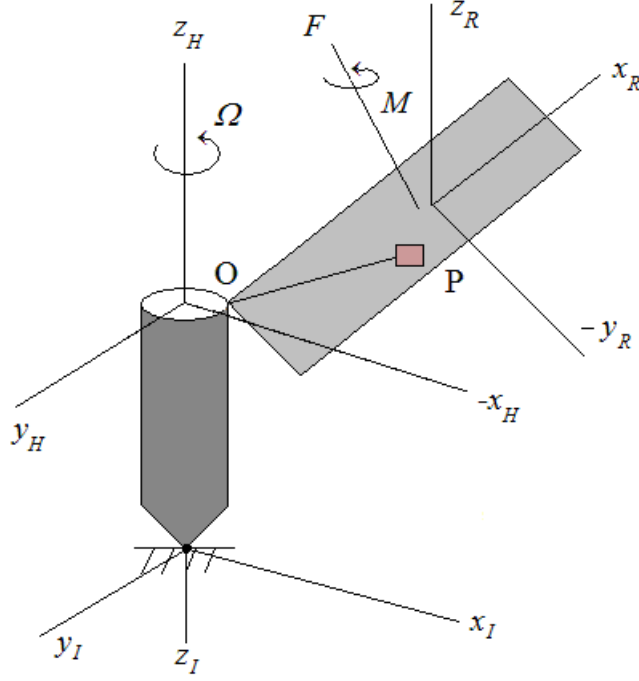
Figure 2.1: Scheme of Rotating Blade Connected to Axially Rotating Hub

In Fig. 2.1 the hub rotates around z_I, which is inertially fixed for this simple example, with constant angular velocity, Ω. The reference axes x_I and y_I are attached to the hub, F and M are the total force and moment acting on the blade at its center of gravity, while x_R, y_R, and z_R are unit vectors of a blade rotating frame and x_H, y_H, and z_H are unit vectors of the hub frame. Ignoring the blade thickness, the position of a generic point P on the blade in the rotating frame is

$$_R r^{OP} = \begin{bmatrix} r_{P_1} & r_{P_2} & 0 \end{bmatrix}^T \tag{2.1}$$

Using the Transport Theorem [45, 46] the velocity of the generic point is expressed as

$$^I \vec{V}^{OP} = \frac{\partial}{\partial t} \vec{r}^{OP} + {}^I \vec{\omega}^R \otimes \vec{r}^{OP} \tag{2.2}$$

10

where $^I\vec{\omega}^R$ is the angular velocity of the rotating frame with respect to the inertial frame

and in the hub frame it is

$$_H^I\omega^R = \begin{bmatrix} 0 & 0 & \Omega \end{bmatrix}^T \tag{2.3}$$

Assuming that the blade is rigid, the velocity of the generic point is

$$^I\vec{V}^{OP} = {}^I\vec{\omega}^R \otimes \vec{r}^{OP} \tag{2.4}$$

The acceleration of the generic point, also expressed using the Transport Theorem, is

$$^I\vec{a}^{OP} = \frac{\partial}{\partial t}({}^I\vec{\omega}^R \otimes \vec{r}^{OP}) + {}^I\vec{\omega}^R \otimes ({}^I\vec{\omega}^R \otimes \vec{r}^{OP}) \tag{2.5}$$

To obtain Newton-Euler equations of the helicopter, Eqs. 2.4 and 2.5 will be modified

later on to account for the motion of the hub and helicopter with respect to the inertial

(gravitational) frame.

The helicopter moment equation is derived using Euler's Law (see [45]) and it is

$$^I\dot{\vec{h}} = \frac{\partial}{\partial t}{}^I\vec{h} + {}^I\vec{\omega}^A \otimes {}^I\vec{h} \tag{2.6}$$

where $^I\vec{h}$ and $^I\vec{\omega}^A$ are the angular momentum and angular velocity of the helicopter

with respect to the inertial frame. These are given by

$$^I\vec{h} = I \, ^I\vec{\omega}^A, \qquad _A^I\omega^A = \begin{bmatrix} p & q & r \end{bmatrix}^T \tag{2.7}$$

where the inertia matrix is

$$I = \begin{bmatrix} I_{xx} & 0 & -I_{xz} \\ 0 & I_{yy} & 0 \\ -I_{xz} & 0 & I_{zz} \end{bmatrix} \tag{2.8}$$

11

Using Eqs. 2.7 and 2.8 the helicopter moment equation is

$$M_A = \begin{bmatrix} L \\ M \\ N \end{bmatrix} = \begin{bmatrix} I_{xx}\dot{p} - (I_{yy} - I_{zz})qr - I_{xz}(pq + \dot{r}) \\ I_{yy}\dot{q} - (I_{zz} - I_{xx})pr + I_{xz}(p^2 - r^2) \\ I_{zz}\dot{r} - (I_{xx} - I_{yy})pq - I_{xz}(\dot{p} - rq) \end{bmatrix} \tag{2.9}$$

To obtain the helicopter force equation, Newton's 2nd Law is used. This is simply

$$^I\vec{F} = M_a \; {}^I\frac{d\vec{V}_{cg}}{dt} = M_a \left[\frac{\partial \vec{V}_{cg}}{\partial t} + {}^I\vec{\omega}^A \otimes \vec{V}_{cg} \right] \tag{2.10}$$

where the helicopter's center of gravity velocity in the aircraft frame is

$$_A V_{cg} = \begin{bmatrix} u & v & w \end{bmatrix}^T \tag{2.11}$$

and M_a is the helicopter mass. Accounting also for the helicopter gravitational force, the

helicopter force equation is

$$F_A = \begin{bmatrix} X \\ Y \\ Z \end{bmatrix} = \begin{bmatrix} M_a(\dot{u} + qw - rv) + M_a g \sin(\theta_A) \\ M_a(\dot{v} + ru - pw) - M_a g \cos(\theta_A)\sin(\phi_A) \\ M_a(\dot{w} + pv - qu) - M_a g \cos(\theta_A)\sin(\phi_A) \end{bmatrix} \tag{2.12}$$

The rotational kinematic equation of the helicopter is derived using the helicopter's

angular velocities (p, q, r) and Euler orientation angles (ϕ_A, θ_A, ψ_A). For the 3-2-1

rotation sequence [45, 47] (general aviation assumption), the rotational kinematic

equation is

$$\begin{bmatrix} p \\ q \\ r \end{bmatrix} = \begin{bmatrix} \dot{\phi}_A - \dot{\psi}_A \sin(\theta_A) \\ \dot{\psi}_A \cos(\theta_A)\sin(\phi_A) + \dot{\theta}_A \cos(\phi_A) \\ \dot{\psi}_A \cos(\theta_A)\cos(\phi_A) - \dot{\theta}_A \sin(\phi_A) \end{bmatrix} \tag{2.13}$$

2.2 Nondimensionalization

Nondimensionalization is widely used in all engineering disciplines. In helicopter dynamics the general rules of nondimensionalization (see [48] [p.142] for details) are:

i. Lengths are nondimensionalized by the main rotor radius, R

$$\hat{l} = \frac{l}{R} \tag{2.14}$$

ii. Time is nondimensionalized by the main rotor angular speed, $1/\Omega$

$$\hat{t} = \frac{t}{1/\Omega} \tag{2.15}$$

iii. Linear velocities are nondimensionalized by the main rotor's tip path speed, ΩR

$$\hat{u} = \frac{u}{\Omega R}, \quad \hat{v} = \frac{v}{\Omega R}, \quad \hat{w} = \frac{w}{\Omega R} \tag{2.16}$$

iv. Angular velocities are nondimensionalized by the main rotor angular speed, Ω

$$\hat{p} = \frac{p}{\Omega} \quad \hat{q} = \frac{q}{\Omega} \quad \hat{r} = \frac{r}{\Omega} \tag{2.17}$$

v. Flapping, flapwise bending, and lagging springs are nondimensionalized by $I_b \Omega^2$

$$k_\beta = \frac{K_\beta}{I_b \Omega^2}, \qquad k_\delta = \frac{K_\delta}{I_b \Omega^2}, \qquad k_\zeta = \frac{K_\zeta}{I_b \Omega^2} \tag{2.18}$$

vi. Tail rotor thrust coefficient is nondimensionalized by $I_b \Omega^2 / R$

$$k_T = \frac{K_T R}{I_b \Omega^2} \tag{2.19}$$

2.3 Nondimensionalized Dynamic and Kinematic Equations of The Helicopter

After application of the previous nondimensionalization rules, the nondimensionalized dynamic and kinematic equations are obtained as follows.

Force Equations:

$$\frac{d}{d\psi}\hat{u} + \hat{q}\,\hat{w} - \hat{r}\,\hat{v} + \frac{g\sin(\theta_A)}{\Omega^2\,R} = \frac{X}{\Omega^2\,R\,M_a}$$

$$\frac{d}{d\psi}\hat{v} + \hat{r}\,\hat{u} - \hat{p}\,\hat{w} - \frac{g\cos(\theta_A)\sin(\phi_A)}{\Omega^2\,R} = \frac{Y}{\Omega^2\,R\,M_a} \qquad (2.20)$$

$$\frac{d}{d\psi}\hat{w} + \hat{p}\,\hat{v} - \hat{q}\,\hat{u} - \frac{g\cos(\theta_A)\cos(\phi_A)}{\Omega^2\,R} = \frac{Z}{\Omega^2\,R\,M_a}$$

Moment Equations:

$$\frac{d}{d\psi}\hat{p} - \hat{q}\,\hat{r}\left(\frac{I_{yy}}{I_{xx}} - \frac{I_{zz}}{I_{xx}}\right) - \frac{I_{xz}}{I_{xx}}\left(\hat{p}\,\hat{q} + \frac{d}{d\psi}\hat{r}\right) = \frac{L}{I_{xx}\,\Omega^2}$$

$$\frac{d}{d\psi}\hat{q} - \hat{p}\,\hat{r}\left(\frac{I_{zz}}{I_{yy}} - \frac{I_{xx}}{I_{yy}}\right) + \frac{I_{xz}}{I_{yy}}\left(\hat{p}^2 - \hat{q}^2\right) = \frac{M}{I_{yy}\,\Omega^2} \qquad (2.21)$$

$$\frac{d}{d\psi}\hat{r} - \hat{p}\,\hat{q}\left(\frac{I_{xx}}{I_{zz}} - \frac{I_{yy}}{I_{zz}}\right) - \frac{I_{xz}}{I_{zz}}\left(\hat{q}\,\hat{r} - \frac{d}{d\psi}\hat{p}\right) = \frac{N}{I_{zz}\,\Omega^2}$$

Kinematic Equations:

$$\hat{p} = \frac{d}{d\psi}\phi_A - \frac{d}{d\psi}\psi_A\sin(\theta_A)$$

$$\hat{q} = \frac{d}{d\psi}\psi_A\cos(\theta_A)\sin(\phi_A) + \frac{d}{d\psi}\theta_A\cos(\phi_A) \qquad (2.22)$$

$$\hat{r} = \frac{d}{d\psi}\psi_A\cos(\theta_A)\cos(\phi_A) - \frac{d}{d\psi}\theta_A\sin(\phi_A)$$

2.4 Blade Aerodynamics

The following general key assumptions are made to derive blade aerodynamic equations in this dissertation.

Key Modeling Assumptions:

-The radial component of blade section oncoming air velocity is negligible.

-The tangential component of blade section oncoming air velocity is much bigger than its perpendicular component.

-Linear and incompressible aerodynamics is considered.

-Blade unsteady flow is ignored.

-The Mach number and angle of attack are small.

-Quasi-steady flow is considered [45].

To obtain aerodynamic forces acting on blades, blade element theory (see [45] and [49] [pp. 45-57]) is used. The aerodynamic force acting on a blade element is

$$\vec{f}_{aero} = d\vec{L} + d\vec{D} \qquad (2.23)$$

where the infinitesimal lift and drag forces acting on any blade element, $d\vec{L}$ and $d\vec{D}$, are

$$d\vec{L} = \frac{1}{2}\rho\, V_{Total}^2\, c_l\, c\, dr\, \hat{V}_n, \qquad d\vec{D} = \frac{1}{2}\rho\, V_{Total}^2\, c_d\, c\, dr\, \hat{V}_t \qquad (2.24)$$

where V_{Total} is the total oncoming air velocity of the blade element. Assuming that $U_T \gg U_P$ and U_R is negligible, the infinitesimal lift and drag forces acting on the blade element are

$$d\vec{L} = \frac{1}{2} \rho \, U_T^2 \, c_l \, c \, dr \, \hat{V}_n, \qquad d\vec{D} = \frac{1}{2} \rho \, U_T^2 \, c_d \, c \, dr \, \hat{V}_t \qquad (2.25)$$
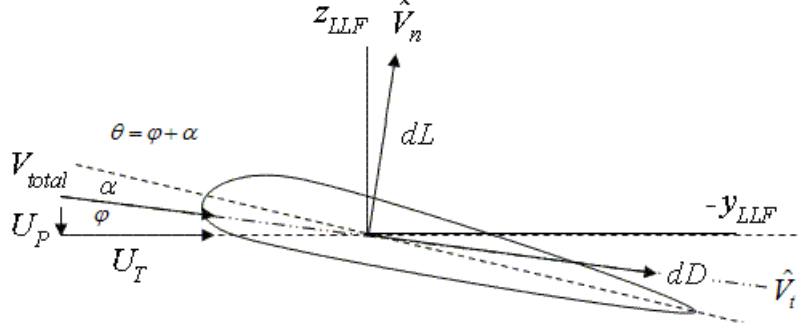
Figure 2.2: Blade Element-Infinitesimal Lift and Drag

Assuming that 1) the blade section profile drag coefficient is $c_d = \delta_0 + \delta_2 \alpha^2$ [50] [p. 591], 2) linear and incompressible aerodynamics exist, and the blade element lift coefficient is $c_l = a_0 \, \alpha$, 3) $dL \gg dD \ (U_P / U_T)$ [51] [p. 118], the infinitesimal aerodynamic force and moment acting on the blade element become

$$d_{LLF} F_{aero} = \frac{\gamma I_b}{2R^3} \begin{bmatrix} 0 \\ -\left(\theta \, U_T^2 - U_P \, U_T \right) \frac{U_P}{U_T} - \frac{1}{a_0} \left(\delta_0 + \delta_2 \left(\theta - \frac{U_P}{U_T} \right)^2 \right) \\ \theta \, U_T^2 - U_P \, U_T \end{bmatrix} dx \qquad (2.26)$$

$$d_{LLF} M_{aero} = \begin{bmatrix} 0 & -xR \, (d_{LLF} F_{aero})_{III} & xR \, (d_{LLF} F_{aero})_{II} \end{bmatrix}^T \qquad (2.27)$$

Here $\gamma = R^4 \rho a c / I_b$ is the Lock number and x is the nondimensional position of the blade element from the blade hinge (see Figs. 2.3 and 2.4).

2.5 Blade Dynamics

For this dissertation the following general key assumptions are made to derive blade dynamic equations.

Key Modeling Assumptions:

-Strip theory is used (see [45] and [50][pp. 133-137]).

-Aircraft's acceleration is small with respect to any blade strip acceleration.

-Flapping and lagging hinge offsets are located at the same position.

The last assumption requires further clarification. There are several helicopter flap-lag-pitch hinges configurations commonly used in practice and widely described in the literature. These configurations are illustrated in Fig. 2.3. For example, for the first configuration the flap hinge is closest to the main rotor hub. The pitch hinge is far from the main rotor hub. The lag hinge is between them. For the third configuration flap and lag hinges are aligned and the pitch hinge is far from them with respect to the main rotor. The type-3 configuration is chosen (*Sikorsky S58, Westland Sea King, Westland Wessex*) for helicopter model.
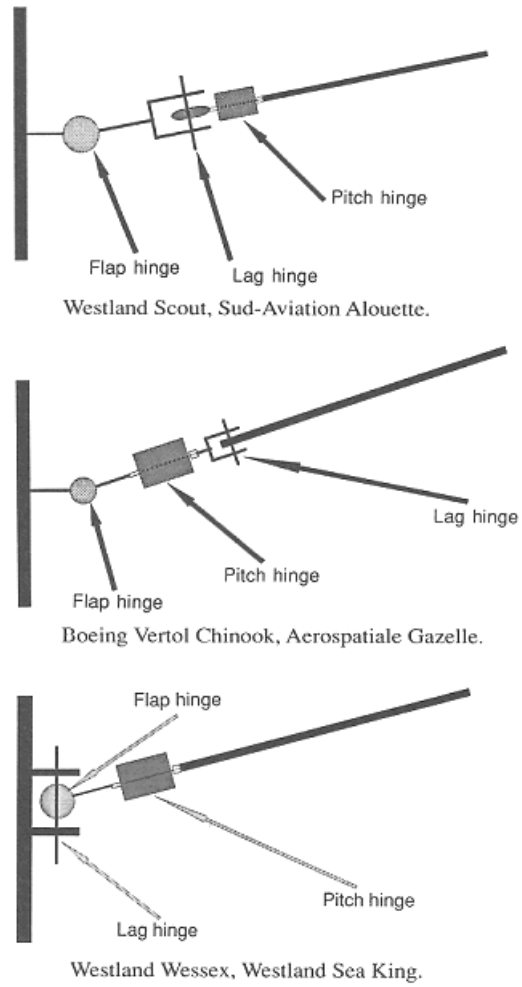
Figure 2.3: Flap-Lag-Pitch Hinges Configurations (Taken from [52] [p. 87])
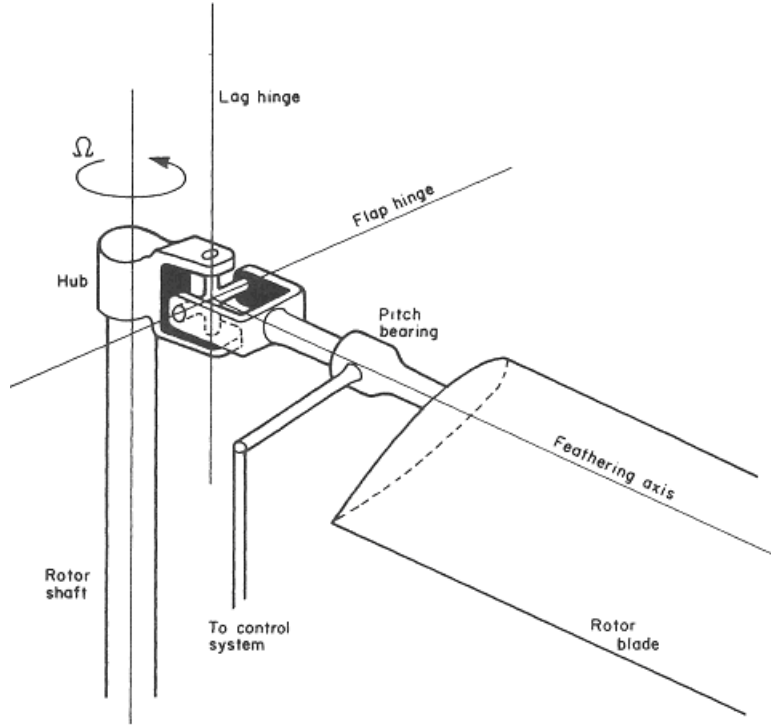
Figure 2.4: Fully Articulated Main Rotor with Type-3 Configuration
(Taken from [49] [p. 7])

The type-3 configuration is depicted in detail, together with other required components, in Fig. 2.4. The absolute acceleration of a blade strip point, P, at position $\vec{r}^{\,P}$ from the helicopter's center of gravity is

$$
{}^{I}\vec{a}^{\,P} = \frac{\partial}{\partial t} \left({}^{I}\vec{\omega}^{\,R} \otimes \vec{r}^{\,P} \right) + {}^{I}\vec{\omega}^{\,R} \otimes \left({}^{I}\vec{\omega}^{\,R} \otimes \vec{r}^{\,P} \right) \tag{2.28}
$$

where

$$
{}^{I}\vec{\omega}^{\,R} = {}^{I}\vec{\omega}^{\,A} + {}^{A}\vec{\omega}^{\,R} \tag{2.29}
$$

These angular velocities in specific frames are

19

$$\prescript{I}{A}{\omega}^{A} = \Omega \begin{bmatrix} \hat{p} & \hat{q} & \hat{r} \end{bmatrix}^{T}, \qquad \prescript{A}{H}{\omega}^{R} = \Omega \begin{bmatrix} 0 & 0 & 1 \end{bmatrix}^{T} \tag{2.30}$$

For the strip theory application, the blades are modeled as flat rods (without thickness) in the blade span direction (see Figs. 2.6 and 2.7). The position of strip P on the blade with respect to the helicopter's center of gravity, including flapping and lead-lagging motions specifically, is

$$\prescript{}{R}{r}^{P} = \begin{bmatrix} eR + xR\cos(\beta(\psi))\cos(\zeta(\psi)) \\ -xR\sin(\zeta(\psi)) \\ hR + xR\sin(\beta(\psi))\cos(\zeta(\psi)) \end{bmatrix} \tag{2.31}$$

Using $\prescript{I}{}{\vec{a}}^{P}$ (Eq. 2.28) and the blade's moment of inertia $I_{b} = (1/3)m\,R^{3}(1-e)^{3}$, the infinitesimal inertial force and moment acting on any blade strip are

$$d\vec{F}_{I} = -\frac{3I_{b}}{R^{2}(1-e)^{3}} \, \prescript{I}{}{\vec{a}}^{P} \, dx, \quad d\vec{M}_{I} = \vec{r} \otimes d\vec{F}_{I} \tag{2.32}$$

where

$$\prescript{}{R}{r} = \begin{bmatrix} xR & 0 & 0 \end{bmatrix}^{T} \tag{2.33}$$

2.6 Blade Flapping and Lead-Lagging Motions

During forward flight, the local oncoming air velocity of each blade changes significantly. The advancing blades move faster than retreating blades, causing an important aerodynamic phenomenon called "dissymmetry of lift" (see Fig. 2.5). The dominant effect of this phenomenon is that the helicopter tends to roll. This dissymmetry is the main difference between helicopter flight and fixed-wing aircraft. In order to solve the rolling problem experienced by helicopters during forward flight, the blades are

joined to the rotor hub via flexible articulations that allow each blade to experience different angles of attack. This idea was first proposed by Spanish inventor, Juan de la Cierva [53] [p. 64]. This added flexibility enables the flapping motion, which is an "up and down" motion with respect to the rotating frame (Fig. 2.6).
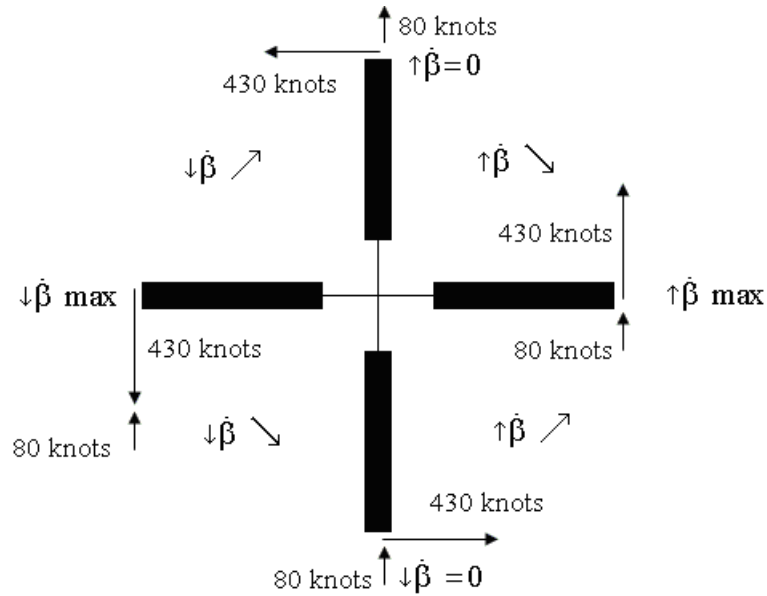
**Figure 2.5: Velocity Distribution During Forward Flight and
Blade Flapping Motion**
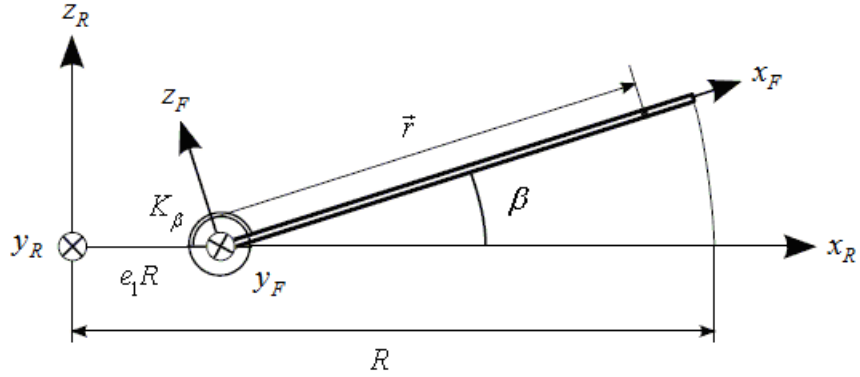
Figure 2.6: Blade Flapping Motion
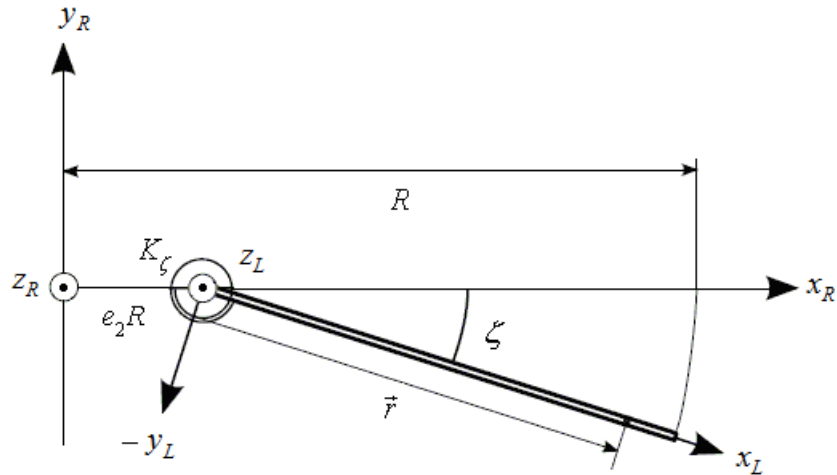
Figure 2.7: Blade Lead-Lagging Motion

When Juan de la Cierva invented the flapping hinge, he fixed the problem of the non-symmetric aerodynamics. However, after flying for a short time, another important problem was revealed: structural distress always occurs due to the in-plane bending moment at the blade root. After Cierva understood that this in-plane bending moment is very high, he decided to add another hinge (lag hinge), thus solving this problem also

[53] [p. 65]. The lag hinge allows a "forward and backward" motion of the blade in the rotating frame. This motion is called lead-lag motion (see Fig. 2.7).

The lagging hinge solved another problem, namely the "ground resonance" effect (see Fig. 2.8). When the helicopter comes close to the ground, the perpendicular component of oncoming air velocity becomes smaller, and therefore, the angle of attack becomes larger. Due to the increase in lift, the rotor produces more thrust than required and this causes the helicopter to climb. Since lagging motion reduces the tangential component of oncoming air velocity, this problem can be solved with the lagging hinge.
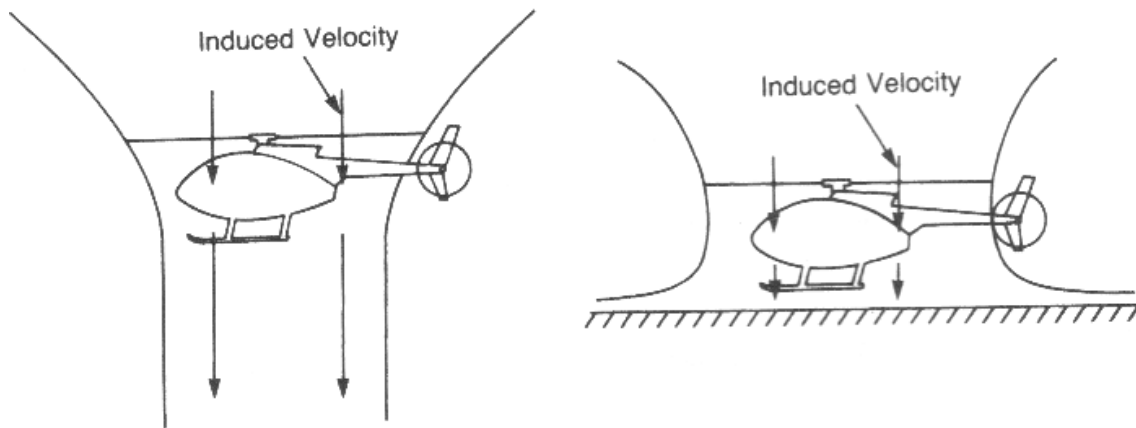
Figure 2.8: Ground Effect (Taken from [54] [p. 64])

2.7 Reference Frames

Defining reference frames is crucial to derive the dynamic and kinematic equations of the helicopter. Gravity, aircraft, hub, rotating, flapping, lead-lagging, and flapping&lead-lagging frames are used in this dissertation and G, A, H, R, F, L and LF subscripts are

23

used to refer to them, respectively. All transformation matrices used in this dissertation are defined next (see [45] for more details).

i. Transformation matrices from the aircraft frame to the hub frame and from the hub frame to the aircraft frame are

$$T_{H \leftarrow A} = \begin{bmatrix} -1 & 0 & 0 \\ 0 & 1 & 0 \\ 0 & 0 & -1 \end{bmatrix}, \qquad T_{A \leftarrow H} = \begin{bmatrix} -1 & 0 & 0 \\ 0 & 1 & 0 \\ 0 & 0 & -1 \end{bmatrix} \tag{2.34}$$

ii. Transformation matrices from the gravitational frame to aircraft frame and from the aircraft frame to the gravitational frame are

$$T_{A \leftarrow G} = \begin{bmatrix} \cos(\theta_A)\cos(\psi_A) & \cos(\theta_A)\sin(\psi_A) & -\sin(\phi_A) \\ \sin(\phi_A)\sin(\theta_A)\cos(\psi_A) - \cos(\phi_A)\sin(\psi_A) & \sin(\phi_A)\sin(\theta_A)\sin(\psi_A) + \cos(\phi_A)\cos(\psi_A) & \sin(\phi_A)\cos(\theta_A) \\ \cos(\phi_A)\sin(\theta_A)\cos(\psi_A) + \sin(\phi_A)\sin(\psi_A) & \cos(\phi_A)\sin(\theta_A)\sin(\psi_A) - \sin(\phi_A)\cos(\psi_A) & \cos(\phi_A)\cos(\theta_A) \end{bmatrix} \tag{2.35}$$

$$T_{G \leftarrow A} = \begin{bmatrix} \cos(\theta_A)\cos(\psi_A) & \sin(\phi_A)\sin(\theta_A)\cos(\psi_A) - \cos(\phi_A)\sin(\psi_A) & \cos(\phi_A)\sin(\theta_A)\cos(\psi_A) + \sin(\phi_A)\sin(\psi_A) \\ \cos(\theta_A)\sin(\psi_A) & \sin(\phi_A)\sin(\theta_A)\sin(\psi_A) + \cos(\phi_A)\cos(\psi_A) & \cos(\phi_A)\sin(\theta_A)\sin(\psi_A) - \sin(\phi_A)\cos(\psi_A) \\ -\sin(\phi_A) & \sin(\phi_A)\cos(\theta_A) & \cos(\phi_A)\cos(\theta_A) \end{bmatrix} \tag{2.36}$$

iii. Transformation matrices from the hub frame to the rotating frame and from the rotating frame to the hub frame are

$$T_{R \leftarrow H} = \begin{bmatrix} \cos(\psi_A) & \sin(\psi_A) & 0 \\ -\sin(\psi_A) & \cos(\psi_A) & 0 \\ 0 & 0 & 1 \end{bmatrix}, \qquad T_{H \leftarrow R} = \begin{bmatrix} \cos(\psi_A) & -\sin(\psi_A) & 0 \\ \sin(\psi_A) & \cos(\psi_A) & 0 \\ 0 & 0 & 1 \end{bmatrix} \tag{2.37}$$

iv. Transformation matrices from the rotating frame to the flapping frame and from the flapping frame to the rotating frame are

$$T_{F \leftarrow R} = \begin{bmatrix} \cos(\beta(\psi)) & 0 & \sin(\beta(\psi)) \\ 0 & 1 & 0 \\ -\sin(\beta(\psi)) & 0 & \cos(\beta(\psi)) \end{bmatrix}, \qquad T_{R \leftarrow F} = \begin{bmatrix} \cos(\beta(\psi)) & 0 & -\sin(\beta(\psi)) \\ 0 & 1 & 0 \\ \sin(\beta(\psi)) & 0 & \cos(\beta(\psi)) \end{bmatrix} \tag{2.38}$$

v. Transformation matrices from the rotating frame to the lead-lagging frame and from the lead-lagging frame to the rotating frame are

$$
T_{L\leftarrow R} = \begin{bmatrix} \cos(\zeta(\psi)) & -\sin(\zeta(\psi)) & 0 \\ \sin(\zeta(\psi)) & \cos(\zeta(\psi)) & 0 \\ 0 & 0 & 1 \end{bmatrix}, \quad T_{R\leftarrow L} = \begin{bmatrix} \cos(\zeta(\psi)) & \sin(\zeta(\psi)) & 0 \\ -\sin(\zeta(\psi)) & \cos(\zeta(\psi)) & 0 \\ 0 & 0 & 1 \end{bmatrix} \quad (2.39)
$$

vi. Transformation matrices from the rotating frame to the flapping&lead-lagging frame and from the flapping&lead-lagging frame to the rotating frame are

$$
T_{LF\leftarrow R} = \begin{bmatrix} \cos(\zeta(\psi))\cos(\beta(\psi)) & -\sin(\zeta(\psi)) & \cos(\zeta(\psi))\sin(\beta(\psi)) \\ \sin(\zeta(\psi))\cos(\beta(\psi)) & \cos(\zeta(\psi)) & \sin(\zeta(\psi))\sin(\beta(\psi)) \\ -\sin(\beta(\psi)) & 0 & \cos(\beta(\psi)) \end{bmatrix} \quad (2.40)
$$

$$
T_{R\leftarrow FL} = \begin{bmatrix} \cos(\zeta(\psi))\cos(\beta(\psi)) & \sin(\zeta(\psi))\cos(\beta(\psi)) & -\sin(\beta(\psi)) \\ -\sin(\zeta(\psi)) & \cos(\zeta(\psi)) & 0 \\ \cos(\zeta(\psi))\sin(\beta(\psi)) & \sin(\zeta(\psi))\sin(\beta(\psi)) & \cos(\beta(\psi)) \end{bmatrix} \quad (2.41)
$$

2.8 Blade Flexibility

For this dissertation the following general key assumptions are made to model blade flexibility.

Key Modeling Assumptions:

-Flapwise bending is dominant.

-Lagwise bending, axial displacements, and torsion are ignored.

For helicopter modeling, lumped system modeling [8] was used for blade flexibility instead of solving nonlinear partial differential equations (PDEs) and integro-differential equations (IDEs) [9, 10] or using finite element methods [11]. In this approach the blades

are divided into rigid segments joined by flapwise bending springs and dampers (see Fig. 2.9).

The flapping angle of the $(i+1)$-*th* blade segment is

$$_{i+1}\beta(\psi) = \beta(\psi) + \sum_{k=1}^{i} \delta(\psi)_k, \qquad i = 1,...,n-1 \tag{2.42}$$

where n is the number of blade segments, $\delta(\psi)_k$ is the deflection angle of the *k-th* flapwise bending spring, $_{i+1}\beta(\psi)$ is the flapping angle of the $(i+1)$-*th* blade segment, and $\beta(\psi)$ is the root flapping angle.
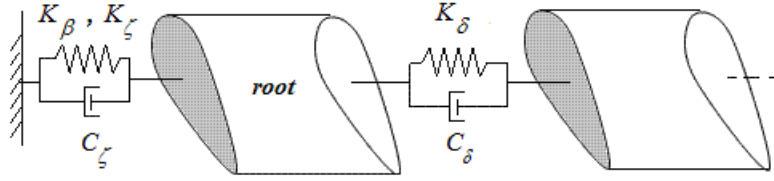
Figure 2.9: Lumped System Modeling for Blade Flexibility

It is assumed that the deflection angles are small. For helicopter modeling the blades are divided into three segments.

2.9 Multi-Blade Equations

The following general key assumptions are made to derive multi-blade equations for this dissertation.

Key Modeling Assumptions:

-The blades are identical.

-Each blade motion is synchronous.

-Higher harmonic terms are neglected.

Most helicopters have at least two blades or more and each blade moves differently than others. This is very important for helicopter dynamics and aerodynamics. Therefore, the discussions in previous sections are extended for multi-blade main rotor models. After ignoring higher harmonic terms (and also using 4 blades for the main rotor), the blade flapping, lead-lagging and flapwise bending motions are described by

$$\Theta_i(\psi) = \Theta_0 + \Theta_{1c}\cos(\psi_i) + \Theta_{1s}\sin(\psi_i) + \Theta_{0d}(-1)^i \tag{2.43}$$

where the blade azimuth angle is

$$\psi_i = \psi - (\pi/2)(i-1), \ i = 1,...,4 \tag{2.44}$$

and Θ is the generic notation for any of the three angles mentioned in the above while Θ_0, Θ_c, Θ_s, and Θ_d are collective, two cyclic and differential components, respectively. Synchronous flapping motion is illustrated in Fig. 2.10 (see [47][pp. 102-106] for more discussion).
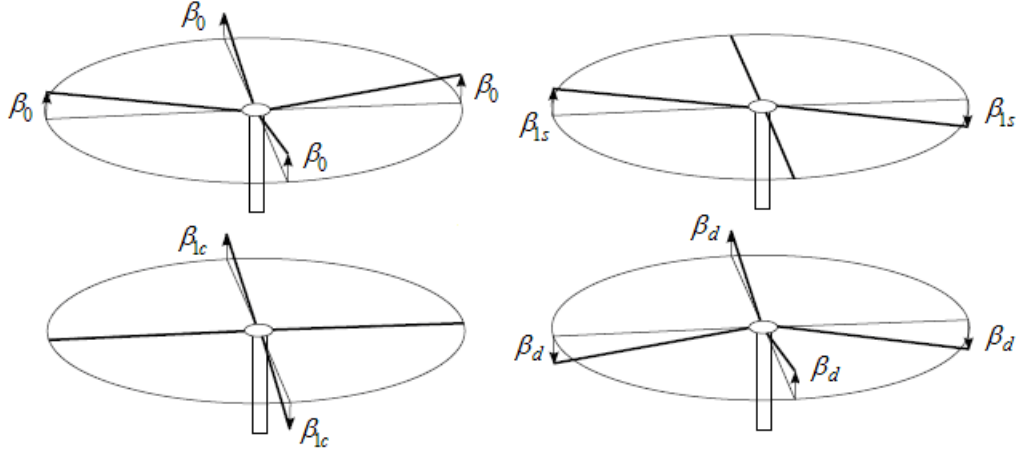
Figure 2.10: Synchronous Blade Flapping

2.10 Fuselage Aerodynamics

For this dissertation the following general key assumptions are made to derive fuselage aerodynamic equations.

Key Modeling Assumptions:

-The fuselage is in the uniform downwash of the main rotor.

-Stationary incompressible aerodynamics exists.

-The fuselage is a regular body which is a good assumption for slender body theory.

-The linear velocities are much larger than the velocities due to the fuselage rotation.

Fuselage aerodynamic modeling is generally done computationally or experimentally. However, in this dissertation an analytical approach [55] is used, derived using slender body theory, to obtain fuselage aerodynamic equations. For a body of revolution (Fig. 2.11), the infinitesimal aerodynamic forces and moments acting on a fuselage strip of length ds are

$$d\vec{f}_{Lift} = \rho \vec{V}_\perp V_1 2\pi R_f(s) \frac{d}{ds} R_f(s), \qquad d\vec{M}_{Lift} = \vec{r}_{AS} \otimes d\vec{f}_{Lift} \tag{2.45}$$

$$d\vec{f}_{Drag} = \frac{1}{2}\rho |\vec{V}| \vec{V} 2 R_f(s) c_{d_f} + \frac{1}{2}\rho |\vec{V}_\perp| \vec{V}_\perp 2 R_f(s) c_{d_p} \, ds, \qquad d\vec{M}_{Drag} = \vec{r}_{AS} \otimes d\vec{f}_{Drag} \tag{2.46}$$

where $R_f(s)$ is the fuselage radius at distance s along the fuselage reference line (FRL) measured from the nose, $\vec{r}_{AS}$ is the position vector of s, $\vec{V}$ is the local air velocity, $\vec{V}_\perp$ and V_1 are the local air velocity's components perpendicular and parallel to FRL, respectively.
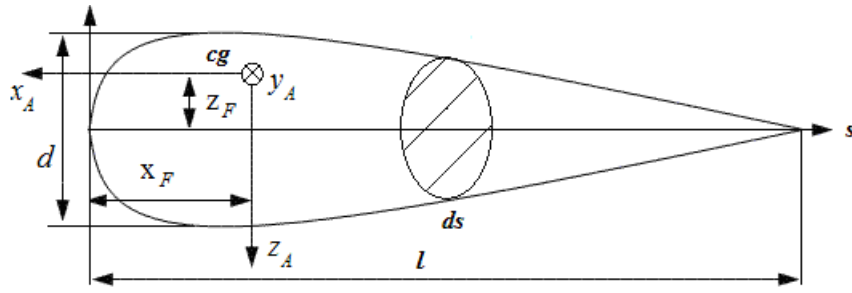
Figure 2.11: Fuselage Shape

The pressure drag coefficient, c_{d_p}, and the skin friction drag coefficient, c_{d_f}, are estimated from [56] [pp. 2.1, 3.9]. The profile function of the fuselage radius is

$$R_f(s) = 2d\left(\sqrt{\frac{s}{l}} - \frac{s}{l} \right) \tag{2.47}$$

where l and d are the fuselage length and height, respectively (see Fig. 2.11). Assuming that the fuselage is in uniform downwash, $\vec{V}$ is

$$\vec{V} = -{}^{I}\vec{V}_{S} + {}^{I}\vec{V}_{\lambda_{0}} \tag{2.48}$$

where the kinematic velocity at distance s on the FRL and the uniform downwash are

$$
{}^{I}\vec{V}_{S} = {}^{I}\vec{V}_{A} + {}^{I}\vec{\omega}^{A} \otimes \vec{r}_{AS}, \qquad {}^{I}_{A}V_{\lambda_{0}} = \begin{bmatrix} 0 & 0 & \lambda_{0} \end{bmatrix}^{T} \tag{2.49}
$$

where $\vec{r}_{AS}$ in aircraft frame is ${}_{A}r_{AS} = R\begin{bmatrix} x_{F} - s & 0 & z_{F} \end{bmatrix}^{T}$. Integrating the infinitesimal aerodynamic forces and moments along the fuselage span, the fuselage aerodynamic force and moment are obtained.

2.11 Landing Gear Aerodynamics

The following general key assumptions are made to derive landing gear aerodynamic equations for this dissertation.

Key Modeling Assumptions:

-Main rotor inflow effect on the landing gear is ignored.

-Stationary incompressible aerodynamics exists.

-The linear velocities are much larger than the velocities due to the landing gear rotation.

-Drag decrease due to the landing gear being retractable is ignored.

Rough drag coefficients for several landing gear configurations are given in Fig. 2.12. For the case helicopter "Puma SA 330", the landing gear is the semi-retracting tricycle type, with twin wheels on each unit, and all of the units (the nose and tail units are under the fuselage) are *partially exposed* when retracted. The drag coefficient is chosen with respect to the nose and tail wheels' areas, strut shape, and *e*/*d* ratio (see Fig. 2.12). The nose and tail units (landing gear) are modeled as a single rigid body to simplify

derivation of related equations. Specifically, a single rigid body is considered at the geometric center of the three units and the corresponding drag force and moment are computed and placed at this center. After determining the landing gear parameters, the landing gear drag force and moment (around helicopter's center of gravity) are

$$\vec{D}_{lg} = \frac{1}{2}\rho \left| {}^{I}\vec{V}_T \right| {}^{I}\vec{V}_T S_{lg} c_{d_{lg}}, \quad \vec{M}_{lg} = \vec{r}_T \otimes \vec{D}_{lg} \tag{2.50}$$
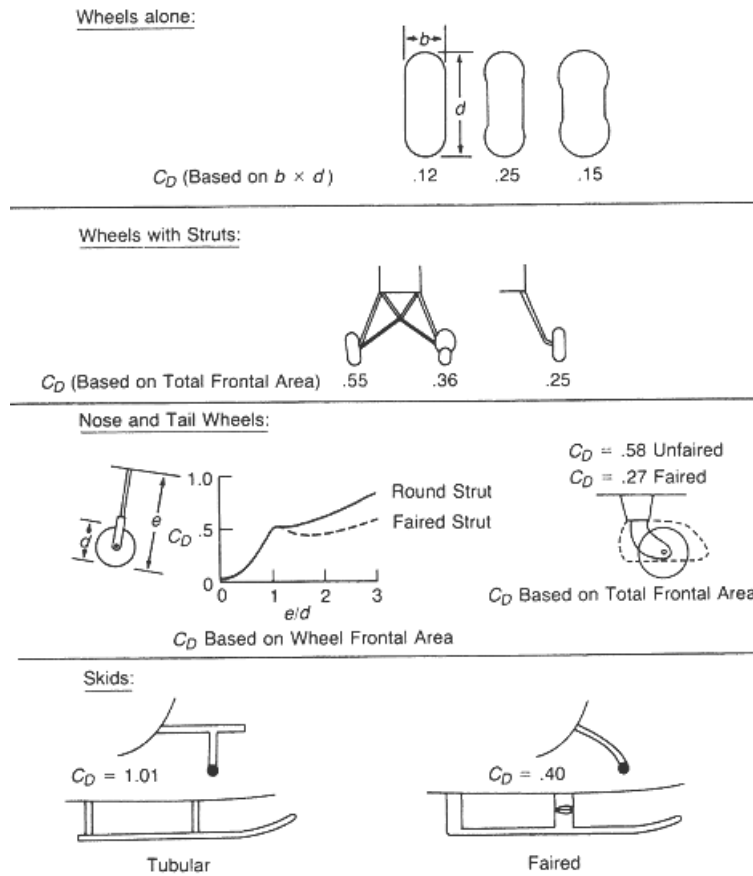
Figure 2.12: Landing Gear Drag (Taken from [54] [p. 303])

31

2.12 Empennage Aerodynamics

For this dissertation the following general key assumptions are made to derive empennage aerodynamic equations.

Modeling Assumptions:

-The tail rotor does not flap, is not canted, creates a force in anti-torque direction, and its inflow is ignored.

-Interactional aerodynamics between tail rotor and main rotor is ignored.

- The linear velocities are much larger than the velocities due to the tail rotor hub&shaft and horizontal stabilizer rotations.
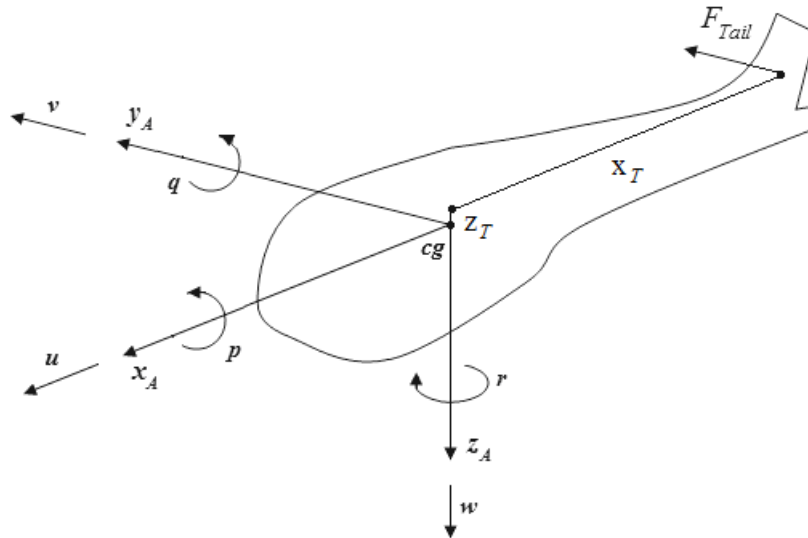
Figure 2.13: Tail Rotor Subsystem

The tail rotor subsystem is illustrated in Fig 2.13. The flapping motion can also be modeled for the tail rotor, but it does not result in important contributions to forces and

moments. Therefore, the flapping motion for the tail rotor is not modeled for this dissertation. Using the tail rotor modeling assumptions, its thrust is

$$_A F_{Tail} = \begin{bmatrix} 0 & K_T \theta_T & 0 \end{bmatrix}^T \tag{2.51}$$

where K_T is the maximum thrust coefficient, chosen to keep the collective pitch angle of tail rotor, $\theta_T \leq 1$. The tail rotor moment around helicopter's center of gravity is

$$_A M_{Tail} = \begin{bmatrix} z_T K_T \theta_T & 0 & x_T K_T \theta_T \end{bmatrix}^T \tag{2.52}$$
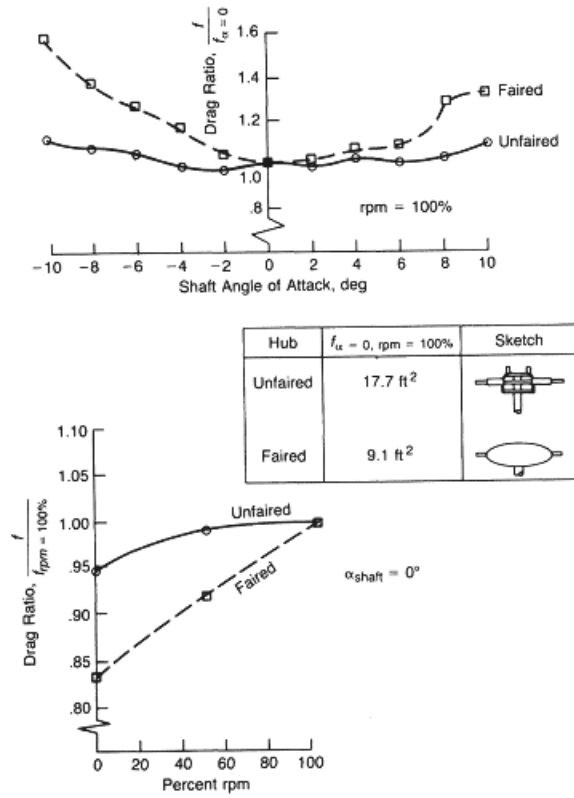
Figure 2.14: Tail Rotor Hub&Shaft Drag (Taken from [54] [p. 299])

The tail rotor hub and shaft's frontal area and drag coefficient are given for several helicopters in [54] [p. 298] for the case of 0% rpm. The effects of tail rotor shaft angle of attack and percentage rpm with respect to being unfaired or faired are given in Fig. 2.14. For the Puma SA 330 helicopter the drag coefficient is 0.98 for 0% rpm (static case). The hub&shaft is unfaired and the shaft angle of attack is assumed zero, which yields the drag coefficient equal to 1.03 (0.98*1/0.95).

The tail rotor hub&shaft drag force and moment are

$$\vec{D}_{h\&s} = \frac{1}{2}\rho \left| {}^{I}\vec{V}_{T} \right| {}^{I}\vec{V}_{T} S_{h\&s} c_{d_{h\&s}}, \quad \vec{M}_{h\&s} = \vec{r}_{T} \otimes \vec{D}_{h\&s} \tag{2.53}$$

where the frontal area and drag coefficient of the tail rotor hub&shaft, $S_{h\&s}$ and $c_{d_{h\&s}}$, are estimated from [54] [pp. 298, 299] (Puma SA 330 and Bo 105 have unfaired and faired tail rotor hub, respectively). The position of the tail rotor (and also the horizontal stabilizer) with respect to the helicopter's center of gravity, and the local air velocity of the tail rotor are, respectively,

$$_{A}r_{T} = \begin{bmatrix} -x_{T} & 0 & -z_{T} \end{bmatrix}^{T}, \quad {}^{I}\vec{V}_{T} = - {}^{I}\vec{V}_{A} - {}^{I}\vec{\omega}^{A} \otimes \vec{r}_{T} \tag{2.54}$$

The horizontal stabilizer has an aerodynamic shape which is similar with the main rotor blades shape. Using the blade element theory and considering the taper ratio of the horizontal stabilizer along its span, the infinitesimal aerodynamic lift and drag forces acting on any horizontal stabilizer blade section are

$$d\vec{L}_{hs} = \frac{1}{2}\rho V_{hs}^{2} c_{l_{hs}} c_{hs} dx_{hs} \hat{V}_{n_{hs}}, \quad d\vec{D}_{hs} = \frac{1}{2}\rho V_{hs}^{2} c_{d_{hs}} c_{hs} dr_{hs} \hat{V}_{total_{hs}} \tag{2.55}$$

where V_{hs} is the oncoming horizontal stabilizer blade section airspeed, $c_{l_{hs}}$ (flowfield is also effective on its magnitude [47] [p.150]) and $c_{d_{hs}}$ are the lift and drag coefficients of any horizontal stabilizer blade section, respectively (see [47] [pp. 149-151, 265] for more details), and x_{hs} is the distance from the connection point between the fuselage and horizontal stabilizer to any horizontal stabilizer blade section. The horizontal stabilizer blade chord length, c_{hs}, is

$$c_{hs} = c_{hs_0} - k_{hs}\, x_{hs} \tag{2.56}$$

where k_{hs} is the linear decrease ratio of the horizontal stabilizer chord length along its span. The infinitesimal moment of the horizontal stabilizer section around helicopter's center of gravity is

$$\vec{M}_{hs} = \vec{r}_{hs} \otimes (d\vec{L}_{hs} + d\vec{D}_{hs}) \tag{2.57}$$

where $\vec{r}_{hs}$ is the position vector of any horizontal stabilizer blade section with respect to the helicopter's center of gravity.

2.13 Momentum Theory and Inflow

For this dissertation the following general key assumptions are made to apply momentum theory for the flight conditions examined.

Key Modeling Assumptions:

-There is no sudden increase or decrease (i.e. discontinuity) in air velocity while passing through the rotor disc.

-Stationary incompressible aerodynamics exists.

2.13.1 Momentum Theory for Hover and Climbing

When the air passes through the rotor disc, there is a jump in the pressure. This jump creates thrust which is equal to

$$T = \Delta p \; S \tag{2.58}$$

In Fig. 2.15 S_0, S_1, S_3 are upstream, rotor disc, and downstream areas, respectively. In this moving control volume, for far upstream the pressure is the ambient pressure, p_∞, and the velocity is the climbing velocity, v_c. Stations 1 and 2 include the regions before and after rotor disc in control volume, respectively. Some additional mass flow, $\dot{m}_q$, enters the moving control volume. In this streamtube v_i and v_3 are referring to the velocity increase for airflow around the rotor disc and far downstream, respectively. It is important that there is no velocity jump at the rotor disc, but the pressure increases (Δp) while airflow is passing through the rotor disc.
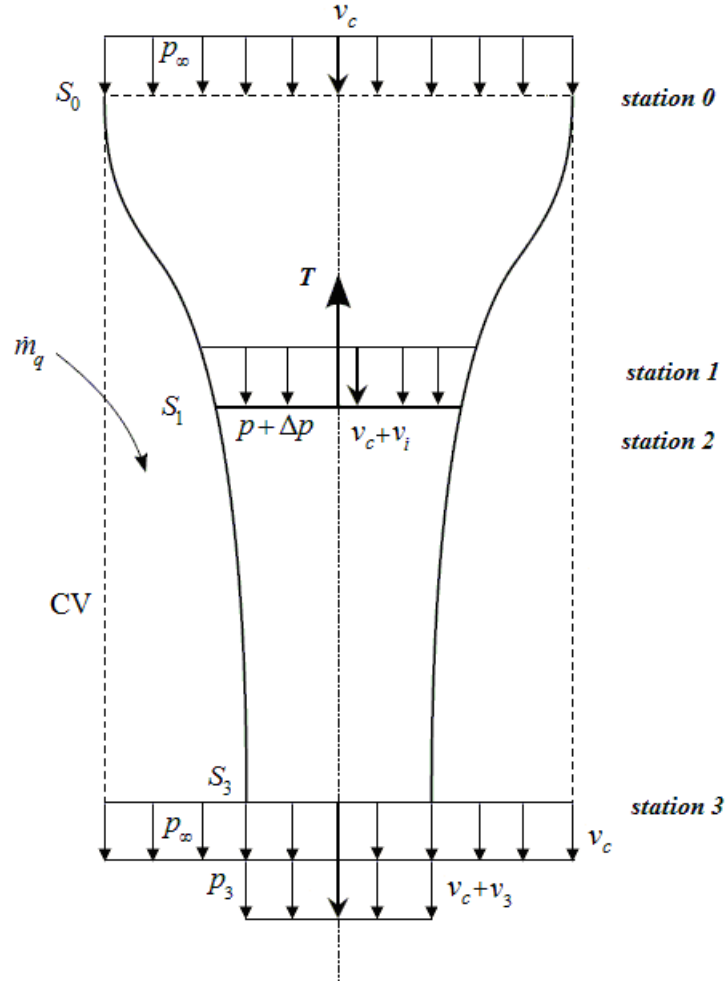
Figure 2.15: Momentum Theory for Axial Flight

The continuity equation for the cylindrical control volume between stations 0-3 (see Fig. 2.15) is

$$\rho S_0 v_c + \dot{m}_q = \rho(S_0 - S_3)v_c + \rho S_3(v_c + v_3) \tag{2.59}$$

The mass flow coming from the outer cylindrical control volume is obtained using the continuity equation (Eq. 2.59) and it is

$$\dot{m}_q = \rho\, S_3\, v_3 \tag{2.60}$$

The continuity equation between stations 2-3 is

$$\rho A(v_c + v_i) = \rho S_3 (v_c + v_3) \tag{2.61}$$

Including mass flow coming from the outer cylindrical control volume and using entrance and exit pressures and velocities, the force equilibrium equation for the vertical direction is

$$T = -\rho S_0 v_c^2 - S_0 p_\infty - (\rho S_3 v_3) v_c + \rho (S_0 - S_3) v_c^2 + (S_0 - S_3) p_\infty + p_3 S_3 + \rho S_3 (v_c + v_3)^2 \tag{2.62}$$

Using the continuity equation (Eq. 2.61) and the thrust equation (Eq. 2.58), the pressure jump at the rotor disc by eliminating the cross section areas is

$$\Delta p = \frac{(v_c + v_i)}{(v_c + v_3)} (p_3 - p_\infty) + \rho (v_c + v_i) v_3 \tag{2.63}$$

The thrust without eliminating the cross sections is

$$T = S_3 (p_3 - p_\infty) + \rho A (v_c + v_i) v_3 \tag{2.64}$$

Applying the Bernoulli equation to the stations 0-1 and 2-3, the results are

$$p_\infty + \frac{1}{2} \rho v_c^2 = p + \frac{1}{2} \rho (v_c + v_i)^2 \tag{2.65}$$

$$p + \Delta p + \frac{1}{2} \rho (v_c + v_i)^2 = p_3 + \frac{1}{2} \rho (v_c + v_3)^2 \tag{2.66}$$

To find an alternative equation for pressure jump at the rotor disc, subtract Eq. 2.66 from Eq. 2.65 and the result is

$$\Delta p = p_3 - p_\infty + \rho (v_c + \frac{1}{2} v_3) v_3 \tag{2.67}$$

Using Eqs. 2.67 and 2.63, the resulting equation related to the pressure jump at the rotor disc is

$$\left(p_3 - p_\infty\right)\frac{v_3 - v_i}{v_c + v_3} = \rho v_3\left(v_i - \frac{1}{2}v_3\right) \tag{2.68}$$

If it is assumed that $p_3 = p_\infty$, the induced velocity and rotor thrust are

$$v_i = \frac{1}{2}v_3, \qquad T = 2\rho S_1\left(v_c + v_i\right)v_i \tag{2.69}$$

2.13.2 Working States for Vertical Flight

For hover the induced velocity using the thrust (Eq. 2.68) is

$$v_{i0} = \sqrt{\frac{T}{2\rho S_1}} \tag{2.70}$$

For hover the thrust is also equal to the helicopter weight. For climbing this equality is not valid because of inertias and fuselage drag. However, if these effects are ignored, hover and climb can be better compared. Assuming that the thrust is equal to the helicopter weight for the climb (assumed to be a uniform climb), the induced velocity at the rotor disc is

$$v_i = -\frac{v_c}{2} \pm \sqrt{\left(\frac{v_c}{2}\right)^2 + v_{i0}^2} \tag{2.71}$$

There are two solutions for the induced velocity, but the positive solution is physically correct for climbing. Nondimesionalizing Eq. 2.71, the induced velocity for climbing is

$$\left(\frac{v_i}{v_{i0}}\right) = -\frac{1}{2}\left(\frac{v_c}{v_{i0}}\right) + \frac{1}{2}\sqrt{\left(\frac{v_c}{v_{i0}}\right)^2 + 4} \tag{2.72}$$

Eq. 2.72 is valid for climb velocities ratios $v_c/v_{i0} \geq 0$ and the rotor state is defined as *normal working state* for this particular case.

The thrust equation and induced velocity for descent ($-v_c$ is used to emphasize descent) are given by

$$T = -2\rho S_1 (v_c + v_i) v_i \tag{2.73}$$

$$\left(\frac{v_i}{v_{i0}}\right) = -\frac{1}{2}\left(\frac{v_c}{v_{i0}}\right) - \frac{1}{2}\sqrt{\left(\frac{v_c}{v_{i0}}\right)^2 - 4} \tag{2.74}$$
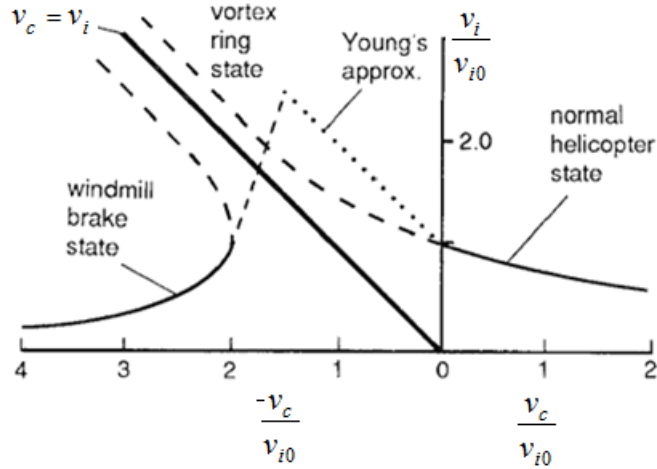
Figure 2.16: Working States for Axial Flight (Taken from [47] [p. 118])

Using Eq. 2.74 it is seen that the induced velocity is real just for $v_c/v_{i0} \leq -2$ and this particular condition is defined as *windmill break state*. All working states are illustrated in Fig. 2.16 (see [47] for more details).

2.13.3 Momentum Theory for Forward Flight

Applying the conservation of momentum and Bernoulli's theory (see [48, 49, 51] for more details), the air velocity of the ultimate slipstream (see Fig. 2.17), rotor thrust, and mass flow rate are

$$v_3 = 2v_i, \quad T = 2\dot{m}v_i, \quad \dot{m} = \rho S_1 U \tag{2.75}$$
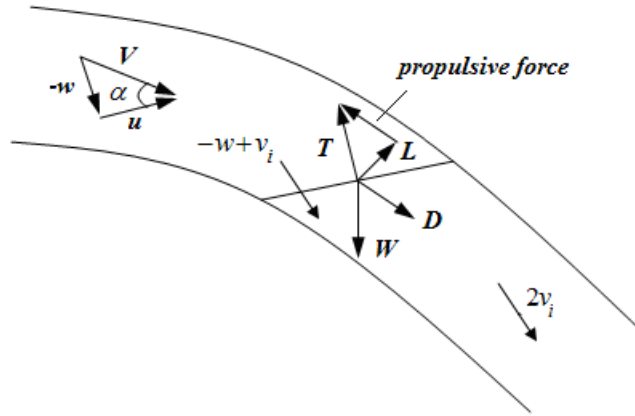
Figure 2.17: Momentum Theory for Forward Flight

In Fig. 2.17 T, L, D are main rotor thrust, lift and drag, respectively and W is the helicopter weight. The velocity at the rotor disc U is

$$U = \sqrt{u^2 + v^2 + \left(-w + v_i\right)^2} \tag{2.76}$$

The rotor thrust for forward flight using the momentum theory and the formula for U is

$$T = 2\rho S_1 v_i \sqrt{u^2 + v^2 + \left(-w + v_i\right)^2} \tag{2.77}$$

For much faster forward velocities such that $V_\infty = \sqrt{u^2 + v^2 + w^2} \gg v_i$, the thrust equation is

$$T = 2\rho S_1 v_i V_\infty \qquad (2.78)$$

Nondimensionalizing the rotor thrust (Eq. 2.77) by the rotor tip path speed ΩR and using the fact that the disc area is πR_d^2, the nondimensional thrust becomes

$$\frac{T}{2\rho\pi\ \Omega^2 R_d^4} = \lambda_0 \sqrt{\hat{u}^2 + \hat{v}^2 + \left(-\hat{w} + \lambda_0\right)^2} \qquad (2.79)$$

2.13.4 Linear Inflow Model

The main rotor sucks in air molecules while rotating. This effect is important for the main rotor aerodynamics and should be modeled. There are many approaches in the helicopter literature to include this effect. Since creating control oriented helicopter models is one of the major goals of this dissertation, linear static inflow model is selected. Its cyclic components, λ_c, λ_s, are (see [51] [p. 160], Pitt&Peters)

$$\lambda_c = \lambda_0 \frac{15\pi}{23} \tan\left(\frac{\chi}{2}\right), \qquad \lambda_s = 0, \qquad \chi = \tan^{-1}\left(\frac{\hat{u}}{\hat{w} + \lambda_0}\right) \qquad (2.80)$$

where χ is the wake skew angle. The uniform component of the linear inflow, λ_0, is computed numerically using the momentum theory and it is

$$\frac{T}{2\rho\pi\ \Omega^2 R_d^4} = \lambda_0 \sqrt{\hat{u}^2 + \hat{v}^2 + \left(\lambda_0 - \hat{w}\right)^2} \qquad (2.81)$$
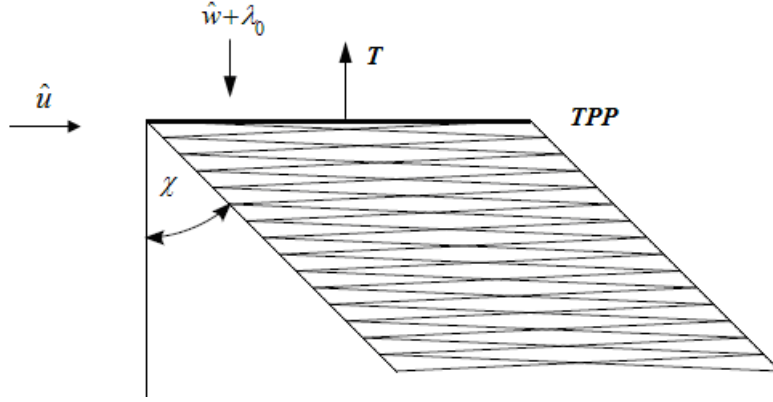
Figure 2.18: Wake Skew Angle

There is one other famous linear inflow approach in the helicopter literature, namely the dynamic inflow theory developed by Pitt&Peters. In this theory inflow parameters change with time as follows [47][p.128]

$$
\left[M \right] \begin{Bmatrix} \dot{\lambda}_0 \\ \dot{\lambda}_c \\ \dot{\lambda}_s \end{Bmatrix} + \left[L \right]^{-1} \begin{Bmatrix} \lambda_0 \\ \lambda_c \\ \lambda_s \end{Bmatrix} = \begin{Bmatrix} C_T \\ C_L \\ C_M \end{Bmatrix}
\tag{2.82}
$$

where the matrices M and L are the mass and gain functions, while C_T, C_L and C_M are the thrust, rolling and pitching moment perturbations, respectively. For advanced aerodynamics oriented design this theory is widely used, but for this dissertation control oriented modeling is a priority and therefore, the linear static inflow theory is preferred.

2.14 Model Simplification

At the end of this modeling process, implemented using Maple, we find the nonlinear governing equations of motion in implicit form:

$$
f(\dot{x}, x, \upsilon) = 0
\tag{2.83}
$$

where $f \in \mathbb{R}^{44}$, $x \in \mathbb{R}^{41}$ and $\upsilon \in \mathbb{R}^4$ for straight level flight and $f \in \mathbb{R}^{45}$, $x \in \mathbb{R}^{41}$ and $\upsilon \in \mathbb{R}^4$ for maneuvering flight. Note that the discrepancy between the size of f (44) and the size of x (41) is due to the three static downwash equations for straight level flight. For maneuvering flight there is an additional flight path angle algebraic equation.

For the helicopter model, 44 and 45 governing equations of motion are obtained for straight level and maneuvering flights, respectively. There are 9 fuselage equations (6 Newton-Euler and 3 kinematic equations), 8 flapping equations, 8 lagging equations, 16 blade flexibility equations (3 blade segments are used for blade flexibility), and 3 main rotor downwash equations for straight level flight. There is an additional flight path angle equation for maneuvering flight.

Unfortunately the number of terms in Eq. 2.83 is huge (of the order 10^5). To reduce this number a new ordering scheme (modified version of [57]) is applied. The idea behind this method is to neglect terms whose relative magnitude with respect to the largest term in an expression is smaller than a specific amount. To apply the ordering scheme to the dynamic equations, each term is assigned an order of magnitude based on physical considerations. For example the trim value of β is $3-6$ degrees [51] [p. 174] and the trim value of ζ is small [51] [p. 195]. The trim values of collective β and ζ are generally larger than the trim values of cyclic β and ζ. The trim values of differential β and ζ are zero. Therefore, their orders are chosen as

$$\left|\beta_0\right| = \left|\zeta_0\right| = 0.2\,\text{rad}, \quad \left|\beta_c\right| = \left|\beta_s\right| = \left|\zeta_c\right| = \left|\zeta_s\right| = 0.1\,\text{rad}, \quad \left|\beta_d\right| = \left|\zeta_d\right| = 0.1\,\text{rad} \tag{2.84}$$

The orders of u, v, w are determined by ignoring p, q, r. For many helicopters (e.g. Puma SA 330, Bo 105) the maximum forward speed is around 70 m/s. Therefore, the

order of u is chosen as 70 m/s. Because of severe drag limitation, the order of v is chosen as 35 m/s. Since w is generally smaller than 12 m/s, the order of w is chosen as 12 m/s. The order of blade tip speed is around 202.5 m/s for many helicopters. Therefore, the orders of nondimensional linear velocities are $\hat{u} = 0.35\,(70/202.5)$, $\hat{v} = 0.18\,(35/202.5)$, $\hat{w} = 0.06\,(12/202.5)$. The orders of p, q, r and $(d/dt)p, (d/dt)q, (d/dt)r$ are chosen as $(\pi/2)(1/s)$ and $(44.4\,\pi/2)(1/s^2)$. The maximum main rotor speed is chosen 44.4 rad/s (for Bo 105) and it is used to nondimensionalize angular velocities and accelerations. This value is selected based on a literature review of several helicopters: 44.4 rad/s was the maximum value over all of the helicopters with published data. The downwash at hover is assumed to be maximum. This was decided after many numerical experiments carried out by us before applying the ordering scheme. Therefore, λ_0's order is chosen as 0.06 (12/202.5). The order of λ_c is chosen same with λ_0. The bounds of main rotor control inputs are given in [54] [pp. 684-701]. The maximum values for θ_0 and θ_c are around 20 degrees. Since θ_c takes negative and positive values and θ_s has same order with θ_c, their orders are chosen as

$$|\theta_0| = 0.35\,\text{rad}, \qquad |\theta_c| = 0.175\,\text{rad}, \qquad |\theta_s| = 0.175\,\text{rad} \qquad (2.85)$$

Before applying the ordering scheme, the dynamic equations are nondimensionalized [48] [p. 142]. The order of each helicopter quantity in nondimensional fashion is listed in Table 2.1. The orders of lumped system parameters are defined using energy approaches and this approach is summarized next. First, the total force acting on a blade was found using rigid blade model parameters and it was distributed linearly over the blade span. Using Euler-Bernoulli beam theory, the corresponding weighted (i.e. averaged)

displacement distribution was found for each of the flexible blade segments (the root segment was assumed rigid). Then these averages are used to compute the orders for flapwise bending angles (note: the average is placed at the midpoint of each segment). Finally, the orders of flapwise bending spring stiffness coefficient and damper damping ratio were obtained using orders of flapwise bending angles, flapping angles and flapping spring stiffness coefficient (It was assumed that there is an inverse relation between the artificial spring stiffness coefficient and bending angle, see Appendix A.1 for more details).

Table 2.1: Nondimensional Orders of Helicopter Parameters

Symbol(s)	Order	Symbol(s)	Order	Symbol(s)	Order
$\hat{u}$	0.35	$_2\ddot{\beta}_c, \, _2\dot{\beta}_c, \, _2\beta_c$	0.15	k_ζ	0.25
$\hat{v}$	0.18	$_2\ddot{\beta}_s, \, _2\dot{\beta}_s, \, _2\beta_s$	0.15	c_ζ	0.1
$\hat{w}$	0.06	$_2\ddot{\beta}_d, \, _2\dot{\beta}_d, \, _2\beta_d$	0.15	k_T	0.064
$\hat{p},\hat{q},\hat{r}$	0.035	$_3\ddot{\beta}_0, \, _3\dot{\beta}_0, \, _3\beta_0$	0.45	e	0.15
$\dot{\hat{p}},\dot{\hat{q}},\dot{\hat{r}}$	0.035	$_3\ddot{\beta}_c, \, _3\dot{\beta}_c, \, _3\beta_c$	0.225	λ_0, λ_c	0.06
θ_0	0.35	$_3\ddot{\beta}_s, \, _3\dot{\beta}_s, \, _3\beta_s$	0.225	γ	9
θ_c, θ_s	0.18	$_3\ddot{\beta}_d, \, _3\dot{\beta}_d, \, _3\beta_d$	0.225	$\cos(\psi)$	1
θ_T	1	$\ddot{\zeta}_0, \dot{\zeta}_0, \zeta_0$	0.2	$\sin(\psi)$	1
θ_{tw}	-0.14	$\ddot{\zeta}_c, \dot{\zeta}_c, \zeta_c$	0.1	$\hat{d}$	0.4
$\ddot{\beta}_0, \dot{\beta}_0, \beta_0$	0.2	$\ddot{\zeta}_s, \dot{\zeta}_s, \zeta_s$	0.1	$\hat{l}$	1.8
$\ddot{\beta}_c, \dot{\beta}_c, \beta_c$	0.1	$\ddot{\zeta}_d, \dot{\zeta}_d, \zeta_d$	0.1	$\hat{z}_F$	0.07
$\ddot{\beta}_s, \dot{\beta}_s, \beta_s$	0.1	k_δ	0.2	$\hat{x}_F$	0.57
$\ddot{\beta}_d, \dot{\beta}_d, \beta_d$	0.1	c_δ	0.1	$\hat{z}_T$	0.35
$_2\ddot{\beta}_0, \, _2\dot{\beta}_0, \, _2\beta_0$	0.3	k_β	0.25	$\hat{x}_T$	1.2

$(\dot{x} = (d/d\psi)x(\psi))$

Table 2.2: Number of Terms Before and After Applying The New Ordering Scheme

	X	Y	Z	L	M	N
Original	182444	182444	74489	326312	326312	226157
New	3490	3410	385	1700	1690	2471

This ordering scheme implemented using Maple resulted in significant reduction in the number of terms. Table 2.2 gives these numbers for external forces (X, Y, Z) and moments (L, M, N) before and after applying the ordering scheme to helicopter model with 1% specific amount.

CHAPTER 3:

Trim, Linearization, and Model Validation

3.1 Trim

3.1.1 Straight Level Flight

For this particular case trim is defined as the condition for which straight level flight with constant velocity is achieved. For the helicopter model 25 trim equations (3 force and 3 moment helicopter equations, 8 flapping and lagging equations, 8 flapwise bending equations, and 3 main rotor downwash equations) and 25 unknowns are obtained for straight level flight (i.e. 0=0 equations are ignored). The trim values of angular velocities and yaw angle are equal to zero. The helicopter linear velocities can be written as functions of V_A and roll and pitch angles of the helicopter. The vector of trim unknowns in nondimensional fashion is

$$x_0 = [\underbrace{\theta_{0_0}, \theta_{c_0}, \theta_{s_0}, \theta_{T_0}}_{controls}, \underbrace{\phi_{A_0}, \theta_{A_0}}_{Euler}, \underbrace{\beta_{0_0}, \beta_{c_0}, \beta_{s_0}, \beta_{d_0}}_{flapping}, \underbrace{{}_2\beta_{0_0}, {}_2\beta_{c_0}, {}_2\beta_{s_0}, {}_2\beta_{d_0}, {}_3\beta_{0_0}, {}_3\beta_{c_0}, {}_3\beta_{s_0}, {}_3\beta_{d_0}}_{flapwise\ bending}, \underbrace{\varsigma_{0_0}, \varsigma_{c_0}, \varsigma_{s_0}, \varsigma_{d_0}}_{lead-lagging}, \underbrace{\chi_0, \lambda_{0_0}, \lambda_{c_0}}_{downwash}]^T$$

(3.1)

where all trim angles are given in radians. Matlab's *f*solve command was used to solve the 25 nondimensionalized trim equations for hover and different straightforward velocities. The results thus found were verified by inserting them into the governing equations of motion obtained after the application of the new ordering scheme. Very small numbers (around 10^{-10}) were obtained showing that the trimming procedure is correct. For some specific flight conditions, such as hover ($V_A = 1$ kt is assumed hover for numerical reasons) and $V_A = 80$ kts, the trims are

$$_{hover}\,x_0 = [\underbrace{0.2686,0.0094,-0.0255,0.0952}_{\theta_{0_0},\theta_{c_0},\theta_{s_0},\theta_{T_0}}\,,\underbrace{-0.0057,0.0238}_{\phi_{A_0},\theta_{A_0}}\,,\underbrace{0.0472,\,0.0230,0.0021,0}_{\beta_{0_0},\beta_{c_0},\beta_{s_0},\beta_{d_0}}\,,\underbrace{0.0681,0.0283,0.0032,0}_{2\beta_{0_0},2\beta_{c_0},2\beta_{s_0},2\beta_{d_0}}\,,$$

$$\underbrace{0.0855,0.0319,0.0045,0}_{3\beta_{0_0},3\beta_{c_0},3\beta_{s_0},3\beta_{d_0}}\,,\underbrace{0.0172,-0.0009,-0.0027,0}_{\zeta_{0_0},\zeta_{c_0},\zeta_{s_0},\zeta_{d_0}}\,,\underbrace{0.0237,0.5579,0.0014}_{\chi_0,\lambda_{0_0},\lambda_{c_0}}]^T$$

$$(3.2)$$

$$_{80kts}\,x_0 = [\underbrace{0.2493,0.0243,-0.1147,0.0594}_{\theta_{0_0},\theta_{c_0},\theta_{s_0},\theta_{T_0}}\,,\underbrace{-0.0035,0.0312}_{\phi_{A_0},\theta_{A_0}}\,,\underbrace{0.0524,0.0327,-0.0005,0}_{\beta_{0_0},\beta_{c_0},\beta_{s_0},\beta_{d_0}}\,,\underbrace{0.0660,0.0432,-0.0097,0}_{2\beta_{0_0},2\beta_{c_0},2\beta_{s_0},2\beta_{d_0}}\,,$$

$$\underbrace{0.0729,0.0553,-0.0276,0}_{3\beta_{0_0},3\beta_{c_0},3\beta_{s_0},3\beta_{d_0}}\,,\underbrace{0.0123,-0.0048,-0.0048,0}_{\zeta_{0_0},\zeta_{c_0},\zeta_{s_0},\zeta_{d_0}}\,,\underbrace{1.4617,0.0162,0.0298}_{\chi_0,\lambda_{0_0},\lambda_{c_0}}]^T$$

$$(3.3)$$

3.1.2 Maneuvering Flight

In this study level banked turn without sideslip and helical turn without sideslip are examined (see [45, 47, 51, 54, 58-60] for more details). For maneuvering flight the aircraft linear velocities are (see Fig. 3.1)

$$\begin{bmatrix} u & v & w \end{bmatrix}^T = \begin{bmatrix} V_A \cos(\alpha_F)\cos(\beta_F) & V_A \sin(\beta_F) & V_A \sin(\alpha_F)\cos(\beta_F) \end{bmatrix}^T \tag{3.4}$$

were fuselage angle of attack, α_F, and sideslip, β_F, are given by

$$\alpha_F = \tan^{-1}(w/u), \qquad \beta_F = \sin^{-1}(v/V_A) \tag{3.5}$$
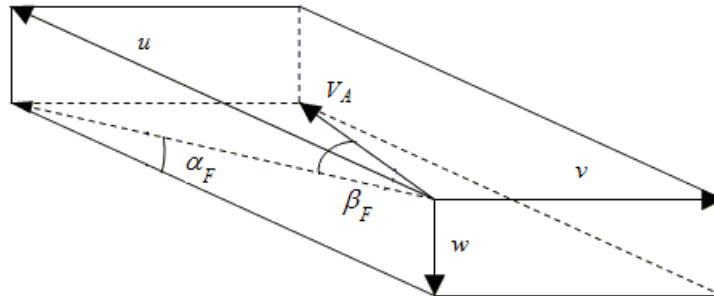
Figure 3.1: Fuselage Angle of Attack and Sideslip

Level banked turn is a maneuver in which the helicopter banks towards the center of the turning circle. For helicopters the fuselage roll angle, ϕ_A, is in general slightly different than the bank angle, ϕ_B. For coordinated banked turn $\phi_A = \phi_B$, but this is not the focus of this work. A picture describing these angles for a particular case ($\theta_A = 0$) is given in Fig. 3.2, where $F_{resultant}$ is the sum of the gravitational force (W) and the centrifugal force (F_{cf}).
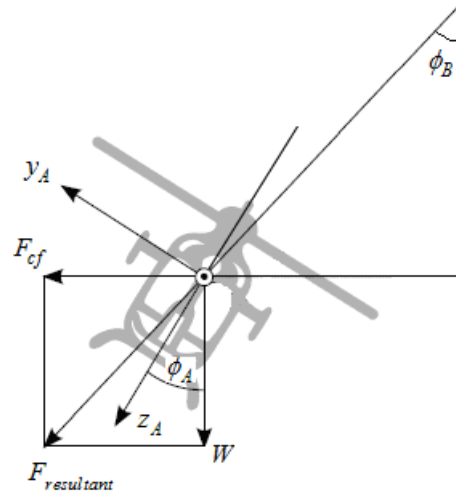
Figure 3.2: Level Banked Turn

Helical turn is a maneuver in which the helicopter moves along a helix with constant speed (see Fig. 3.3).
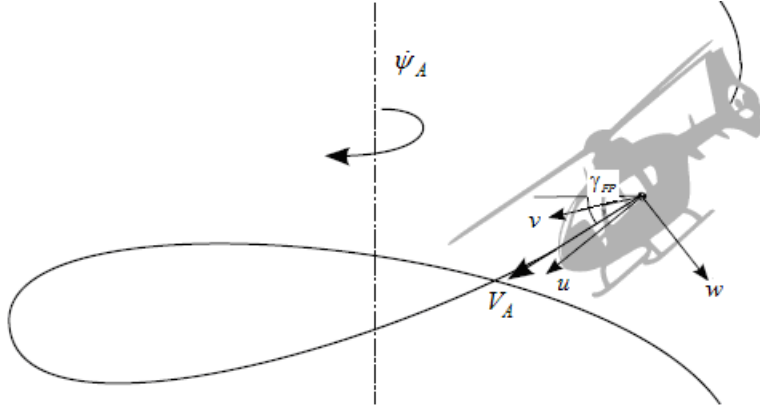
Figure 3.3: Helical Turn

In a helical turn, the flight path angle is different than zero being given by

$$\sin(\gamma_{FP}) = \sin(\theta_A)\cos(\alpha_F)\cos(\beta_F) - \sin(\phi_A)\cos(\theta_A)\sin(\beta_F) - \cos(\phi_A)\cos(\theta_A)\sin(\alpha_F)\cos(\beta_F) \qquad (3.6)$$

A picture describing the flight path angle for a particular case ($\phi_A = 0$, $\beta_F = 0$) is given in Fig. 3.4.
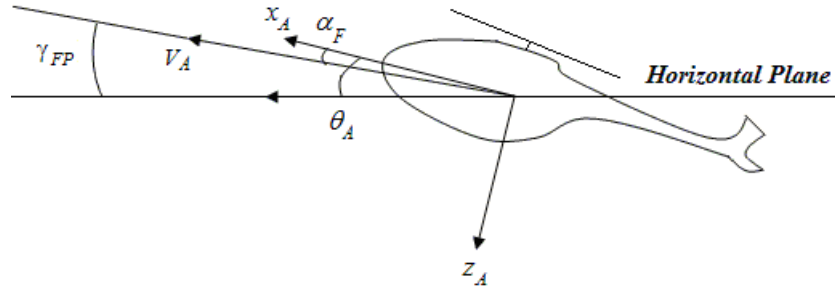
Figure 3.4: Flight Path Angle

Note that $\dot{\psi}_A > 0$ is a clockwise turn and $\dot{\psi}_A < 0$ is a counterclockwise turn (viewed from the top) while $\gamma_{FP} > 0$ is referring to the ascending (climbing) flight and $\gamma_{FP} < 0$ is referring to the descending flight.

In this dissertation, trim is also defined as the condition for which level banked or helical turn with constant V_A and zero sideslip is achieved. For the helicopter model 29 trim equations (i.e. 0=0 equations are ignored) and 29 unknowns were obtained for particular maneuvers (level banked or helical turn). The vector of trim unknowns in nondimensional fashion for maneuvering flight is

$$
\begin{aligned}
x_0 = [& \theta_{0_0}, \theta_{c_0}, \theta_{s_0}, \theta_{T_0}, \hat{p}, \hat{q}, \hat{r}, \theta_{A_0}, \phi_{A_0}, \beta_{0_0}, \beta_{c_0}, \beta_{s_0}, \beta_{d_0}, \zeta_{0_0}, \zeta_{c_0}, \zeta_{s_0}, \zeta_{d_0}, {}_2\beta_{0_0}, \\
& {}_2\beta_{c_0}, {}_2\beta_{s_0}, {}_2\beta_{d_0}, {}_3\beta_{0_0}, {}_3\beta_{c_0}, {}_3\beta_{s_0}, {}_3\beta_{d_0}, \lambda_{0_0}, \lambda_{c_0}, \chi_0, \alpha_F]^T
\end{aligned}
\tag{3.7}
$$

Matlab's *f*solve command was used to solve these 29 trim equations. The results thus found were verified by inserting them into the governing equations of motion obtained after the application of the new ordering scheme. Very small numbers (around 10^{-10}) were obtained showing that the trimming procedure is correct for these particular maneuvers. Numerous numerical experiments resulted in trim values that are in the range reported in the literature (see references in the model simplification sub-section). For some specific maneuvering flight conditions, such as hover and $V_A = 80\,\text{kts}$ with $\dot{\psi}_A = 0.1\,\text{rad/s}$, $\gamma_{FP} = 0.1\,\text{rad}$, the trims are

$$
\begin{aligned}
{}_{hover}x_0 = [& \underbrace{0.2695, 0.0094, -0.0267, 0.0909}_{\theta_{0_0}, \theta_{c_0}, \theta_{s_0}, \theta_{T_0}}, \underbrace{0.0001, 0.0037, 0.1246}_{\hat{p}, \hat{q}, \hat{r}}, \underbrace{-0.0009, 0.0246}_{\theta_{A_0}, \phi_{A_0}}, \\
& \underbrace{0.0472, 0.0236, 0.0016, 0}_{\beta_{0_0}, \beta_{c_0}, \beta_{s_0}, \beta_{d_0}}, \underbrace{0.0173, -0.0010, -0.0028, 0}_{\zeta_{0_0}, \zeta_{c_0}, \zeta_{s_0}, \zeta_{d_0}}, \underbrace{0.0681, 0.0290}_{{}_2\beta_{0_0}, {}_2\beta_{c_0}}, \\
& \underbrace{0.0027, 0}_{{}_2\beta_{s_0}, {}_2\beta_{d_0}}, \underbrace{0.0854, 0.03285, 0.0038, 0}_{{}_3\beta_{0_0}, {}_3\beta_{c_0}, {}_3\beta_{s_0}, {}_3\beta_{d_0}}, \underbrace{0.0579, 0.0026, 0.0433, 0.1246}_{\lambda_{0_0}, \lambda_{c_0}, \chi_0, \alpha_{F_0}}]^T
\end{aligned}
\tag{3.8}
$$

$$_{80kts}x_0 = [\underbrace{0.2253, 0.0149, -0.0708, 0.0090}_{\theta_{0_0}, \theta_{c_0}, \theta_{s_0}, \theta_{T_0}}, \underbrace{0.0001, 0.0014, 0.0034}_{\hat{p}_0, \hat{q}_0, \hat{r}_0}, \underbrace{0.3883, -0.0177}_{\theta_{A_0}, \phi_{A_0}},$$
$$\underbrace{0.0573, -0.0003, 0.00205, 0}_{\beta_{0_0}, \beta_{c_0}, \beta_{s_0}, \beta_{d_0}}, \underbrace{0.0062, -0.0033, -0.0006, 0}_{\zeta_{0_0}, \zeta_{c_0}, \zeta_{s_0}, \zeta_{d_0}}, \underbrace{0.0700, 0.0030}_{_2\beta_{0_0}, _2\beta_{c_0}},$$
$$\underbrace{-0.0094, 0}_{_2\beta_{s_0}, _2\beta_{d_0}}, \underbrace{0.0738, 0.0105, -0.0293, 0}_{_3\beta_{0_0}, _3\beta_{c_0}, _3\beta_{s_0}, _3\beta_{d_0}}, \underbrace{0.0173, 0.0298, 1.3977, 0.0890}_{\lambda_{0_0}, \lambda_{c_0}, \chi_0, \alpha_{F_0}}]^T$$

(3.9)

3.2 Linearization

After finding trim values, the helicopter model was linearized using Maple, yielding continuous linear time-invariant (LTI) systems. For the helicopter model there are 9 fuselage and 32 main rotor states (there is an additional flight path angle equation for helical turn). There are 3 main rotor and 1 tail rotor control inputs. The implicit linearization method is summarized next. For a given set of governing equations of any system

$$f(\dot{x}, x, \upsilon) = 0 \tag{3.10}$$

any linearized state-space model is derived using the mathematical relations

$$df = \left(\left.\frac{\partial f}{\partial \dot{x}}\right|_{trim}\right)\delta\dot{x} + \left(\left.\frac{\partial f}{\partial x}\right|_{trim}\right)\delta x + \left(\left.\frac{\partial f}{\partial \upsilon}\right|_{trim}\right)\delta\upsilon = 0 \tag{3.11}$$

$$0 = \delta\dot{x} + \left(\left.\frac{\partial f}{\partial \dot{x}}\right|_{trim}\right)^{-1}\left(\left.\frac{\partial f}{\partial x}\right|_{trim}\right)\delta x + \left(\left.\frac{\partial f}{\partial \dot{x}}\right|_{trim}\right)^{-1}\left(\left.\frac{\partial f}{\partial \upsilon}\right|_{trim}\right)\delta\upsilon \tag{3.12}$$

$$\delta\dot{x} = A\,\delta x + B\,\delta\upsilon \tag{3.13}$$

where

$$A = -\left(\left.\frac{\partial f}{\partial \dot{x}}\right|_{trim}\right)^{-1}\left(\left.\frac{\partial f}{\partial x}\right|_{trim}\right), \quad B = -\left(\left.\frac{\partial f}{\partial \dot{x}}\right|_{trim}\right)^{-1}\left(\left.\frac{\partial f}{\partial \upsilon}\right|_{trim}\right) \tag{3.14}$$

Tables 3.1 and 3.2 summarize the state and control vectors for the linearized models.

Table 3.1: State Vector of Linearized Models

State Variable	Quantity	State Variable	Quantity
x_1	$\hat{u}$	x_{21}	$\dot{x}_{20}$
x_2	$\hat{v}$	x_{22}	ζ_{1s}
x_3	$\hat{w}$	x_{23}	$\dot{x}_{22}$
x_4	$\hat{p}$	x_{24}	ζ_d
x_5	$\hat{q}$	x_{25}	$\dot{x}_{24}$
x_6	$\hat{r}$	x_{26}	$_2\beta_0$
x_7	ϕ_A	x_{27}	$\dot{x}_{26}$
x_8	θ_A	x_{28}	$_2\beta_c$
x_9	ψ_A	x_{29}	$\dot{x}_{28}$
x_{10}	β_0	x_{30}	$_2\beta_s$
x_{11}	$\dot{x}_{10}$	x_{31}	$\dot{x}_{30}$
x_{12}	β_{1c}	x_{32}	$_2\beta_d$
x_{13}	$\dot{x}_{12}$	x_{34}	$_3\beta_0$
x_{14}	β_{1s}	x_{35}	$\dot{x}_{34}$
x_{15}	$\dot{x}_{14}$	x_{36}	$_3\beta_c$
x_{16}	β_d	x_{37}	$\dot{x}_{36}$
x_{17}	$\dot{x}_{16}$	x_{38}	$_3\beta_s$
x_{18}	ζ_0	x_{39}	$\dot{x}_{38}$
x_{19}	$\dot{x}_{18}$	x_{40}	$_3\beta_d$
x_{20}	ζ_{1c}	x_{41}	$\dot{x}_{40}$

Table 3.2: Control Vector of Linearized Model

Control Variable	Quantity	Control Variable	Quantity
u_1	θ_0	u_3	θ_{1s}
u_2	θ_{1c}	u_4	θ_T

3.3 Structure of State-Space Models

The structure of the state space model is given in Eqs. 3.15 and 3.16. The "*" elements in A and B matrices represent nonzero numbers.

$$A = \begin{bmatrix}
* & * & * & * & * & * & 0 & * & 0 & * \\
* & * & * & * & * & * & * & * & 0 & * \\
* & * & * & * & * & * & * & * & 0 & * \\
* & * & * & * & * & * & 0 & 0 & 0 & * \\
* & * & * & * & * & * & 0 & 0 & 0 & * \\
* & * & * & * & * & * & 0 & 0 & 0 & * \\
0 & 0 & 0 & * & * & * & 0 & 0 & 0 & 0 & 0 & 0 & 0 & 0 & 0 & 0 & 0 & 0 & 0 & 0 & 0 & 0 & 0 & 0 & 0 & 0 & 0 & 0 & 0 & 0 & 0 & 0 & 0 & 0 & 0 & 0 & 0 & 0 & 0 & 0 & 0 & 0 \\
0 & 0 & 0 & 0 & * & * & 0 & 0 & 0 & 0 & 0 & 0 & 0 & 0 & 0 & 0 & 0 & 0 & 0 & 0 & 0 & 0 & 0 & 0 & 0 & 0 & 0 & 0 & 0 & 0 & 0 & 0 & 0 & 0 & 0 & 0 & 0 & 0 & 0 & 0 & 0 & 0 \\
0 & 0 & 0 & 0 & * & * & 0 & 0 & 0 & 0 & 0 & 0 & 0 & 0 & 0 & 0 & 0 & 0 & 0 & 0 & 0 & 0 & 0 & 0 & 0 & 0 & 0 & 0 & 0 & 0 & 0 & 0 & 0 & 0 & 0 & 0 & 0 & 0 & 0 & 0 & 0 & 0 \\
0 & 0 & 0 & 0 & 0 & 0 & 0 & 0 & 0 & * & 0 & 0 & 0 & 0 & 0 & 0 & 0 & 0 & 0 & 0 & 0 & 0 & 0 & 0 & 0 & 0 & 0 & 0 & 0 & 0 & 0 & 0 & 0 & 0 & 0 & 0 & 0 & 0 & 0 & 0 & 0 & 0 \\
* & * & * & * & * & * & 0 & 0 & 0 & * \\
0 & 0 & 0 & 0 & 0 & 0 & 0 & 0 & 0 & 0 & 0 & 0 & * & 0 & 0 & 0 & 0 & 0 & 0 & 0 & 0 & 0 & 0 & 0 & 0 & 0 & 0 & 0 & 0 & 0 & 0 & 0 & 0 & 0 & 0 & 0 & 0 & 0 & 0 & 0 & 0 & 0 \\
* & * & * & * & * & * & 0 & 0 & 0 & * \\
0 & 0 & 0 & 0 & 0 & 0 & 0 & 0 & 0 & 0 & 0 & 0 & 0 & * & 0 & 0 & 0 & 0 & 0 & 0 & 0 & 0 & 0 & 0 & 0 & 0 & 0 & 0 & 0 & 0 & 0 & 0 & 0 & 0 & 0 & 0 & 0 & 0 & 0 & 0 & 0 & 0 \\
* & * & * & * & * & * & 0 & 0 & 0 & * \\
0 & 0 & 0 & 0 & 0 & 0 & 0 & 0 & 0 & 0 & 0 & 0 & 0 & 0 & * & 0 & 0 & 0 & 0 & 0 & 0 & 0 & 0 & 0 & 0 & 0 & 0 & 0 & 0 & 0 & 0 & 0 & 0 & 0 & 0 & 0 & 0 & 0 & 0 & 0 & 0 & 0 \\
0 & 0 & 0 & 0 & 0 & 0 & 0 & 0 & 0 & 0 & 0 & 0 & 0 & 0 & * & * & 0 & 0 & 0 & 0 & 0 & 0 & * & * & 0 & 0 & 0 & 0 & 0 & 0 & * & * & 0 & 0 & 0 & 0 & 0 & 0 & 0 & 0 & 0 & 0 \\
0 & 0 & 0 & 0 & 0 & 0 & 0 & 0 & 0 & 0 & 0 & 0 & 0 & 0 & * & 0 & 0 & 0 & 0 & 0 & 0 & 0 & 0 & 0 & 0 & 0 & 0 & 0 & 0 & 0 & 0 & 0 & 0 & 0 & 0 & 0 & 0 & 0 & 0 & 0 & 0 & 0 \\
0 & 0 & 0 & 0 & 0 & 0 & 0 & 0 & 0 & 0 & 0 & 0 & 0 & 0 & * & * & 0 & 0 & 0 & 0 & 0 & 0 & 0 & 0 & 0 & 0 & 0 & 0 & 0 & 0 & 0 & 0 & 0 & 0 & 0 & 0 & 0 & 0 & 0 & 0 & 0 & 0 \\
0 & 0 & 0 & 0 & 0 & 0 & 0 & 0 & 0 & 0 & 0 & 0 & 0 & 0 & 0 & * & 0 & 0 & 0 & 0 & 0 & 0 & 0 & 0 & 0 & 0 & 0 & 0 & 0 & 0 & 0 & 0 & 0 & 0 & 0 & 0 & 0 & 0 & 0 & 0 & 0 & 0 \\
0 & 0 & 0 & 0 & 0 & 0 & 0 & 0 & 0 & 0 & 0 & 0 & 0 & 0 & 0 & 0 & * & * & * & * & 0 & 0 & 0 & 0 & 0 & 0 & 0 & 0 & 0 & 0 & 0 & 0 & 0 & 0 & 0 & 0 & 0 & 0 & 0 & 0 & 0 & 0 \\
0 & 0 & 0 & 0 & 0 & 0 & 0 & 0 & 0 & 0 & 0 & 0 & 0 & 0 & 0 & 0 & 0 & * & 0 & 0 & 0 & 0 & 0 & 0 & 0 & 0 & 0 & 0 & 0 & 0 & 0 & 0 & 0 & 0 & 0 & 0 & 0 & 0 & 0 & 0 & 0 & 0 \\
0 & 0 & 0 & 0 & 0 & 0 & 0 & 0 & 0 & 0 & 0 & 0 & 0 & 0 & 0 & 0 & * & * & * & * & 0 & 0 & 0 & 0 & 0 & 0 & 0 & 0 & 0 & 0 & 0 & 0 & 0 & 0 & 0 & 0 & 0 & 0 & 0 & 0 & 0 & 0 \\
0 & 0 & 0 & 0 & 0 & 0 & 0 & 0 & 0 & 0 & 0 & 0 & 0 & 0 & 0 & 0 & 0 & 0 & 0 & * & 0 & 0 & 0 & 0 & 0 & 0 & 0 & 0 & 0 & 0 & 0 & 0 & 0 & 0 & 0 & 0 & 0 & 0 & 0 & 0 & 0 & 0 \\
0 & 0 & 0 & 0 & 0 & 0 & 0 & 0 & 0 & 0 & 0 & 0 & 0 & 0 & 0 & 0 & 0 & 0 & * & * & 0 & 0 & 0 & 0 & 0 & 0 & 0 & 0 & 0 & 0 & 0 & 0 & 0 & 0 & 0 & 0 & 0 & 0 & 0 & 0 & 0 & 0 \\
0 & 0 & 0 & 0 & 0 & 0 & 0 & 0 & 0 & 0 & 0 & 0 & 0 & 0 & 0 & 0 & 0 & 0 & 0 & * & 0 & 0 & 0 & 0 & 0 & 0 & 0 & 0 & 0 & 0 & 0 & 0 & 0 & 0 & 0 & 0 & 0 & 0 & 0 & 0 & 0 & 0 \\
* & * & * & * & * & * & 0 & 0 & 0 & 0 & 0 & 0 & 0 & 0 & * \\
0 & 0 & 0 & 0 & 0 & 0 & 0 & 0 & 0 & 0 & 0 & 0 & 0 & 0 & 0 & 0 & 0 & 0 & 0 & 0 & 0 & 0 & 0 & 0 & * & 0 & 0 & 0 & 0 & 0 & 0 & 0 & 0 & 0 & 0 & 0 & 0 & 0 & 0 & 0 & 0 & 0 \\
* & * & * & * & * & * & 0 & 0 & 0 & 0 & 0 & 0 & 0 & 0 & * \\
0 & 0 & 0 & 0 & 0 & 0 & 0 & 0 & 0 & 0 & 0 & 0 & 0 & 0 & 0 & 0 & 0 & 0 & 0 & 0 & 0 & 0 & 0 & 0 & 0 & 0 & * & 0 & 0 & 0 & 0 & 0 & 0 & 0 & 0 & 0 & 0 & 0 & 0 & 0 & 0 & 0 \\
* & * & * & * & * & * & 0 & 0 & 0 & * \\
0 & 0 & 0 & 0 & 0 & 0 & 0 & 0 & 0 & 0 & 0 & 0 & 0 & 0 & 0 & 0 & 0 & 0 & 0 & 0 & 0 & 0 & 0 & 0 & 0 & 0 & 0 & 0 & * & 0 & 0 & 0 & 0 & 0 & 0 & 0 & 0 & 0 & 0 & 0 & 0 & 0 \\
0 & 0 & 0 & 0 & 0 & 0 & 0 & 0 & 0 & 0 & 0 & 0 & * & * & * & * & * & 0 & 0 & * & * & 0 & 0 & 0 & 0 & 0 & 0 & * & * & * & 0 & 0 & 0 & 0 & 0 & 0 & 0 & * & * \\
0 & 0 & 0 & 0 & 0 & 0 & 0 & 0 & 0 & 0 & 0 & 0 & 0 & 0 & 0 & 0 & 0 & 0 & 0 & 0 & 0 & 0 & 0 & 0 & 0 & 0 & 0 & 0 & 0 & 0 & * & 0 & 0 & 0 & 0 & 0 & 0 & 0 \\
* & * & * & * & * & * & 0 & 0 & 0 & * \\
0 & 0 & 0 & 0 & 0 & 0 & 0 & 0 & 0 & 0 & 0 & 0 & 0 & 0 & 0 & 0 & 0 & 0 & 0 & 0 & 0 & 0 & 0 & 0 & 0 & 0 & 0 & 0 & 0 & 0 & 0 & 0 & * & 0 & 0 & 0 & 0 \\
* & * & * & * & * & * & 0 & 0 & 0 & * \\
0 & 0 & 0 & 0 & 0 & 0 & 0 & 0 & 0 & 0 & 0 & 0 & 0 & 0 & 0 & 0 & 0 & 0 & 0 & 0 & 0 & 0 & 0 & 0 & 0 & 0 & 0 & 0 & 0 & 0 & 0 & 0 & 0 & 0 & * & 0 & 0 \\
* & * & * & * & * & * & 0 & 0 & 0 & * \\
0 & 0 & 0 & 0 & 0 & 0 & 0 & 0 & 0 & 0 & 0 & 0 & 0 & 0 & 0 & 0 & 0 & 0 & 0 & 0 & 0 & 0 & 0 & 0 & 0 & 0 & 0 & 0 & 0 & 0 & 0 & 0 & 0 & 0 & 0 & 0 & * \\
0 & 0 & 0 & 0 & 0 & 0 & 0 & 0 & 0 & 0 & 0 & 0 & 0 & * & * & 0 & 0 & 0 & 0 & 0 & 0 & * & * & 0 & 0 & 0 & 0 & 0 & 0 & * & * & 0 & 0 & 0 & 0 & 0 & 0 & * & *
\end{bmatrix} \quad (3.15)$$

$$
B = \begin{bmatrix}
* & * & * & * \\
* & * & * & * \\
* & * & * & * \\
* & * & * & * \\
* & * & * & * \\
* & * & * & * \\
0 & 0 & 0 & 0 \\
0 & 0 & 0 & 0 \\
0 & 0 & 0 & 0 \\
0 & 0 & 0 & 0 \\
* & * & * & * \\
0 & 0 & 0 & 0 \\
* & * & * & * \\
0 & 0 & 0 & 0 \\
* & * & * & * \\
0 & 0 & 0 & 0 \\
* & * & * & * \\
0 & 0 & 0 & 0 \\
* & * & * & * \\
0 & 0 & 0 & 0 \\
* & * & * & * \\
0 & 0 & 0 & 0 \\
* & * & * & * \\
0 & 0 & 0 & 0 \\
* & * & * & * \\
0 & 0 & 0 & 0 \\
* & * & * & * \\
0 & 0 & 0 & 0 \\
* & * & * & * \\
0 & 0 & 0 & 0 \\
* & * & * & * \\
0 & 0 & 0 & 0 \\
* & * & * & * \\
0 & 0 & 0 & 0 \\
* & * & * & * \\
0 & 0 & 0 & 0 \\
* & * & * & * \\
0 & 0 & 0 & 0 \\
* & * & * & * \\
0 & 0 & 0 & 0 \\
* & * & * & * \\
0 & 0 & 0 & 0 \\
* & * & * & * \\
0 & 0 & 0 & 0 \\
* & * & * & *
\end{bmatrix}
\tag{3.16}
$$

3.4 Model Validation

Puma SA 330 was used to validate the models previously developed with most technical data taken from [47] (see Appendix A.2). A good match with results in the literature for many flight conditions was ascertained. For example, most of the flight dynamics modes (eigenvalues of the linearized systems) of the helicopter model for hover and $V_A = 80$ kts, shown in Table 3.3, match well with the results reported in [47] [pp. 282-287]. The 4th mode does not match well due to some modeling discrepancy between the control oriented helicopter model and Helisim, however, the qualitative behavior is similar (exponentially stable mode). All the modes in this section are given for straight level flight; see Appendix B to ascertain how they change for maneuvering flight.

**Table 3.3: Flight Dynamic Modes Comparison**

MODE	HOVER		80 KTS	
	Control Oriented Model	Helisim	Control Oriented Model	Helisim
1st	$0.1753 \pm 0.5816i$	$0.2772 \pm 0.5008i$	$-0.5294 \pm 2.5879i$	$-0.1854 \pm 1.0546i$
2nd	$0.0779 \pm 0.4357i$	$-0.0410 \pm 0.5691i$	$-0.0166 \pm 0.1572i$	$-0.0085 \pm 0.2074i$
3rd	-0.1514	-0.2697	-0.02752	-0.1358
4th	-1.1540	-0.3262	-1.0737	-1.5163
5th	$-0.9987 \pm 0.3405i$	$-1.2990 \pm 0.2020i$	$-1.1014 \pm 2.2242i$	$-0.9252 \pm 1.0503i$

The qualitative behavior of flapping and lagging modes is also identical with the one described in [47] [p. 137]. For example, the flapping modes are much farther away from the imaginary axis compared to the lagging modes. Both the flapping and lagging modes
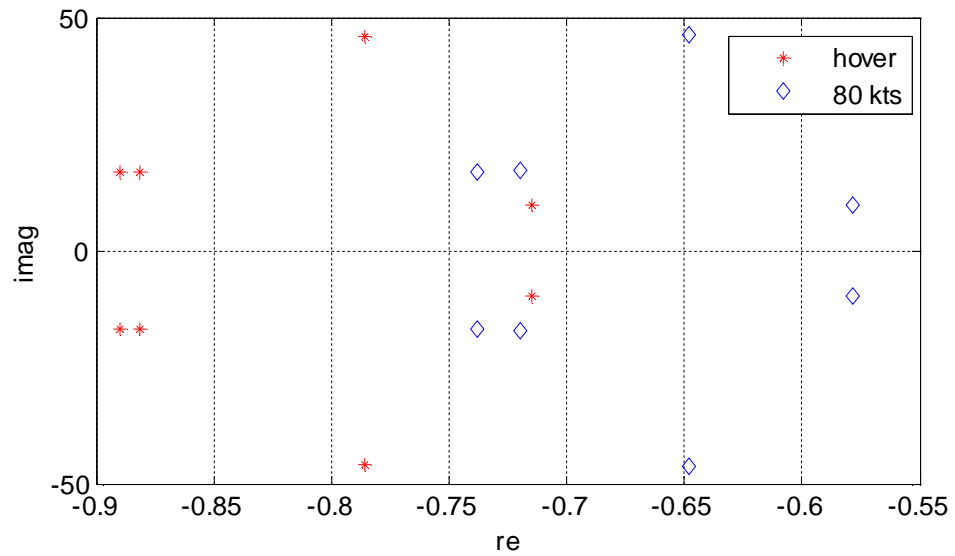
change slightly with V_A, and the magnitude of the frequency bound for the flapping

modes is larger than the one for the lagging modes (see Figs. 3.6 and 3.7).
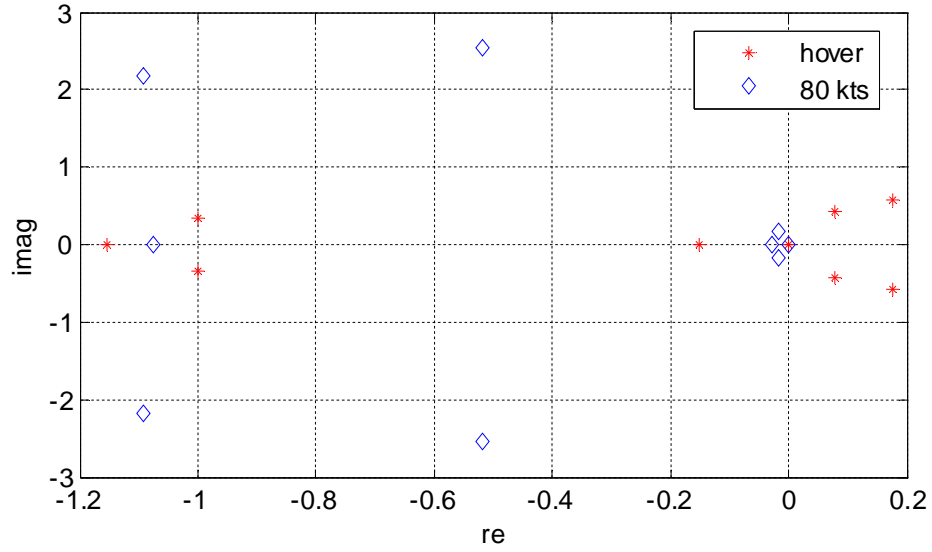
Figure 3.5: Flight Dynamics Modes for Straight Level Flight
(Hover and V_A=80 kts)
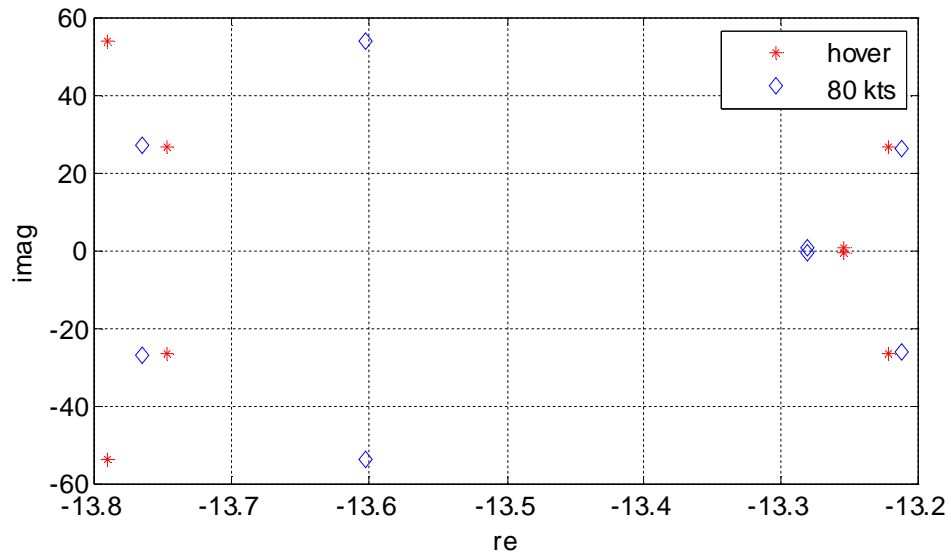
Figure 3.6: Flapping Modes for Straight Level Flight
(Hover and V_A=80 kts)

Figure 3.7: Lead-Lagging Modes for Straight Level Flight
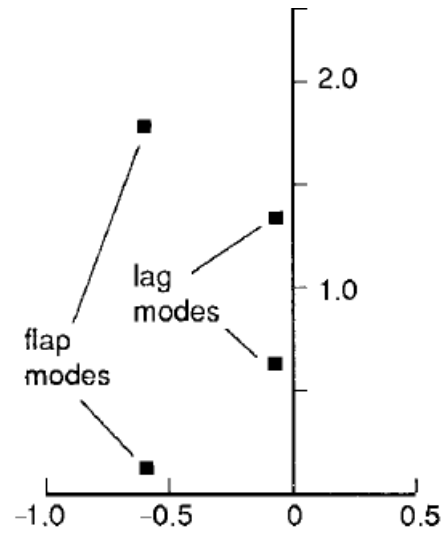**(Hover and V_A=80 kts)**

61

**Figure 3.8: Typical Nondimensionalized Flapping and
Lead-Lagging Modes ([47] [p. 137])**

CHAPTER 4:

Variance Constrained Controllers

4.1 Controllability and Observability of Linear Time Invariant (LTI) Systems

Consider a continuous LTI system

$$\dot{x}_p(t) = A_p x_p(t) + B_p \mathrm{u}(t), \quad y(t) = C_p x_p(t) + D_p \mathrm{u}(t) \tag{4.1}$$

where $x_p(t)$ is the state vector, u is the control vector, and y is the output vector. The state $x_p(t)$ is said to be controllable at instant $t = t_0$ if there is a piecewise continuous input u(t) that drives the state from the initial state to any final state $x_p(t_f)$ in a finite time interval $[t_0, t_f]$. If every state $x_p(t_0)$ of the system (i.e. Eq. 4.1) is controllable in a finite time interval, the system is said to be controllable. The system (Eq. 4.1) is controllable if and only if (see [61] [pp. 716-717])

$$rank\left(\begin{bmatrix} B_p & A_p B_p & A_p^{2} B_p & ..... & A_p^{n-1} B_p \end{bmatrix}\right) = n \tag{4.2}$$

where n is the number of system states.

For the system in Eq. 4.1 , the state $x_p(t_0)$ is said to be observable if given any input u(t), there exists a finite time $t_f \geq t_0$ such that the knowledge of u(t) for $t_0 \leq t \leq t_f$, matrices A, B, C, D, and the output y(t) for $t_0 \leq t \leq t_f$ are sufficient to determine $x_p(t_0)$. If all the states of the system are observable for a finite time t_f, the system is called observable. The system (Eq. 4.1) is observable if and only if (see [61] [pp.719-720])

$$rank\left(\begin{bmatrix} C_p & C_p A_p & C_p A_p^{2} & .... & C_p A_p^{n-1} \end{bmatrix}^{T}\right) = n \tag{4.3}$$

A LTI system (Eq. 4.1) is stabilizable if the uncontrollable modes are stable, and detectable if the unstable modes are observable [62][p. 21].

4.2 Linear Quadratic Regulator (LQR) Controllers

For a given controllable or stabilizable and observable or detectable LTI system, LQR controller (finite horizon) minimizes the quadratic cost function [62][p. 9]

$$V = \int_0^T [x_p(\tau)^T Q\, x_p(\tau) + u(\tau)^T R\, u(\tau)]dt + x_p(T)^T M\, x_p(T) \qquad (4.4)$$

where Q and M are positive semidefinite matrices and R is positive definite matrix. Solution of Eq. 4.4 gives a state-feedback control law:

$$u(t) = -K\, x_p(t) \qquad (4.5)$$

When T approaches infinity, the problem (Eq. 4.4) is called the steady-state LQR problem [62][pp. 20,21]. The steady-state solution can be found by solving the algebraic Riccati equation (ARE)

$$0 = A_p^T P + PA_p - PB_p R^{-1} B_p^T P + C_p^T Q C_p \qquad (4.6)$$

Here P is the positive definite steady-state solution of ARE. The optimal control law is

$$\overset{*}{u}(t) = -R^{-1}B^T P\, x_p(t) \qquad (4.7)$$

This control law makes the closed-loop system asymptotically stable.

4.3 Linear Quadratic Gaussian Regulator (LQG) Controllers

For the LQR it is assumed that all the states are measured and there is no noise in the system, but this is not realistic for many physical systems. Therefore, another controller called "LQG" is developed. For a continuous LTI system

$$\dot{x}_p(t) = A_p x_p(t) + B_p u(t) + D_p w_p, \quad y = C_p x_p, \quad z = M_p x_p + v \tag{4.8}$$

where z represents sensor measurements, w_p and v are zero-mean uncorrelated Gaussian white noises with intensities of W and V, respectively.

The LQG control consists of two problems (separation principle [62][pp. 108-113]). The first problem is estimation of all the states $x_p(t)$ using Kalman filter (see [62][pp. 103-107] for more details) and the second problem is solving LQR using the estimated states $\hat{x}_p(t)$.

4.4 Variance Constrained Controllers

Because helicopters are subject to input and output limitations and a key requirement is minimization of control energy, output variance constrained control (OVC) and input variance constrained control (IVC) [12-19] are investigated. The OVC problem is summarized next. Given a continuous LTI system (Eq. 4.8) and a positive definite input penalty $R > 0$, find a full order dynamic controller

$$\dot{x}_c = A_c x_c + F z, \quad u = G x_c \tag{4.9}$$

to solve the problem

$$\min_{A_c, F, G} E_\infty u^T R u \tag{4.10}$$

subject to

$$E_\infty \ y_i^2 \le \sigma_i^2, \qquad i = 1, ..., n_y \tag{4.11}$$

where σ_i^2 is the upper bound imposed on the *i-th* output variance, and n_y the number of outputs. OVC solution reduces to a LQG problem by choosing the output penalty $Q > 0$ depending on the inequality constraints. An algorithm for the selection of Q is presented in [15,16]. After converging on Q, OVC parameters are

$$A_c = A_p + B_p G - F M_p, \qquad F = X M_p^T V^{-1}, \qquad G = -R^{-1} B_p^T K \tag{4.12}$$

where X and K are solutions of two algebraic Riccati equations:

$$0 = X A_p^T + A_p X - X M_p^T V^{-1} M_p X + D_p W_p D_p^T \tag{4.13}$$

$$0 = K A_p + A_p^T K - K B_p R^{-1} B_p^T K + C_p^T Q C_p \tag{4.14}$$

IVC problem is dual of OVC: for a given output penalty $Q > 0$, a full order dynamic controller (Eq. 4.9) for Eq. 4.8 must be found to solve

$$\min_{A_c, F, G} \ E_\infty y^T Q y \tag{4.15}$$

subject to

$$E_\infty \ u_i^2 \le \mu_i^2, \qquad i = 1, ..., n_u \tag{4.16}$$

where μ_i^2 is the upper bound variance imposed on the *i-th* input, and n_u is the number of inputs. IVC solution reduces to a LQG problem by choosing $R > 0$. An algorithm for the selection of R is presented in [15]. After converging on R, IVC is obtained using Eq. 4.12. Compared to LQG, OVC and IVC provide an intelligent way of choosing Q and R,

which guarantees satisfaction of constraints. If the σ_i^2 and μ_i^2 constraints are exactly satisfied (equalities are met) using specific variance constrained algorithm, these constraints are called hard constraints.

4.5 OVC and IVC Results

OVC and IVC are evaluated for the helicopter model for several flight conditions. Results for maneuvering flight conditions are summarized next (see Appendix D.1 for straight level flight results).

For the numerical experiments reported next the sensor measurements were helicopter linear velocities, angular velocities and Euler angles. The noise intensities were $W = 10^{-7} I_{41}$, $V = 10^{-7} I_9$. For numerous maneuvering flights (i.e. level banked turn and helical turn with different V_A, $\dot{\psi}_A$ and γ_{FP}), OVC performance is evaluated. Closed loop stability robustness is thoroughly investigated. For this purpose the following scenarios were considered: a) a controller designed for a nominal flight condition (e.g. $V_A = 40$ kts, $\dot{\psi}_A = 0.1$ rad/s, $\gamma_{FP} = 0.1$ rad) is used for different V_A (e.g. $V_A = 20$ kts, $\dot{\psi}_A = 0.1$ rad/s, $\gamma_{FP} = 0.1$ rad, etc.), the key question being "Does this controller stabilize flight conditions that are different from the nominal one?"; b) a controller designed for an "inertial certain" model (i.e. when there are no variations in helicopter inertial parameters) is used on the same type of model which experiences uncertainties in all helicopter inertial parameters (helicopter mass and helicopter inertia matrix elements). The key question is "Are the corresponding closed loop systems stable for these significant modeling uncertainties?" A synopsis of scenarios is given in Table 4.1 while Table 4.2 summarizes some results that answer these questions.

Description of scenarios studied is given next. The 1st OVC is designed for the helicopter model which is linearized for $V_A = 40\,\mathrm{kts}$, $\dot{\psi}_A = 0.1\,\mathrm{rad/s}$, $\gamma_{FP} = 0.1\,\mathrm{rad}$, $R_{turn} = 204.73\,\mathrm{m}$ and it is evaluated for the same model for different V_A (line 1 in Table 4.2). The 2nd OVC is designed for the helicopter model which is linearized for $V_A = 80\,\mathrm{kts}$, $\dot{\psi}_A = 0.1\,\mathrm{rad/s}$, $\gamma_{FP} = 0.1\,\mathrm{rad}$, $R_{turn} = 409.46\,\mathrm{m}$ and evaluated for the same model for different V_A (line 2 in Table 4.2). The 3rd OVC is identical with the 1st OVC, but it is evaluated for control model with 10% uncertain helicopter inertial parameters for different V_A (line 3 in Table 4.2). The 4th OVC is identical with the 2nd OVC, but it is evaluated for the helicopter model with 10% uncertain helicopter inertial parameters for different V_A (line 4 in Table 4.2). The design parameters and convergence properties are described next.

Table 4.1: OVC Scenarios

	Design Model	Nominal Design V_A	Evaluation Model	Evaluation V_A
1st	Inertial Certain	40 kts	Inertial Certain	Hover to 80 kts
2nd	Inertial Certain	80 kts	Inertial Certain	Hover to 80 kts
3rd	Inertial Certain	40 kts	10% Helicopter Inertia Variation	Hover to 80 kts
4th	Inertial Certain	80 kts	10% Helicopter Inertia Variation	Hover to 80 kts

("Inertial Certain" refers to the situation when there are no variations in helicopter inertial parameters)

Table 4.2: Stability Robustness Analysis for OVC

	Hover		10 kts		20 kts		30 kts		40 kts		50 kts		60kts		70 kts		80 kts		
	CL	OL	CL	OL	CL	OL	CL	OL	CL	OL	CL	OL	CL	OL	CL	OL	CL	OL	L
1st	ES	U	ES	U	ES	U	ES	U	ES	MS	ES	MS	ES	MS	ES	U	ES	U	9
2nd	ES	U	ES	U	ES	U	ES	U	ES	MS	ES	MS	ES	MS	ES	U	ES	U	9
3rd	ES	U	ES	U	ES	U	ES	U	ES	MS	ES	MS	ES	MS	ES	U	ES	U	9
4th	ES	U	ES	U	ES	U	ES	U	ES	MS	ES	MS	ES	MS	ES	U	ES	U	9

(CL: Closed Loop, OL: Open Loop, L: Length of Stability Interval, ES: Exponentially Stable, MS: Marginally Stable, U: Unstable)
(L is the number of velocity intervals for which the CL system is ES)

4.5.1 OVCs Design

For all of the numerical experiments reported next, the convergence tolerance for the OVC algorithm was 10^{-6}, while σ^2 was set to $10^{-4}\begin{bmatrix}1 & 1 & 0.1\end{bmatrix}$. All OVCs were designed using the helicopter Euler angles as the outputs while the inputs were all four helicopter controls. After 4 iterations the OVC design algorithm converges and the 1st OVC satisfies these constraints with the convergence error $7.2661*10^{-7}$. After 6 iterations, the 2nd OVC satisfies these constraints with the convergence error $2.9103*10^{-7}$. The 3rd and 4th OVCs are identical with the 1st and 2nd OVCs respectively and they are evaluated for the helicopter model with 10% helicopter inertial parameters reduction (in Table 4.2) for different V_A.

In Fig. 4.1 the output and input variances are shown for different V_A using the 1st OVC while in Fig. 4.2 the output and input variances are shown for different helicopter

inertia variations using the 1st OVC. In this figure $\Delta I / I$ refers to the relative variation in all helicopter inertial properties (all of them are changed by the same percentage). Note that output and input variance figures (i.e. Figs. 4.1, 4.2, 4.4, and 4.5) are found using fixed F and G gains and step 3 in Appendix B for maneuvering flight.

4.5.2 OVC Discussion

It can be easily seen from Table 4.2 that for the helical turn with $\dot{\psi}_A = 0.1\,\text{rad/s}$, $\gamma_{FP} = 0.1\,\text{rad}$ the OVCs are robustly stable with respect to variations in V_A. The length of stability intervals (L) is also large (1st and 2nd lines in Table 4.2). Moreover, OVCs are robustly stable with respect to helicopter inertial properties variation (3rd and 4th lines in Table 4.2). Extensive numerical experiments show that OVCs are also robustly stable both with respect to variations in V_A and inertial properties for level banked turns and different helical turns (see Appendix D.2). However, it is remarked that L decreases if different values for output constraints are enforced. For example, if for the scenarios described before σ^2 is reduced to $\sigma^2 = 10^{-6}\begin{bmatrix}1 & 1 & 1\end{bmatrix}$, L decreases to 4 and 3 for the 1st and 2nd lines respectively in Table 4.2. Similarly, if σ^2 is increased to $\sigma^2 = 10^{-3}\begin{bmatrix}1 & 1 & 1\end{bmatrix}$, L decreases to 6 for the 1st and 2nd lines in Table 4.2 (see Appendix D.2 for more details). These results show that there is no direct correlation between σ^2 and L (i.e. the dependency between σ^2 and L is very nonlinear).

Clearly from Figs. 4.1 and 4.2 the output variance constraints are satisfied at the nominal flight conditions. If one wants to ensure satisfaction of constraints over larger velocity and inertial parameters variation intervals, a safety factor can be introduced in

70

the design. Input variances also display small values. In Fig. 4.3 behaviors of helicopter Euler angles and all controls are given using 1st OVC.
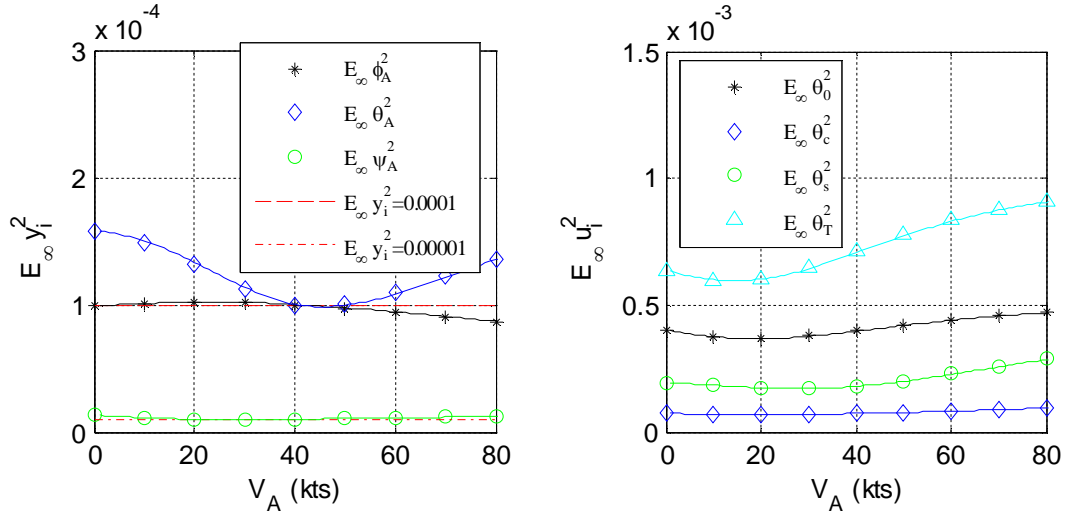

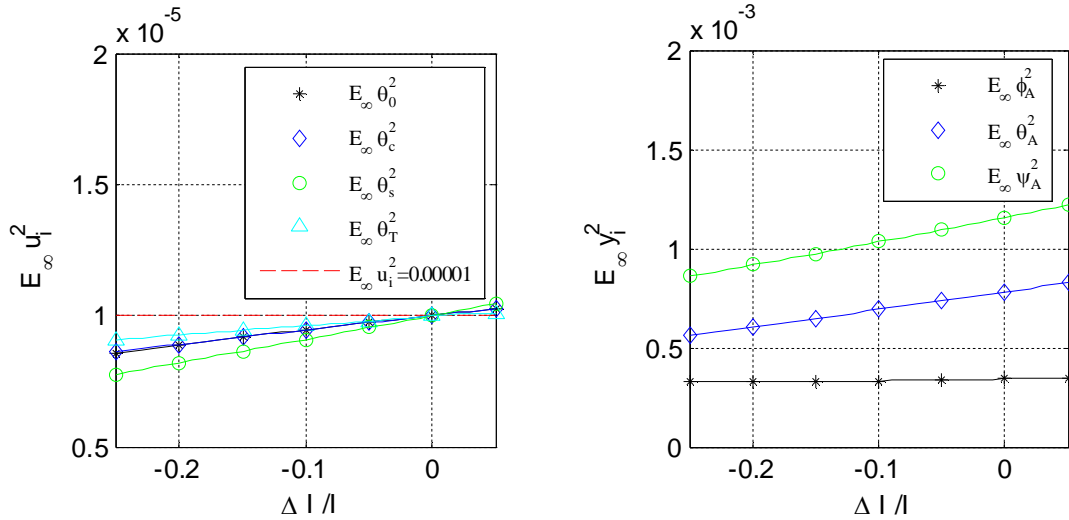**Figure 4.1: Output and Input Variances for The 1st OVC**

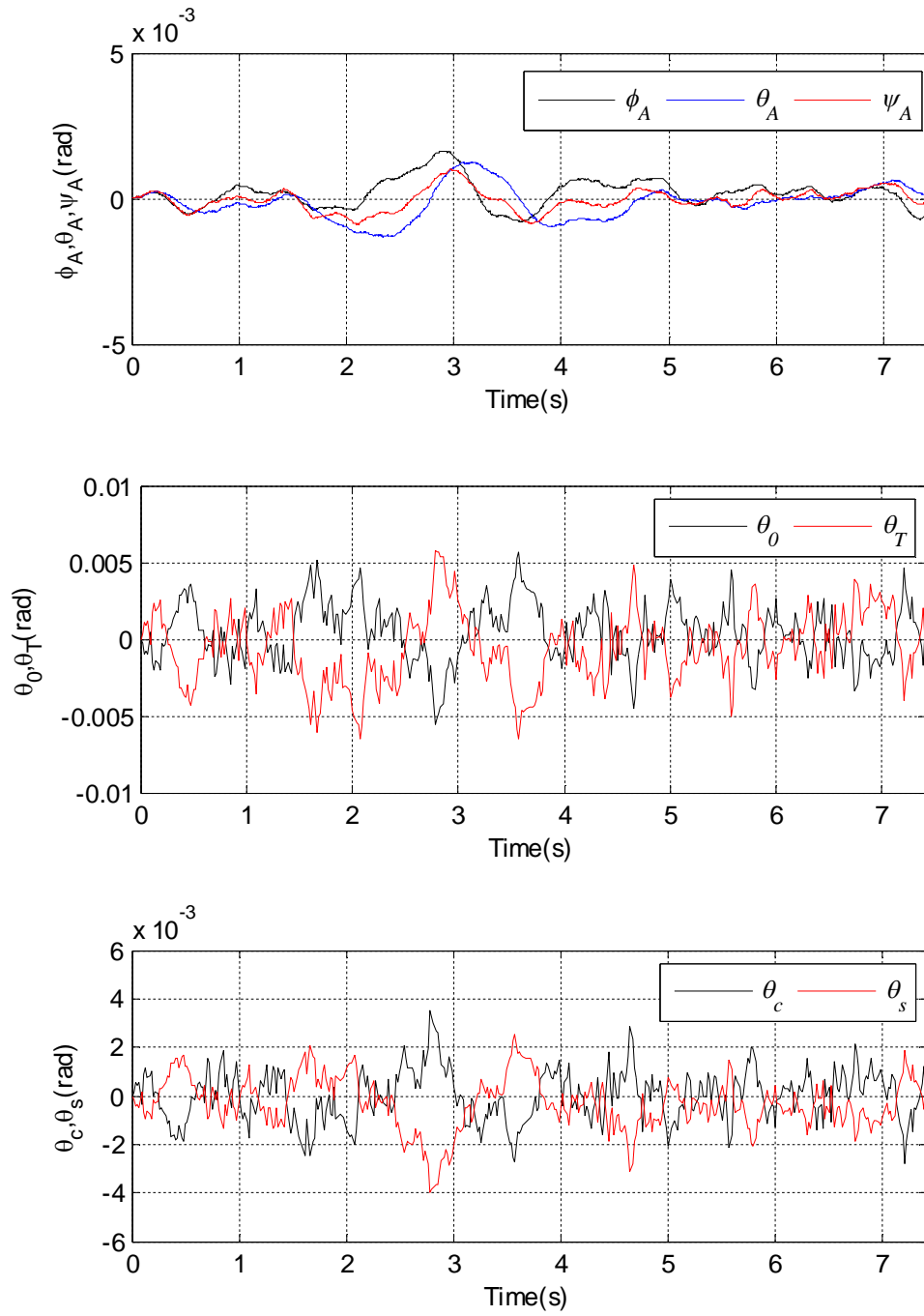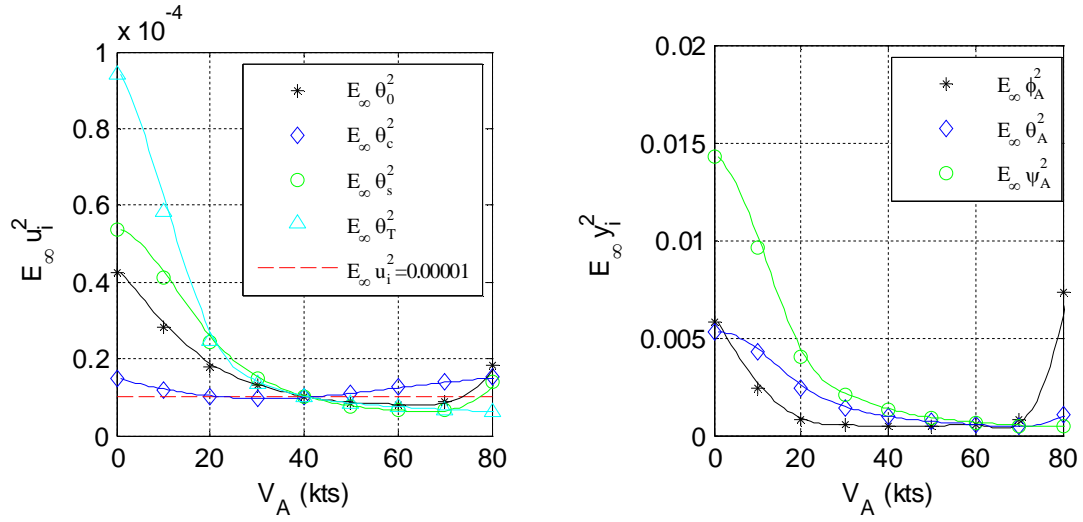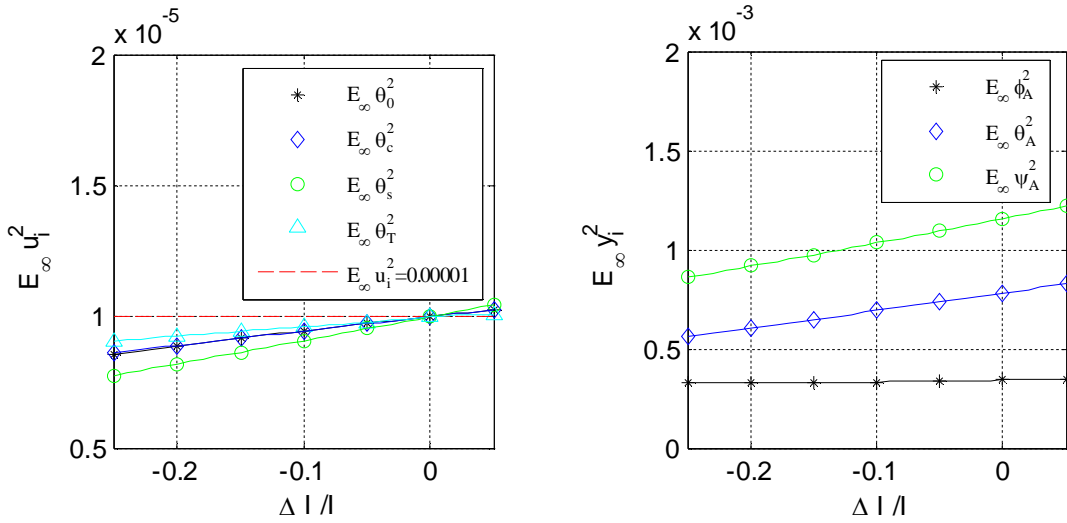**Figure 4.2: Output and Input Variances for The 3rd OVC**

Figure 4.3: Responses of Euler Angles and All Controls Using The 1st OVC

4.5.3 IVCs Design

IVCs are evaluated in a similar manner with OVCs. Stability robustness results are summarized in Table 4.3.

Table 4.3: Stability Robustness Analysis for IVC

	Hover		10 kts		20 kts		30 kts		40 kts		50 kts		60kts		70 kts		80 kts		
	CL	OL	CL	OL	CL	OL	CL	OL	CL	OL	CL	OL	CL	OL	CL	OL	CL	OL	*L*
1st	ES	U	ES	U	ES	U	ES	U	ES	MS	ES	MS	ES	MS	ES	U	ES	U	9
2nd	ES	U	ES	U	ES	U	ES	U	ES	MS	ES	MS	ES	MS	ES	U	ES	U	9
3rd	ES	U	ES	U	ES	U	ES	U	ES	MS	ES	MS	ES	MS	ES	U	U	U	8
4th	ES	U	ES	U	ES	U	ES	U	ES	MS	ES	MS	ES	MS	ES	U	ES	U	9

In all of the numerical experiments reported next the convergence tolerance for the IVC algorithm was 10^{-7}, while μ^2 was set to $10^{-5}\begin{bmatrix} 1 & 1 & 1 & 1 \end{bmatrix}$. All IVCs were designed using all four helicopter controls, while the outputs were all three helicopter Euler angles. After 14 iterations, the 1st IVC satisfies these constraints with the convergence error $6.0214*10^{-8}$. After 22 iterations, the 2nd IVC satisfies these constraints with the convergence error $8.3133*10^{-8}$. The 3rd and 4th IVCs are identical with 1st and 2nd IVCs respectively and they are evaluated for the helicopter model with 10% helicopter inertial quantities reduction for different V_A.

In Fig. 4.4 the output and input variances are shown for different V_A using the 1st IVC while in Fig. 4.5 the output and input variances are shown for different helicopter inertia variations using the 1st IVC.

4.5.4 IVC Discussion

Similarly with the OVCs, IVCs are also robustly stable both with respect to variations in V_A and helicopter inertial properties for the helical turn with $\dot{\psi}_A = 0.1\,\text{rad/s}$, $\gamma_{FP} = 0.1\,\text{rad}$ and there is no direct correlation between the magnitudes of input constraints (μ^2) and the length of stability interval (**L**). Extensive numerical experiments show that IVCs are also robustly stable both with respect to variations in V_A and inertial properties for level banked turns and different helical turns (see Appendix D.2).

Clearly from Figs. 4.4 and 4.5 the output variance constraints are satisfied at the nominal flight conditions. Similarly with OVC if one wants to ensure satisfaction of constraints over a larger velocity interval, a safety factor can be introduced in the design. Output variances also display small values. In Fig. 4.6 behaviors of helicopter Euler angles and all controls are given using 1st IVC.

Figure 4.4: Output and Input Variances for The 1st IVC

Figure 4.5: Output and Input Variances for The 3rd IVC
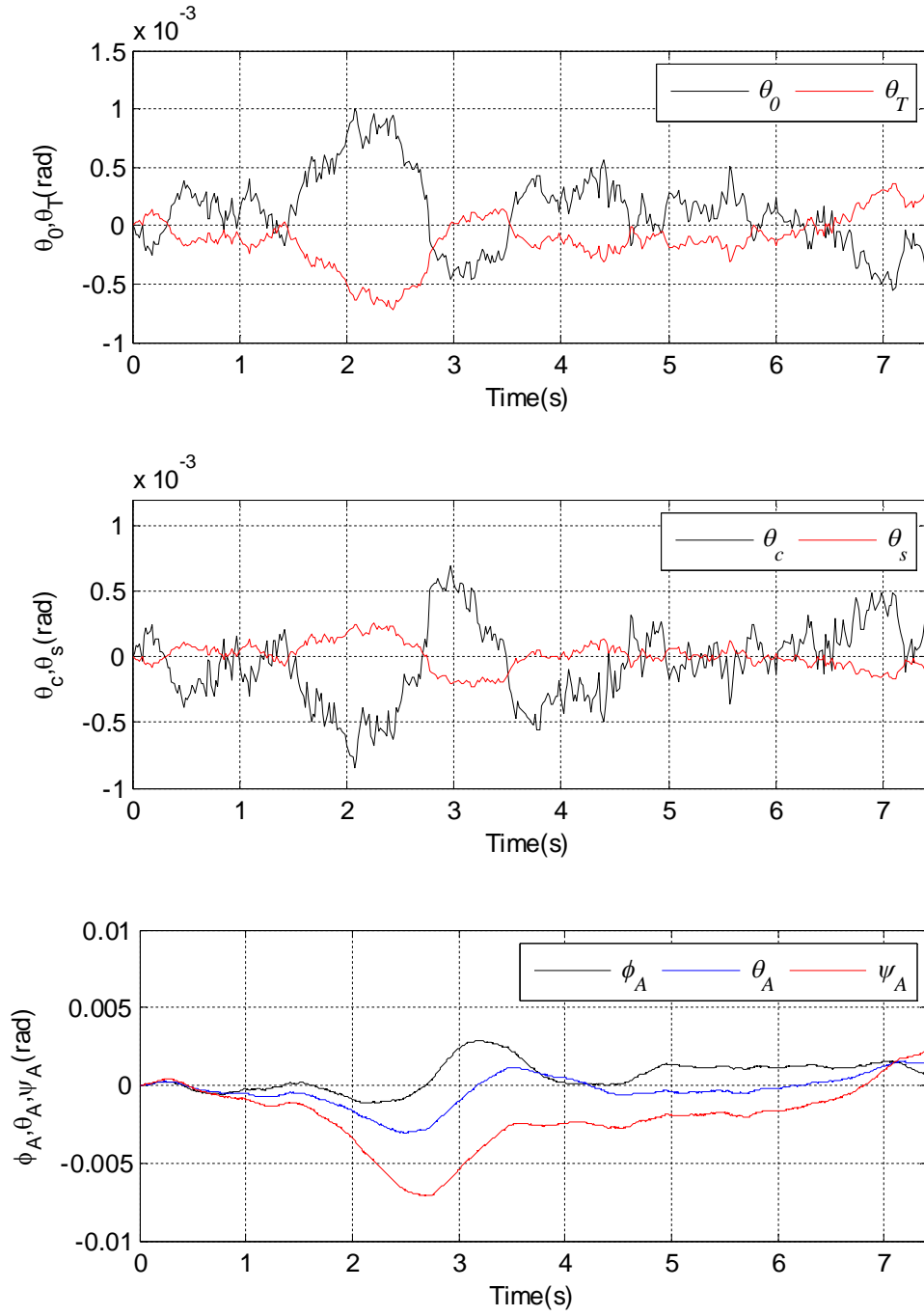
Figure 4.6: Responses of Euler Angles and All Controls Using The 1st IVC

4.6 Sensor Failure with Variance Constrained Controllers

Here a new idea is investigated, namely adaptive switching between controllers which are adequate for different sets of sensors, but satisfy the same performance requirements. The question analyzed next is if the controller can be changed adaptively to satisfy the same variance constraints when the set of measurements changes due to sensor failure. Therefore, in the following sections OVC and IVC designs are investigated with different sets of measurements.

For this purpose the same scenarios as in section 4.5 were examined. The 1st to 4th sets of OVCs and IVCs were redesigned using the same models (see Table 4.1) and the same constraints (i.e. $\sigma^2 = 10^{-4}\begin{bmatrix} 1 & 1 & 0.1 \end{bmatrix}$ for OVC, $\mu^2 = 10^{-5}\begin{bmatrix} 1 & 1 & 1 & 1 \end{bmatrix}$ for IVC) like for the designs which do not experience sensor failure. The sensor failure scenarios considered are summarized in Tables 4.5-4.7 (see Table 4.4 for details). The first column in each table displays the measurements that are no longer available due to sensor failure. For example, in the first line of Table 4.5, ϕ_A and θ_A measurements from the initial set of 9 measurements $(u, v, w, p, q, r, \phi_A, \theta_A, \psi_A)$ are not available thus reducing the set of measurements to 7 $(u, v, w, p, q, r, \psi_A)$.

The first important observation is that the number of iterations required to design OVCs and IVCs with sensor failure is usually higher than the number of iterations required when sensor failure does not occur. For example, for the first sensor failure (when ϕ_A and θ_A measurements are not available) the number of iterations for convergence of the 1st and 2nd OVCs is 18 compared to 4 and 6 iterations when sensor failure does not occur.

77

Closed loop stability robustness with respect to variations in V_A and helicopter inertial properties is also examined as in section 4.5. The results are summarized in Tables 4.5 and 4.6. For example, "Hover to 80kts" means that the closed loop system is exponentially stable for $V_A \in [0,80]$ kts and $\dot{\psi}_A = 0.1$ rad/s, $\gamma_{FP} = 0.1$ rad. It can be seen from these tables that the length of the stability interval (**L**) for all the sensor failure scenarios is close to **L** when sensor failure does not occur.

Table 4.4: Sensor Failure Scenarios

Case	Active Sensors	# Active Sensors	Failed Sensors	# Failed Sensors
1st Failure	$u,v,w,$ p,q,r,ψ_A	7	ϕ_A, θ_A	2
2nd Failure	$p,q,r,$ ϕ_A, θ_A, ψ_A	6	u,v,w	3
3rd Failure	$u,v,w,$ ϕ_A, θ_A, ψ_A	6	p,q,r	3

Table 4.5: Closed Loop Stability Robustness for OVC (CL is ES)

Failed Sensors	1st	2nd	3rd	4th
1st (ϕ_A, θ_A)	Hover to 80 kts	Hover to 80 kts	Hover to 80 kts	Hover to 80 kts
2nd (u, v, w)	Hover to 80 kts	Hover to 80 kts	Hover to 80 kts	Hover to 80 kts
3rd (p, q, r)	Hover to 80 kts	Hover to 80 kts	Hover to 80 kts	Hover to 80 kts

Table 4.6: Closed Loop Stability Robustness for IVC (CL is ES)

Failed Sensors	1st	2nd	3rd	4th
1st (ϕ_A, θ_A)	Hover to 80 kts	Hover to 80 kts	Hover to 70 kts	Hover to 80 kts
2nd (u, v, w)	20 kts to 80 kts	30 kts to 80 kts	20 kts to 80 kts	30 kts to 80 kts
3rd (p, q, r)	Hover to 70 kts	Hover to 80 kts	Hover to 70 kts	Hover to 80 kts

Extensive numerical experiments show that the behaviors of output and input variances with respect to variations in V_A and helicopter inertial properties with sensor failure are qualitatively similar with the behaviors observed when sensors do not fail (see Appendix E).

Table 4.7: Control Energy Comparison

Failed Sensors	OVC Cost		IVC Cost	
	1st and 3rd	2nd and 4th	1st and 3rd	2nd and 4th
1st (ϕ_A, θ_A)	0.003607	0.004830	0.001944	0.0006781
2nd (u, v, w)	0.001910	0.002633	0.002541	0.0005914
3rd (p, q, r)	0.002225	0.0022632	0.001587	0.0004429
(no failure)	0.001365	0.001526	0.001449	0.0003809

The control energy (i.e. cost) of resulting OVCs and IVCs is summarized in Table 4.7. It can be seen that the control energy of OVCs and IVCs with sensor failure is higher than the control energy when sensor failure does not occur. Note that the control energy of OVC and IVC design is found using (see [17])

$$J = E_\infty \ \mathrm{u}^T R \mathrm{u} = trace\left(RGX_cG^T\right) \tag{4.17}$$

where G and X_c are computed using OVC and IVC algorithms (see Appendix C). For OVC R is selected by the user, whereas for IVC it is computed using IVC algorithm.

A final important observation is that the results (i.e. number of iterations, stability robustness, input and output variances, and control energy) with sensor failure are qualitatively similar for level banked turns and different helical turns (see Appendix E).

4.7 Adaptive Switching with Variance Constrained Controllers

The behavior of the closed loop system when switching between controllers occurs due to 1st sensor failure scenario for 1st OVC and IVC is examined using Matlab. Simulations (initial conditions are chosen as zero deviation from trim conditions) showed in Figs. 4.5-4.8 indicate that 1st OVC and IVC designs are robust to 1st sensor failure. In these figures the bold vertical line represents the instant when ϕ_A, θ_A measurements fail. The sensor failure occurs when $\psi = 200$rad (or t=7.4s). In Figs. 4.7 and 4.8, responses of helicopter Euler angles and all controls are given using 1st OVC and 1st IVC, respectively. Extensive numerical experiments show that OVC and IVC are robust to other sensor failures (i.e. 2nd and 3rd failures in Tables 4-6). Similar results are found for level banked turns and different helical turns (see Appendix E).
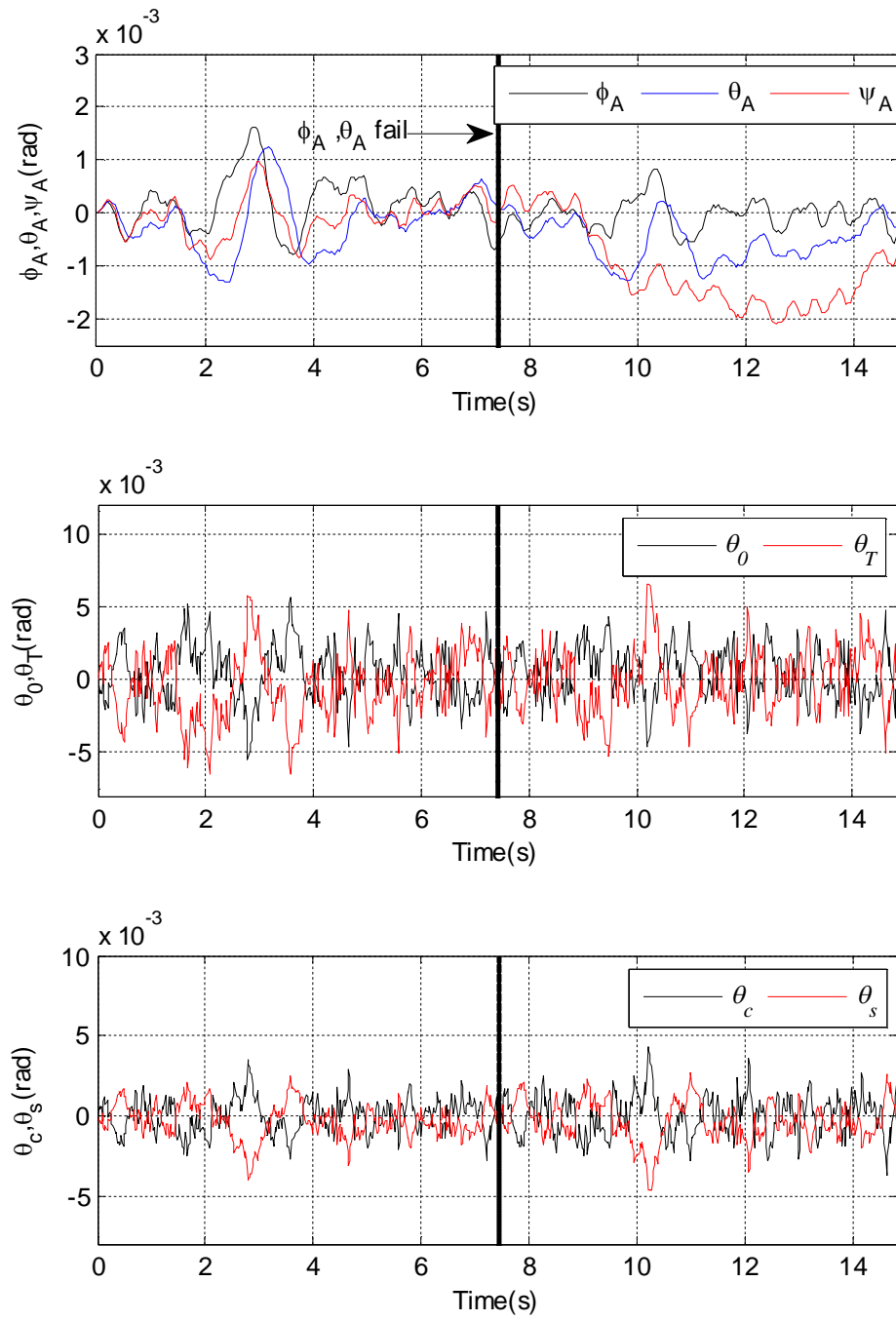
Figure 4.7: OVC Switching
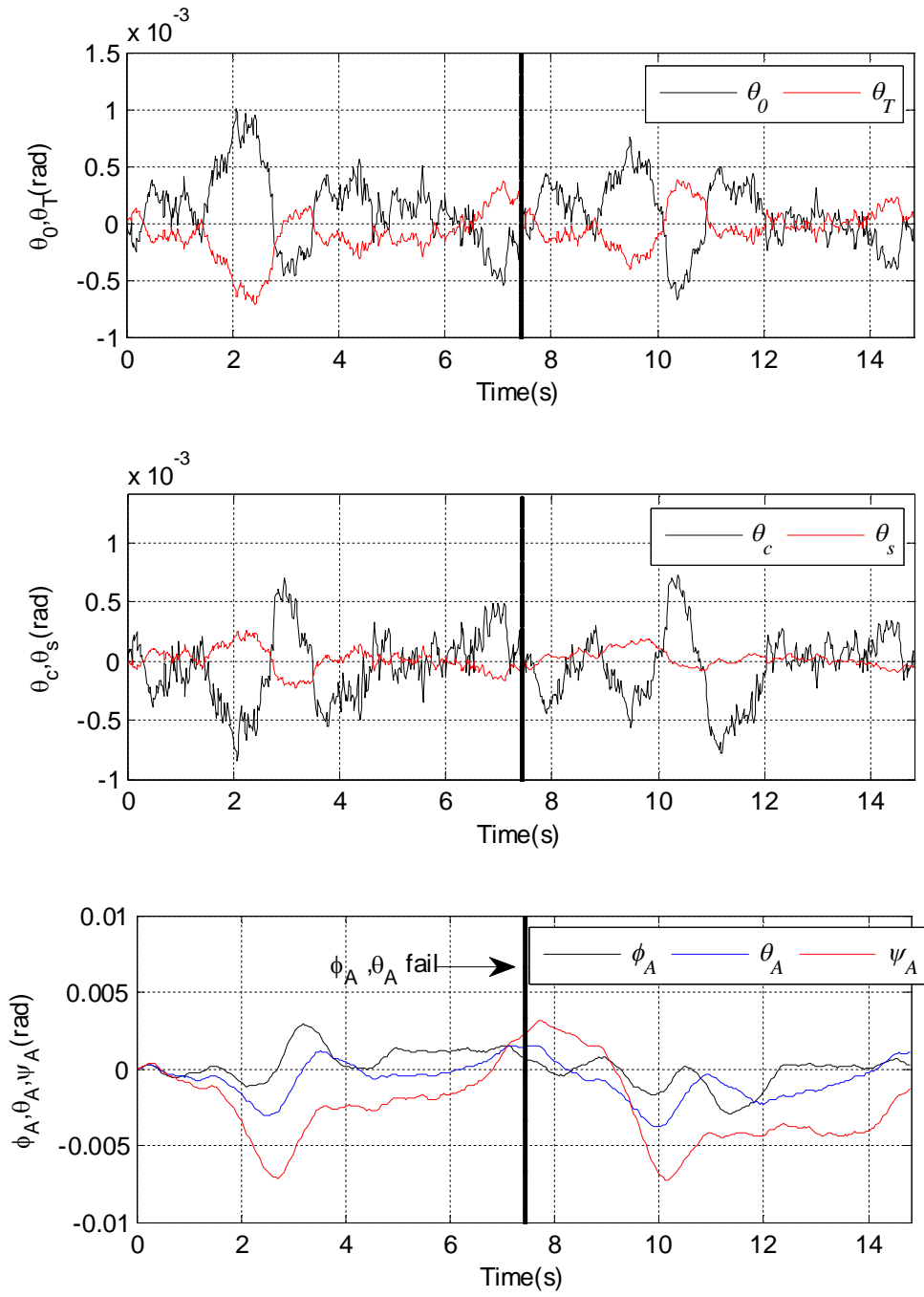
Figure 4.8: IVC Switching

4.8 Other Safe Switching Between Controllers Approaches

In [63] an approach to detect and isolate the aircraft sensor and control surface/actuator failures affecting the mean of the Kalman filter innovation sequence was presented on a F-16 fighter aircraft dynamic model. A robust Kalman filter (RKF) was designed in order to isolate the detected sensor and control surface failures and this RFK satisfies the Doyle-Stein condition. The use of the RKF was very useful in the isolation of sensor and control surface failures as it was insensitive to the latter failures.

In [64] the iterative feedback tuning (IFT) safe switching algorithm was extended for the case of multivariable nonlinear systems with unknown descriptions. The proposed scheme incorporates multivariable IFT techniques, with a multivariable step-wise safe switching algorithm. Using the IFT algorithm for tuning safe switching controllers eliminated the need for identifying the MIMO (Multi-Input Multi-Output) linear models that describe the plant around trim points. Instead of that, specific experiments proposed by multivariable IFT have to be performed, in order to tune the parameters of "common" MIMO controllers, which are controllers that satisfy the design requirements simultaneously for two MIMO linear systems corresponding to adjacent trim points. Controller tuning is based on the optimization of a cost criterion appropriately defined, so as to express the desired closed-loop performance characteristics simultaneously for two adjacent operating areas.

In [65,66] a fundamentally different approach than in [64] was proposed. The following situation was considered: given a control system with an LPV (linear parameter varying) plant and a stabilizing LPV controller, switching to new controller to get better performance was performed. This approach does not require a plant model, requires only

closed-loop data with only a small amount of external excitation, uses standard identification methods, and gives as few incorrect analysis results.

In [67] the goal of stabilizing an uncertain plant by means of switching through an infinite candidate controller set was solved, provided that feasibility (existence of at least one stabilizing solution in the candidate controller set) holds. The focus was on how a given candidate controller set should be pruned based on data in order to adaptively converge to a controller in the candidate set that achieves and maintains stable behavior and acceptable performance. Though this data driven process requires no prior knowledge of the plant model, this does not mean that their formulation is model-free. Plant models, when available, play an essential role in determining and designing the candidate controller set.

CHAPTER 5:

Robustness Tools

In this chapter other tools that can be used to examine robustness properties of controllers are discussed. Some of them are also evaluated on our previously developed complex, control oriented, physics based helicopter models and on the control systems designed for these helicopter models.

5.1 Gain and Phase Margins

The concept of stability margins, specifically gain and phase margins, refers to stability *robustness* in feedback control systems. In general, robustness refers to a system's ability to tolerate small changes (e.g. in the system parameters) without undergoing a qualitative change in behavior (e.g. from stability to instability). To quantify this property gain margin and phase margin are widely used for robustness studies.

Gain Margin (GM) is one of the most frequently used criteria for measuring relative stability of control systems. In the frequency domain, gain margin is used to indicate the closeness of the intersection of the negative real axis made by the Nyquist plot of the closed loop transfer function, $L(j\omega)$ to the (-1, j0) point (see Fig. 5.1). The gain margin shows how much the system gain may be increased without loosing stability. A formula that can be used to compute the gain margin is [61]

$$\text{gain margin} = GM = 20\log_{10}\frac{1}{|L(j\omega_p)|} = -20\log_{10}|L(j\omega_p)|\,dB \tag{5.1}$$

Phase Margin (PM) is defined as the angle (in degrees) through which the $L(j\omega)$ plot must be rotated about the origin so that the gain crossover passes through the (-1, j0).

The phase margin shows how large a delay may be inserted in control loop without loosing stability. A formula that can be used to compute the phase margin is [61]

$$\text{phase margin}=\angle\ L(j\omega_g)-180^0 \tag{5.2}$$
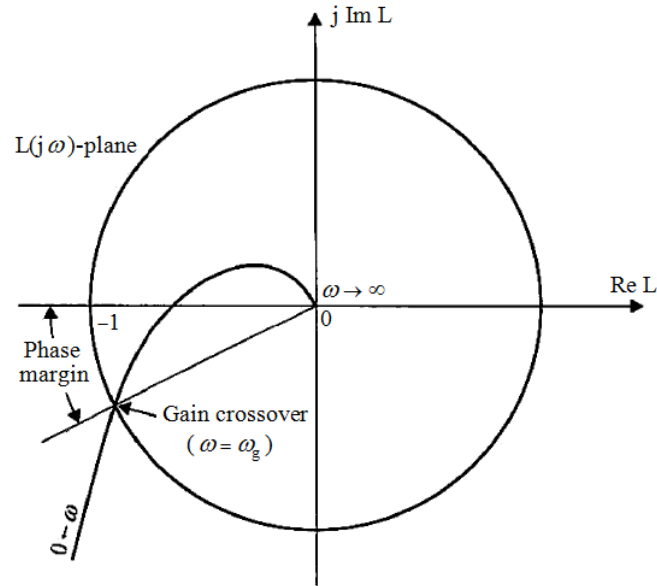
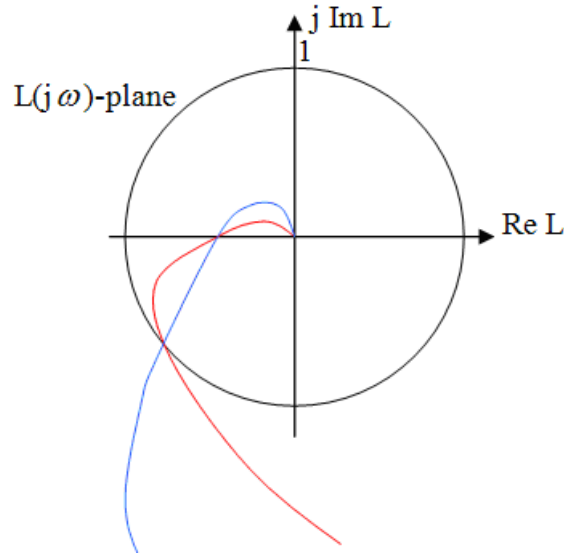**Figure 5.1: Phase Margin Defined in The *L(jw)*-Plane ([61][pp. 454])**

Figure 5.2: Stability Margins Example

In the example in Fig. 5.2 the red and blue lines correspond to systems that have the same phase and gain margins, but the "blue system" is obviously more robust (i.e. far from -1).

Phase and gain margins have the big advantage that they are easy to understand (see Figs. 5.1 and 5.2). Unfortunately they are strictly defined only for SISO (Single-Input Single-Output) systems. For MIMO (Multi-Input Multi-Output) systems new robustness measures have to be defined. Recent research along these lines led to the introduction of the Generalized Stability Margin (GSM), gap metric, and v-gap metric.

5.2 Generalized Stability Margin, Gap Metric and v-Gap Metric

As noted before, robustness for SISO systems is easily examined using Phase and Gain Margins. Unfortunately, these tools are not useful for MIMO systems such as the

helicopter models developed in this dissertation. Therefore, novel tools, adequate for MIMO systems, are examined in this sub section.

5.2.1 Generalized Stability Margin

For a given closed loop system $[P,C]$ where P is a MIMO plant model and C is the control system, the definition of generalized stability margin is [68,69]

$$b_{P,C} := \begin{cases} \left\| \begin{bmatrix} P \\ I \end{bmatrix} (I - CP)^{-1} \begin{bmatrix} -C & I \end{bmatrix} \right\|_{\infty}^{-1} & \text{if } [P,C] \text{ is stable} \\ 0 & \text{otherwise} \end{cases} \tag{5.3}$$

5.2.2 Gap Metric

To define the gap metric the graph of an operator must be defined. Specifically, the graph of the operator P is the subspace of $H_2 \times H_2$ consisting of all pairs (u, y) such that $y = Pu$. This is given by

$$\text{graph}(P) = \begin{pmatrix} M \\ N \end{pmatrix} H_2 := G_P \tag{5.4}$$

and it is a closed subspace of H_2.

The gap between two closed subspaces P_1 and P_2 is defined by [70,71]

$$\delta_g(P_1, P_2) = \left\| \Pi \begin{pmatrix} M_1 \\ N_1 \end{pmatrix}_{K_1} - \Pi \begin{pmatrix} M_2 \\ N_2 \end{pmatrix}_{K_2} \right\| \tag{5.5}$$

Here Π_K denotes the orthogonal projection onto K, and $P_1 = N_1 M_1^{-1}$ and $P_2 = N_2 M_2^{-1}$ are normalized right coprime factorizations.

5.2.3 *v*-Gap Metric

One issue with the gap metric is that it is very conservative. To alleviate this disadvantage the *v*-Gap metric has been invented. For given $P_0, P_1 \in R^{pxq}$ the definition for the *v*-gap metric is [68,69]

$$\delta_v(P_0, P_1) := \begin{cases} \left\| \tilde{G}_1 G_0 \right\|_\infty & if \;\; \det(G_1^* G_0)(\mathrm{jw}) \neq 0 \;\; \forall \omega \in (-\infty, \infty) \;\; \text{and} \;\; wno \;\; \det(G_1^* G_0) = 0 \\ 1 & otherwise \end{cases} \qquad (5.6)$$

where wno g is the winding number about the origin of g(s) and s follows the standard Nyquist D-Contour.

An important result is that if $\delta_v(P_1, P_2)$ is small then any satisfactory controller for P_1 (in the sense of $b_{P_1,C}$ being large) will also be satisfactory for P_2. This result is also valid for the gap metric. Finally, it should be noted that the quantities $b_{P,C}, \delta_g(P_1, P_2)$, and $\delta_v(P_0, P_1)$ are always between in [0,1].

5.3 Applications

In the following we present some GSM and gap computations for our helicopter models. Consider the flexible blade helicopter model linearized around $V_A = 40\text{kts}$ straight level flight condition. Consider also the flexible blade helicopter model linearized around $V_A = 80\text{kts}$ straight level flight condition. If we compute the gap and *v*-gap metric between these models we find 0.8484 and 0.8483. Moreover, the gap and *v*-gap metric between two flexible blade helicopter models, both linearized around $V_A = 40\text{kts}$ straight level flight condition with one model experiencing 10% reduction in all helicopter inertial

parameters, are 0.08575 and 0.08568. However, the GSM is very small, i.e. $8.9297.10^{-4}$, which would indicate that robustness properties are poor. Definitely this is not the case, as indicated in the previous chapter via extensive simulations. The discrepancy between the small GSM value and the good robustness properties of previously tested controllers can be explained by the facts that a) GSM is very conservative by nature and b) GSM computation assumes that all elements in the plant matrices are perturbed. This is not the case in our helicopter models, because for example A_p matrix (see Eq. 4.1) has a clear structure (e.g. there are elements which are always zero).

CHAPTER 6:

Constrained Model Predictive Control

In this chapter, MPC controllers, which account for output and input constraints simultaneously, are designed. MPC theory is increasingly attractive because of its effective use of models for prediction, potential for online adaptation, and constraints satisfaction. A brief description of MPC is given next (see [72-74]).

In constrained MPC, a cost function $V(k)$:

$$V(k) = \sum_{i=H_w}^{H_p} \left\| \hat{y}(k+i\,|\,k) - r(k+i\,|\,k) \right\|^2_{Q(i)} + \sum_{i=0}^{H_u-1} \left\| \Delta \hat{u}_p(k+i\,|\,k) \right\|^2_{R(i)} \tag{6.1}$$

is minimized subject to the discretized dynamic equations and some constraints:

$$E \begin{bmatrix} \Delta U(k) \\ \mathbf{1} \end{bmatrix} \le 0; \ F \begin{bmatrix} U(k) \\ \mathbf{1} \end{bmatrix} \le 0; \ G \begin{bmatrix} Y(k) \\ \mathbf{1} \end{bmatrix} \le 0 \tag{6.2}$$

where

$$\Delta U(k) = \begin{bmatrix} \Delta\hat{u}_1(k\,|\,k) & . & \Delta\hat{u}_1(k+H_u-1\,|\,k) \\ . & . & . \\ \Delta\hat{u}_{n_u}(k\,|\,k) & . & \Delta\hat{u}_{n_u}(k+H_u-1\,|\,k) \end{bmatrix}, \ U(k) = \begin{bmatrix} \hat{u}_1(k\,|\,k) & . & \hat{u}_1(k+H_u-1\,|\,k) \\ . & . & . \\ \hat{u}_{n_u}(k\,|\,k) & . & \hat{u}_{n_u}(k+H_u-1\,|\,k) \end{bmatrix}$$

$$Y(k) = \begin{bmatrix} \hat{y}_1(k+H_w\,|\,k) & . & \hat{y}_1(k+H_p\,|\,k) \\ . & . & . \\ \hat{y}_{n_y}(k+H_w\,|\,k) & . & \hat{y}_{n_y}(k+H_p\,|\,k) \end{bmatrix}, \tag{6.3}$$

E, F, and G are suitable matrices, n_y and n_u are the number of outputs and inputs, H_p and H_u are prediction and control horizons, and $r(k+i\,|\,k)$ is the reference trajectory to be tracked (Fig. 6.1). Usually $H_u \le H_p$ to decrease computational work. Sometimes

penalizing tracking errors does not start immediately (i.e. $H_w > 1$) because of the delay between applying an input and seeing any effect. The optimization problem in Eqs. 6.1-6.3 is equivalent to a quadratic programming problem [72] [pp. 81-83]. After solving it, only the first control in the resulting optimal control policy is applied and the optimization control problem is repeated for the next time horizon.
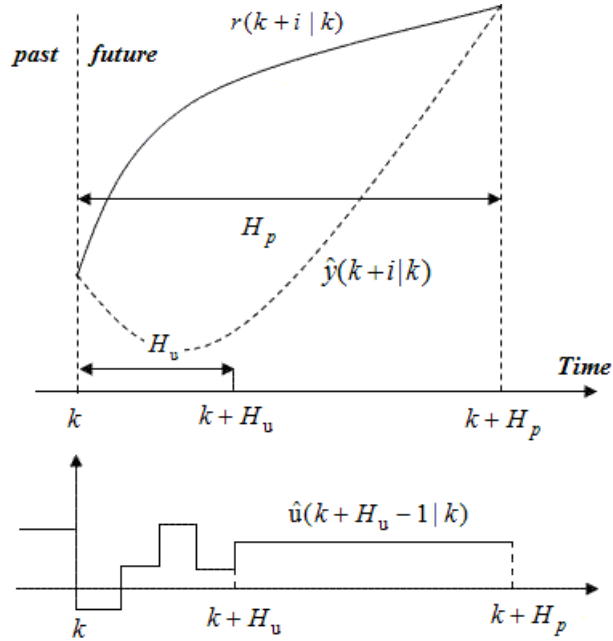
Figure 6.1: MPC Representation

The ability of MPC to track discontinuous trajectories while obeying heterogeneous constraints for maneuvering flight and in the event of sensor failure is investigated. For this purpose MPC design was analyzed using linearized helicopter models, which were discretized using a nondimensionalized sampling time of 1rad that corresponds to 0.037s. This is much lower (around 50 times) than the period of any flight dynamics mode (see [75] for a discussion on sampling time selection).

For the results presented next, the helicopter model, which is linearized around a helical turn ($V_A = 40\,\text{kts}$, $\dot{\psi}_A = 0.1\,\text{rad/s}$, $\gamma_{FP} = 0.1\,\text{rad}$, $R_{turn} = 204.73\,\text{m}$), is used. Plant and sensor uncorrelated white Gaussian noises with intensities of $W = 10^{-7}I_{41}$, $V = 10^{-7}I_{n_s}$ (n_s is the number of non-failed sensors) respectively were introduced in the linearized model.

In the first example, the helicopter must track a reference trajectory ($r(k+i\,|\,k)$ in Eq. 6.1) for which the roll angle has a prescribed time variation and the other two Euler angles are forced to be zero. The parameters used for MPC design were (all angles are given in radians):

Output and input constraints:

$$\begin{bmatrix} -1 & -0.02 & -0.02 \end{bmatrix}^T \leq \begin{bmatrix} \phi_A & \theta_A & \psi_A \end{bmatrix}^T \leq \begin{bmatrix} 1 & 0.02 & 0.02 \end{bmatrix}^T$$

$$\begin{bmatrix} |p| & |q| & |r| \end{bmatrix}^T \leq \begin{bmatrix} 1 & 1 & 1 \end{bmatrix}^T (rad\,/\,\text{s})$$

$$\begin{bmatrix} 0 & -0.18 & -0.18 & 0 \end{bmatrix}^T \leq \begin{bmatrix} \theta_0 & \theta_c & \theta_s & \theta_T \end{bmatrix}^T \leq \begin{bmatrix} 0.35 & 0.18 & 0.18 & 1 \end{bmatrix}^T$$

$$\begin{bmatrix} |\Delta\theta_0| & |\Delta\theta_c| & |\Delta\theta_s| & |\Delta\theta_T| \end{bmatrix}^T \leq \begin{bmatrix} 0.175 & 0.09 & 0.09 & 0.5 \end{bmatrix}^T$$

Other MPC parameters:

$H_p = 20$ and $H_u = 1$

For the second and third examples, measurements of two Euler angles (θ_A, ψ_A) and linear velocities (u, v, w), respectively are not available due to sensor failure. The trajectories and parameters used for MPC design are the same as in the first example.

In the fourth example, for the evaluation of the robustness of the MPC designs it was considered that all helicopter inertial parameters (helicopter mass and helicopter inertia

matrix elements) are uncertain. There is no sensor failure for this example. We considered that the plant model's inertial parameters decrease by 10% , while the internal model, which is used to produce MPC signals, is not aware of these uncertainties. We then simulated the response of the plant affected by these uncertainties. The trajectories and sensors used for MPC design are the same as in the first example. Some MPC parameters are changed: $H_p = 10$, and $W = 10^{-4} I_{41}$.

The length of simulation interval for all the MPC examples is 200rad (or 7.4s). There is a discontinuity in the desired trajectory at instant $\psi = 100 \, \text{rad}$ (or $t = 3.7 \, \text{s}$). Calculation time of all the MPCs is around 0.2 rad (0.0074s) which is 20% of the sampling time. Note that for the MPC simulations, black, blue and green colors are referring to the first, second, and third components of Euler angles, linear velocities, and angular velocities, respectively.
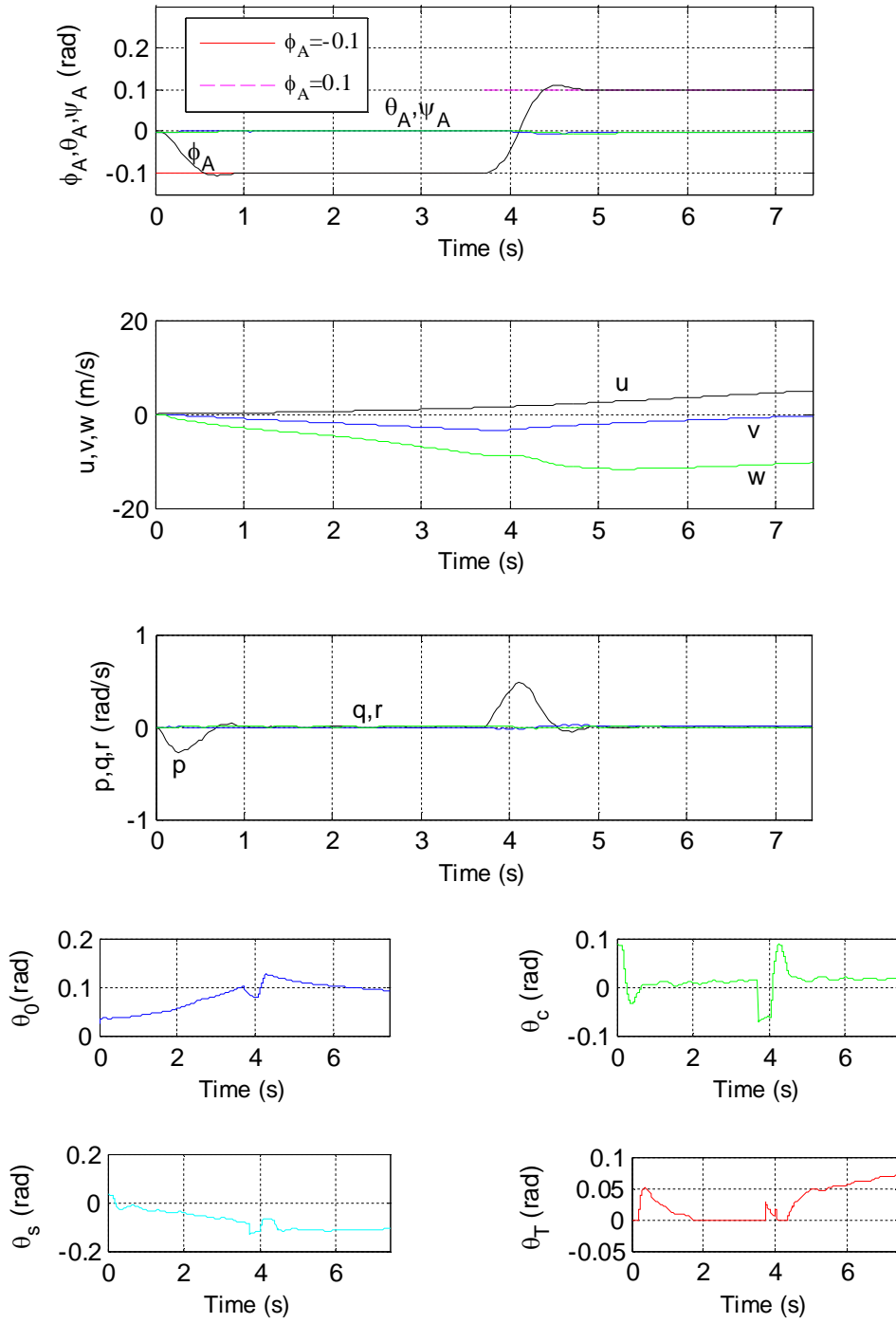
Figure 6.2: 1ˢᵗ MPC Example (No Sensor Failure)
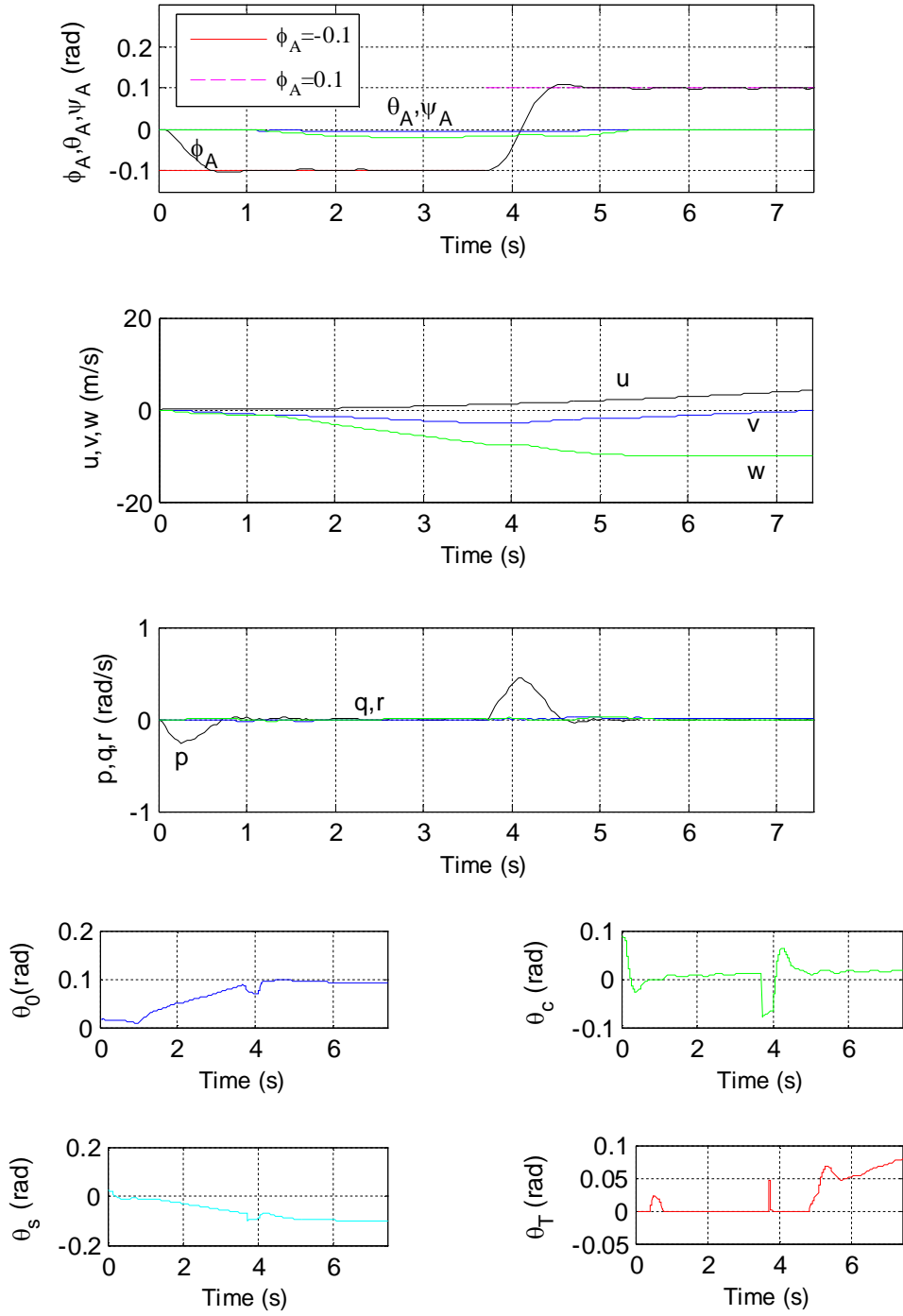
Figure 6.3: 2nd MPC Example (1st Sensor Failure)
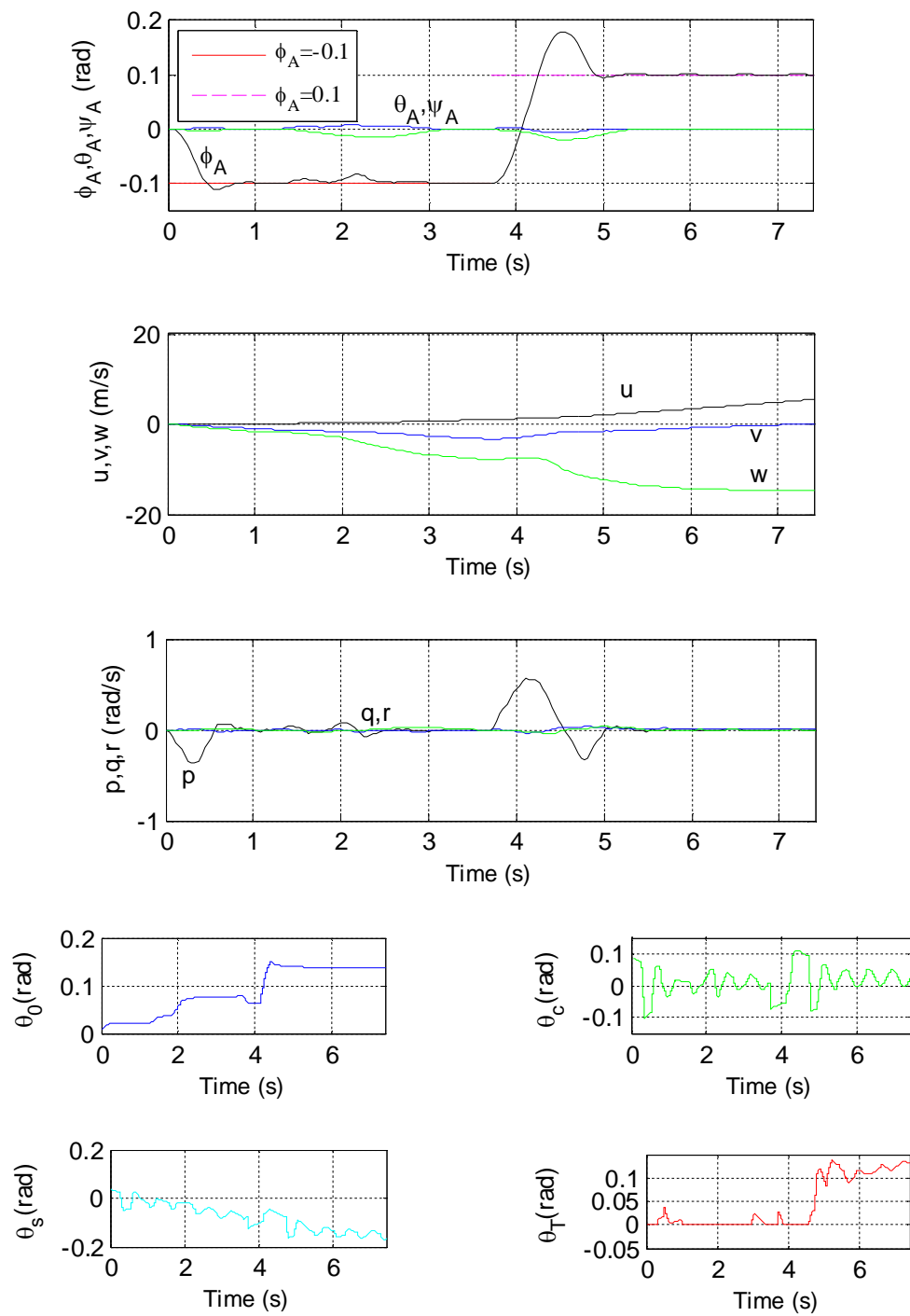
Figure 6.4: 3rd MPC Example (2nd Sensor Failure)
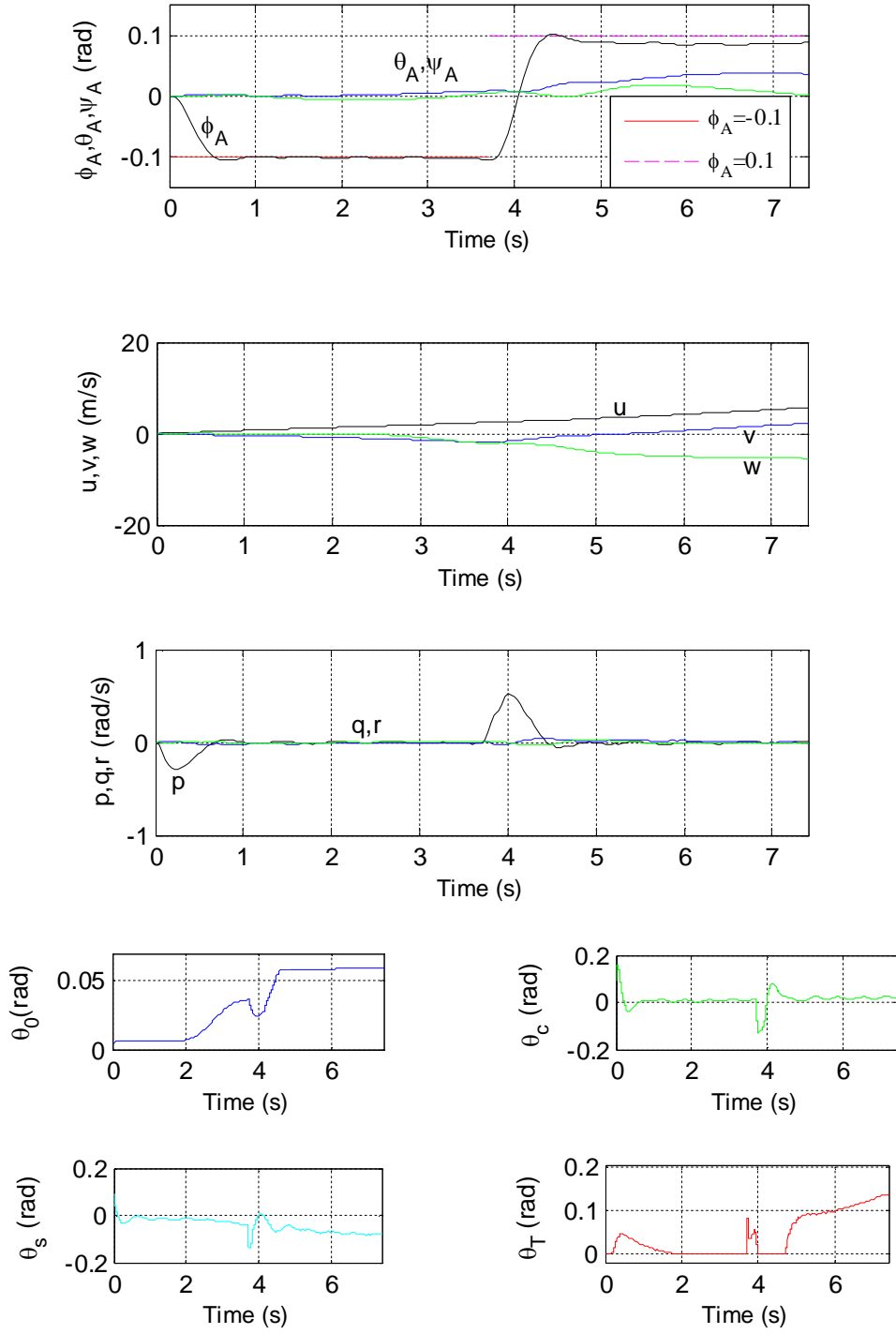
Figure 6.5: 4ᵗʰ MPC Example (Robustness, No Sensor Failure)

The first observation is that in all nominal designs MPC satisfied the constraints (see Figs. 6.2-6.5, plots of $p, q, r, \phi_A, \theta_A, \psi_A, \theta_0, \theta_c, \theta_s, \theta_T$). When modeling uncertainties (i.e. variation of helicopter inertial properties) were also considered, nominal MPC satisfied the constraints.

The second important observation is that when sensor failure occurs, the overshoot of helicopter roll angle is bigger than when there is no sensor failure. For example, the overshoot of helicopter roll angle in Fig. 6.2 is obviously less than the roll angle overshoots in Figs. 6.3 and 6.4. The biggest helicopter roll angle overshoot with sensor failure is seen when linear velocities (u,v,w) measurements fail (see Fig. 6.4), whereas this overshoot is smaller when some Euler angle measurements (i.e. ϕ_A, θ_A) fail (see Fig. 6.3). The examples suggest that, for the problem analyzed in this section, loosing velocity measurements (i.e. u, v, w or p, q, r) is more dangerous than loosing some Euler angle measurements (i.e. ϕ_A, θ_A). When angular velocity measurements (i.e. p, q, r) fail, the MPC example defined in this section is not feasible.

Another important observation is that when modeling uncertainties (i.e. variation in *all* helicopter inertial properties) are considered, MPC becomes less successful in tracking strong discontinuities. The internal models which produce control signals are still satisfying the constraints. However, some plant outputs (i.e. θ_A, ψ_A) violate the constraints when this model experiences uncertainties (see Fig. 6.5). This example shows that MPC has robustness limitations: when modeling uncertainties (i.e. variation in helicopter inertial quantities) exist and also hard constraints on outputs and inputs are imposed, MPC is not very successful in tracking discontinuous trajectories.

A final observation is that the other states which are not included in the reference trajectory tracked by MPC (u, v, w, p, q, r) do not experience catastrophic behavior (e.g. large and fast variations) as shown in Figs. 6.2-6.5.

We also remark that extensive numerical experiments with level banked turns and different helical turns indicate that all the observations discussed in this section are still valid (see Appendix F).

The previous MPC examples are also examined with the helicopter model which is linearized around a hover turn ($V_A = 1\,\text{kt}$, $\dot{\psi}_A = 0.1\,\text{rad/s}$, $\gamma_{FP} = 0.1\,\text{rad}$, $R_{turn} = 5.12\,\text{m}$). All the MPC design parameters and trajectories are chosen the same with the previous set of examples. The previous discussion is also valid for hover turn (see Appendix F for more examples).
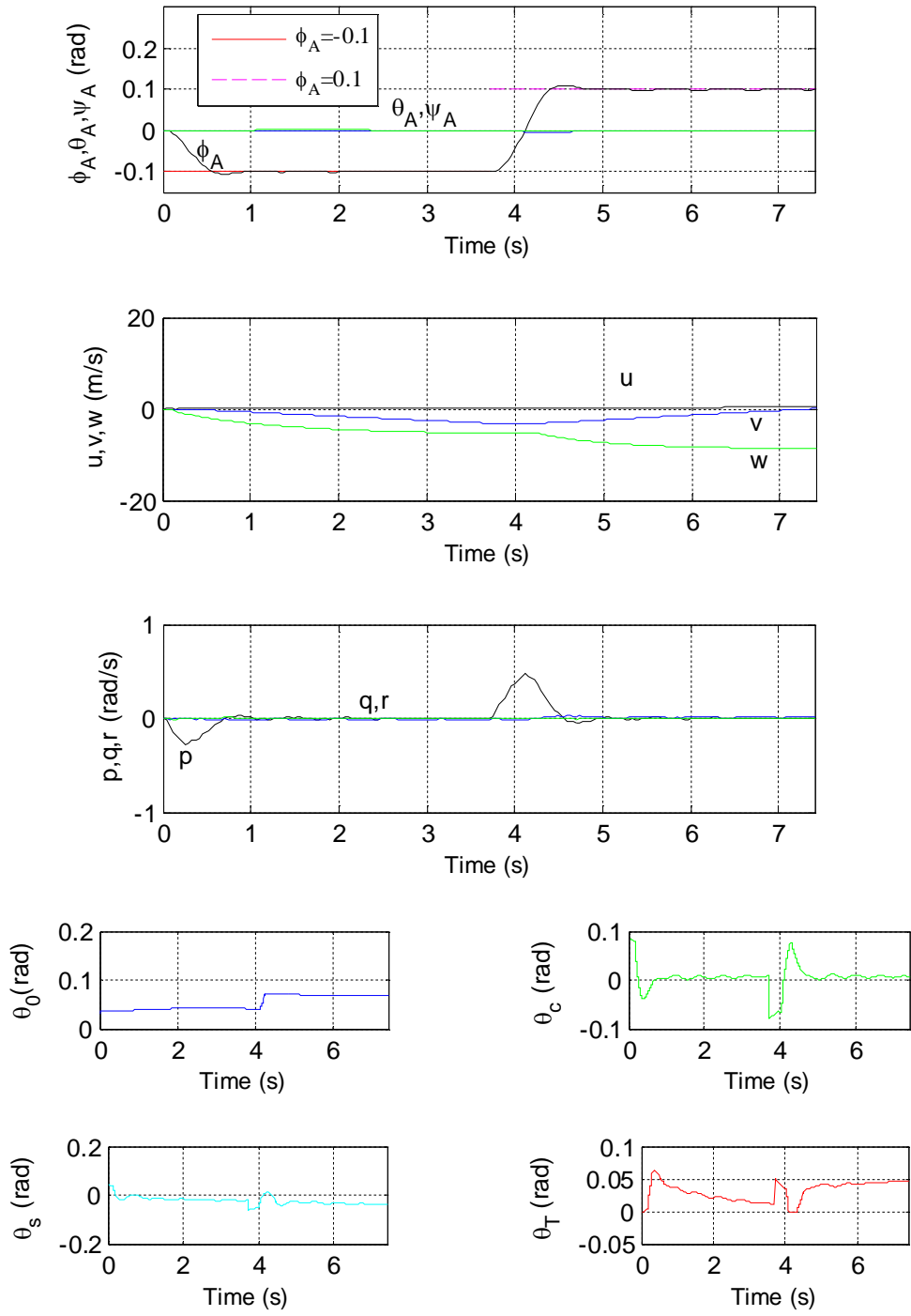
Figure 6.6: 1st MPC Example for Hover Turn (No Sensor Failure)
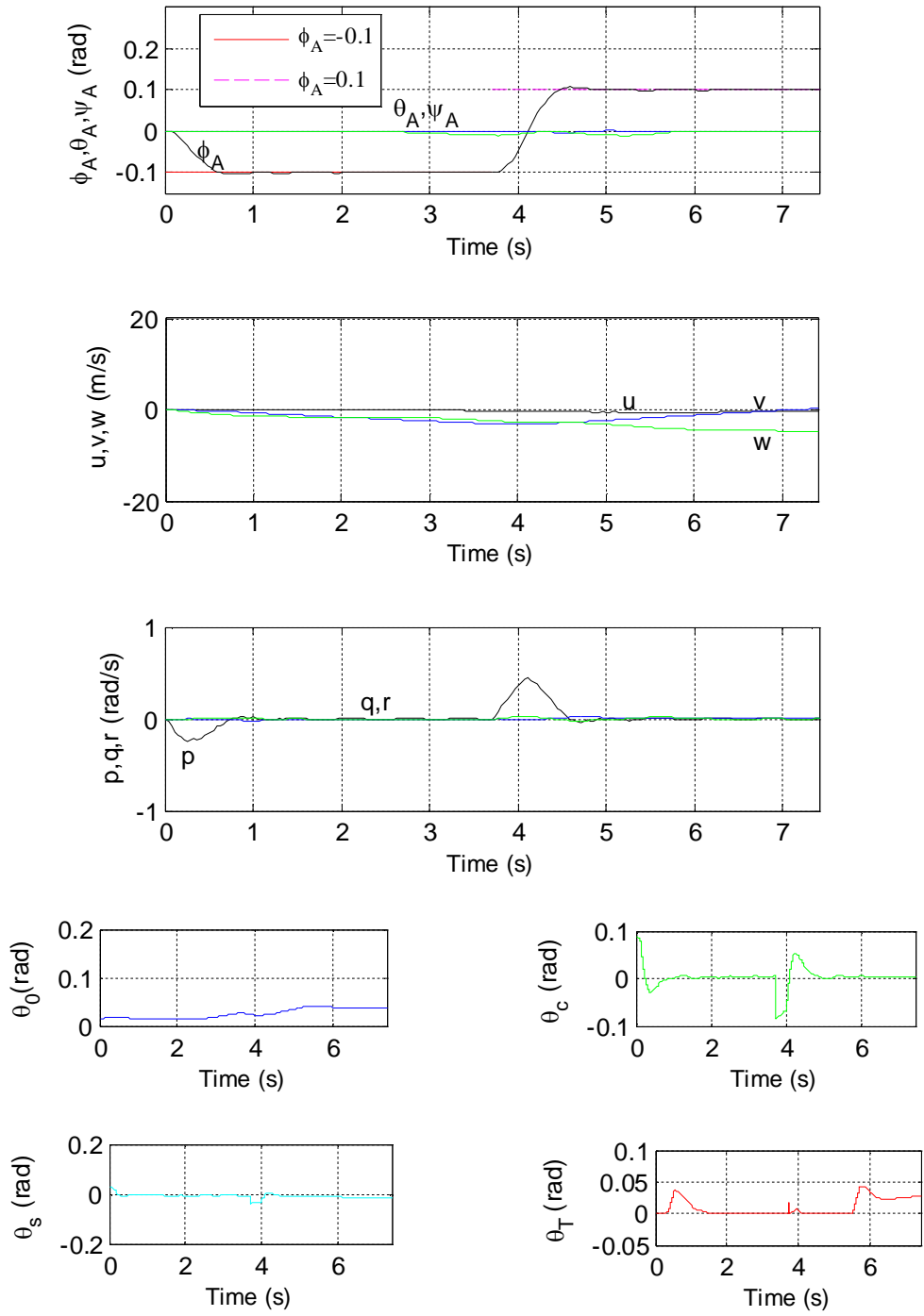
Figure 6.7: 2nd MPC Example for Hover Turn (1st Sensor Failure)
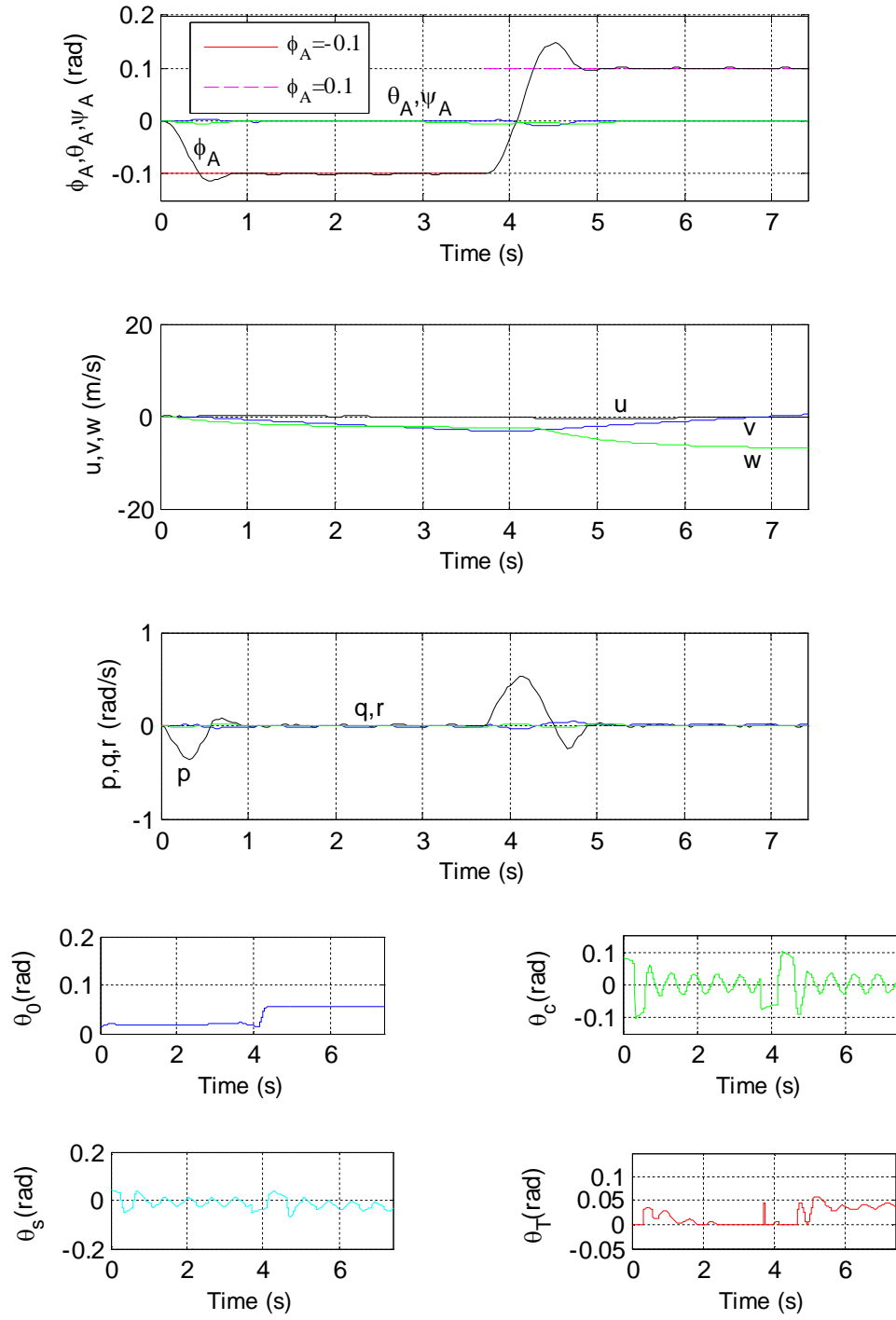
Figure 6.8: 3rd MPC Example for Hover Turn (2nd Sensor Failure)
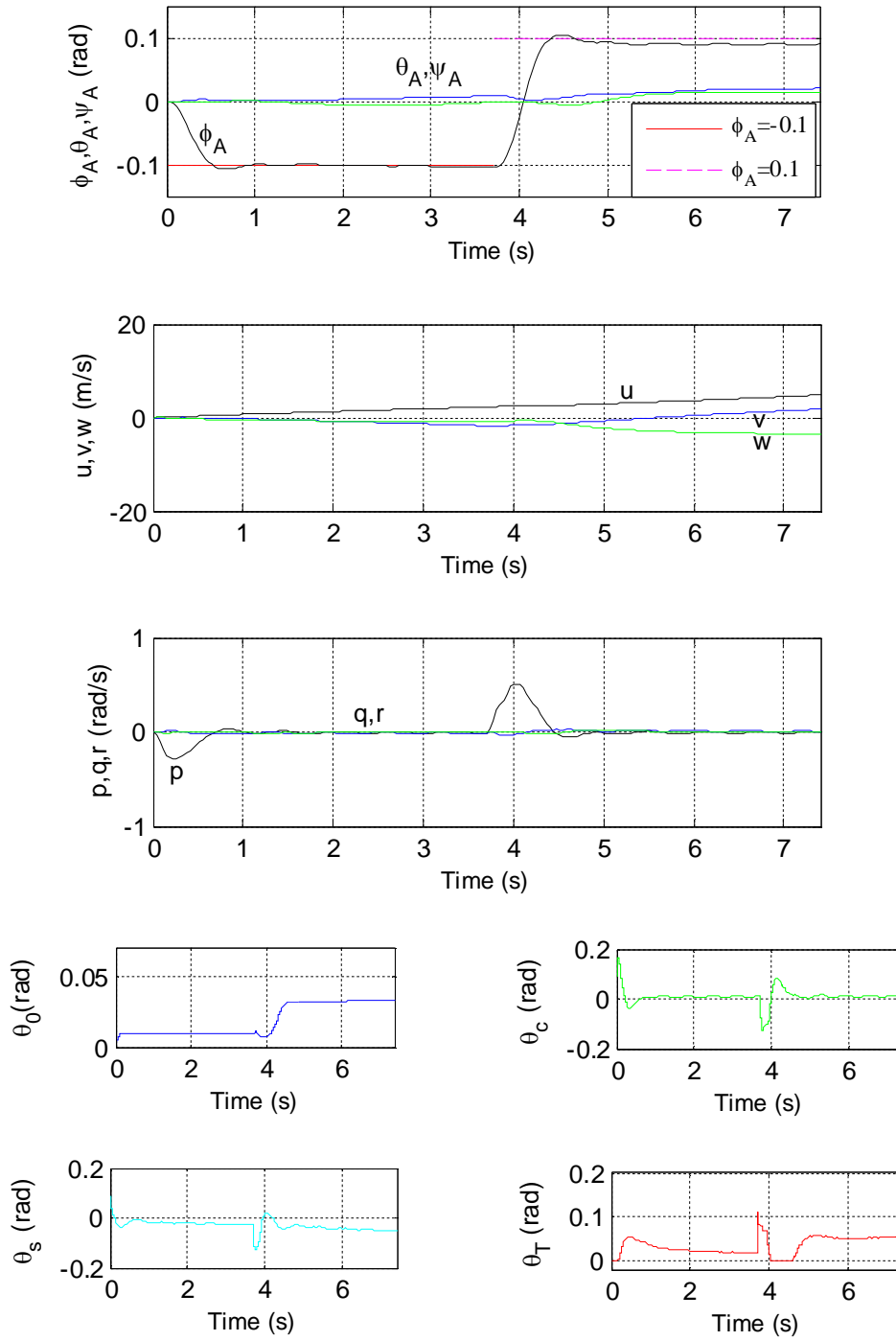
Figure 6.9: 4th MPC Example for Hover Turn (Robustness, No Sensor Failure)

CHAPTER 7:

Simultaneous Model and Control System Design

In this chapter, simultaneous helicopter plant and control system design are examined. The derivative of J (cost of OVC) with respect to x (set of optimization parameters) cannot be computed analytically. This recommends the application of certain stochastic optimization techniques. Specifically, in this article SPSA [43], which has proven effective in solving other complex problems [44], including optimization of non-differentiable functions [76], has been selected to solve the problem:

$$\min_{A_c,F,G,x} \quad J = E_\infty \, \mathbf{u}^T R \mathbf{u} \tag{7.1}$$

subject to Eqs. 4.8, 4.9 and 4.11 where $x = \{c, K_\beta m, R, \theta_{tw}, \Omega\}$ is the set of plant optimization parameters. The elements of x are constrained, i.e. $x_{i_{min}} \leq x_i \leq x_{i_{max}}$ (see Table 7.1).

Table 7.1: Design Variables and Constraints

Design Variable	Nominal Value	Lower Bound $\Delta x_i / x_i$	Upper Bound $\Delta x_i / x_i$
c	0.5401 m	-0.05	0.05
K_β	48149 Nm/rad	-0.05	0.05
m	9.1 kg/m	-0.05	0.05
R	7.5 m	-0.05	0.05
θ_{tw}	-0.14 rad	-0.05	0.05
Ω	27 rad/s	-0.05	0.05

SPSA has many advantages. For example, SPSA uses only two evaluations of the objective for the evaluation of the gradient [43]. Also, numerical experiments indicated

that SPSA is more efficient in finding the global minimum compared to other computationally expensive algorithms like genetic algorithms and fast simulated annealing [77]. Moreover, the SPSA was also successful in solving constrained optimization problems [78]. Finally, under certain conditions (see [43]) strong convergence of the SPSA has been theoretically proved.

7.1 Formulation

Let x denote the vector of optimization variables. In classical SPSA, if $x_{[k]}$ is the estimate of x at k-th iteration, then

$$x_{[k+1]} = x_{[k]} - a_k g_{[k]} \tag{7.2}$$

where a_k is a decreasing sequence of positive numbers and $g_{[k]}$ is the estimate of the objective's gradient at $x_{[k]}$, computed using a simultaneous perturbation as follows. Let $\Delta_{[k]} \in R^p$ be a vector of p mutually independent mean-zero random variables $\left\{\Delta_{[k]1} \quad \Delta_{[k]2} \quad .... \quad \Delta_{[k]p}\right\}$ satisfying certain conditions (see [76, 79]). Then $g_{[k]}$ is

$$g_{[k]} = \left[\frac{\Gamma_+ - \Gamma_-}{2d_k \Delta_{[k]1}} ...... \frac{\Gamma_+ - \Gamma_-}{2d_k \Delta_{[k]p}}\right]^T \tag{7.3}$$

where Γ_+ and Γ_- are estimates of the objective evaluated at $x_{[k]} + d_k \Delta_{[k]}$ and $x_{[k]} - d_k \Delta_{[k]}$, respectively.

In this study a novel adaptive SPSA (see Appendix H) that accounts for the constraints that the optimization variables must be between lower and upper limits is developed to

solve related problems. All the perturbed vector elements, $x_{[k]} + d_k \Delta_{[k]}$ and $x_{[k]} - d_k \Delta_{[k]}$,

are also required to be between the prescribed lower and upper limits. Using these

requirements and the guidelines provided in [43] for the selection of sequences a_k, d_k,

we chose d_k as

$$d_k = \min \left\{ d / k^{\Theta}, 0.95 \min_i \left\{ \min \left\{ \eta_{l_i} \right\}, \min \left\{ \eta_{u_i} \right\} \right\} \right\} \tag{7.4}$$

Here η_l and η_u are vectors whose components are $(x_{[k]i} - x_{min_i}) / \Delta_{[k]i}$ for each positive

$\Delta_{[k]i}$ and $(x_{[k]i} - x_{max_i}) / \Delta_{[k]i}$ for each negative $\Delta_{[k]i}$, respectively. Likewise, we selected

a_k as

$$a_k = \min \left\{ a / (S+k)^{\lambda}, 0.95 \min_i \left\{ \min(\mu_{i_l}), \min(\mu_{i_u}) \right\} \right\} \tag{7.5}$$

where μ_l and μ_u are vectors whose components are $(x_{[k]i} - x_{min_i}) / g_{[k]i}$ for each

positive $g_{[k]i}$ and $(x_{[k]i} - x_{max_i}) / g_{[k]i}$ for each negative $g_{[k]i}$, respectively. The other

SPSA parameters d, a, λ, Θ, S are chosen using guidelines provided in [43, 80-82]. The

resulting algorithm is described next.

7.2 Algorithm

Step 1: Set $k=1$ and choose initial values for the optimization parameters, $x = x_{[k]}$, and

choose a specific flight condition.

Step 2: Compute A_p and B_p, use them to design OVC, to obtain the current value of the

objective, Γ_k (note that $\Gamma_k = J_k$ for OVC and rigid blade helicopter model is used for

both plant and control system design).

Step 3: Compute $g_{[k]}$ using (7.3) with d_k given by (7.4).

Step 4: If $\left\| a_k g_{[k]} \right\| < \delta x$, where a_k is given by (7.5) and δx is the minimum allowed variation of x, or $k+1$ is greater than the maximum number of iterations allowed, exit, else calculate the next estimate of x, $x_{[k+1]}$, using (7.2), set $k=k+1$ and return to Step 2.

7.3 Results

The helicopter model was linearized for $V_A = 40$ kts (20.5782m/s), $\gamma_{FP} = 0$ rad, $\dot{\psi}_A = 0$ rad/s (straight level flight) and used to perform simultaneous helicopter plant and control system design. We used nominal values of helicopter parameters as initial conditions. The OVCs were designed for this flight condition with $\sigma^2 = 10^{-4} \begin{bmatrix} 1 & 1 & 0.1 \end{bmatrix}$ (variance constraints on helicopter Euler angles).

Using SPSA parameters: $S = 10$, $\lambda = 0.602$, $a = 100$, $d = 20$, $\Theta = 0.101$, and the algorithm in section 7.2, 33.5% of the control effort, J, is saved. Table 7.1 summarizes the optimization parameters and their lower and upper bounds while Table 7.2 gives their optimum values. It can be seen from Fig. 7.1 that the convergence of SPSA is very fast.

To evaluate the performance of the redesigned helicopter, the new model was linearized around different straight level flight conditions (i.e. between $V_A = 1$ kt (0.5145 m/s) to 80 kts (41.1565 m/s)). Then at each flight condition the corresponding OVC was designed and its cost, J_r, was computed. At the same flight conditions the initial helicopter (before redesign) was also linearized, the corresponding OVCs were designed, and nominal cost, J_n, was computed. Then the relative variation of the cost,

109

$\%J = 100(J_n - J_r)/J_n$, was computed for each flight condition. Fig. 7.2 shows variation of $\%J$ with respect to (w.r.t.) V_A. It is clear from Fig. 7.2 that using the redesigned helicopter considerable control energy is saved for each flight condition.

This scenario was repeated for helical turns ($V_A = 1$ kt to 80 kts, $\gamma_{FP} = 0.1$ rad, $\dot{\psi}_A = 0.1$ rad/s) and led to a similar conclusion: substantial cost savings are obtained using the redesigned helicopter (i.e. the one obtained using the 1st design point).

To further convince ourselves of the advantages of simultaneous helicopter plant and control system design, two other flight conditions were used to redesign the helicopter: $V_A = 1$ kt and $V_A = 80$ kts (straight level flights). The same SPSA parameters were used and two different redesigned helicopters were obtained. The same analysis was performed as before, leading to very similar conclusions: SPSA converges very fast, optimal design variables are very close, but not identical to the ones in Table 7.2 (see Tables 7.3 and 7.4), and the behaviors of $\%J$ w.r.t. V_A is similar to the previous one (see Fig. 7.2).

Table 7.2: Optimum Design Variables (1st Design Point)

Design Variable	Optimum Value	Change $\Delta x_i / x_i$
c	0.5671 m	0.04999
K_β	50327.2608 Nm/rad	0.04524
m	8.6883 kg/m	-0.04524
R	7.1269 m	-0.04975
θ_{tw}	-0.1337 rad	-0.04524
Ω	25.6503 rad/s	-0.04999

Table 7.3: Optimum Design Variables (2nd Design Point, 1kt)

Design Variable	Optimum Value	Change $\Delta x_i / x_i$
c	0.5670 m	0.04975
K_β	45982.2950 Nm/rad	-0.04500
m	8.6905 kg/m	-0.04500
R	25.6503 m	-0.04999
θ_{tw}	-0.1330 rad	-0.04975
Ω	25.6503 rad/s	-0.04999

Table 7.4: Optimum Design Variables (3rd Design Point, 80 kts)

Design Variable	Optimum Value	Change $\Delta x_i / x_i$
c	0.5661 m	0.04817
K_β	50264.6671 Nm/rad	0.04394
m	8.6973 kg/m	-0.04425
R	7.1676 m	-0.04432
θ_{tw}	-0.1339 rad	-0.04357
Ω	25.6503 rad/s	-0.04999
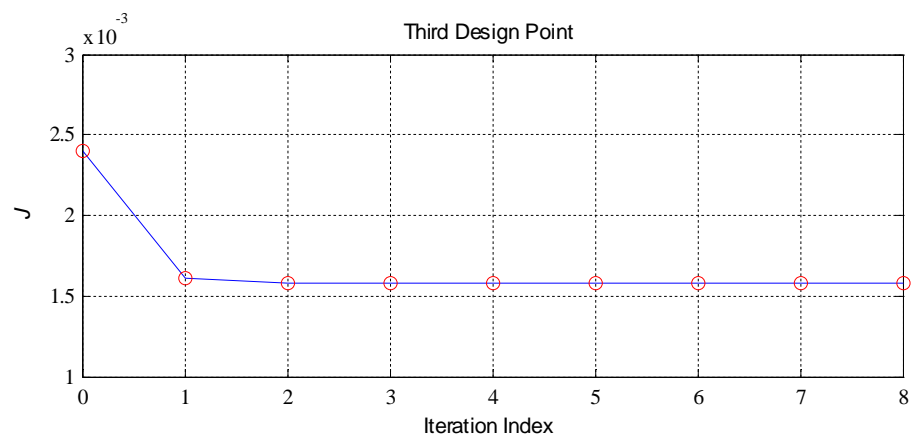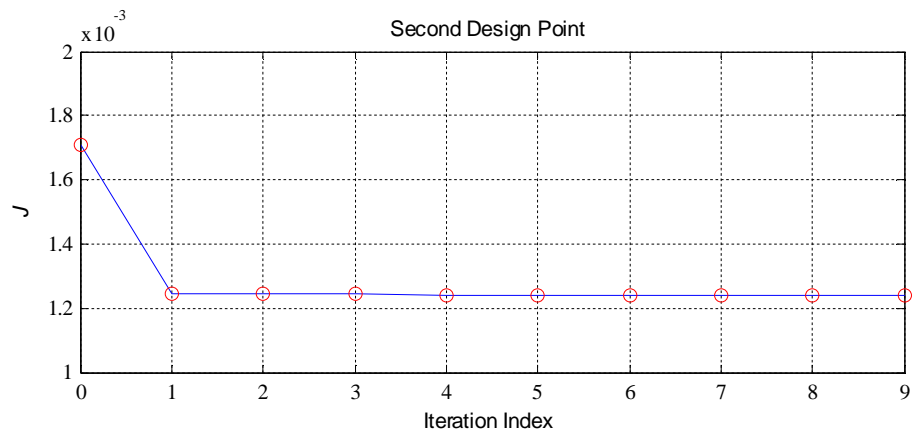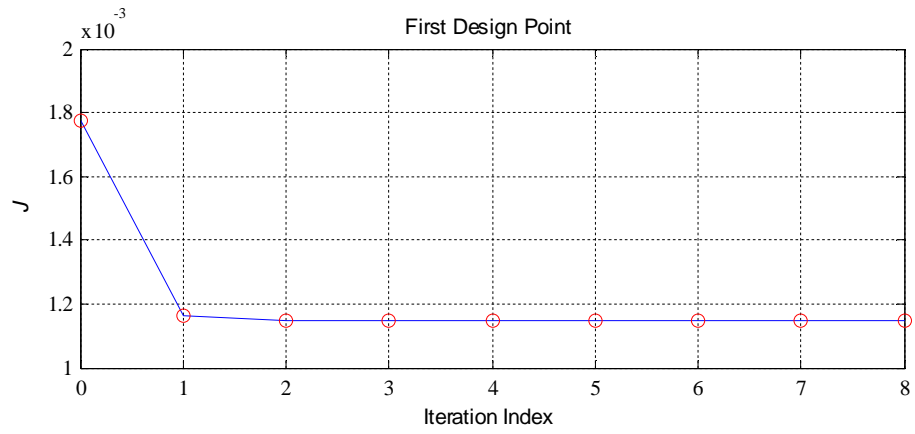
Figure 7.1: Cost Optimization Using SPSA
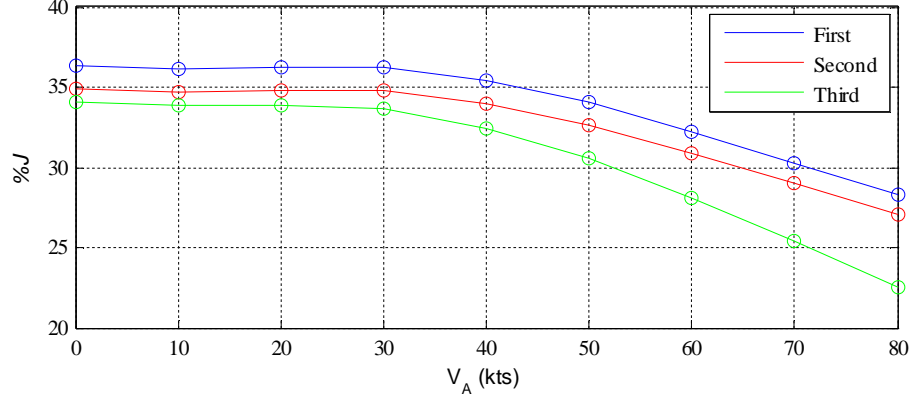
Figure 7.2: Relative Energy Save w.r.t. V_A for All Design Points

To better analyze simultaneous design idea, the following study was performed. The 1st OVC was designed for the initial (nominal) model linearized around $V_A = 40$ kts $\gamma_{FP} = 0$ rad, $\dot{\psi}_A = 0$ rad/s and the 2nd OVC was designed for the redesigned model (i.e. the one obtained using the 1st design point) linearized around $V_A = 40$ kts $\gamma_{FP} = 0$ rad, $\dot{\psi}_A = 0$ rad/s. Then the 1st OVC was evaluated for the nominal model linearized around $V_A = 40$ kts, $\gamma_{FP} = 0$ rad, $\dot{\psi}_A = 0$ rad/s and the 1st closed loop system was found. Moreover, the 2nd OVC was evaluated for the redesigned model linearized around $V_A = 40$ kts, $\gamma_{FP} = 0$ rad, $\dot{\psi}_A = 0$ rad/s and the 2nd closed loop system was found.

In Figs. 7.3 and 7.4 responses of helicopter Euler angles and all controls are given before and after simultaneous helicopter plant and control system design, respectively. It is clear from Fig. 7.3 that behaviors of helicopter Euler angles are very similar before and after redesign. The variances of outputs of interest (i.e. helicopter Euler angles) are very close and satisfy the constraint Eq. 4.11 before and after redesign. It can be seen from Fig. 7.4 that input variations from trim values slightly decrease after redesign, which

explains the considerable reduction of control effort. The other outputs (i.e. linear velocities, angular velocities, blade flapping and lagging angles) do not experience catastrophic behavior (see Appendix H, Figs. H.1 to H.8). This good behavior is explained by the exponentially stabilizing effect of OVC. Similar study was performed for a helical turn (i.e. $\gamma_{FP} = 0.1$ rad, $\dot{\psi}_A = 0.1$ rad/s) and the results are summarized in Figs. 7.5 and 7.6. For this purpose the redesigned model obtained using the 1st design point was used.
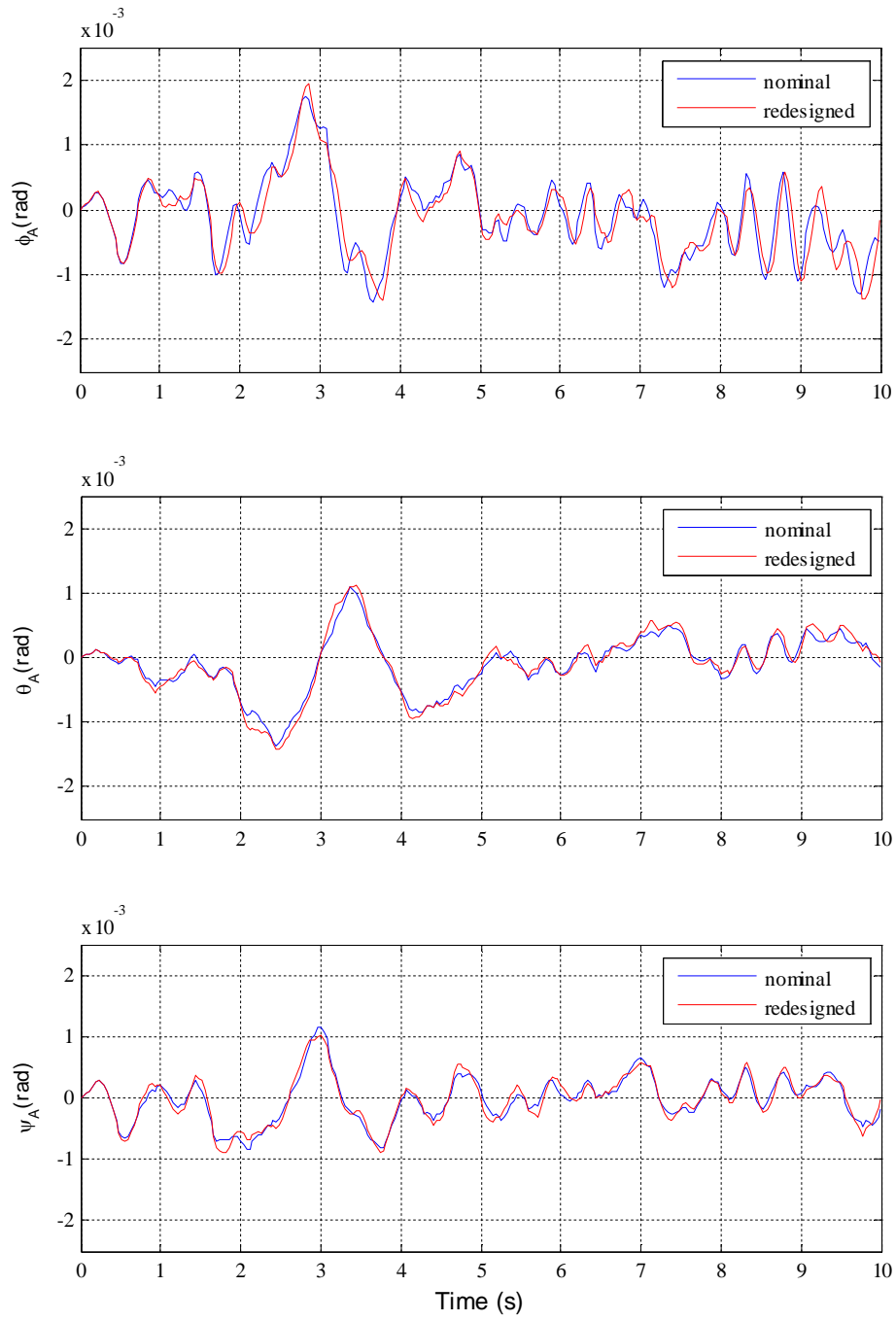
Figure 7.3: Helicopter Euler Angles Before and After Redesign
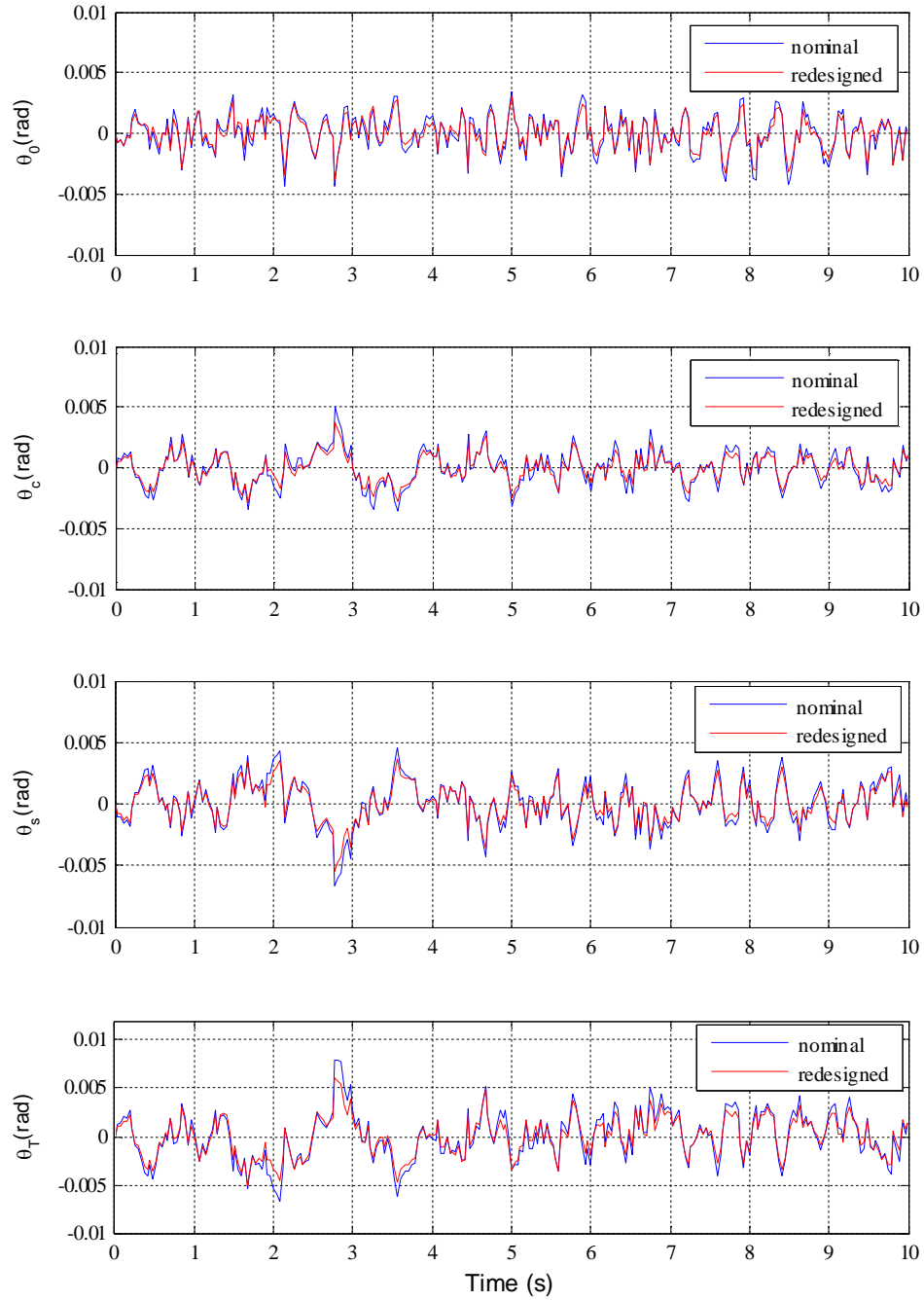
Figure 7.4: All Helicopter Controls Before and After Redesign
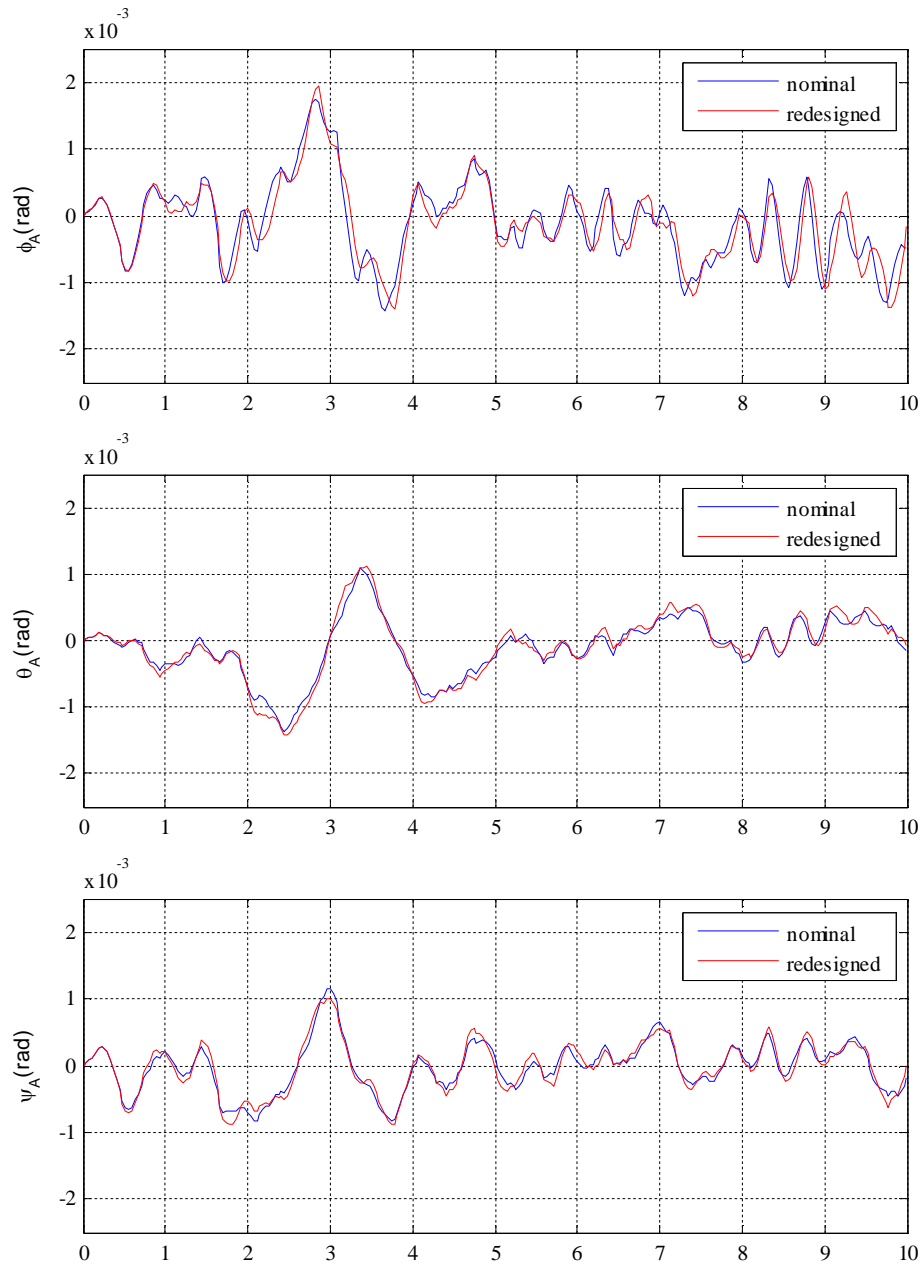
Figure 7.5: Helicopter Euler Angles Before and After Redesign for Helical Turn
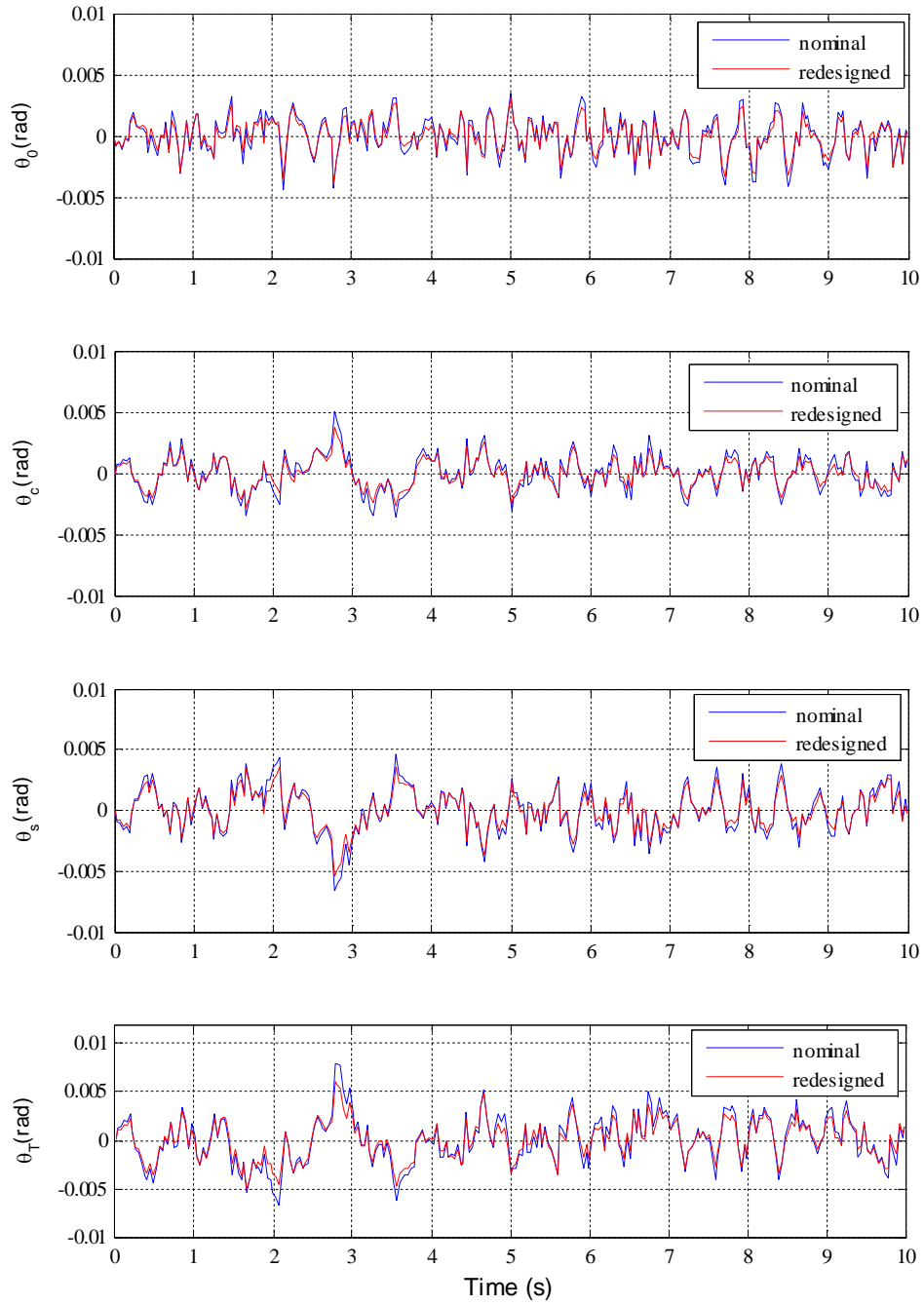
Figure 7.6: All Helicopter Controls Before and After Redesign for Helical Turn

Closed loop stability robustness of OVC with respect to modeling uncertainties was also investigated by using the redesigned helicopter and the results are given in Appendix H (see Figs. H.9 to H.11).

CHAPTER 8:

Conclusions and Future Work

8.1 Conclusions

Control oriented helicopter models are derived using physics principles. The new ordering scheme is very effective at reducing the number of terms in these models while preserving key characteristics of the initial models. Validation of the models used for control against data from the literature indicates that the control oriented modeling process correctly captures essential helicopter dynamics, including flight dynamics, flapping, and lead-lagging modes and trims.

The models are further used for control design, first for variance constrained controllers with inequality constraints on outputs or inputs. Key advantages of such controllers are their easy implementation and fast convergence of control design algorithms, even for the most complex model (i.e. flexible blade model). All variance constrained controllers exponentially stabilize the nominal flight condition while satisfying the constraints. Closed loop stability robustness analysis revealed that all these controllers are robust when variations in helicopter straight level velocity are considered. They are also robustly stable with respect to modeling uncertainties. Second, the models are also used for constrained model predictive control (MPC) design. The studies show that tracking of discontinuous trajectories using MPC is feasible. MPC is also robust to modeling uncertainties. Even though the MPC solution is computationally expensive compared to variance constrained control, calculation times for our MPCs are relatively small.

Control oriented, physics based, complex helicopter models are also used for control design for helical and level banked turns. Models linearized around these flight conditions are used for the design of constrained controllers: output variance constrained control (OVC), input variance constrained control (IVC), and constrained model predictive control (MPC). OVC and IVC studies show that all variance constrained controllers exponentially stabilize the nominal maneuvering flight condition while satisfying the constraints. Closed loop stability robustness analysis revealed that all these controllers are robust when uncertainty in helicopter velocity is considered. They are also robustly stable with respect to uncertainty in helicopter inertial parameters. An important observation is that there is no correlation between the length of stability interval, L, and the magnitudes of output or input constraints. Furthermore, adaptive switching in response to sensor failure was investigated. The studies show that the switching idea is feasible for OVC and IVC.

For the MPC scenario, similar studies were carried out. MPC can handle simultaneously numerous constraints, including discontinuities. The studies show that tracking of discontinuous maneuvering trajectories using MPC is feasible. Even though MPC solution is computationally expensive compared to variance constrained control, calculation times for the MPCs are relatively small. Limitations of MPC robustness were also revealed: when discontinuities must be tracked and hard output and input constraints obeyed, MPC becomes less successful in trajectory tracking when there are uncertainties in helicopter inertial parameters. The adaptive switching idea in response to sensor failure was also investigated for MPC and the results show that it is feasible for MPC.

Finally, simultaneous helicopter plant and control system design is investigated using a stochastic optimization method to save active control effort. Complex, control oriented, physics based helicopter models (i.e. rigid blade model) are used for this purpose. An effective algorithm which performs simultaneous design is developed and illustrated on straight level flights and helical turns.

Simultaneous perturbation stochastic approximation (SPSA) always works well for our problems (i.e. converges very fast). Considerable reduction of control effort is obtained via simultaneous design with very small (5%) changes in some helicopter parameters. Furthermore, the behaviors of fuselage and blade states before and after redesign are very similar. These states do not display bad behavior (i.e. very large amplitudes and fast oscillations). The variances of the outputs of interest (i.e. helicopter Euler angles) are very close and satisfy the constraints before and after redesign. The inputs also display smaller variations from trim values after redesign. This explains the considerable reduction of control effort observed after simultaneous design.

Furthermore, variance constrained controllers which are designed for the redesigned helicopters have strong robustness with respect to the variations in flight conditions and all helicopter inertial properties.

8.2 Future Work

Trailing edge flaps can be added to previously developed complex control oriented physics based models to save more active control energy. For this purpose simultaneous helicopter trailing edge flaps and a specific variance constrained controllers can be studied. These trailing edge flaps can also be used for noise and vibration reduction, and control redundancy in case of failures and emergency.

Moving horizontal tailplane idea can be used on previously developed complex control oriented physics based models to save more control effort. This idea also reduces the control inputs of trailing edge flaps.

Simplified nonlinear helicopter model (e.g. rigid body model and flapping blades) can be used to better check robustness properties of used controllers.

Comparison between the semi exact model (i.e. the model obtained by using small angle assumption for blade angles) and simplified model can be examined using nonlinear and linear models to better characterize robustness of controllers.

Finally μ-synthesis can be used to obtain less conservative theoretical results of the helicopter models than when GSM was used.

REFERENCES

[1]   Phillips, W. H., " Effect of Steady Rolling on Longitudinal and Directional Stability", *NACA TN 1627*, 1948.

[2]   Sahasrabudhe, V., Celi, R., and Tits, A., "Integrated Rotor-Flight Control System Optimization with Aeroelastic and Handling Qualities Constraints", *Journal of Guidance, Control, and Dynamics*, Vol. 20, No. 2, 1997, pp. 217-225.

[3]   Sahasrabudhe, V. and Celi, R., "Efficient Treatment of Moderate Amplitude Constraints for Handling Qualities Design Optimization", *Journal of Aircraft*, Vol. 34, No. 6, 1997, pp. 730-739.

[4]   Sahasrabudhe, V. and Celi, R., "Improvement of Off-Design Characteristics in Integrated Rotor-Flight Control System Optimization", *Proceedings of 53rd Annual of the American Helicopter Society*, Virginia Beach, VA, 1997.

[5]   Kim, F., Celi, R., and Tischler, M., "High Order State Space Simulation Models of Helicopter Flight Mechanics", *Journal of the American Helicopter Society*, Vol. 38, No. 2, 1993.

[6]   Kim, F., Celi, R., and Tischler, M., "Forward Flight Trim Calculation and Frequency Response Validation of a High-Order Helicopter Simulation Model", *Journal of Aircraft*, Vol. 30, No. 6, 1993, pp. 854-863.

[7]   Fusato, D. and Celi, R., "Multidisciplinary Design Optimization for Helicopter Aeromechanics and Handling Qualities", *Journal of Aircraft*, Vol. 43, No. 1, 2006, pp. 241-252.

[8]   Garcia, J. C., "Active Helicopter Rotor Control Using Blade-Mounted Actuators", MS Thesis, MIT, MA, 1994.

[9]   Hodges, D. H. and Dowell, E. H., "Nonlinear Equations of Motion for the Elastic Bending and Torsion of the Twisted Nonuniform Rotor Blades*", NASA TN D-7818*, 1974.

[10]   Hodges, D. H. and Ormiston, R. A., "Stability of Bending and Torsion of Nonuniform Cantilever Rotor Blades in Hover with Variable Structural Coupling", *NASA TN D-8192*, 1976.

[11]   Traugott, J. P., Patil, M. J., and Holzapfel, F., "Nonlinear Dynamics and Control of Integrally Actuated Helicopter Blades," *Aerospace Science and Technology*, Vol. 10, No. 6, 2006, pp. 509-518.

[12]   Skelton, R. E., *Dynamic Systems Control: Linear Systems Analysis and Synthesis*, John Wiley & Sons, 1987, chapter 8.

[13]   Skelton, R. E., Iwasaki, T., and Grigoriadis, K., *A Unified Algebraic Approach to Linear Control Design*, Taylor & Francis, 1998, chapter 4.

[14]   Skelton, R. E. and Lorenzo, M. D., "Space Structure Control Design by Variance Assignment", *Journal of Guidance, Control, and Dynamics*, Vol. 8, No. 4, 1985, pp. 454-462.

[15]   Hsieh, C., Skelton, R. E., and Damra, F. M, "Minimum Energy Controllers with Inequality Constraints on Output Variances", *Optimal Control Application and Methods*, Vol. 10, No. 4, 1989, pp. 347-366.

[16]   Zhu, G. and Skelton, R. E., "Mixed L_2 and L_∞ Problems by Weight Selection in Quadratic Optimal Control", *International Journal of Quadratic Optimal Control*, Vol. 63, No. 5, 1991, pp. 1161-1176.

[17]   Zhu, G., Rotea, M.A., and Skelton, R. E., "A Convergent Algorithm for the Output Covariance Constraint Control Problem", *SIAM Journal on Control and Optimization*, Vol. 35, No. 1, 1997, pp. 341-361.

[18]   Sultan, C. and Skelton, R. E., "Integrated Design of Controllable Tensegrity Structures", *ASME Intl. Mechanical Engineering Congress and Exposition*, Dallas, TX, 1997.

[19]   Skelton, R. E. and Sultan, C., "Controllable Tensegrity, a New Class of Smart structures", *SPIE Intl. Symposium on Smart Structures and Materials*, San Diego, CA, 1997.

[20]   Unneland, K., "Application of a Model Predictive Control to a Helicopter Model", MS Thesis, NTNU, Norway, 2003.

[21]   Dutka, A. S., Ordys, A. W., and Grimble, M. J., "Non-linear Predictive Control of 2 DOF Helicopter Model", *42nd IEEE Conference on Decision and Control*, Maui, HI, 2003.

[22]   Chung, H. and Sastry, S., "Autonomous Helicopter Formation using Model Predictive Control", *AIAA GN&C Conference,* Keystone, CO, 2006.

[23]   Maia, M. H. and Galvao, R. K. H., "Robust Constrained Predictive Control of a 3DOF Helicopter Model with External Disturbances", *ABCM Symposium Series in Mechatronics*, Vol. 3, 2008, pp. 19-26.

[24]   Afonso, R. J. M. and Galvao, R. K. H, "Predictive Control of a Helicopter Model with Tolerance to Actuator Faults", *IEEE Control and Fault Tolerant Systems Conference*, Nice, France, 2010.

[25]   Zhai, Y., Nounou, M., Nounou, H., and Al-Hamidi, Y., "Model Predictive Control of a 3DOF Helicopter System Using Successive Linearization," *International Journal of Engineering, Science and Technology*, Vol. 2, No. 10, 2010, pp. 9-19.

[26]   Bogdanov, A. A. and Wan, E. A., "Model Predictive Neural Control of a High-Fidelity Helicopter Model", *AIAA Guidance Navigation and Control Conference*, Montreal, Canada, 2001.

[27]   Wan, E. A., Bogdanov, A. A., Kieburtz, R., Baptista, A., Carlsson, M., Zhang, Y., and Zulauf, M., *Software Enabled Control: Information Technologies for Dynamical Systems, chap. Model Predictive Neural Control for Aggressive Helicopter Maneuvers*, IEEE Press, Wiley & Sons, 2003.

[28]   Bottasso, C. L. and Riviello, L., "Rotor Trim by a Neural Model-Predictive Auto-Pilot", *in Proceedings of the 32nd European Rotorcraft Forum*, Florence, Italy, 2005.

[29] Dalamagkidis, K., Valavanis, K. P., and Piegl, L. A., "Autonomous Autorotation of Unmanned Rotorcraft Using Nonlinear Model Predictive Control", *Journal of Intelligent and Robotic Systems*, Vol. 57, No. 1, 2010, pp. 351-369.

[30] Dalamagkidis, K., Valavanis, K. P., and Piegl, L. A., "Nonlinear Model Predictive Control with Neural Network Optimization for Autonomous Autorotation of Small Unmanned Helicopters", *IEEE Transactions on Control Systems Technology*, 2010, pp. 1-14.

[31] Sumer, Y. F., "Predictive Control of Multibody Systems for the Simulation of Maneuvering Rotorcraft," MS Thesis, Georgia Tech, 2005.

[32] Tischler, M. B., *Advances in Aircraft Flight Control*, Taylor & Francis, 1996, chapter 4.

[33] Heredia, G. and Ollero, A., "Sensor Fault Detection in Small Autonomous Helicopters Using Observer/Kalman Filter Identification," *IEEE International Conference on Mechatronics*, Malaga, Spain, 2009.

[34] Amato, F., Cosentino, C., and Mattei, M., "A Direct/Functional Redundancy Scheme for Fault Detection and Isolation On an Aircraft," *Aerospace Science and Technology*, Vol. 10, No. 4, 2006, pp. 338-345.

[35] Sagoo, G. K., Gururajan, S., Seanor, B., and Napolitano, M. R., "Evaluation of a Fault Tolerant Scheme in a Six-Degree-of-Freedom Motion Flight Simulator," *Journal of Aerospace Computing, Information, and Communication*, Vol. 7, No. 2, 2010, pp. 47-67.

[36] Waschburger, R., Paiva, H. M., Silva, J. J. R., and Galvao, R. K. H., "Fault Detection in a Laboratory Helicopter Employing a Wavelet-Based Analytical Redundancy Approach," *Conference on Control and Fault Tolerant Systems*, Nice, France, 2010.

[37] Xiao, B. and Hu, Q., "Fault-Tolerant Attitude Control for Flexible Spacecraft Without Angular Velocity Magnitude Measurement," *Journal of Guidance, Control, and Dynamics*, Vol. 34, No. 5, 2011, pp. 1556-1560.

[38] Grigoriadis, K.M., Carpenter, M.J., Zhu, G. and Skelton, R.E., "Optimal Redesign of Linear Systems," *Proceedings of the American Control Conference*, San Francisco, CA, 1993.

[39] Grigoriadis, K.M., Zhu, G., and Skelton, R.E., "Optimal Redesign of Linear Systems," *Journal of Dynamic Systems, Measurement and Control*, Vol.118, No. 3, 1996, pp.598-605.

[40] Ganguli, R., "Optimum Design of a Helicopter Rotor For Low Vibration Using Aeroelastic Analysis and Response Surface Methods," *Journal of Sound and Vibration*, Vol. 258, No. 2, 2002, pp. 327-344.

[41] Celi, R., "Recent Applications of Design Optimization to Rotorcraft-A Survey," *Journal of Aircraft,* Vol. 36, No. 1, 1999, pp. 176-189.

[42] Friedmann, P.P., "Helicopter Vibration Reduction Using Structural Optimization with Aeroelastic/Multidisciplinary Constraints-A Survey," *Journal of Aircraft*, Vol. 28, No. 1, 1991, pp. 8–21.

[43] Spall, J.C., "Multivariable stochastic approximation using a simultaneous perturbation gradient approximation," *IEEE Transactions on Automatic Control*, Vol. 37, 1992, pp. 332-341.

[44] Sultan, C. "Proportional damping approximation using the energy gain and simultaneous perturbation stochastic approximation," *Mechanical Systems and Signal Processing*, Vol. 24, 2010, pp. 2210-2224.

[45] Celi, R., "Helicopter Stability and Control", Class Notes.

[46] Greenwood, D.T., *Advanced Dynamics*, Cambridge University Press, 2003, chapter 1

[47] Padfield, G. D., *Helicopter Flight Dynamics*, AIAA Education Series, 2007, pp.118, 128, 137, 149-151, 265, 266, 282-287, 293, 294.

[48] Done, G. and Balmford, D., *Bramwell's Helicopter Dynamics*, AIAA, 2001, chapters 2, 3 and p. 142.

[49] Johnson, W., *Helicopter Theory*, Princeton University Press, 1994, pp. 7, 45-47.

[50] Dreier, M. E., *Introduction to Helicopter and Tiltrotor Flight Simulation*, AIAA Education Series, 2007, pp. 133-137, 591.

[51] Leishman, J. G., *Principles of Helicopter Aerodynamics*, Cambridge University Press, 2006, pp. 118, 160, 174, 195.

[52] Newman, S., *The Foundations of Helicopter Flight*, 1994, p.87.

[53] Prouty, R. W., *Helicopter Aerodynamics: Volume I*, 2009, pp. 64, 65.

[54] Prouty, R. W., *Helicopter Performance, Stability and Control*, Robert E. Kreiger Publishing Co., 2005 pp. 64, 298, 299, 303, 684-701.

[55] Drela, M., "Integrated Simulation Model for Preliminary Aerodynamic, Structural, and Control-Law Design of Aircraft", *40th Structures, Structural Dynamics and Materials Conference*, Saint Louis, MO, 1999.

[56] Hoerner, S. F., *Fluid Dynamic Drag*, Hoerner Fluid Dynamics, 1965, pp. 2.1, 3.9.

[57] Schwarz, J. L. R., "Ordering Scheme and Reduced Complexity Modeling for a Multi-Rigid Body Helicopter Dynamic Model", MS Thesis, TUM, Germany, 2009.

[58] Chen, R. T. N. and Jeske, J. A., "Kinematic Properties of the Helicopter in Coordinated Turns," NASA Technical Papers 1773, 1981.

[59] Celi, R. "Hingeless Rotor Dynamics in Coordinated Turns," *Journal of the American Helicopter Society*, Vol. 36, No. 4, 1991, pp. 39-47.

[60] Guglieri, G. and Celi, R. "On Some Aspects of Helicopter Flight Dynamics in Steady Turns," *Journal of Guidance, Control, and Dynamics*, Vol. 21, No. 3, 1998, pp. 383-390.

[61] Golnaraghi, K. and Kuo, B. C., *Automatic Control Systems*, John Wiley & Sons, 2009, pp. 716, 717, 719, 720.

[62] Dorata, P., Abdallah, C. T., and Cerone, V., *Linear Quadratic Control*, Krieger, 2000, pp. 9, 20, 21, 103-113.

[63] Hajiyev, C. and Caliskan, F., "Sensor and control surface/actuator failure detection and isolation applied to F-16 flight dynamic," Aircraft Engineering and Aerospace Technology: An International Journal, Vol. 77, No. 2, 2005, pp.152-160.

[64] F. Koumboulis, M. Tzamtzi, and G. Chamilothoris, "Multivariable iterative feedback tuning - a step-wise safe switching approach," 2007 IEEE Conference on Emerging Technologies and Factory Automation (EFTA 2007), pp. 1354–1363, 2007.

[65] Trangbaek, K., "Safe LPV Controller Switching," IEEE 26th Convention of Electrical and Electronics Engineers in Israel, 2010.

[66] Klaus Trangbaek, "Safe LPV Controller Switching," 2011 50th IEEE Conference on Decision and Control and European Control Conference (CDC-ECC), 2011.

[67] Stefanovic, M., "Safe Adaptive Switching Control: Stability and Convergence," IEEE Transactions on Automatic Control, Vol. 53, No. 9, pp.2012-2021.

[68] Vinnicombe, Glenn, Uncertainity and Feedback: H_∞ Loop-Shaping and The v-Gap Metric, chapter 3.

[69] Steele, J. H., "Approximation and Validation of Models with Uncertainty: A Closed Loop Perspective," University of Cambridge, 2001.

[70] Chen, Y. Q., Optimal and Robust Control Lecture Notes, USU.

[71] Georgiou, T. T. and Smith, M. C., "Optimal Robustness in The Gap Metric," *IEEE Transactions on Automatic Control*, Vol. 35, No. 6, 1990, pp. 673-686.

[72] Maciejowski, J. M., *Predictive Control with Constraints*, Prentice Hall, Pearson Education, 2001, pp. 74-83.

[73] Camacho, E. F. and Bordons, C., *Model Predictive Control*, Springer, 1999, pp.167-205.

[74] Mayne, D. Q., Rawlings, J. B., Rao, C. V., and Scokaert, P. O. M., "Constrained Model Predictive Control: Stability and Optimality", *Automatica*, Vol. 36, No. 6, 2000, pp. 789-814.

[75] Shannon, C. E. , "Communication in the Presence of Noise," *Proc. Institute of Radio Engineers*, Vol. 37, No.1, 1949, pp. 10-21.

[76] He, Y., Fu, M.C., and Marcus, S.I., "Convergence of Simultaneous Perturbation Stochastic Approximation for Non-Differentiable Optimization ," *IEEE Transactions on Aerospace and Electronic Systems*, Vol. 48, No. 8, 2003, pp. 1459-1463.

[77] Maryak, J.L. and Chin, D.C., "Global Random Optimization by Simultaneous Perturbation Stochastic Approximation," *Proceedings of The American Control Conference*, Arlington, VA, 2001.

[78] Wang, I.J. and Spall, J.C., Stochastic Optimization with Inequality Constraints Using Simultaneous Perturbations and Penalty Functions," *Proceedings of the Conference on Decision and Control*, Maui, HI, 2003.

[79] Sadegh, P. and Spall, J.C., "Optimal Random Perturbations for Multivariable Stochastic Approximation Using a Simultaneous Perturbation Gradient Approximation," *IEEE Transactions on Automatic Control*, Vol. 43, 1998, pp. 1480-1484.

[80] Spall, J.C., "Implementation of the Simultaneous Perturbation Algorithm For Stochastic Optimization," *IEEE Transactions on Aerospace and Electronic Systems*, Vol. 34, 1998, pp. 817-823.

[81] Fabian, V., *Stochastic Approximation, in: J.J. Rustigi (Ed.), Optimizing Methods in Statistics*, Academic Press, NY, 1971, pp. 439-470.

[82] Chin, D.C., "Comparative Study of Stochastic Algorithms for System Optimization Based on Gradient Approximation," *IEEE Transactions on Systems, Man, and Cybernetics*, Vol. 27, 1997, pp. 244-249.

[83] Morari, M. and Ricker, N. L., "Model Predictive Control Toolbox User's Guide," The Mathworks Inc., Natick, MA, 1998.

APPENDIX A

A.1 Energy Approach for Blade Flexibility

To determine orders of lumped system parameters, the force acting on the blade is distributed linearly along the blade span.
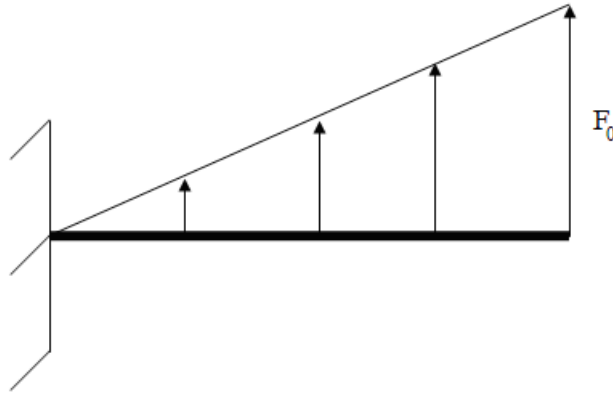
Figure A.1: Force Distribution over Blade Span

Using Euler-Bernoulli beam theory, the flapwise bending displacement function is

$$w_{E\&B} = \frac{F_0}{EI_b}\left(\frac{1}{72}r^4 - \frac{1}{12}r^3R(1-e) + \frac{1}{6}r^2R^2(1-e)^2 \right) \tag{A.1}$$
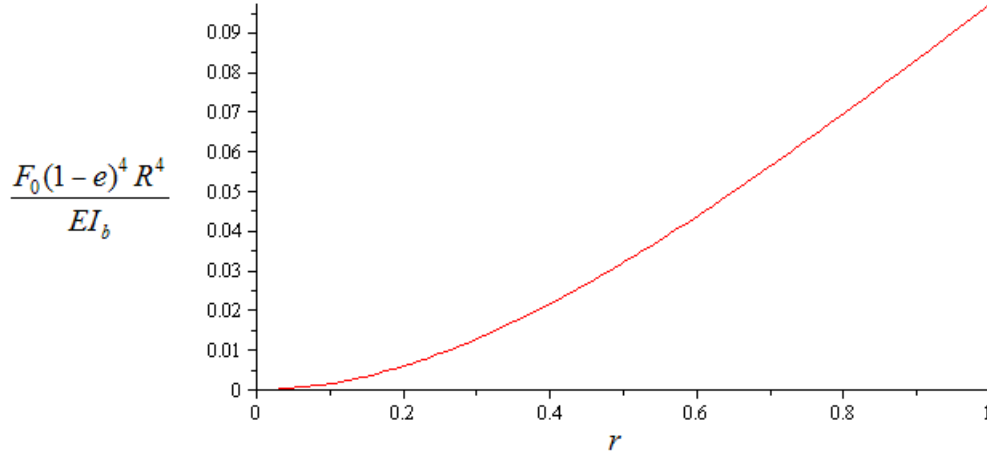
**Figure A.2: Flapwise Bending Displacement Along Blade Span
(Euler-Bernoulli Beam Theory Result)**

where F_0 is the force acting on blade tip, I_b is the blade inertia, and E is the blade's modulus of elasticity.

The weighted (i.e. average) bending displacements for 2ND and 3RD blade segments are (there are three blade segments and the root segment is assumed rigid)

$$\overline{w}_{E\&B_{2ND}} = \frac{1907}{58320}\frac{F_0(1-e)^4 R^4}{EI_b}, \qquad \overline{w}_{E\&B_{3RD}} = \frac{4337}{58320}\frac{F_0(1-e)^4 R^4}{EI_b} \qquad (A.2)$$

The orders of any flapwise bending angle and flapwise bending springs' stiffness are

$$\delta_1 = \frac{\overline{w}_{E\&B_{2ND}}}{R(1-e)/6}, \qquad \delta_2 = \frac{\overline{w}_{E\&B_{3RD}}}{R(1-e)/6}, \qquad K_\delta = \frac{\delta_1 + \delta_2}{2\beta}K_\beta \qquad (A.3)$$

A.2 Helicopter Data

Table A.1: Configuration Data of Puma SA 330

Quantity	Symbol	Magnitude	Reference
Moments of inertia	I_{xx}	9638 kg m^2	[47]
	I_{yy}	33240 kg m^2	
	I_{zz}	25889 kg m^2	
	I_{xz}	2226 kg m^2	
Number of blades	N_b	4	[47]
Rotor radius	R	7.5 m	[47]
Hinge offset	e	0.285 m	[47]
Main rotor angular velocity	Ω	27 rad/s	[47]
Helicopter mass	M_a	5805 kg	[47]
Flapping spring stiffness coefficient	K_β	48149 N m/rad	[47]
Lagging spring stiffness coefficient	K_ζ	100000 N m /rad	[47] •
Lagging damper damping coefficient	C_ζ	10000 N m s/rad	[47] •
Flapwise bending spring stiffness coefficient	K_δ	200000 N m/rad	•
Flapwise bending damper damping coefficient	C_δ	20000 N m s/rad	•
Blade inertia	I_b	1280 kg m^2	[47]
Blade twist	θ_{tw}	-0.14 rad	[47]

Blade profile drag	δ_0	0.01	[50]
Blade induced drag	δ_2	0.4	[50]
Blade lift coefficient	a	5.73 /rad	[47]
Vertical distance helicopter's center of gravity (cg) to hub	h	2.157 m	[47] •
Vertical distance cg to tail rotor	z_T	1.585 m	[47]
Horizontal distance cg to tail rotor	x_T	9 m	[47]
Tail rotor thrust coefficient	K_T	8000 N /rad	•
Vertical distance cg to nose	z_F	0.55 m	[47] •
Horizontal distance cg to nose	x_F	3.80 m	[47] •
Fuselage skin friction coefficient	c_{d_f}	0.02	[56] •
Fuselage pressure drag coefficient	c_{d_p}	1.2	[56] •
Fuselage length	l	14 m	[47] •
Fuselage diameter	d	3 m	[47] •
Lock number	γ	9.374	[47]
Vertical distance cg to landing gear (lg)	z_{lg}	1.91 m	[47] •
Horizontal distance cg to lg	x_{lg}	0.1 m	[47] •
Landing gear drag coefficient	$c_{d_{lg}}$	0.35	[54] •
Landing gear frontal area	S_{lg}	0.51 m^2	[54] •

Tail rotor hub and shaft (h&s) drag coefficient	$c_{d_{h\&s}}$	1.03	[54] •
Tail rotor h&s frontal area	$S_{h\&s}$	0.054 m^2	[54] •
Horizontal stabilizer (hs) lift coefficient	$c_{l_{hs_0}}$	0.0262	[47] •
Drag coefficient of hs	$c_{d_{hs}}$	0.01	[54] •
Linear decrease ratio of hs chord	k_{hs}	0.118	[47] •
Root chord length of hs	c_{hs_0}	0.76 m	[47] •

• : Estimated Quantity

APPENDIX B

Model Modes
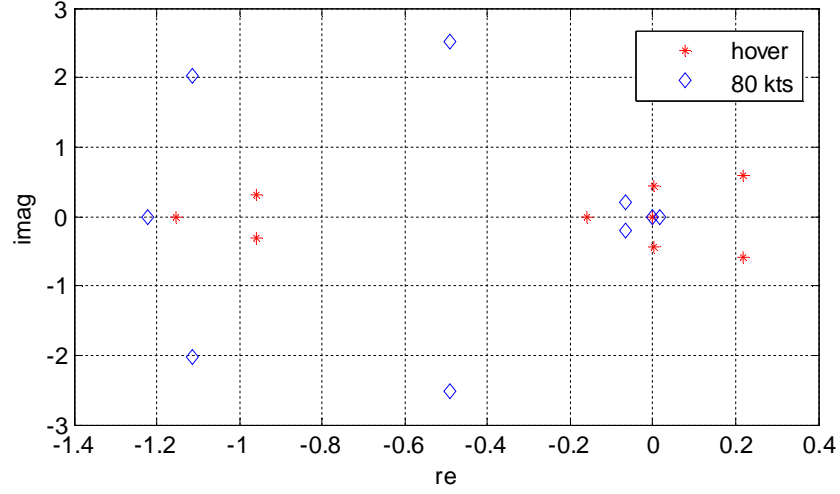
Figure B.1: Flight Dynamics Modes for Helical Turn
($\dot{\psi}_A = 0.1\,\text{rad/s},\ \gamma_{FP} = 0.1\,\text{rad}$)
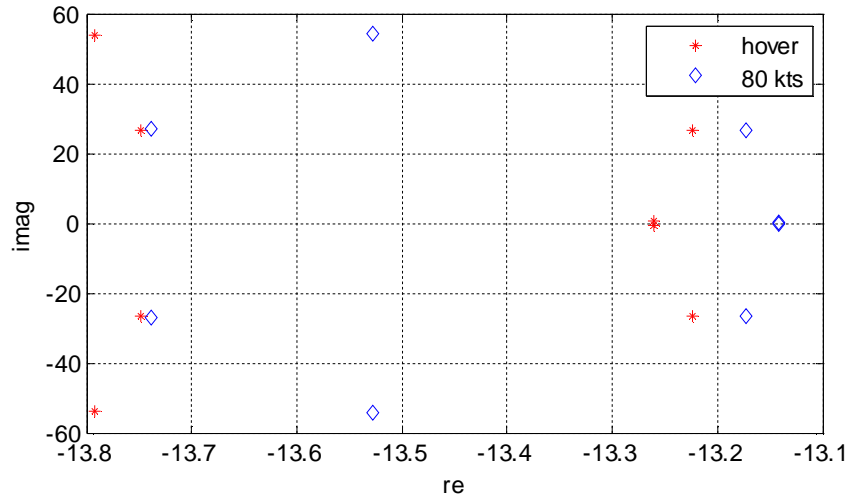
Figure B.2: Flapping Modes for Helical Turn
($\dot{\psi}_A = 0.1\,\text{rad/s},\ \gamma_{FP} = 0.1\,\text{rad}$)
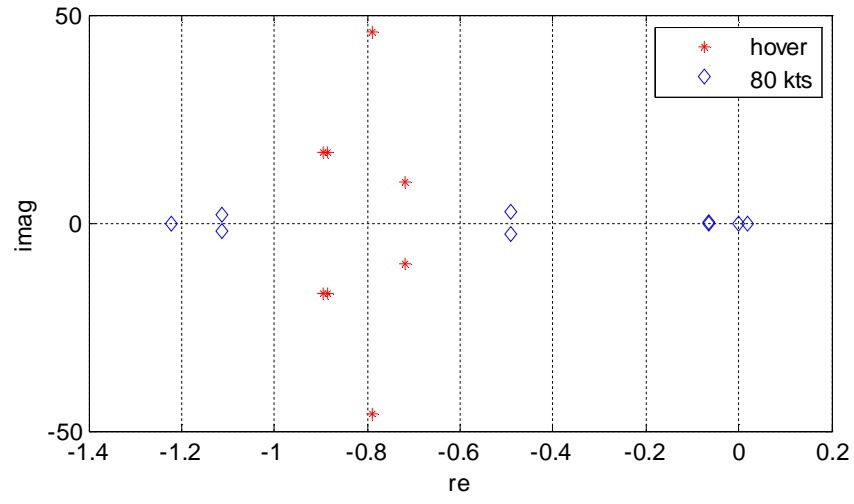
Figure B.3: Lead-Lagging Modes for Helical Turn
$(\dot{\psi}_A = 0.1\,\text{rad/s},\ \gamma_{FP} = 0.1\,\text{rad})$

APPENDIX C

C.1 OVC Algorithm

For the given data $(A_p, B_p, C_p, D_p, M_p, \sigma_i, W, V, R, \epsilon > 0, Q_0, n > 0)$

1. Compute X and F using

$$0 = XA_p^T + A_p X - XM_p^T V^{-1} M_p X + D_p W_p D_p^T \quad \text{and} \quad F = XM_p^T V^{-1}$$

2. Compute K_j and G_j using

$$0 = K_j A_p + A_p^T K_j - K_j B_p R^{-1} B_p^T K_j + C_p^T Q(j) C_p \quad \text{and} \quad G_j = -R^{-1} B_p^T K_j$$

3. Compute X_{c_j} using

$$0 = X_{c_j} (A_p + B_p G_j)^T + (A_p + B_p G_j) X_{c_j} + FVF^T \quad \text{and if} \quad \sum_{i=1}^{n_y} \left\| \sigma_i^2 - C_p (X_{c_j} + X) C_p^T \right\| \leq \epsilon \text{ stop}$$

4. Update $Q(j)$ with

$$q(j+1) = \left[\frac{[C(X_{c_j} + X)C^T]}{\sigma_i^2} \right]^n q(j) \text{ and go to step 2.}$$

C.2 IVC Algorithm

For the given data $(A_p, B_p, C_p, D_p, M_p, \sigma_i, W, V, R, \epsilon > 0, Q_0, n > 0)$

1. Compute X and F using

$$0 = XA_p^T + A_p X - XM_p^T V^{-1} M_p X + D_p W_p D_p^T \quad \text{and} \quad F = XM_p^T V^{-1}$$

2. Compute K_j and G_j using

$$0 = K_j A_p + A_p^T K_j - K_j B_p R(j)^{-1} B_p^T K_j + C_p^T Q C_p \quad \text{and} \quad G_j = -R(j)^{-1} B_p^T K_j$$

3. Compute X_{c_j} using

$$0 = X_{c_j}(A_p + B_p G_j)^T + (A_p + B_p G_j)X_{c_j} + FVF^T \quad \text{and if} \quad \sum_{i=1}^{n_u} \left\| \mu_i^2 - G_j(X_{c_j} + X)G_j^T \right\| \le \epsilon \text{ stop}$$

4. Update $R(j)$ with

$$r(j+1) = \left[\frac{[G_j(X_{c_j} + X)G_j^T]}{\mu_i^2} \right]^n r(j) \text{ and go to step 2.}$$

APPENDIX D

D.1 OVC and IVC Results for Straight Level Flight

For the numerical experiments reported here, the sensor measurements are helicopter linear velocities, angular velocities and Euler angles, and the noise intensities are $W = 10^{-7} I_n$, $V = 10^{-7} I_9$ where n is the number of states. In general V depends on the sensor quality (the high quality sensors correspond to small V) whereas W is dictated by the modeling process. Three models were examined: the first model is described in section IV, the second model is found by reducing the magnitude of all helicopter inertial parameters (helicopter mass and helicopter inertia matrix elements) with 10% compared to first model, and the last model is found by eliminating the blade flexibility from the first model ($n=41$ for the first and second models and $n=25$ for the last model). Note that all these models are linearized around straight level flight condition. Data of output and input variance figures are obtained using fixed Q and R penalties and steps 2-3 in Appendix B for straight level flight. The data obtained using this approach is very close to data which is obtained using the approach for maneuvering flight.

Table D.1: OVC and IVC Scenarios for Straight Level Flight

	Design Model	Nominal Design V_A	Evaluation Model	Evaluation V_A
1st	Rigid Blade	Hover	Rigid Blade	Hover to 80 kts
2nd	Rigid Blade	40 kts	Rigid Blade	Hover to 80 kts
3rd	Rigid Blade	Hover	Flexible Blade	Hover to 80 kts
4th	Rigid Blade	40 kts	Flexible Blade	Hover to 80 kts
5th	Flexible Blade	Hover	Flexible Blade	Hover to 80 kts
6th	Flexible Blade	40 kts	Flexible Blade	Hover to 80 kts
7th	Flexible Blade	Hover	Flexible Blade with 10% Helicopter Inertia Variation	Hover to 80 kts
8th	Flexible Blade	40 kts	Flexible Blade with 10% Helicopter Inertia Variation	Hover to 80 kts

Table D.2: Stability Robustness Analysis of OVC for Straight Level Flight

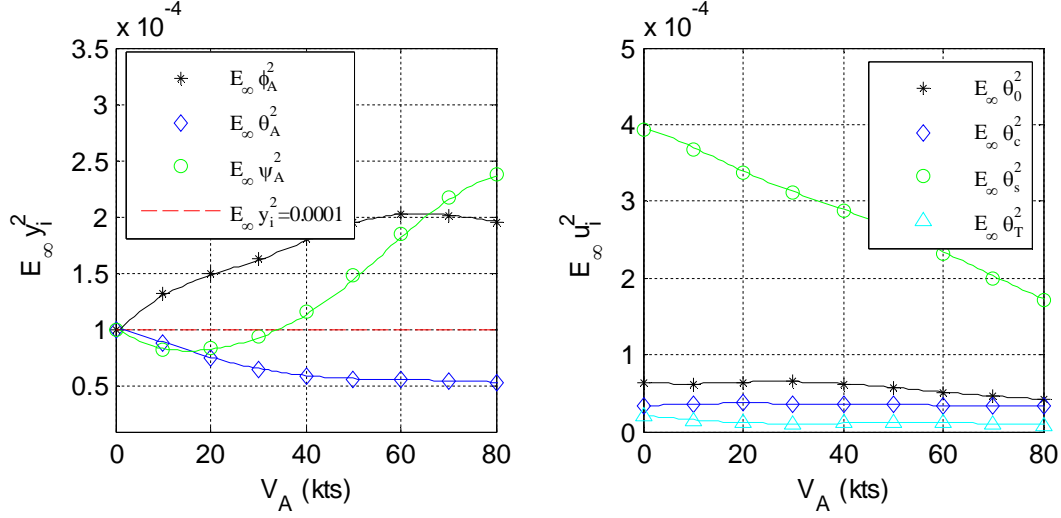|	Hover		10 kts		20 kts		30 kts		40kts		50 kts		60 kts		70 kts		80 kts		
	CL	OL	CL	OL	CL	OL	CL	OL	CL	OL	CL	OL	CL	OL	CL	OL	CL	OL	L
1st	ES	U	ES	U	ES	U	ES	U	ES	MS	ES	MS	ES	MS	ES	MS	ES	MS	9
2nd	ES	U	ES	U	ES	U	ES	U	ES	MS	ES	MS	ES	MS	ES	MS	ES	MS	9
3rd	ES	U	ES	U	ES	U	ES	U	ES	MS	ES	MS	ES	MS	ES	MS	ES	MS	9
4th	ES	U	ES	U	ES	U	ES	U	ES	MS	ES	MS	ES	MS	ES	MS	ES	MS	9
5th	ES	U	ES	U	ES	U	ES	U	ES	MS	ES	MS	ES	MS	ES	MS	ES	MS	9
6th	ES	U	ES	U	ES	U	ES	U	ES	MS	ES	MS	ES	MS	ES	MS	ES	MS	9
7th	ES	U	ES	U	ES	U	ES	U	ES	MS	ES	MS	ES	MS	ES	MS	ES	MS	9
8th	ES	U	ES	U	ES	U	ES	U	ES	MS	ES	MS	ES	MS	ES	MS	ES	MS	9

Table D.3: Stability Robustness Analysis of IVC for Straight Level Flight

	Hover		10 kts		20 kts		30 kts		40kts		50 kts		60 kts		70 kts		80 kts		*L*
	CL	OL	CL	OL	CL	OL	CL	OL	CL	OL	CL	OL	CL	OL	CL	OL	CL	OL	
1st	ES	U	ES	U	ES	U	U	U	U	MS	U	MS	U	MS	U	MS	U	MS	3
2nd	ES	U	ES	U	ES	U	ES	U	ES	MS	ES	MS	U	MS	U	MS	U	MS	6
3rd	ES	U	ES	U	ES	U	ES	U	U	MS	U	MS	U	MS	U	MS	U	MS	4
4th	U	U	ES	U	ES	U	ES	U	ES	MS	U	MS	U	MS	U	MS	U	MS	4
5th	ES	U	ES	U	ES	U	ES	U	U	MS	U	MS	U	MS	U	MS	U	MS	4
6th	ES	U	ES	U	ES	U	ES	U	ES	MS	ES	MS	U	MS	U	MS	U	MS	6
7th	ES	U	ES	U	ES	U	ES	U	U	MS	U	MS	U	MS	U	MS	U	MS	4
8th	ES	U	ES	U	ES	U	ES	U	ES	MS	ES	MS	U	MS	U	MS	U	MS	6

Table D.4: More Stability Robustness Analysis of OVC for Straight Level Flight
$$(\sigma^2 = 10^{-6}\begin{bmatrix}1 & 1 & 1\end{bmatrix})$$

	Hover		10 kts		20 kts		30 kts		40kts		50 kts		60 kts		70 kts		80 kts		*L*
	CL	OL	CL	OL	CL	OL	CL	OL	CL	OL	CL	OL	CL	OL	CL	OL	CL	OL	
1st	ES	U	ES	U	U	U	U	U	U	MS	U	MS	U	MS	U	MS	U	MS	2
2nd	U	U	U	U	U	U	ES	U	ES	MS	U	MS	U	MS	U	MS	U	MS	2
3rd	U	U	U	U	U	U	U	U	U	MS	U	MS	U	MS	U	MS	U	MS	0
4th	U	U	U	U	U	U	U	U	U	MS	U	MS	U	MS	U	MS	U	MS	0
5th	ES	U	ES	U	ES	U	ES	U	ES	MS	U	MS	U	MS	U	MS	U	MS	5
6th	U	U	U	U	U	U	U	U	U	MS	ES	MS	ES	MS	ES	MS	ES	MS	5
7th	ES	U	ES	U	ES	U	ES	U	ES	MS	U	MS	U	MS	U	MS	U	MS	5
8th	U	U	U	U	U	U	U	U	ES	MS	ES	MS	ES	MS	ES	MS	ES	MS	5

Table D.5: More Stability Robustness Analysis of OVC for Straight Level Flight#2

$$(\sigma^2 = 10^{-3}\begin{bmatrix}1 & 1 & 1\end{bmatrix})$$

	Hover		10 kts		20 kts		30 kts		40kts		50 kts		60 kts		70 kts		80 kts		
	CL	OL	CL	OL	CL	OL	CL	OL	CL	OL	CL	OL	CL	OL	CL	OL	CL	OL	L
1st	ES	U	ES	U	ES	U	ES	U	U	MS	U	MS	U	MS	U	MS	U	MS	4
2nd	ES	U	ES	U	ES	U	ES	U	ES	MS	ES	MS	ES	MS	ES	MS	ES	MS	9
3rd	ES	U	ES	U	ES	U	ES	U	ES	MS	U	MS	U	MS	U	MS	U	MS	5
4th	ES	U	ES	U	ES	U	ES	U	ES	MS	ES	MS	ES	MS	ES	MS	ES	MS	9
5th	ES	U	ES	U	ES	U	ES	U	U	MS	U	MS	U	MS	U	MS	U	MS	4
6th	ES	U	ES	U	ES	U	ES	U	ES	MS	ES	MS	ES	MS	ES	MS	ES	MS	9
7th	ES	U	ES	U	ES	U	ES	U	U	MS	U	MS	U	MS	U	MS	U	MS	4
8th	ES	U	ES	U	ES	U	ES	U	ES	MS	ES	MS	ES	MS	ES	MS	U	MS	8

Figure D.1: Output and Input Variances of the 1st OVC for Straight Level Flight
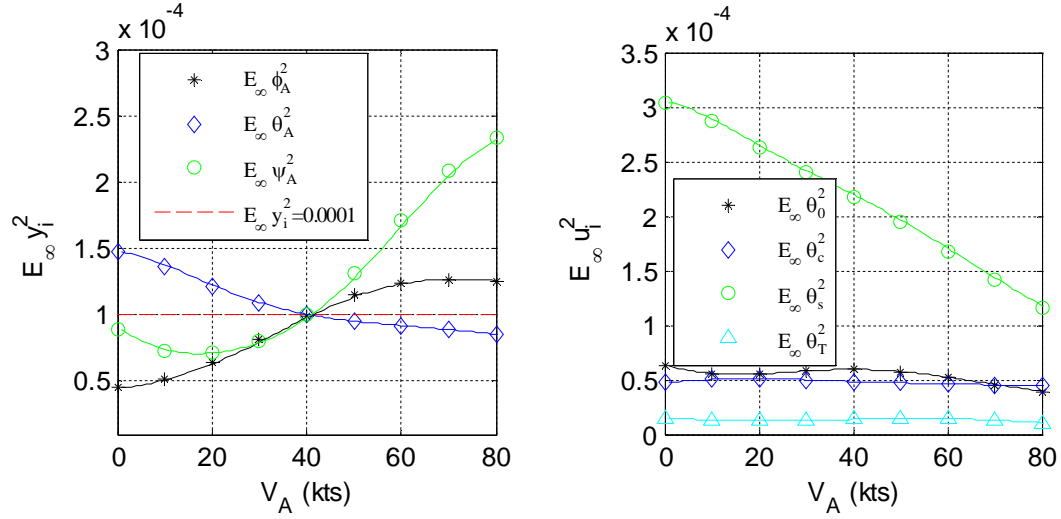
Figure D.2: Output and Input Variances of the 2nd OVC for Straight Level Flight
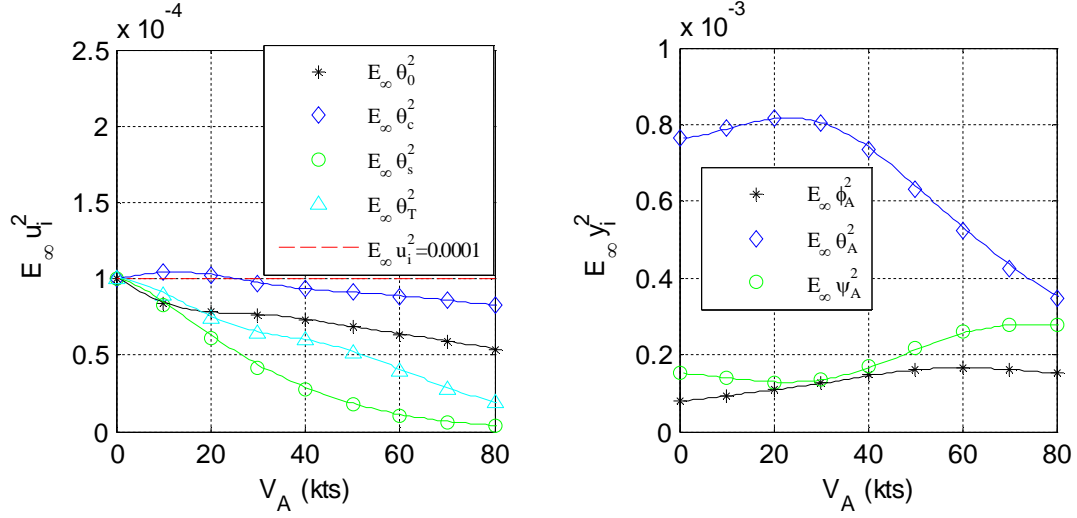
Figure D.3: Output and Input Variances of The 1st IVC for Straight Level Flight
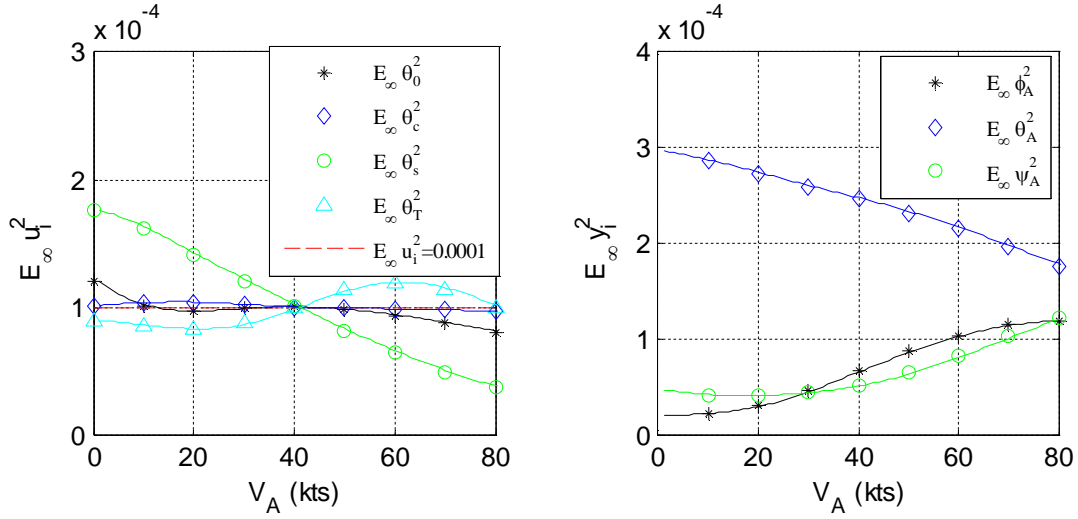
Figure D.4: Output and Input Variances of The 2nd IVC for Straight Level Flight

D.2 Additional OVC and IVC Results for Maneuvering Flight

In this sub-section 1st to 4th set of controllers are designed with the same conditions as the ones in chapter 4 except $\dot{\psi}_A$ and γ_{FP}. The stability robustness analysis of OVC and IVC with all sensor failures are examined for different maneuvers.
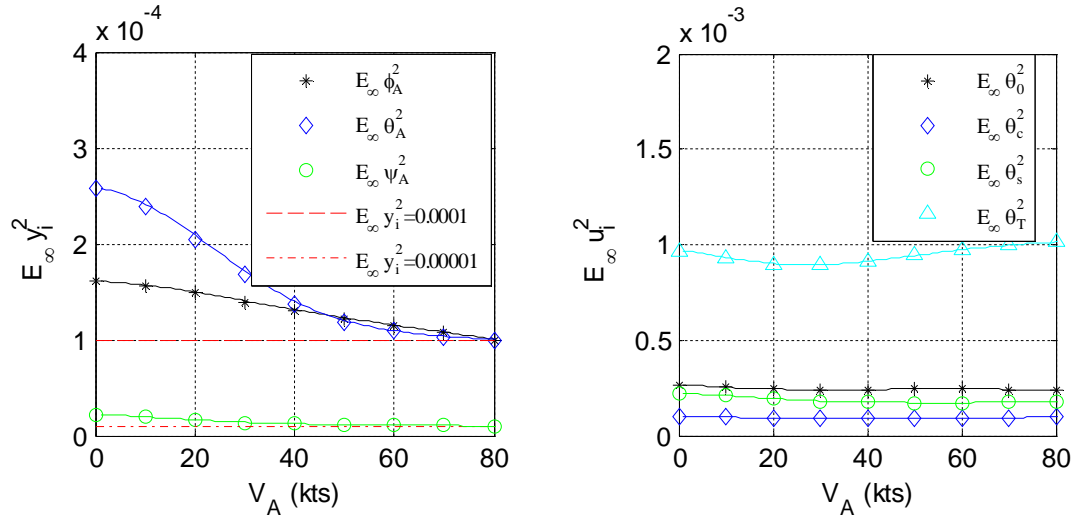
Figure D.5: Output and Input Variances of The 2nd OVC for Helical Turn
($\dot{\psi}_A = 0.1\,\text{rad/s}$, $\gamma_{FP} = 0.1\,\text{rad}$)
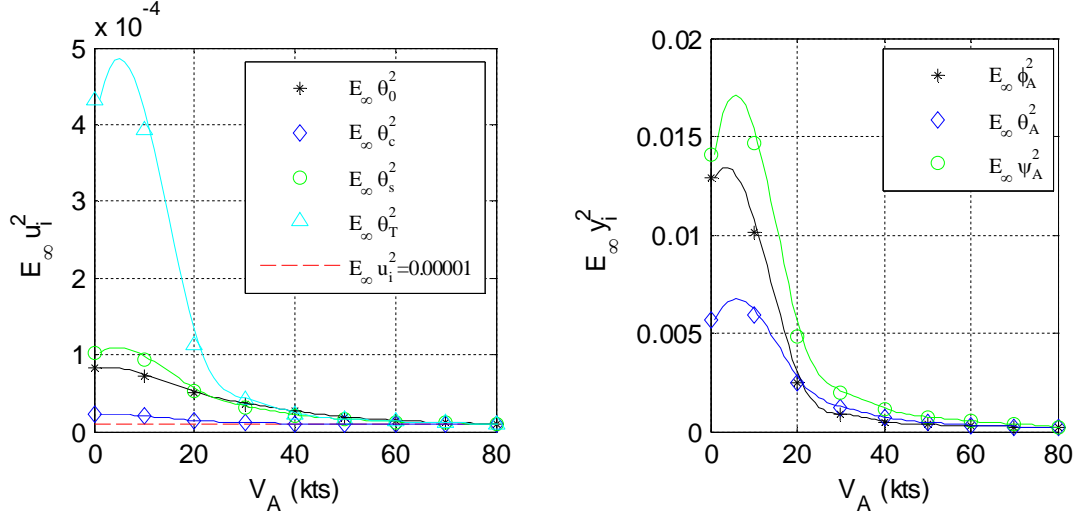
Figure D.6: Output and Input Variances of The 2nd IVC for Helical Turn
($\dot{\psi}_A = 0.1\,\text{rad/s},\ \gamma_{FP} = 0.1\,\text{rad}$)
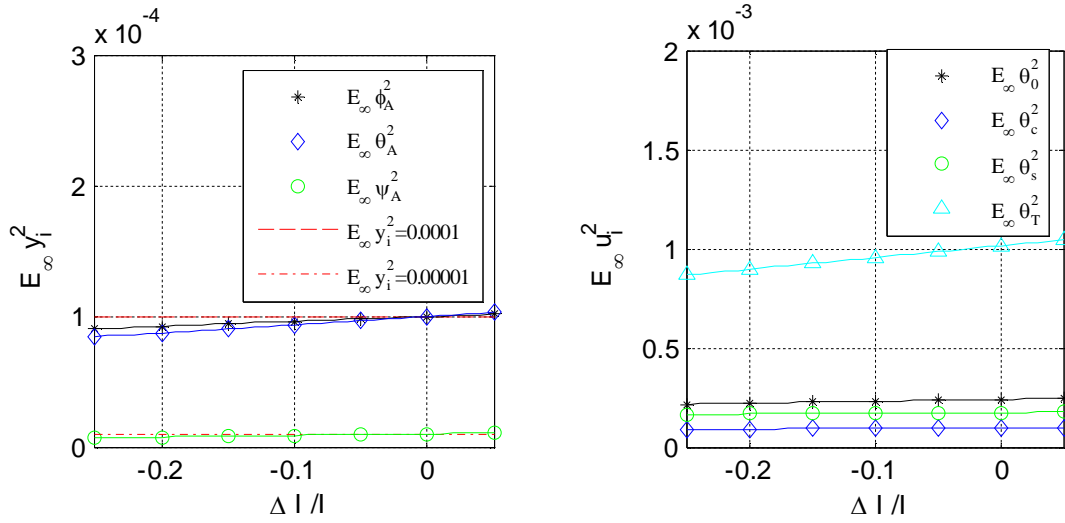
Figure D.7: Output and Input Variances of The 4th OVC for Helical Turn
($\dot{\psi}_A = 0.1\,\text{rad/s},\ \gamma_{FP} = 0.1\,\text{rad}$)
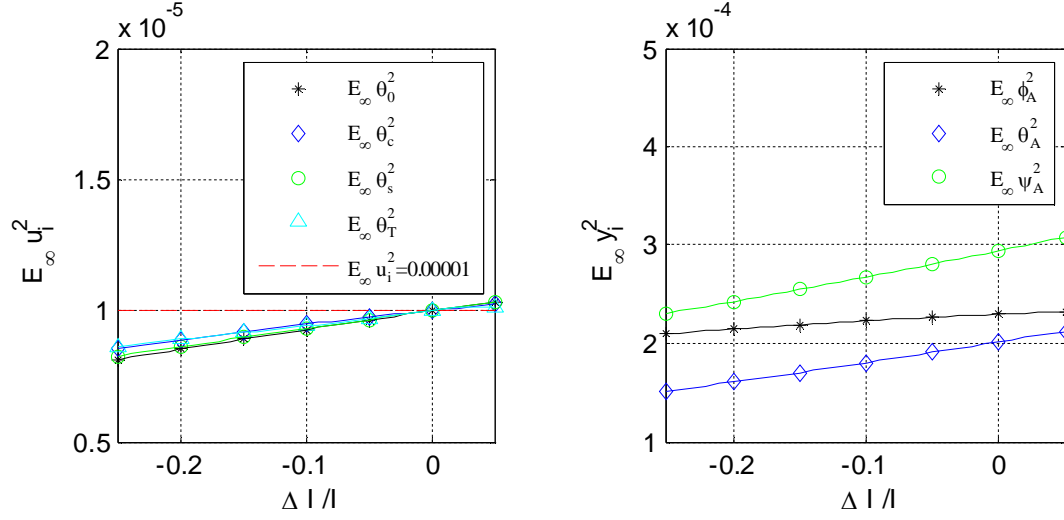
Figure D.8: Output and Input Variances of The 4th IVC for Helical Turn
($\dot{\psi}_A = 0.1\,\text{rad/s}, \ \gamma_{FP} = 0.1\,\text{rad}$)

Table D.6: Stability Robustness Analysis of OVC for Level Banked Turn
($\dot{\psi}_A = 0.1\,\text{rad/s}, \ \gamma_{FP} = 0\,\text{rad}$)

	Hover		10 kts		20 kts		30 kts		40 kts		50 kts		60kts		70 kts		80 kts		
	CL	OL	CL	OL	CL	OL	CL	OL	CL	OL	CL	OL	CL	OL	CL	OL	CL	OL	L
1st	ES	U	ES	U	ES	U	ES	U	ES	MS	ES	MS	ES	MS	ES	U	ES	U	9
2nd	ES	U	ES	U	ES	U	ES	U	ES	MS	ES	MS	ES	MS	ES	U	ES	U	9
3rd	ES	U	ES	U	ES	U	ES	U	ES	MS	ES	MS	ES	MS	ES	U	ES	U	9
4th	ES	U	ES	U	ES	U	ES	U	ES	MS	ES	MS	ES	MS	ES	U	ES	U	9

Table D.7: Stability Robustness Analysis of IVC for Level Banked Turn
$(\dot{\psi}_A = 0.1\,\text{rad/s},\ \gamma_{FP} = 0\,\text{rad})$

	Hover		10 kts		20 kts		30 kts		40 kts		50 kts		60kts		70 kts		80 kts		
	CL	OL	CL	OL	CL	OL	CL	OL	CL	OL	CL	OL	CL	OL	CL	OL	CL	OL	*L*
1st	ES	U	ES	U	ES	U	ES	U	ES	MS	ES	MS	ES	MS	ES	U	ES	U	9
2nd	ES	U	ES	U	ES	U	ES	U	ES	MS	ES	MS	ES	MS	ES	U	ES	U	9
3rd	ES	U	ES	U	ES	U	ES	U	ES	MS	ES	MS	ES	MS	ES	U	ES	U	9
4th	ES	U	ES	U	ES	U	ES	U	ES	MS	ES	MS	ES	MS	ES	U	ES	U	9

Table D.8: Stability Robustness Analysis of OVC for Different Helical Turn
$(\dot{\psi}_A = 0.1\,\text{rad/s},\ \gamma_{FP} = 0.05\,\text{rad})$

	Hover		10 kts		20 kts		30 kts		40 kts		50 kts		60kts		70 kts		80 kts		
	CL	OL	CL	OL	CL	OL	CL	OL	CL	OL	CL	OL	CL	OL	CL	OL	CL	OL	*L*
1st	ES	U	ES	U	ES	U	ES	U	ES	MS	ES	MS	ES	MS	ES	U	ES	U	9
2nd	ES	U	ES	U	ES	U	ES	U	ES	MS	ES	MS	ES	MS	ES	U	ES	U	9
3rd	ES	U	ES	U	ES	U	ES	U	ES	MS	ES	MS	ES	MS	ES	U	ES	U	9
4th	ES	U	ES	U	ES	U	ES	U	ES	MS	ES	MS	ES	MS	ES	U	ES	U	9

Table D.9: Stability Robustness Analysis of IVC for Different Helical Turn

$$(\dot{\psi}_A = 0.1\,\text{rad/s},\ \gamma_{FP} = 0.05\,\text{rad})$$

	Hover		10 kts		20 kts		30 kts		40 kts		50 kts		60kts		70 kts		80 kts		
	CL	OL	CL	OL	CL	OL	CL	OL	CL	OL	CL	OL	CL	OL	CL	OL	CL	OL	*L*
1st	ES	U	ES	U	ES	U	ES	U	ES	MS	ES	MS	ES	MS	ES	U	ES	U	9
2nd	ES	U	ES	U	ES	U	ES	U	ES	MS	ES	MS	ES	MS	ES	U	ES	U	9
3rd	ES	U	ES	U	ES	U	ES	U	ES	MS	ES	MS	ES	MS	ES	U	ES	U	9
4th	ES	U	ES	U	ES	U	ES	U	ES	MS	ES	MS	ES	MS	ES	U	ES	U	9

Table D.10: More Stability Robustness Analysis of OVC for Helical Turn

$$(\dot{\psi}_A = 0.1\,\text{rad/s},\ \gamma_{FP} = 0.1\,\text{rad},\ \sigma^2 = 10^{-6}\begin{bmatrix} 1 & 1 & 1 \end{bmatrix})$$

	Hover		10 kts		20 kts		30 kts		40 kts		50 kts		60kts		70 kts		80 kts		
	CL	OL	CL	OL	CL	OL	CL	OL	CL	OL	CL	OL	CL	OL	CL	OL	CL	OL	*L*
1st	U	U	U	U	U	U	U	U	ES	MS	ES	MS	ES	MS	ES	U	U	U	4
2nd	U	U	U	U	U	U	U	U	U	MS	U	MS	ES	MS	ES	U	ES	U	3
3rd	U	U	U	U	U	U	U	U	ES	MS	ES	MS	ES	MS	ES	U	U	U	4
4th	U	U	U	U	U	U	U	U	U	MS	U	MS	ES	MS	ES	U	ES	U	3

Table D.11: More Stability Robustness Analysis of OVC for Helical Turn#2

$$(\dot{\psi}_A = 0.1\,\text{rad/s},\ \gamma_{FP} = 0.1\,\text{rad},\ \sigma^2 = 10^{-3}\begin{bmatrix}1 & 1 & 1\end{bmatrix})$$

	Hover		10 kts		20 kts		30 kts		40 kts		50 kts		60kts		70 kts		80 kts		
	CL	OL	CL	OL	CL	OL	CL	OL	CL	OL	CL	OL	CL	OL	CL	OL	CL	OL	L
1st	ES	U	ES	U	ES	U	ES	U	ES	MS	ES	MS	ES	MS	U	U	U	U	7
2nd	U	U	U	U	U	U	U	U	ES	MS	ES	MS	ES	MS	ES	U	ES	U	5
3rd	ES	U	ES	U	ES	U	ES	U	ES	MS	ES	MS	ES	MS	U	U	U	U	7
4th	U	U	U	U	U	U	U	U	ES	MS	U	MS	U	MS	U	U	U	U	5

Table D.12: More Stability Robustness Analysis of IVC for Helical Turn

$$(\dot{\psi}_A = 0.1\,\text{rad/s},\ \gamma_{FP} = 0.1\,\text{rad},\ \mu^2 = 10^{-6}\begin{bmatrix}1 & 1 & 1 & 1\end{bmatrix})$$

	Hover		10 kts		20 kts		30 kts		40 kts		50 kts		60kts		70 kts		80 kts		
	CL	OL	CL	OL	CL	OL	CL	OL	CL	OL	CL	OL	CL	OL	CL	OL	CL	OL	L
1st	U	U	U	U	U	U	ES	U	ES	MS	ES	MS	ES	MS	ES	U	ES	U	6
2nd	U	U	U	U	U	U	ES	U	ES	MS	ES	MS	ES	MS	ES	U	ES	U	6
3rd	U	U	U	U	U	U	ES	U	ES	MS	ES	MS	ES	MS	ES	U	ES	U	6
4th	U	U	U	U	U	U	ES	U	ES	MS	ES	MS	ES	MS	ES	U	ES	U	6

Table D.13: More Stability Robustness Analysis of IVC for Helical Turn#2
$$(\dot{\psi}_A = 0.1\,\text{rad/s},\ \gamma_{FP} = 0.1\,\text{rad},\ \mu^2 = 10^{-3}\begin{bmatrix}1 & 1 & 1 & 1\end{bmatrix})$$

	Hover		10 kts		20 kts		30 kts		40 kts		50 kts		60kts		70 kts		80 kts		
	CL	OL	CL	OL	CL	OL	CL	OL	CL	OL	CL	OL	CL	OL	CL	OL	CL	OL	*L*
1st	ES	U	ES	U	ES	U	ES	U	ES	MS	ES	MS	ES	MS	ES	U	ES	U	9
2nd	U	U	U	U	U	U	ES	U	ES	MS	ES	MS	ES	MS	ES	U	ES	U	6
3rd	ES	U	ES	U	ES	U	ES	U	ES	MS	ES	MS	ES	MS	ES	U	ES	U	9
4th	U	U	U	U	U	U	U	U	ES	MS	ES	MS	ES	MS	ES	U	ES	U	5

Additional OVC and IVC Simulations

In this section 1ˢᵗ OVC and 1ˢᵗ IVC designed with and without sensor failure in chapter 4 are used and the closed loop responses are simulated.
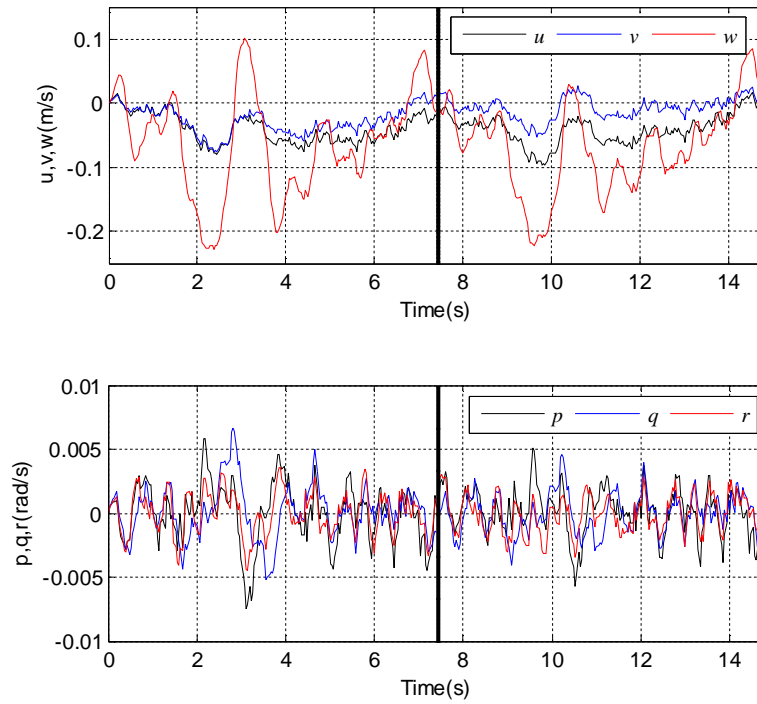
Figure E.1: OVC, 1ˢᵗ Failure, Some Fuselage States
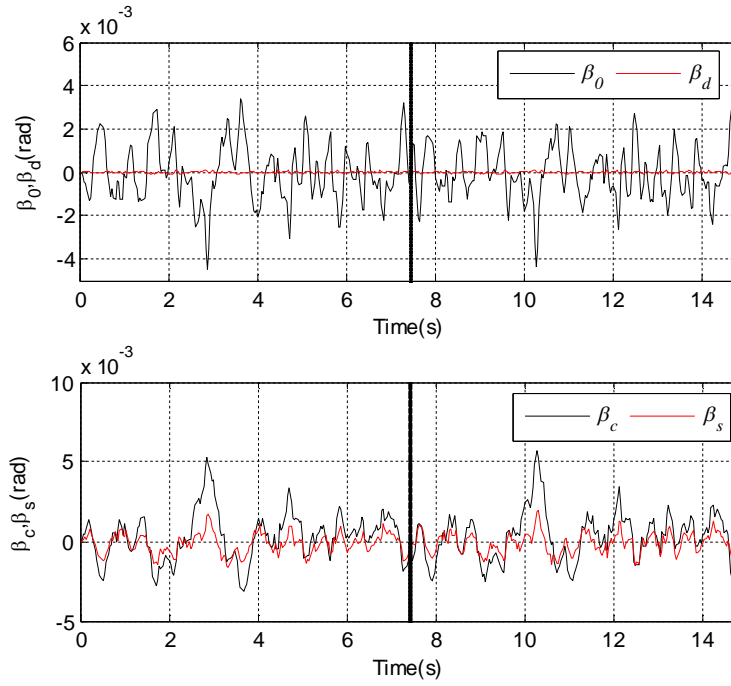
Figure E.2: OVC, 1st Failure, Blade Flapping States
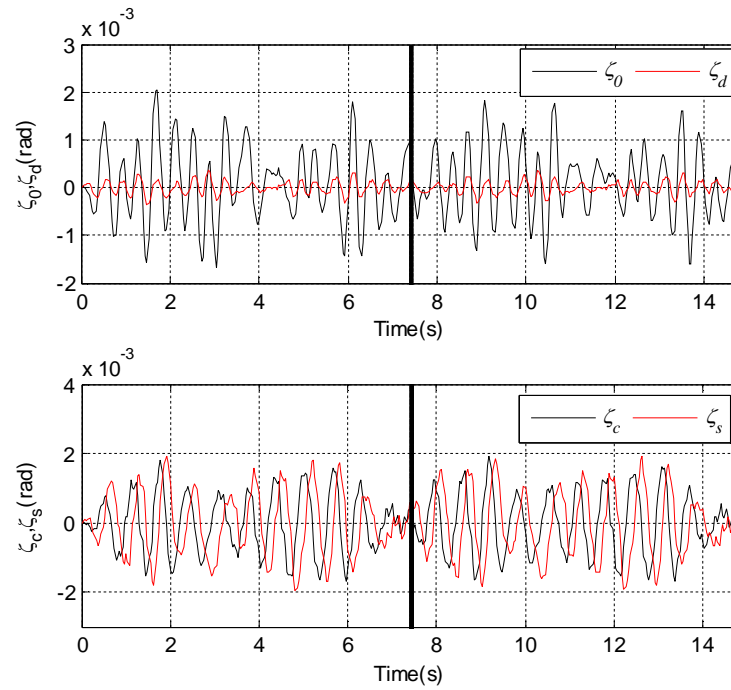
Figure E.3: OVC, 1st Failure, Blade Lagging States

155
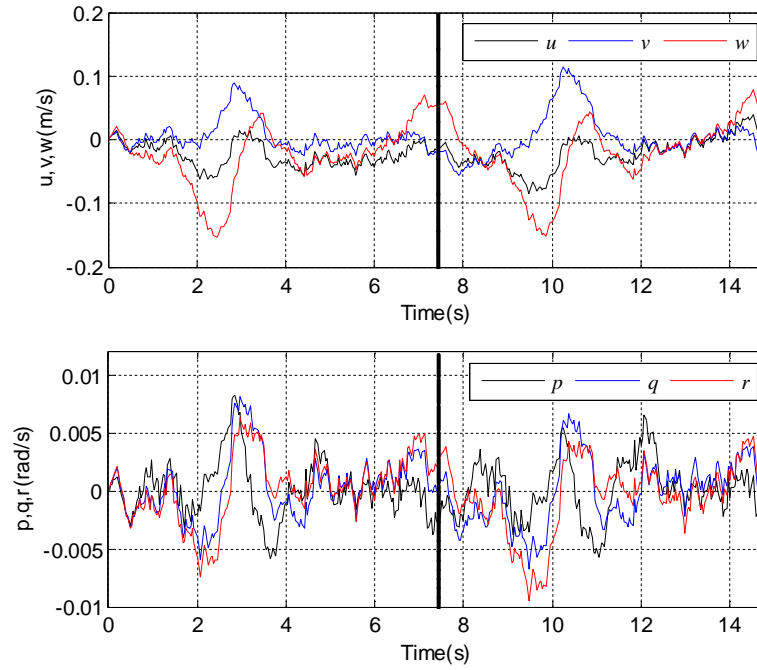
Figure E.4: IVC, 1st Failure, Some Fuselage States
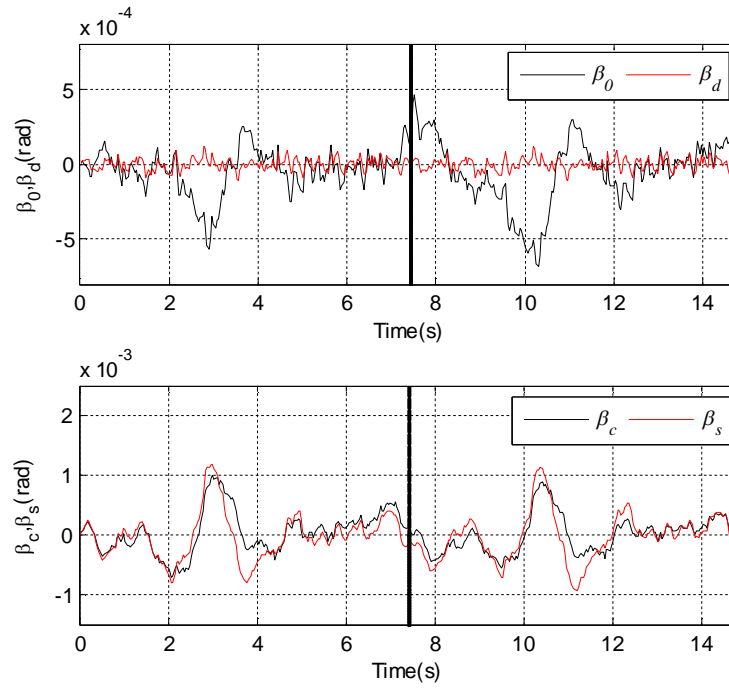
Figure E.5: IVC, 1st Failure, Blade Flapping States
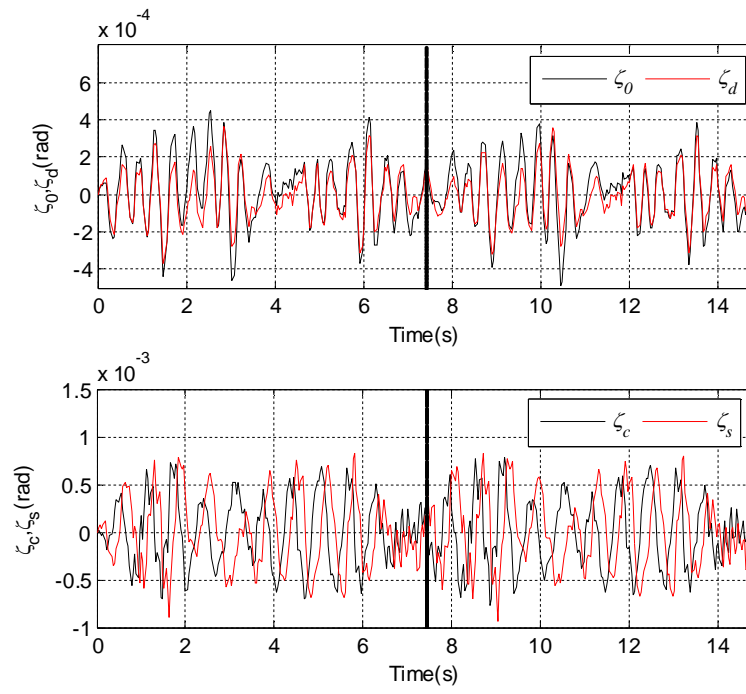
Figure E.6: IVC, 1st Failure, Blade Lagging States
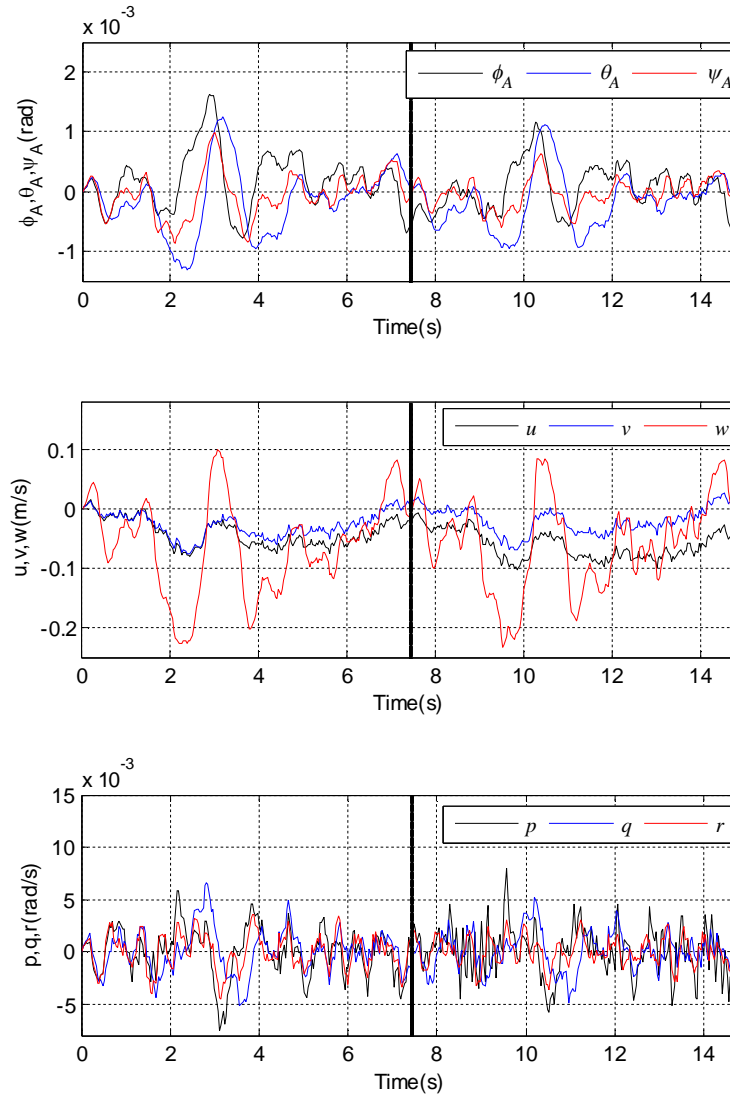
Figure E.7: OVC, 2nd Failure, Fuselage States
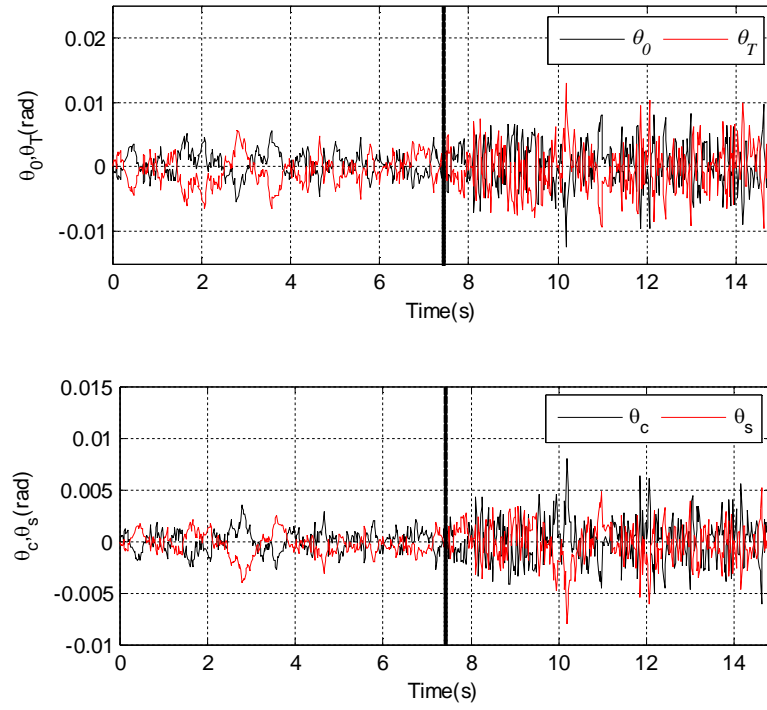
Figure E.8: OVC, 2nd Failure, All Controls
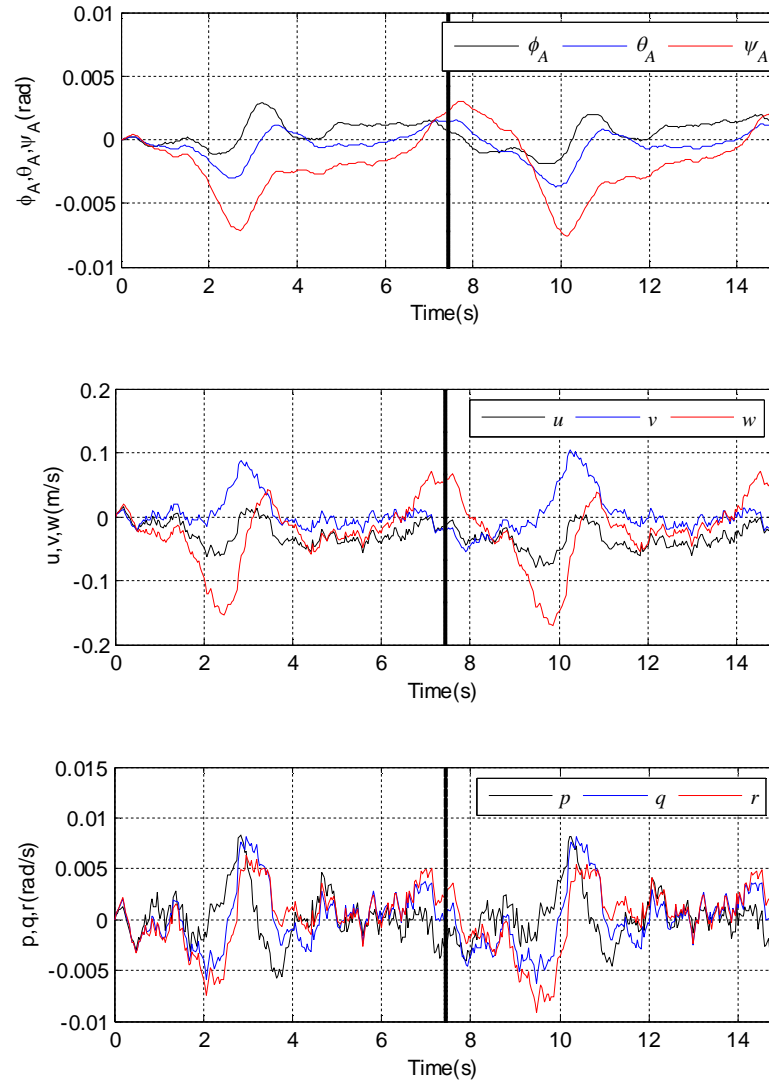
Figure E.9: IVC, 2nd Failure, Fuselage States

160
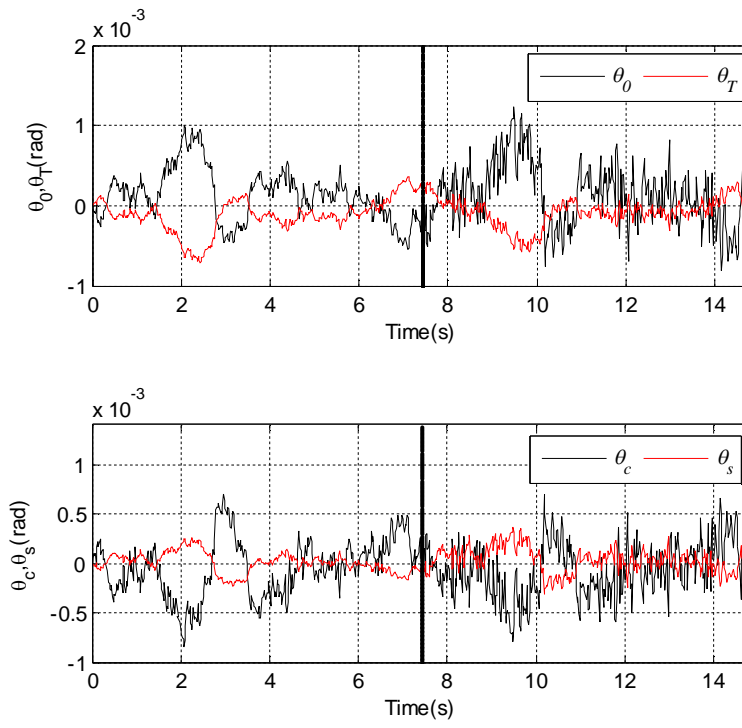
Figure E.10: IVC, 2nd Failure, All Controls
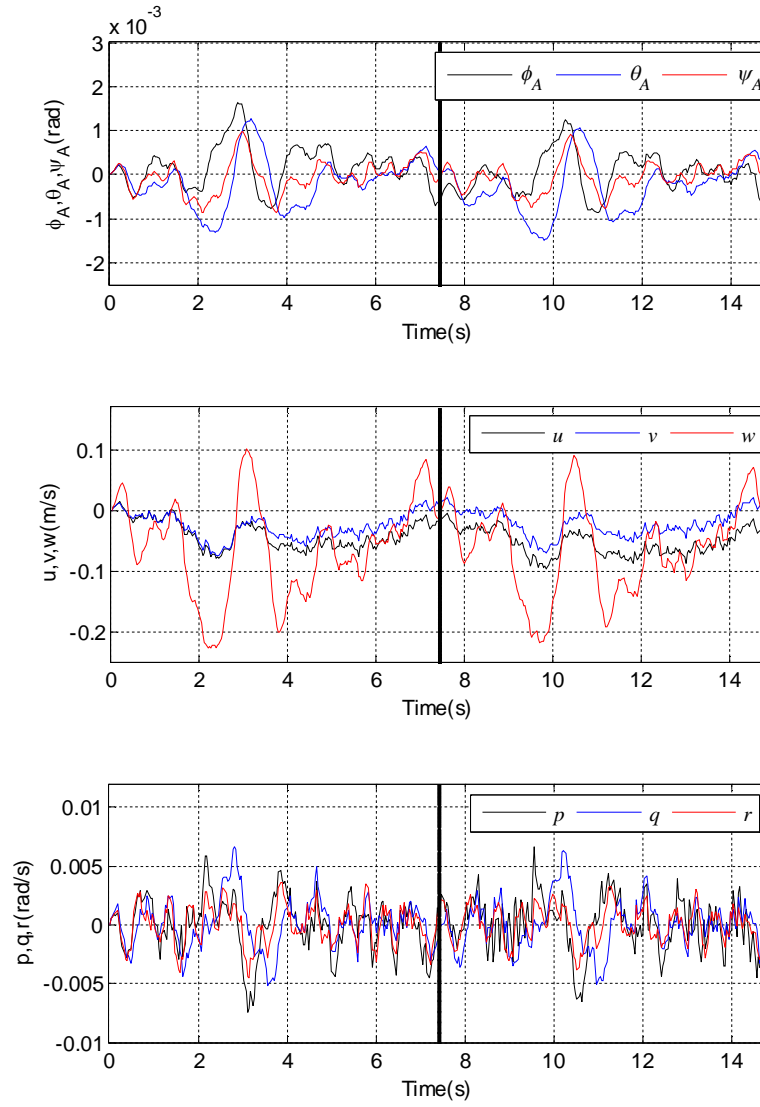
Figure E.11: OVC, 3rd Failure, Fuselage States
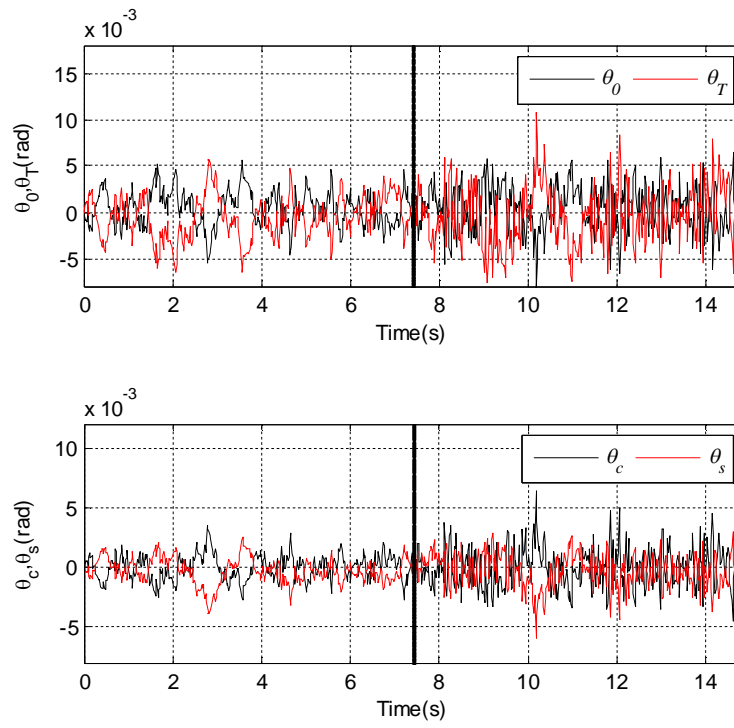
Figure E.12: OVC, 3rd Failure, All Controls
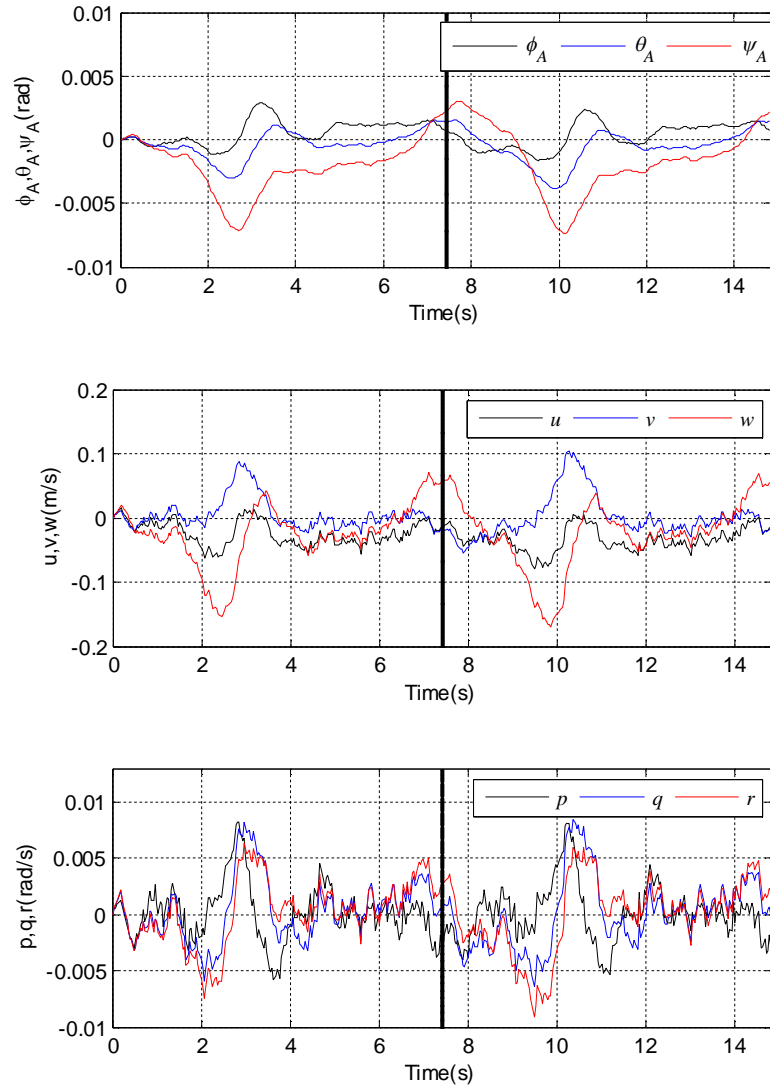
Figure E.13: IVC, 3rd Failure, Fuselage States
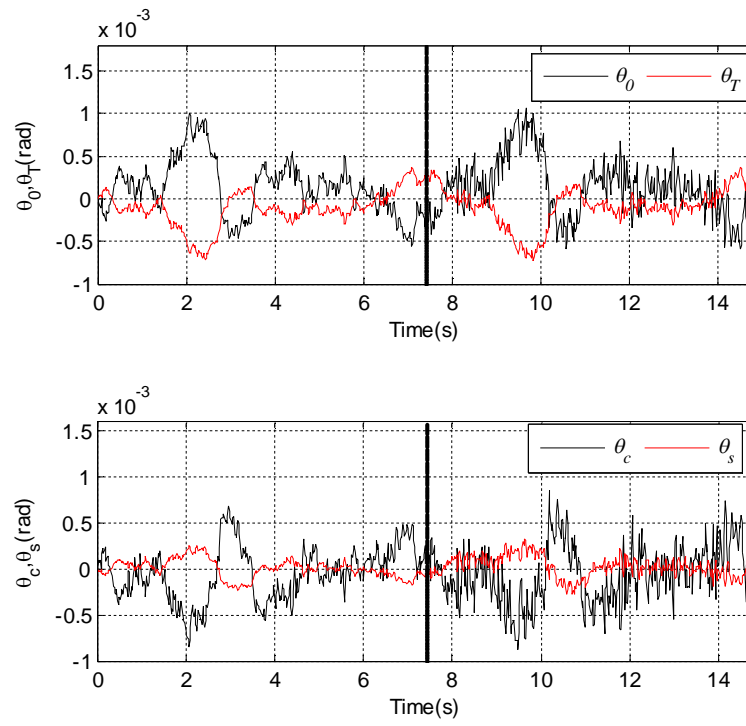
Figure E.14: IVC, 3rd Failure, All Controls

Table E.1: Closed Loop Stability Robustness of OVC for Level Banked Turn
$(\dot{\psi}_A = 0.1 \, \text{rad/s}, \; \gamma_{FP} = 0 \, \text{rad})$

Failed Sensors	1st	2nd	3rd	4th
1st (ϕ_A, θ_A)	Hover to 80 kts	Hover to 80 kts	Hover to 80 kts	Hover to 80 kts
2nd (u, v, w)	Hover to 80 kts	Hover to 80 kts	Hover to 80 kts	Hover to 80 kts
3rd (p, q, r)	Hover to 80 kts	Hover to 80 kts	Hover to 80 kts	Hover to 80 kts

Table E.2: Closed Loop Stability Robustness of IVC for Level Banked Turn
$(\dot{\psi}_A = 0.1 \, \text{rad/s}, \; \gamma_{FP} = 0 \, \text{rad})$

Failed Sensors	1st	2nd	3rd	4th
1st (ϕ_A, θ_A)	Hover to 80 kts	Hover to 80 kts	Hover to 80 kts	Hover to 80 kts
2nd (u, v, w)	20 kts to 80 kts	30 kts to 80 kts	20 kts to 80 kts	30 kts to 80 kts
3rd (p, q, r)	Hover to 80 kts	Hover to 80 kts	Hover to 70 kts	Hover to 80 kts

Table E.3: Closed Loop Stability Robustness of OVC for Different Helical Turn
($\dot{\psi}_A = 0.1\,\text{rad/s}, \ \gamma_{FP} = 0.05\,\text{rad}$)

Failed Sensors	1$^{\text{st}}$	2$^{\text{nd}}$	3$^{\text{rd}}$	4$^{\text{th}}$
1$^{\text{st}}$ (ϕ_A, θ_A)	Hover to 80 kts	Hover to 80 kts	Hover to 80 kts	Hover to 80 kts
2$^{\text{nd}}$ (u, v, w)	Hover to 80 kts	Hover to 80 kts	Hover to 80 kts	Hover to 80 kts
3$^{\text{rd}}$ (p, q, r)	Hover to 80 kts	Hover to 80 kts	Hover to 80 kts	Hover to 80 kts

Table E.4: Closed Loop Stability Robustness of IVC for Different Helical Turn
($\dot{\psi}_A = 0.1\,\text{rad/s}, \ \gamma_{FP} = 0.05\,\text{rad}$)

Failed Sensors	1$^{\text{st}}$	2$^{\text{nd}}$	3$^{\text{rd}}$	4$^{\text{th}}$
1$^{\text{st}}$ (ϕ_A, θ_A)	Hover to 80 kts	Hover to 80 kts	Hover to 80 kts	Hover to 80 kts
2$^{\text{nd}}$ (u, v, w)	20 kts to 80 kts	30 kts to 80 kts	20 kts to 80 kts	30 kts to 80 kts
3$^{\text{rd}}$ (p, q, r)	Hover to 80 kts	Hover to 80 kts	Hover to 70 kts	Hover to 80 kts

Table E.5: Control Energy Comparison for Level Banked Turn
($\dot{\psi}_A = 0.1\,\text{rad/s},\ \gamma_{FP} = 0\,\text{rad}$)

Failed Sensors	OVC Cost		IVC Cost	
	1st and 3rd	2nd and 4th	1st and 3rd	2nd and 4th
1st (ϕ_A, θ_A)	0.003404	0.004591	0.001968	0.000642
2nd (u, v, w)	0.001749	0.002301	0.002468	0.000530
3rd (p, q, r)	0.001978	0.001930	0.001581	0.000395
(no failure)	0.001216	0.001304	0.001444	0.000337

Table E.6: Control Energy Comparison for Different Helical Turn
($\dot{\psi}_A = 0.1\,\text{rad/s},\ \gamma_{FP} = 0.05\,\text{rad}$)

Failed Sensors	OVC Cost		IVC Cost	
	1st and 3rd	2nd and 4th	1st and 3rd	2nd and 4th
1st (ϕ_A, θ_A)	0.003504	0.004731	0.001950	0.000659
2nd (u, v, w)	0.001827	0.002455	0.002494	0.000558
3rd (p, q, r)	0.002098	0.002090	0.001579	0.000418
(no failure)	0.001287	0.001409	0.001442	0.000358

Table E.7: Number of Iteration for Helical Turn
($\dot{\psi}_A = 0.1\,\text{rad/s}$, $\gamma_{FP} = 0.1\,\text{rad}$)

	OVC Cost		IVC Cost	
Failed Sensors	1st and 3rd	2nd and 4th	1st and 3rd	2nd and 4th
1st (ϕ_A, θ_A)	18	18	12	26
2nd (u, v, w)	4	6	16	26
3rd (p, q, r)	6	6	14	24
(no failure)	4	6	14	22

Table E.8: Number of Iteration for Level Banked Turn
($\dot{\psi}_A = 0.1\,\text{rad/s}$, $\gamma_{FP} = 0\,\text{rad}$)

	OVC Cost		IVC Cost	
Failed Sensors	1st and 3rd	2nd and 4th	1st and 3rd	2nd and 4th
1st (ϕ_A, θ_A)	18	18	12	26
2nd (u, v, w)	4	6	16	28
3rd (p, q, r)	6	6	14	24
(no failure)	4	6	14	24

Table E.9: Number of Iteration for Different Helical Turn
$(\dot{\psi}_A = 0.1\,\text{rad/s},\ \gamma_{FP} = 0.05\,\text{rad})$

	OVC Cost		IVC Cost	
Failed Sensors	1st and 3rd	2nd and 4th	1st and 3rd	2nd and 4th
1st (ϕ_A, θ_A)	18	18	12	26
2nd (u, v, w)	4	6	16	26
3rd (p, q, r)	6	6	14	24
(no failure)	4	6	14	22

APPENDIX F

Additional MPC Results

F.1 Straight Level Flight Examples

For straight level flight examples, plant and sensor uncorrelated white Gaussian noises with intensities of $W = 10^{-7} I_{41}$, $V = 10^{-7} I_9$ respectively were introduced in the linearized model.

In the first example, the helicopter is required to track a reference trajectory for which the roll angle has a prescribed time variation and the other two Euler angles are forced to be zero. The parameters used for MPC design (all the angles are given in radians) were:

▪Output and input constraints:

$$\begin{bmatrix} -1 & -0.01 & -0.01 \end{bmatrix}^T \leq \begin{bmatrix} \phi_A & \theta_A & \psi_A \end{bmatrix}^T \leq \begin{bmatrix} 0 & 0.01 & 0.01 \end{bmatrix}^T$$

$$\begin{bmatrix} |p| & |q| & |r| \end{bmatrix}^T \leq \begin{bmatrix} 1 & 1 & 1 \end{bmatrix}^T (rad/s)$$

$$\begin{bmatrix} 0 & -0.18 & -0.18 & 0 \end{bmatrix}^T \leq \begin{bmatrix} \theta_0 & \theta_c & \theta_s & \theta_T \end{bmatrix}^T \leq \begin{bmatrix} 0.35 & 0.18 & 0.18 & 1 \end{bmatrix}^T$$

$$\begin{bmatrix} |\Delta\theta_0| & |\Delta\theta_c| & |\Delta\theta_s| & |\Delta\theta_T| \end{bmatrix}^T \leq \begin{bmatrix} 0.175 & 0.09 & 0.09 & 0.5 \end{bmatrix}^T$$

▪ Other MPC parameters:

$H_p = 20$, $H_u = 2$, and $H_w = 1$

The second example is the same with the first example except that the first sensor failure occurs. This MPC example is not feasible with the second and third sensor failures.

In the third example, to evaluate the robustness of our MPC designs it is considered that all helicopter inertial parameters (helicopter mass and helicopter inertia matrix elements) are uncertain. For this purpose it is considered that the plant model's inertial parameters decrease by 10% , while the internal model, which is used to produce MPC signals, is not aware of these uncertainties. Then the response of the plant affected by these uncertainties was simulated (Fig. F.3). The trajectories and parameters used for MPC design are the same as in the first example. It can be observed from Fig. F.3 that the plant outputs slightly violate the constraints due to these uncertainties.

For the fourth example, the helicopter is required to track a reference trajectory for which the pitch angle has a prescribed time variation and the other two Euler angles are forced to be zero. The parameters used for MPC design are the same with previous examples except that

$$\begin{bmatrix} -0.01 & -1 & -0.01 \end{bmatrix}^T \leq \begin{bmatrix} \phi_A & \theta_A & \psi_A \end{bmatrix}^T \leq \begin{bmatrix} 0.01 & 0 & 0.01 \end{bmatrix}^T$$

The fifth problem is the same with the fourth problem except that the first sensor failure occurs. This MPC example is not feasible with the second and third sensor failures. Note also that for all these straight level flight examples the sampling time was 0.037 s (which is equal to 1 rad).
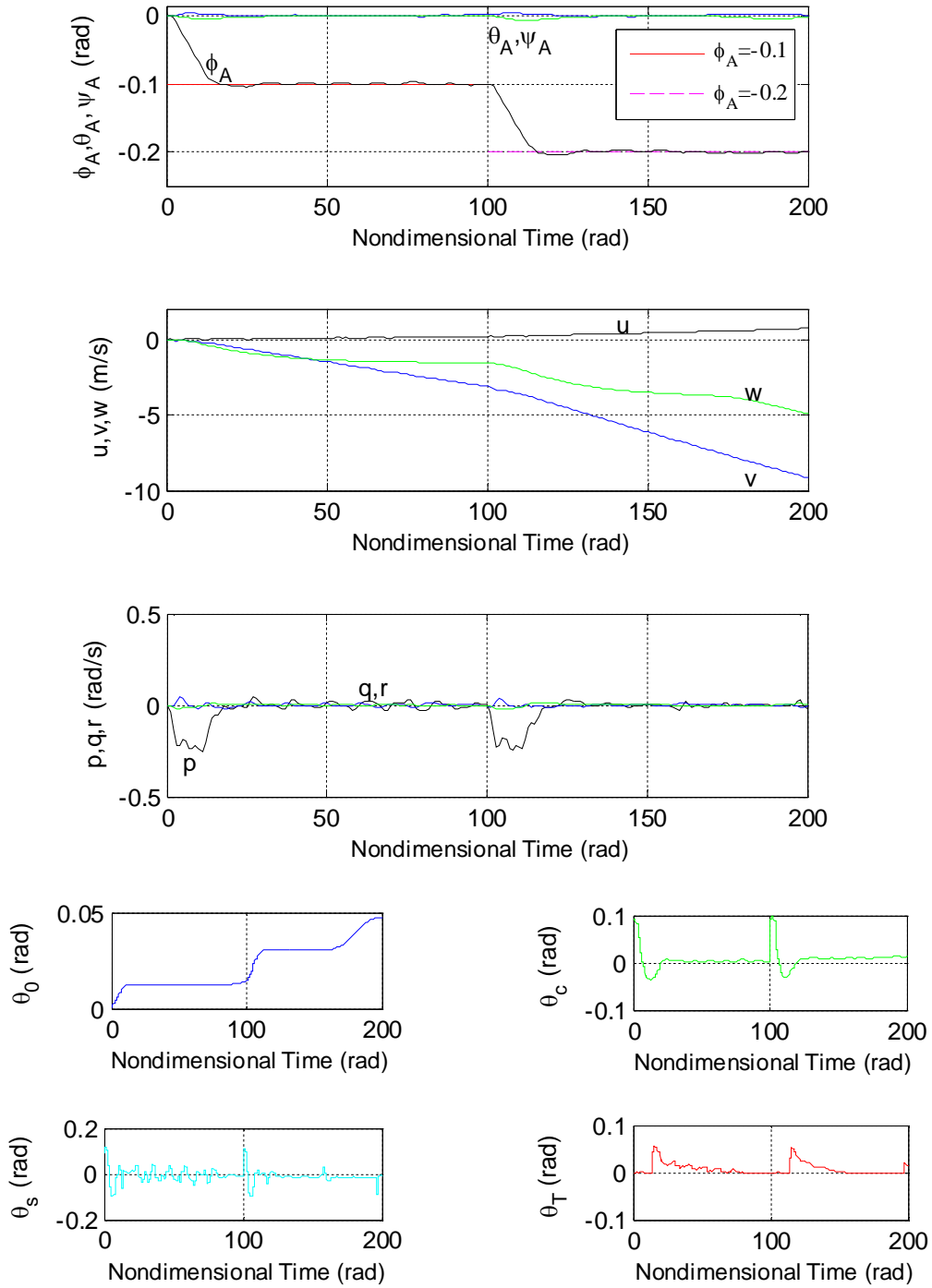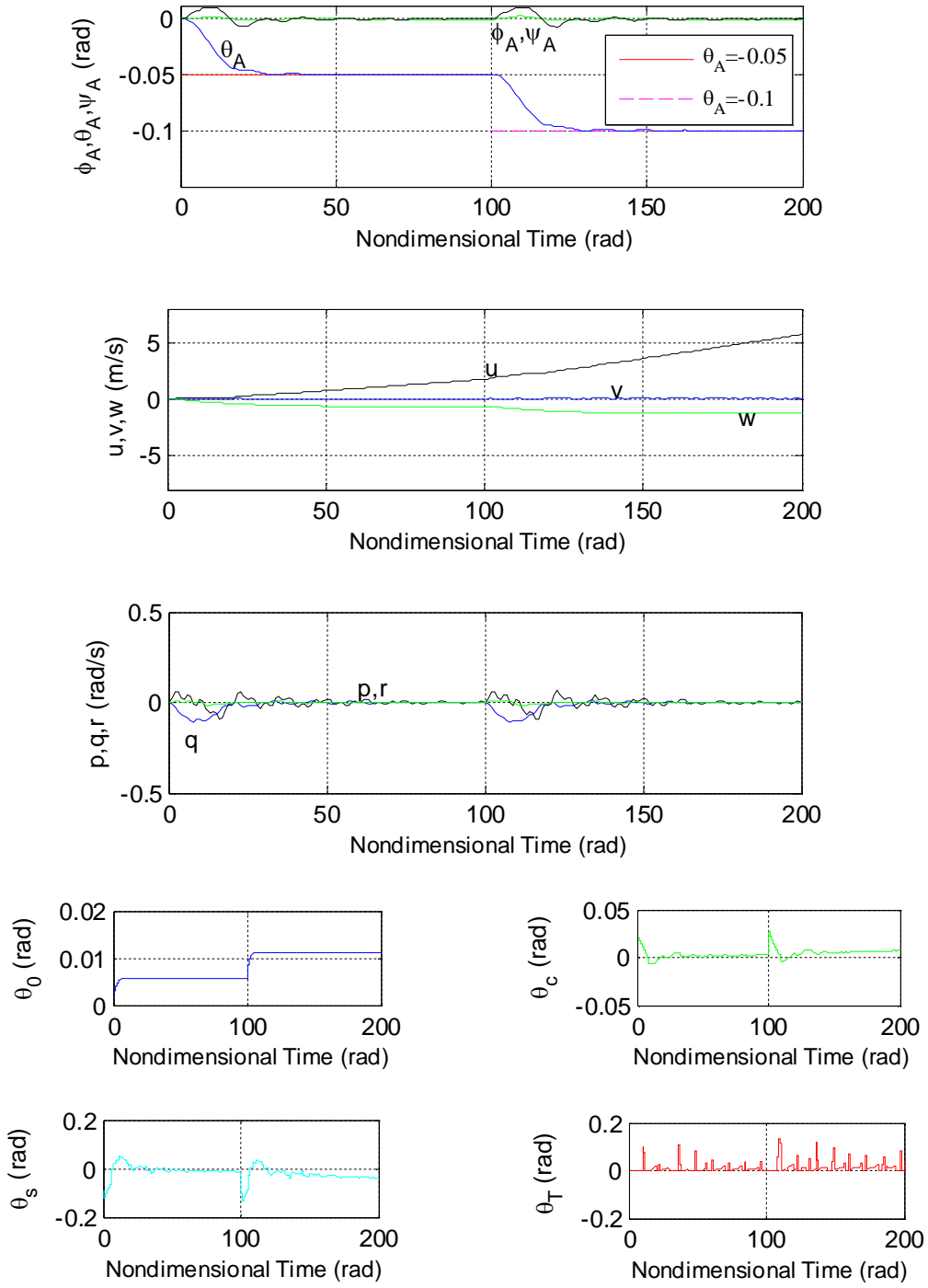
Figure F.1: 1ˢᵗ MPC Example for Hover (No Sensor Failure)
($V_A = 1\,\text{kt}, \ \dot{\psi}_A = 0\,\text{rad/s}, \ \gamma_{FP} = 0\,\text{rad}, \ R_{turn} = 0\,\text{m}$)
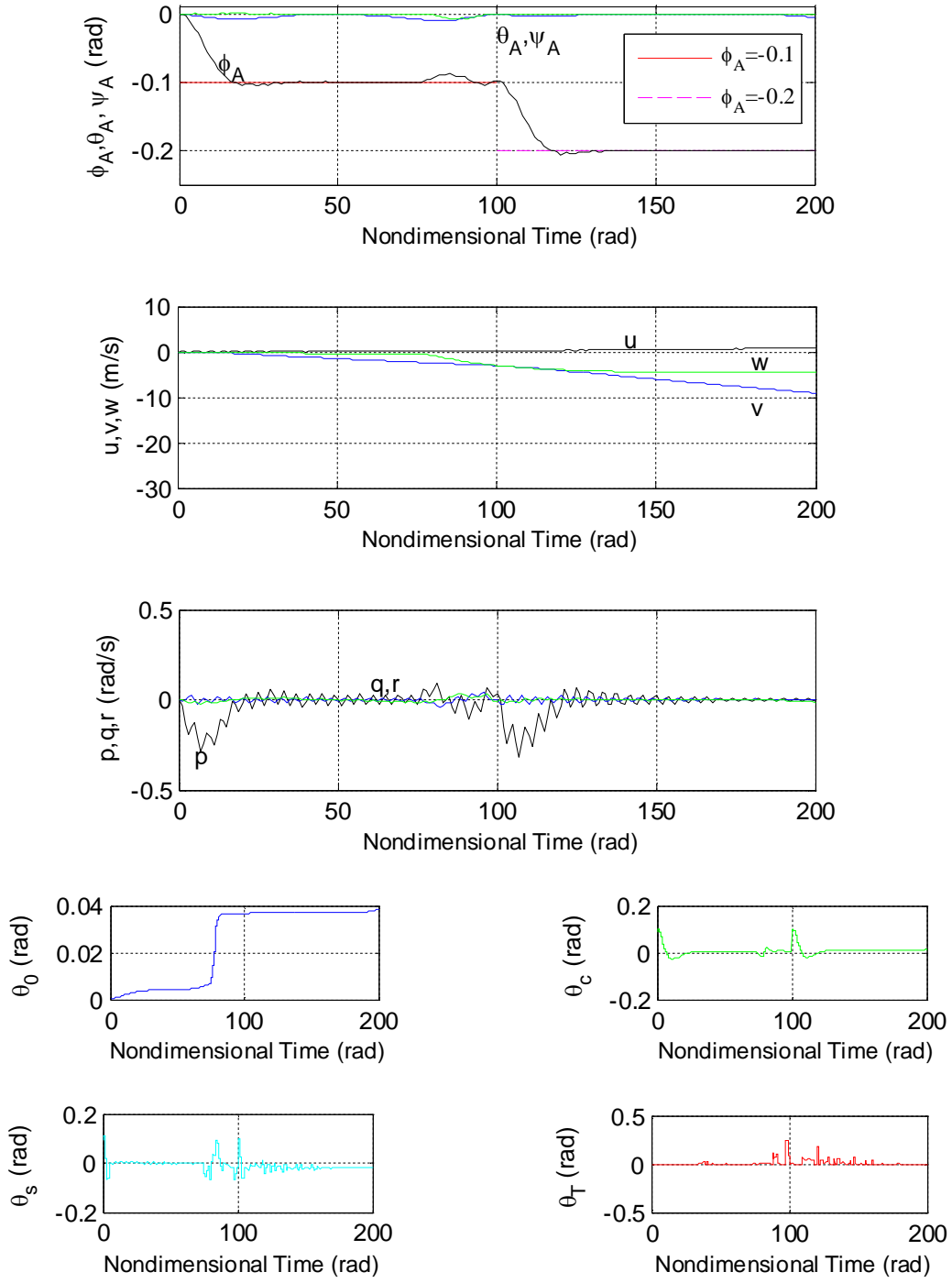
Figure F.2: 2nd MPC Example for Hover (1st Sensor Failure)
($V_A = 1\,\text{kt}$, $\dot{\psi}_A = 0\,\text{rad/s}$, $\gamma_{FP} = 0\,\text{rad}$, $R_{turn} = 0\,\text{m}$)
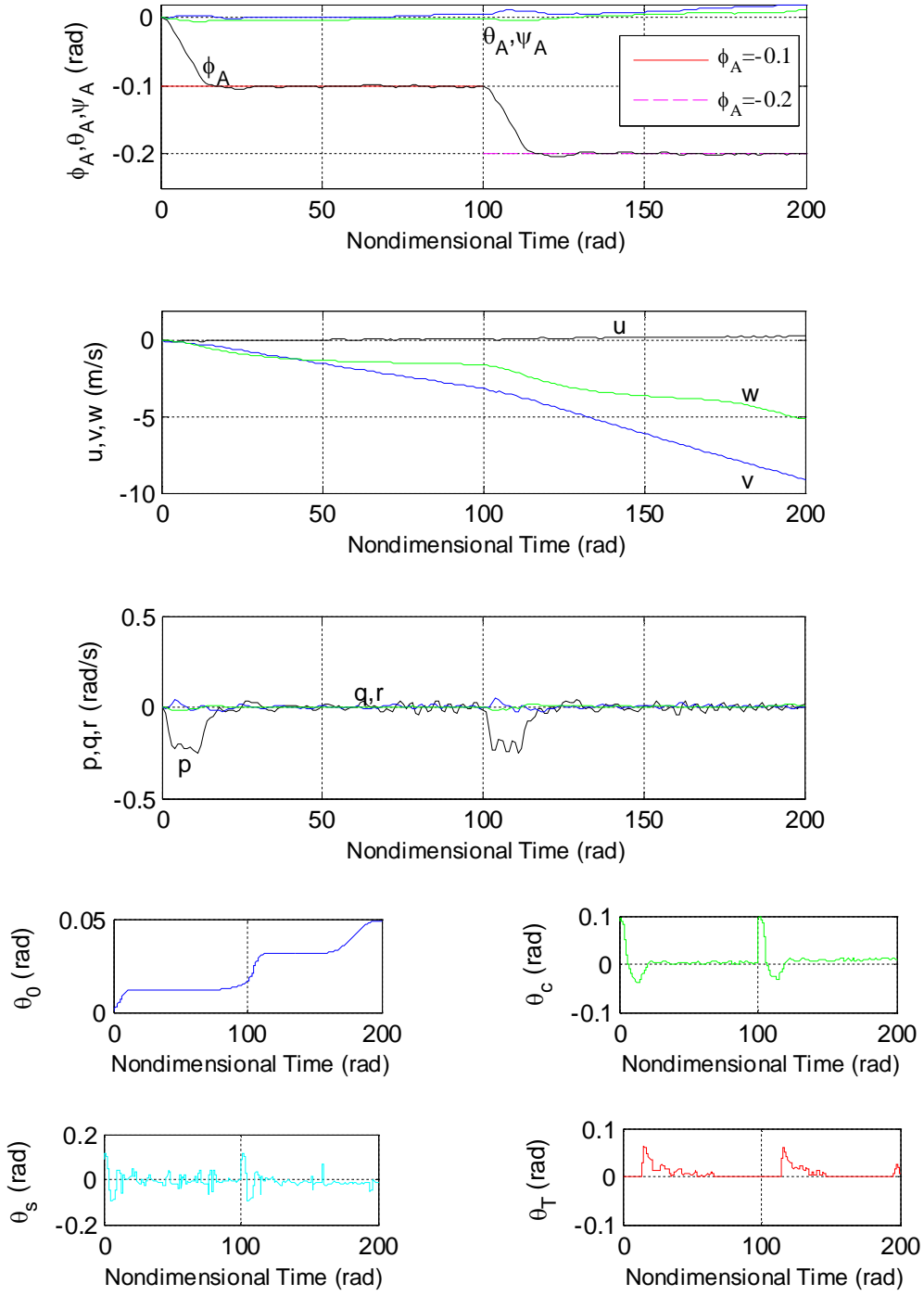
Figure F.3: 3ʳᵈ MPC Example for Hover (Robustness, No Sensor Failure)
$(V_A = 1\,\text{kt},\ \dot{\psi}_A = 0\,\text{rad/s},\ \gamma_{FP} = 0\,\text{rad},\ R_{turn} = 0\,\text{m})$
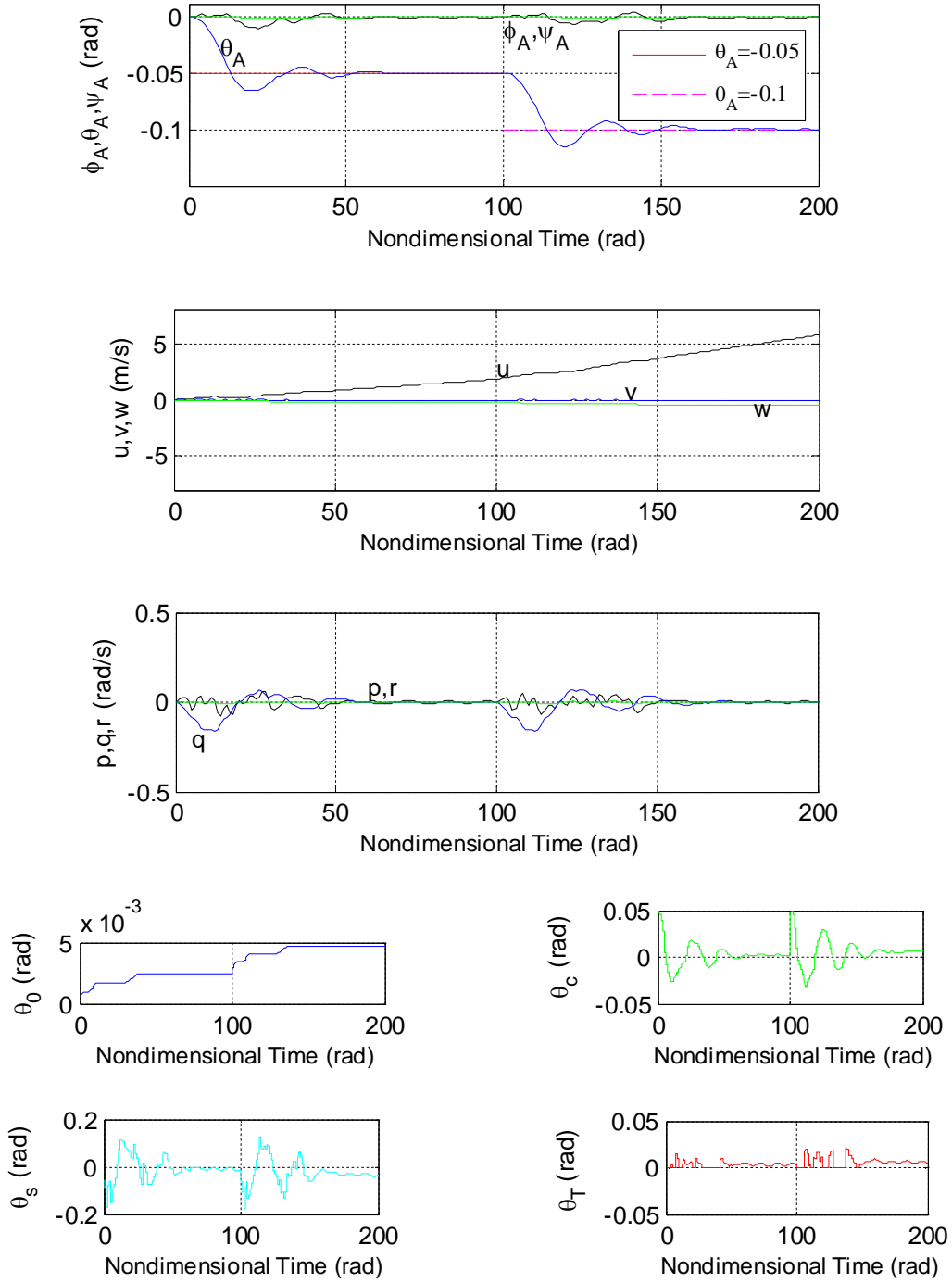
Figure F.4: 4th MPC Example for Hover (No Sensor Failure)

$(V_A = 1\,\text{kt},\ \dot{\psi}_A = 0\,\text{rad/s},\ \gamma_{FP} = 0\,\text{rad},\ R_{turn} = 0\,\text{m})$

Figure F.5: 5th MPC Example for Hover (1st Sensor Failure)
($V_A = 1\,\text{kt}$, $\dot{\psi}_A = 0\,\text{rad/s}$, $\gamma_{FP} = 0\,\text{rad}$, $R_{turn} = 0\,\text{m}$)

F.2 Maneuvering Flight Examples

In this sub-section the MPC examples examined in Chapter 6 are resolved for level banked turn and different helical turn. The MPC parameters of 1st to 4th set of examples are the same with the ones shown in Chapter 6. The 4th example (robustness) is not feasible for level banked turn. The behaviors of outputs and controls are similar with the ones discussed in Chapter 6.
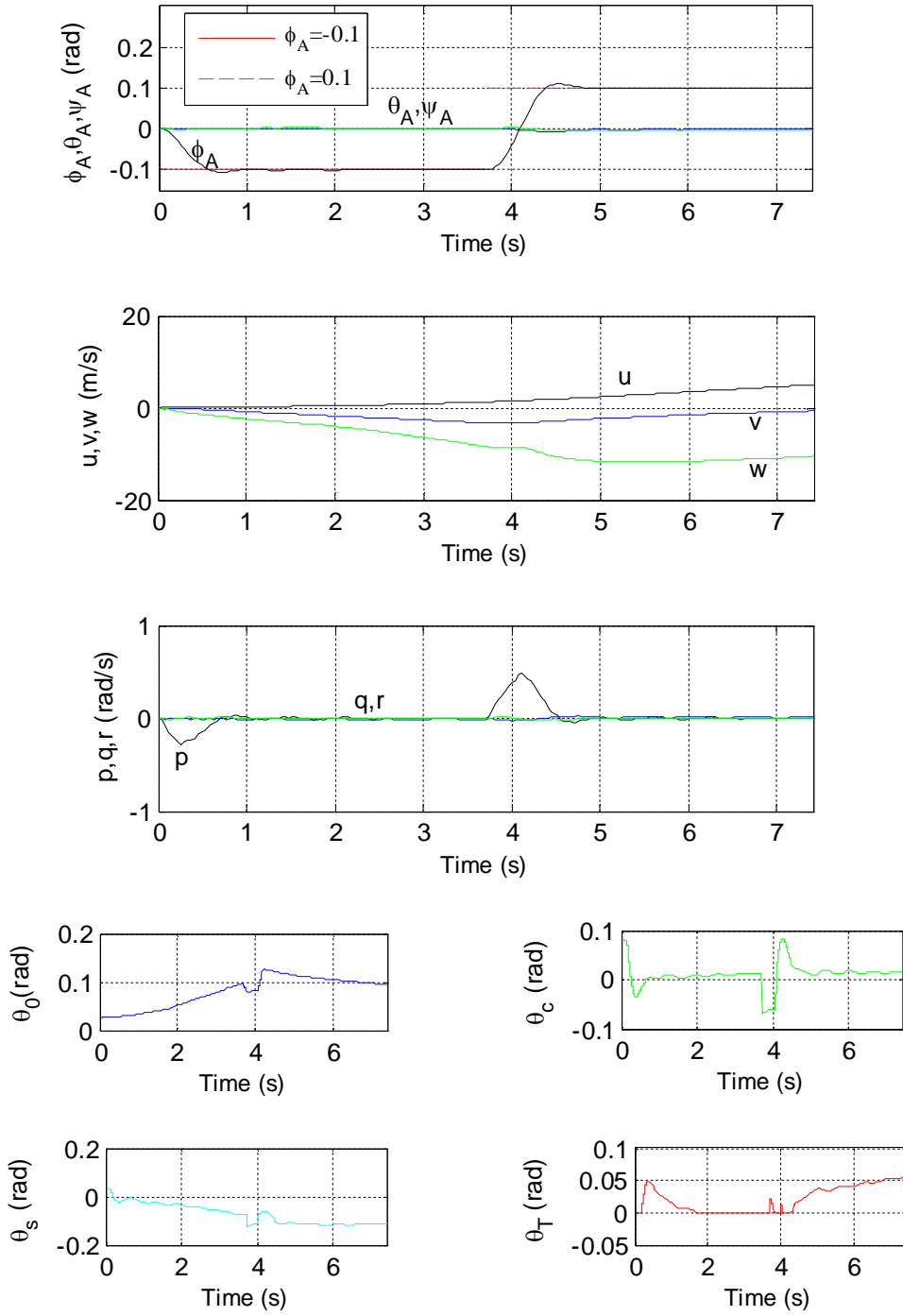
Figure F.6: 1st MPC Example for Level Banked Turn (No Sensor Failure)
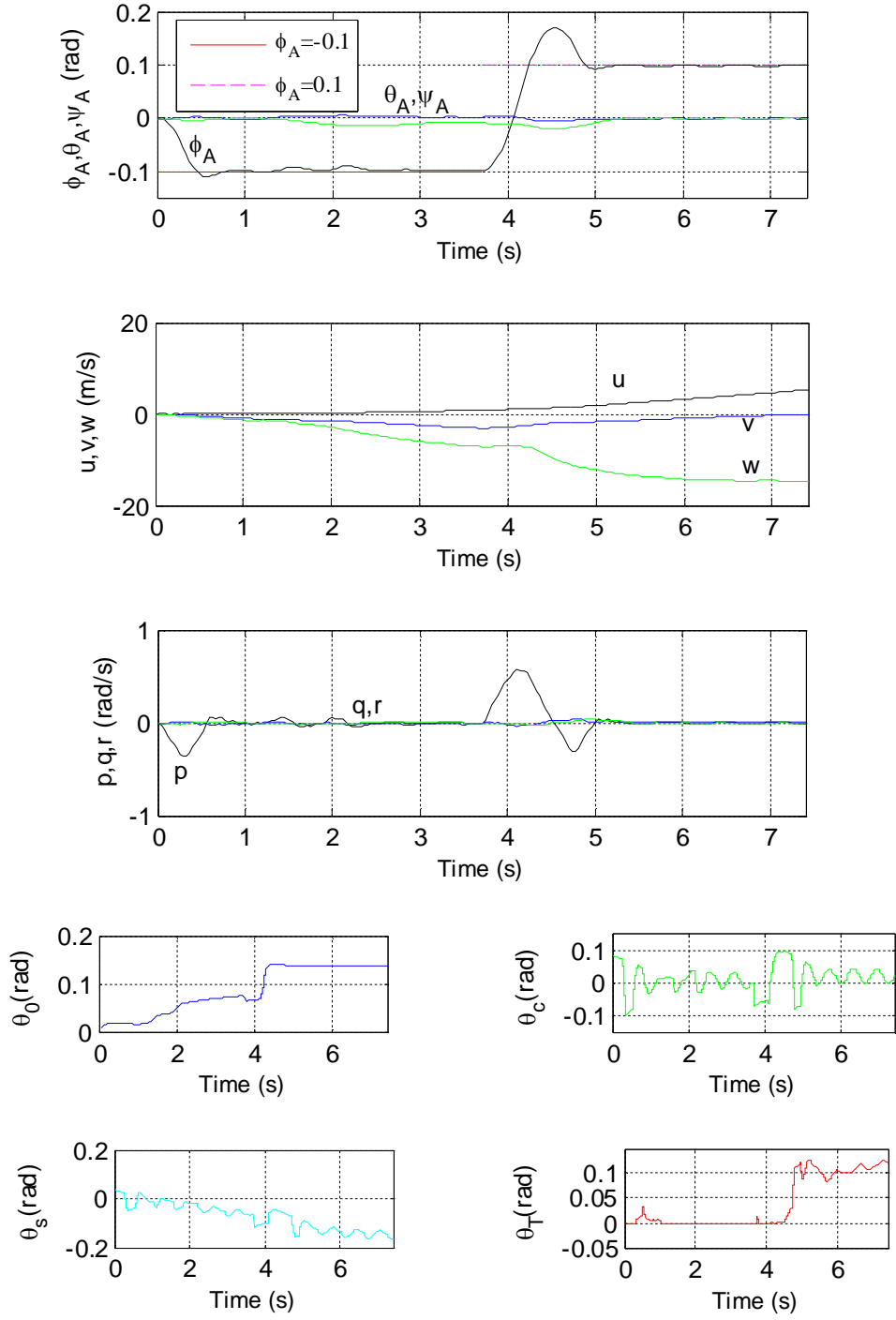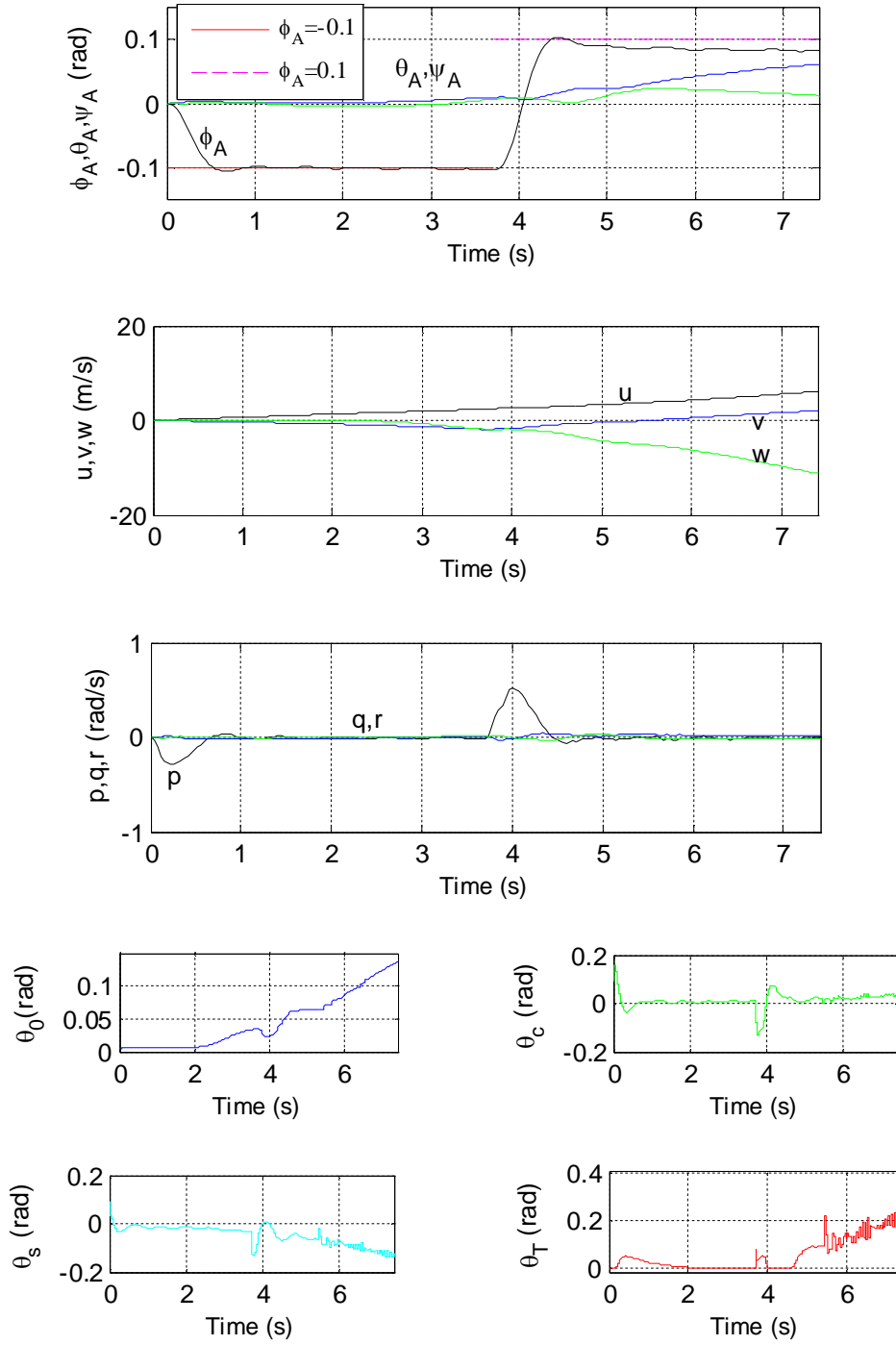($V_A = 40\,\text{kts}$, $\dot{\psi}_A = 0.1\,\text{rad/s}$, $\gamma_{FP} = 0\,\text{rad}$, $R_{turn} = 205.76\text{m}$)
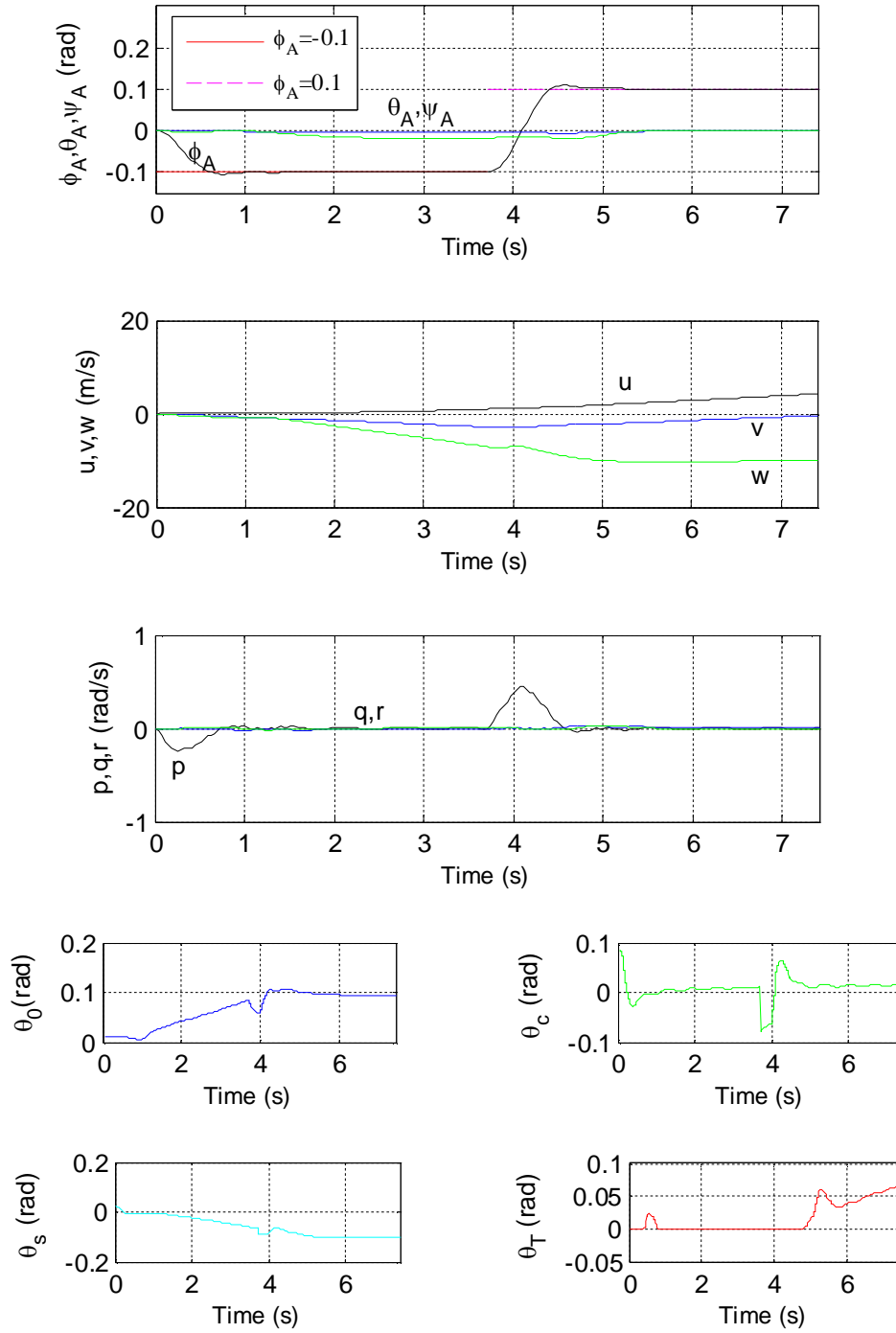
Figure F.7: 2nd MPC Example for Level Banked Turn (1st Sensor Failure)
($V_A = 40\,\text{kts},\ \dot{\psi}_A = 0.1\,\text{rad/s},\ \gamma_{FP} = 0\,\text{rad},\ R_{turn} = 205.76\text{m}$)
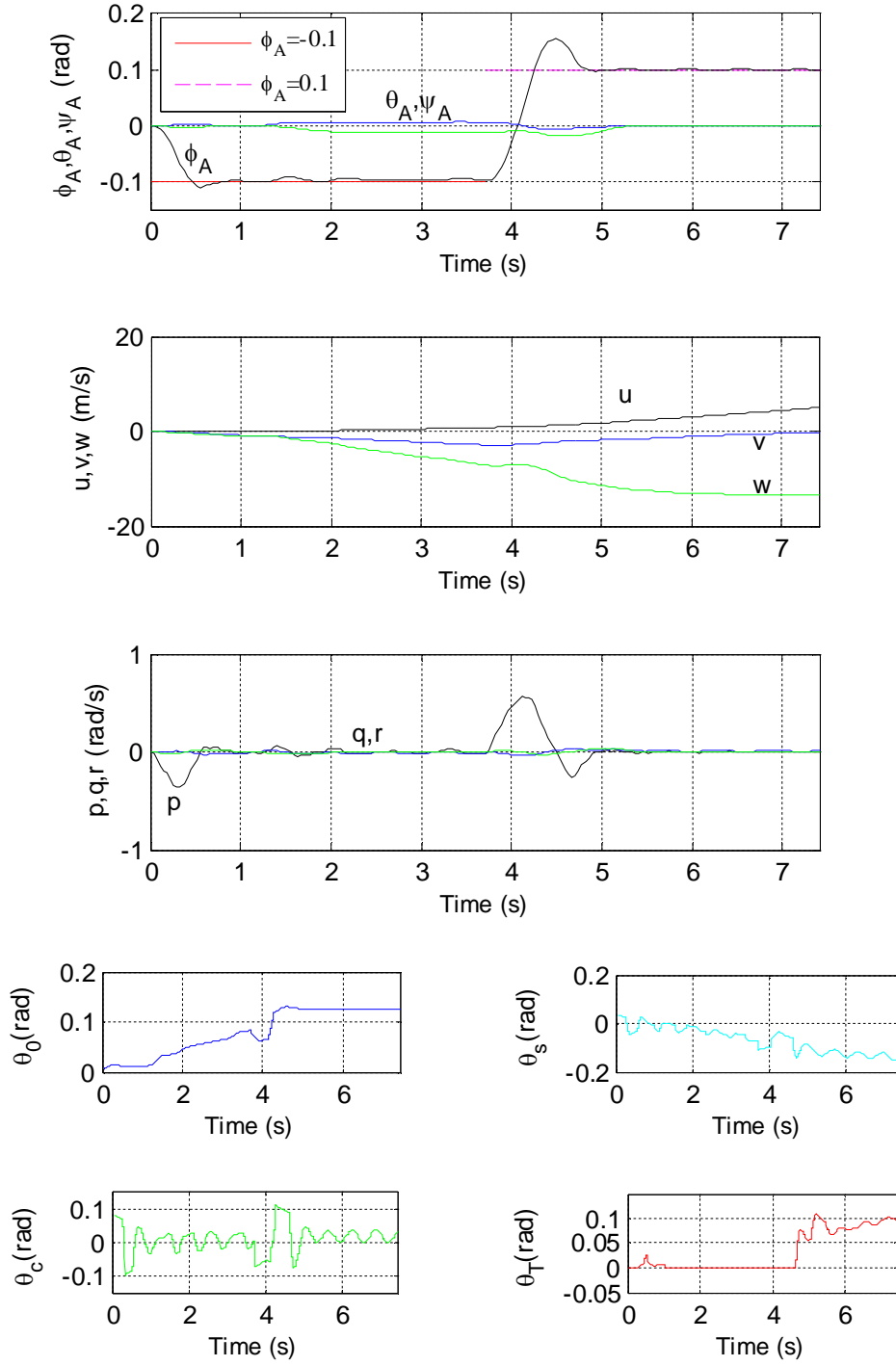
Figure F.8: 3rd MPC Example for Level Banked Turn (2nd Sensor Failure)
($V_A = 40\,\text{kts}$, $\dot{\psi}_A = 0.1\,\text{rad/s}$, $\gamma_{FP} = 0\,\text{rad}$, $R_{turn} = 205.76\text{m}$)

181
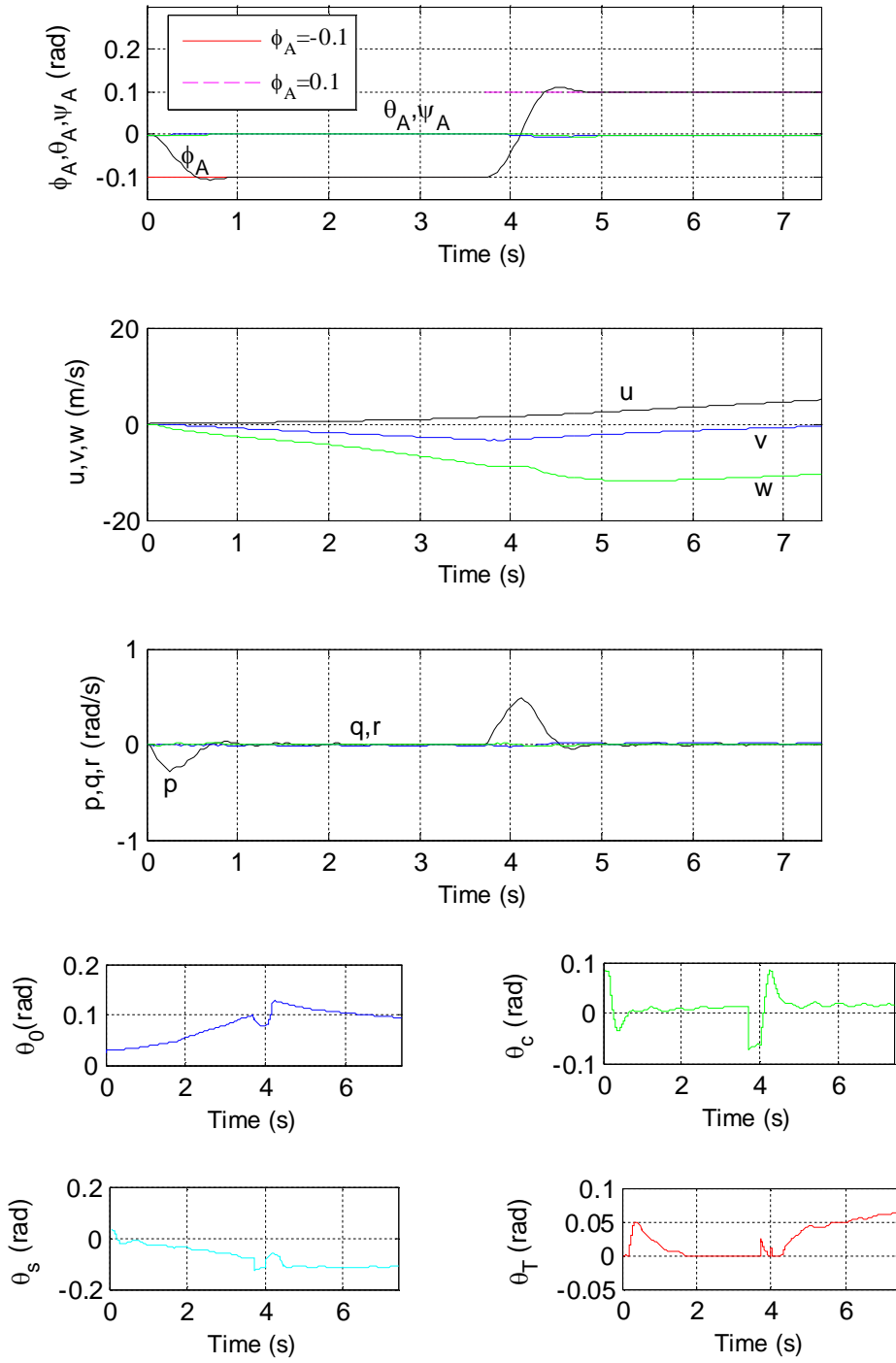
Figure F.9: 1st MPC Example for Different Helical Turn (No Sensor Failure)
($V_A = 40\,\text{kts}$, $\dot{\psi}_A = 0.1\,\text{rad/s}$, $\gamma_{FP} = 0.05\,\text{rad}$, $R_{turn} = 205.50\text{m}$)
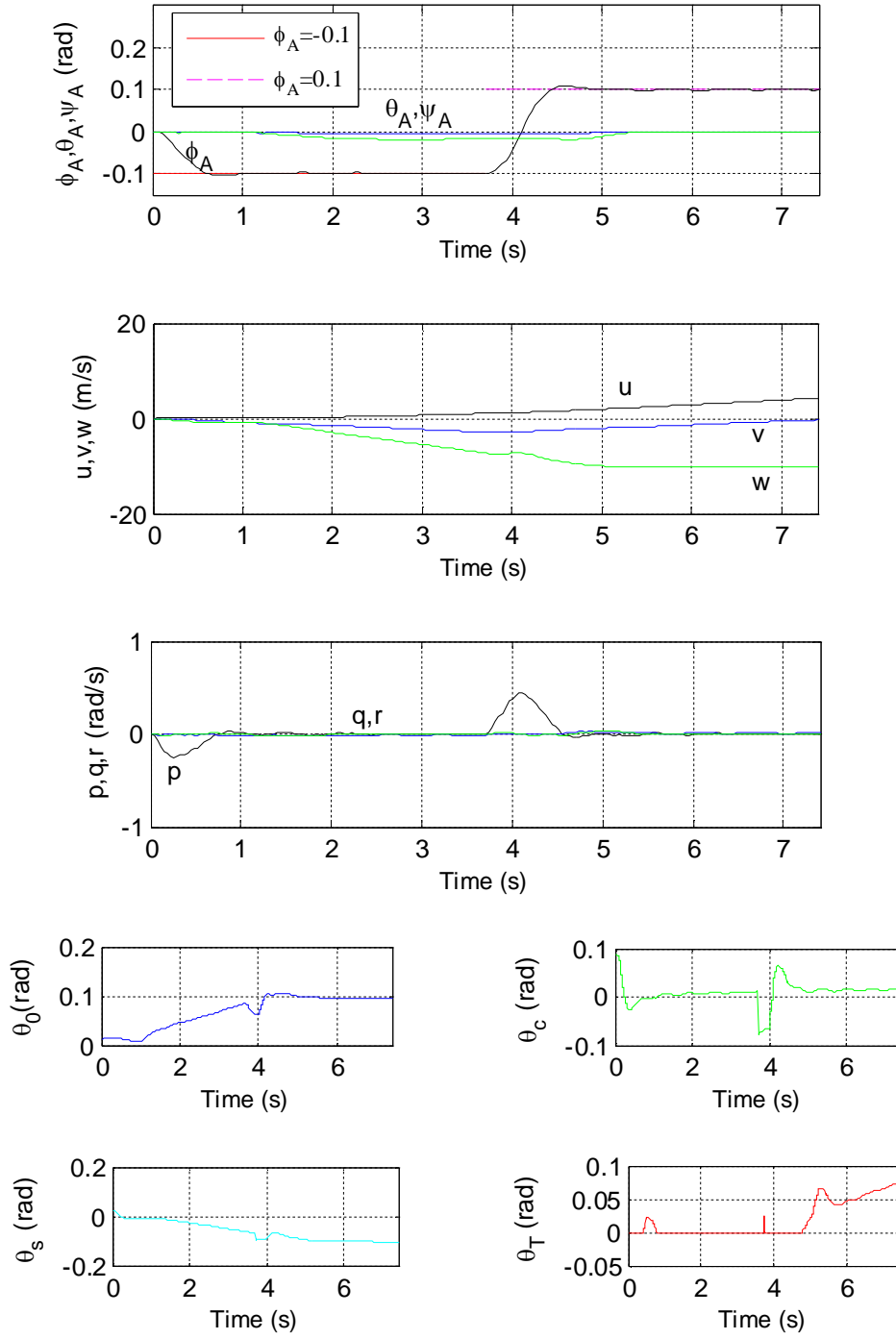
Figure F.10: 2ⁿᵈ MPC Example for Different Helical Turn (1ˢᵗ Sensor Failure)
$(V_A = 40\,\text{kts},\ \dot{\psi}_A = 0.1\,\text{rad/s},\ \gamma_{FP} = 0.05\,\text{rad},\ R_{turn} = 205.50\text{m})$

183

Figure F.11: 3rd MPC Example for Different Helical Turn (2nd Sensor Failure)
($V_A = 40 \, \text{kts}, \; \dot{\psi}_A = 0.1 \, \text{rad/s}, \; \gamma_{FP} = 0.05 \, \text{rad}, \; R_{turn} = 205.50 \text{m}$)

Figure F.12: 4th MPC Example for Different Helical Turn (Robustness, No Sensor Failure)

($V_A = 40\,\text{kts}$, $\dot{\psi}_A = 0.1\,\text{rad/s}$, $\gamma_{FP} = 0.05\,\text{rad}$, $R_{turn} = 205.50\text{m}$)

APPENDIX G

Matlab Commands

i. *fsolve* command is used to solve the trim equations.

ii. *ctrb* and *obsv* commands are used to test controllability and observability of the LTI systems, respectively.

$$n = rank(ctrb(A_p, B_p)), \ n = rank(obsv(A_p, C_p))$$

iii. *are and lqr* commands are used to solve two algebraic Riccati equations, respectively.

$$0 = XA_p^T + A_p X - XM_p^T V^{-1} M_p X + D_p W_p D_p^T \quad \text{and} \quad F = XM_p^T V^{-1} \tag{G.1}$$

$$0 = KA_p + A_p^T K - KB_p R^{-1} B_p^T K + C_p^T Q C_p \quad \text{and} \quad G = -R^{-1} B_p^T K \tag{G.2}$$

$$X = are\left(A_p^T, M_p^T V^{-1} M_p, D_p W_p D_p^T\right), \quad K = lqr\left(A_p, B_p, Q, R\right)$$

iv. *scmpc* command is used to simulate MPC examples (see [83] for details).

APPENDIX H

Adaptive SPSA

For the constrained SPSA, it is required that

$$x_{min} < x_{[k]} + d_k \Delta_{[k]} < x_{max} \text{ and } x_{min} < x_{[k]} - d_k \Delta_{[k]} < x_{max}$$

1. Firstly, examine $d_k \Delta_{[k]i} < 0$

a. $\Delta_{[k]i} = 1$, $d_k < \min\{(x_{[k]i} - x_{min_i})/|\Delta_{[k]i}|\}$ and $d_k < \min\{(x_{max_i} - x_{[k]i})/|\Delta_{[k]i}|\}$

b. $\Delta_{[k]i} = -1$, $d_k > \max\{(x_{min_i} - x_{[k]i})/|\Delta_{[k]i}|\}$ and $d_k > \max\{(x_{[k]i} - x_{max_i})/|\Delta_{[k]i}|\}$

2. Secondly, examine $d_k \Delta_{[k]i} > 0$

c. $\Delta_{[k]i} = 1$, $d_k > \max\{(x_{[k]i} - x_{max_i})/|\Delta_{[k]i}|\}$ and $d_k > \max\{(x_{min_i} - x_{[k]i})/|\Delta_{[k]i}|\}$

d. $\Delta_{[k]i} = -1$, $d_k < \min\{(x_{max_i} - x_{[k]i})/|\Delta_{[k]i}|\}$ and $d_k < \min\{(x_{[k]i} - x_{min_i})/|\Delta_{[k]i}|\}$

It is clear that a, b, c, d, and $d_k = d/k^\Theta$ are simultaneously satisfied by choosing

$$d_k = \min\left\{d/k^\Theta, 0.95\min_i\left\{\min\{\eta_{l_i}\}, \min\{\eta_{u_i}\}\right\}\right\} \tag{H.1}$$

where η_l and η_u are vectors whose components are $(x_{[k]i} - x_{min_i})/\Delta_{[k]i}$ for each positive

$\Delta_{[k]i}$ and $(x_{[k]i} - x_{max_i})/\Delta_{[k]i}$ for each negative $\Delta_{[k]i}$, respectively.

For the constrained SPSA, it is also required that

$$x_{min} < x_{[k]} - a_k g_{[k]} < x_{max}$$

3. Firstly, examine $a_k g_{[k]i} < 0$

e. $g_{[k]i} > 0$, $a_k < \min\left\{(x_{[k]i} - x_{min_i})/g_{[k]i}\right\}$

f. $g_{[k]i} < 0$, $a_k > \max\left\{(x_{[k]i} - x_{min_i})/g_{[k]i}\right\}$

4. Secondly, examine $a_k g_{[k]i} > 0$

g. $g_{[k]i} > 0$, $a_k > \max\left\{(x_{[k]i} - x_{max_i})/g_{[k]i}\right\}$

h. $g_{[k]i} < 0$, $a_k < \min\left\{(x_{[k]i} - x_{max_i})/g_{[k]i}\right\}$

It is clear that e, f, g, h, and $a_k = a/(S+k)^\lambda$ are simultaneously satisfied by choosing

$$a_k = \min\left\{a/(S+k)^\lambda, 0.95\min_i\left\{\min(\mu_{i_l}), \min(\mu_{i_u})\right\}\right\} \tag{H.2}$$

where μ_l and μ_u are vectors whose components are $(x_{[k]i} - x_{min_i})/g_{[k]i}$ for each positive $g_{[k]i}$ and $(x_{[k]i} - x_{max_i})/g_{[k]i}$ for each negative $g_{[k]i}$, respectively.
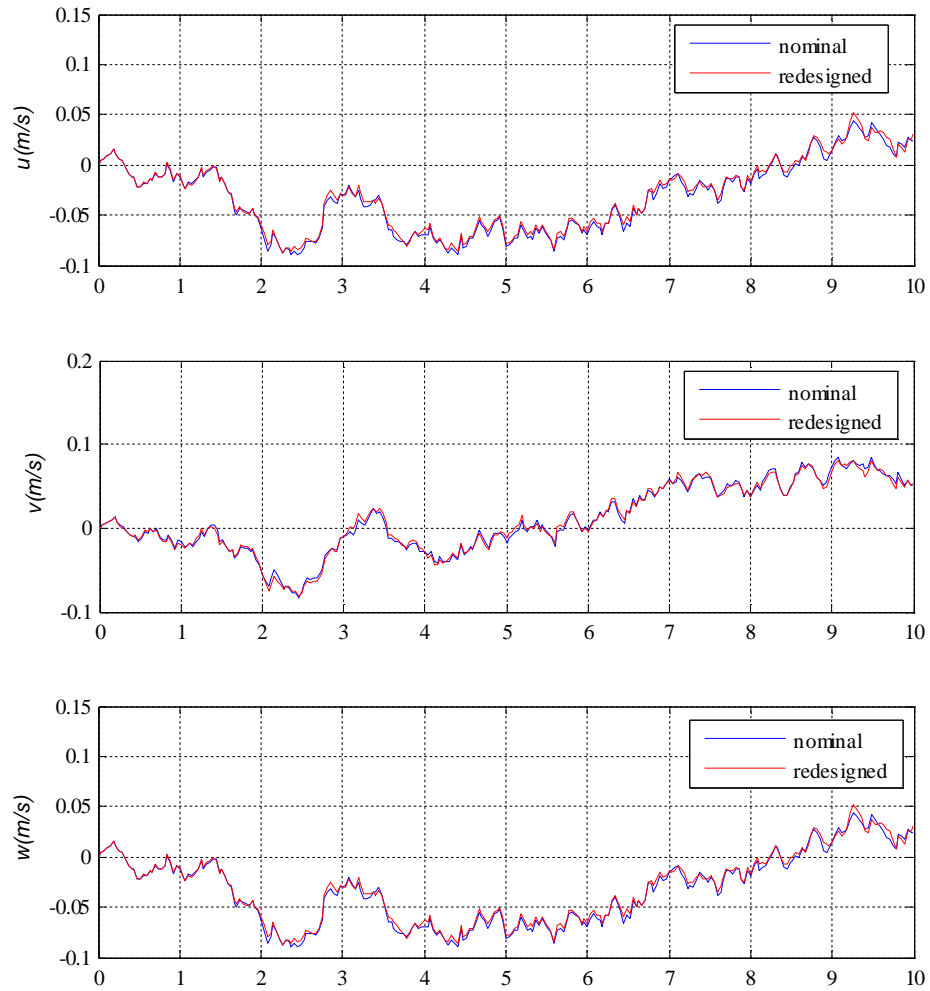
Figure H.1: Helicopter Linear Velocities Before and After Redesign
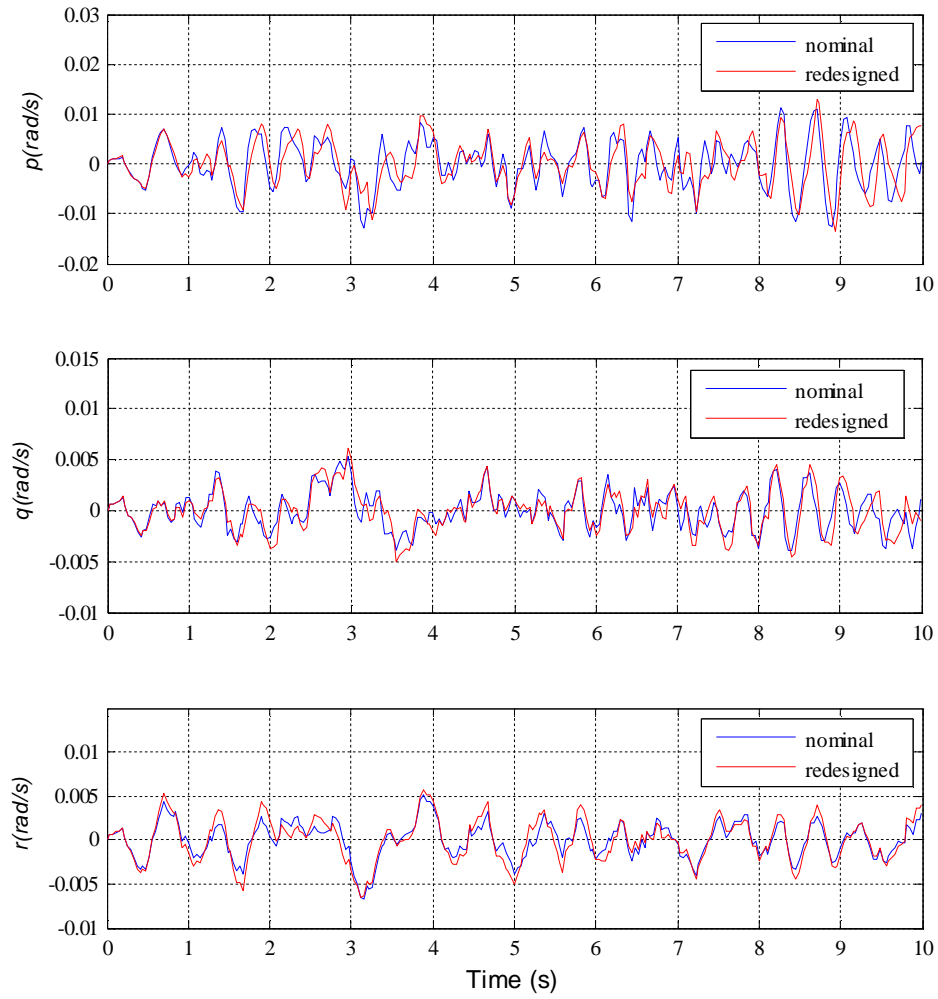
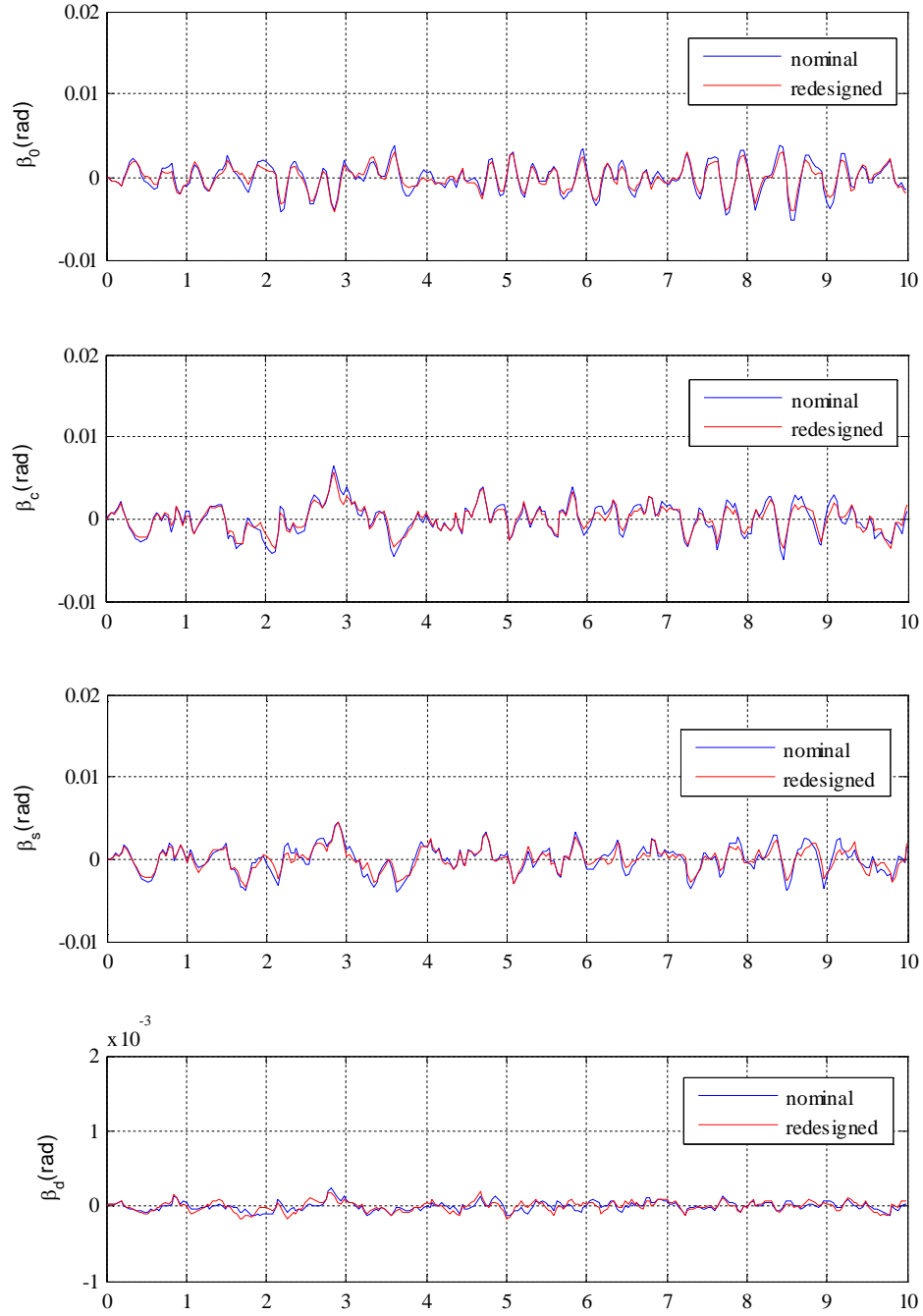**Figure H.2: Helicopter Angular Velocities Before and After Redesign**

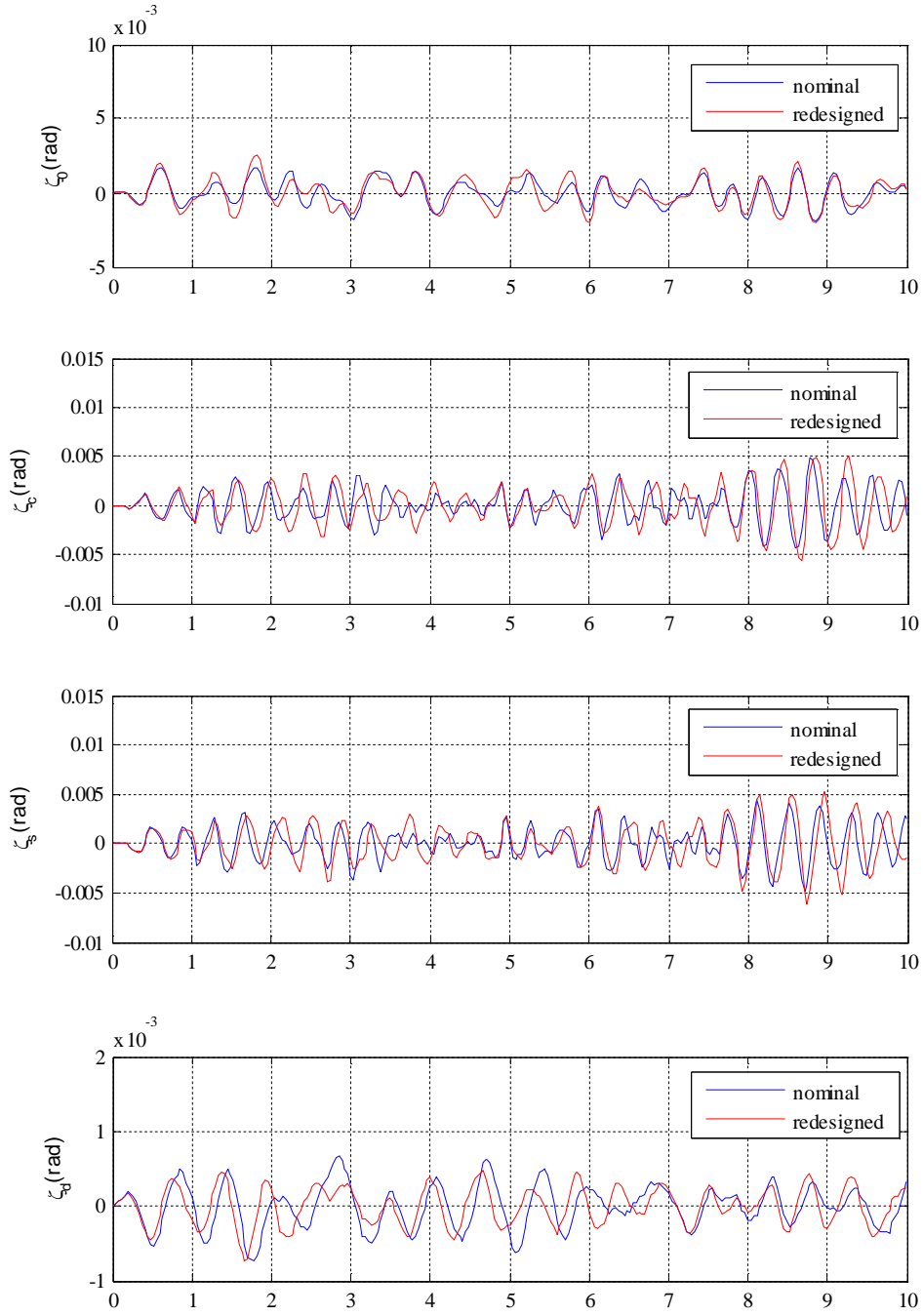**Figure H.3: Blade Flapping States Before and After Redesign**

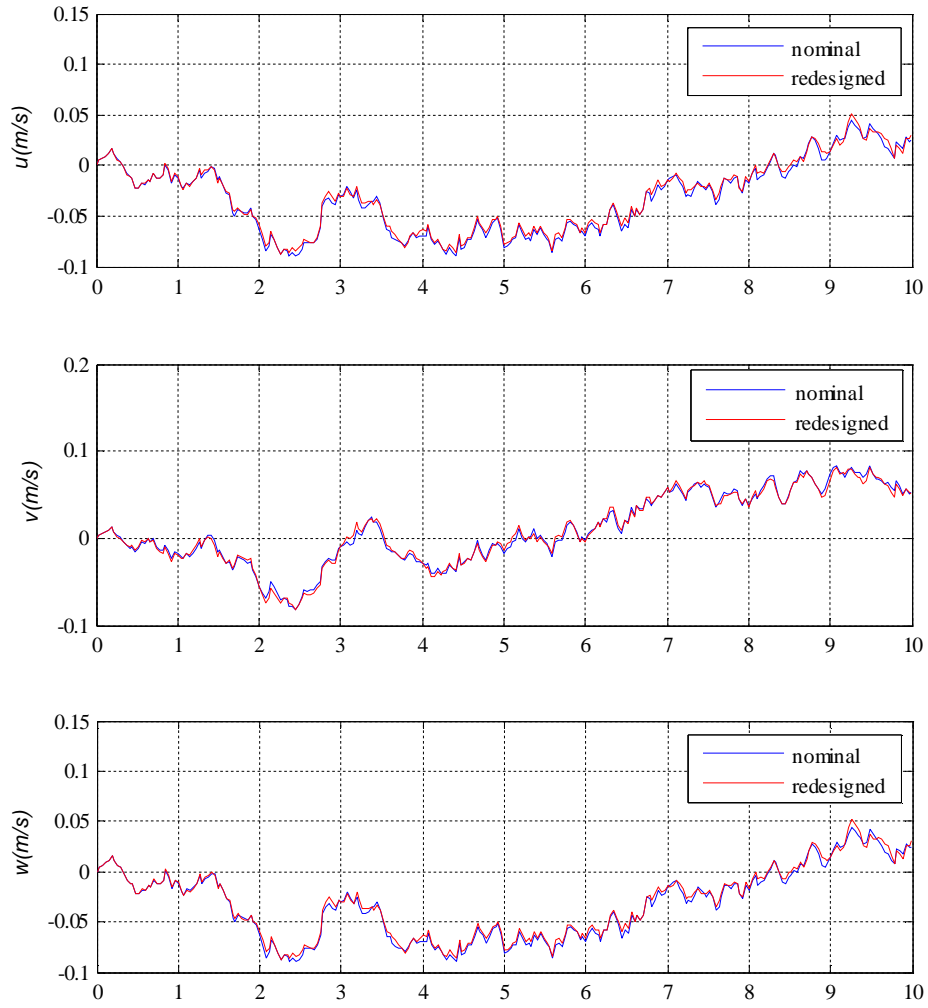**Figure H.4: Blade Main Lagging States Before and After Redesign**

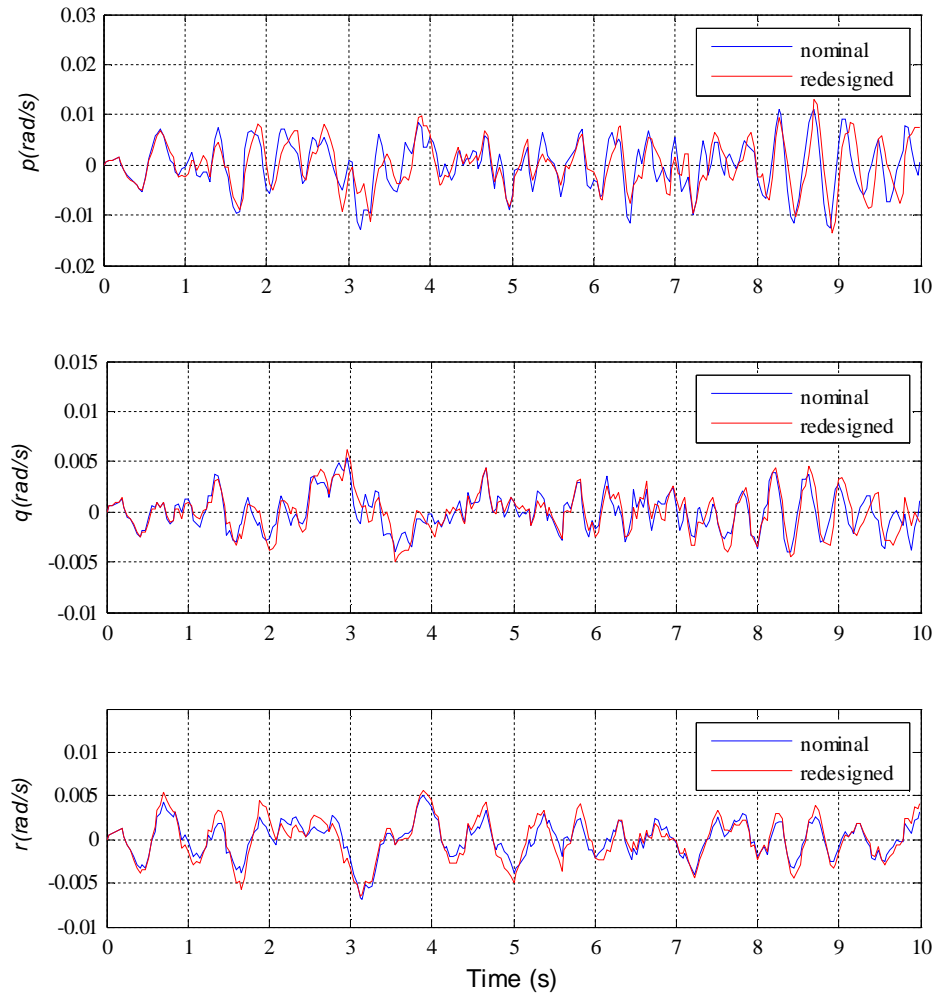**Figure H.5: Helicopter Linear Velocities Before and After Redesign for 2nd Example**

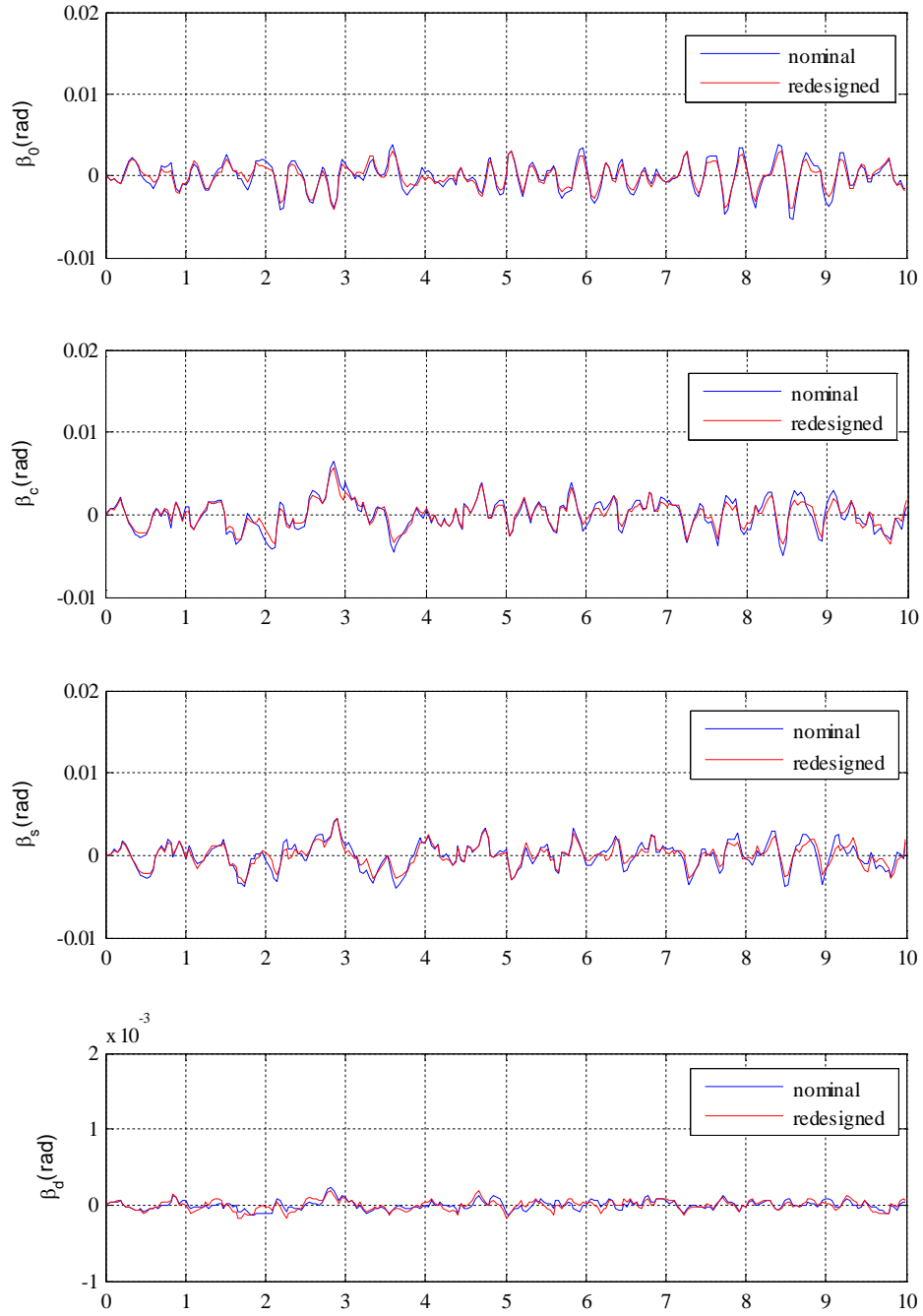**Figure H.6: Helicopter Angular Velocities Before and After Redesign for 2nd Example**

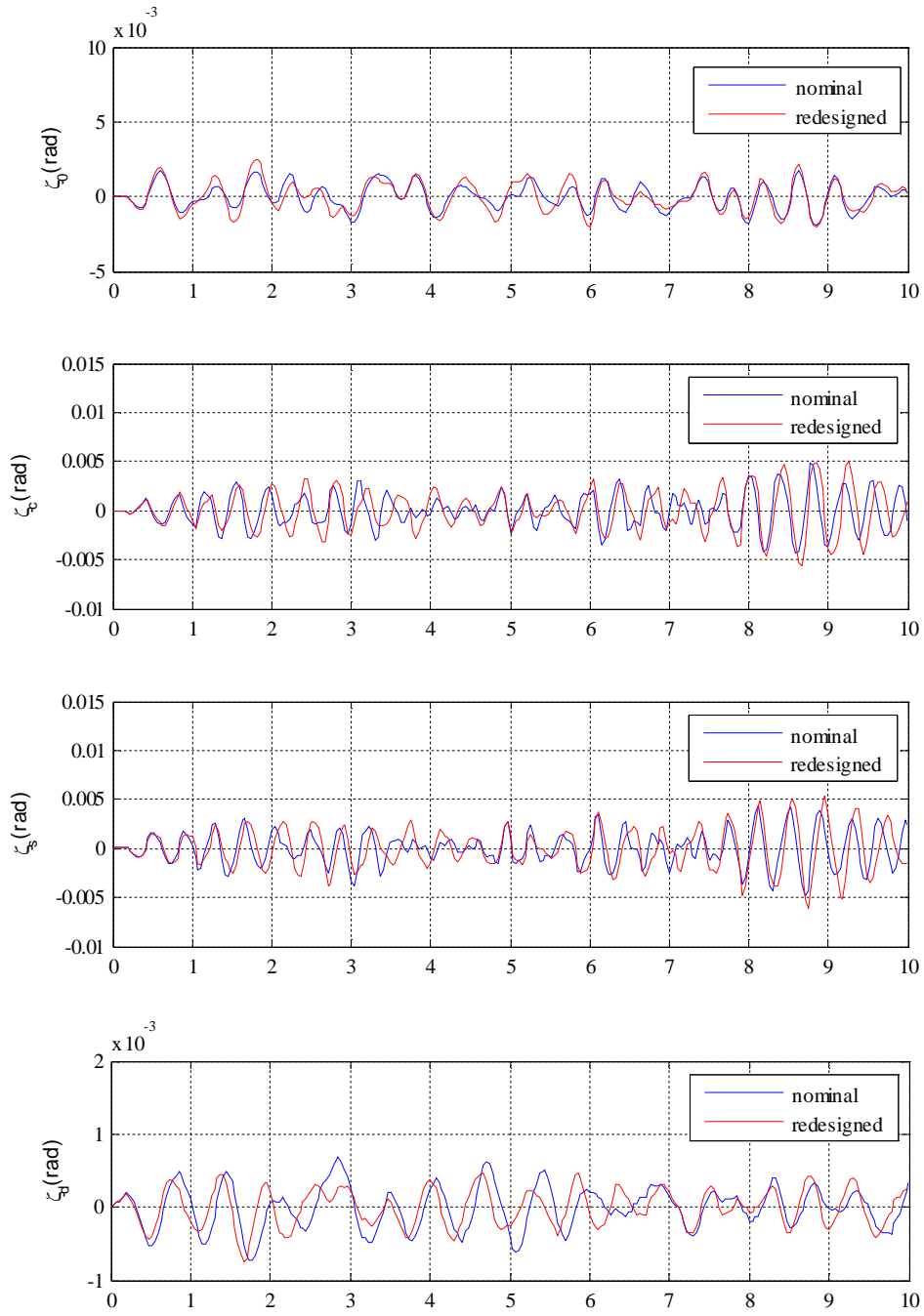**Figure H.7: Blade Flapping States Before and After Redesign for 2nd Example**

Figure H.8: Blade Lagging States Before and After Redesign for 2nd Example

Robustness of OVC was also examined for redesigned helicopter models. For the 1st example, the OVC, which was designed for the redesigned model linearized around $V_A = 40\,\text{kts}$, $\dot{\psi}_A = 0.1\,\text{rad/s}$, $\gamma_{FP} = 0.1\,\text{rad}$, was evaluated for the redesigned model linearized around $V_A = 1\,\text{kt}$, $\dot{\psi}_A = 0.1\,\text{rad/s}$, $\gamma_{FP} = 0.1\,\text{rad}$. For the 2nd example, previous OVC was evaluated for the redesigned model linearized around $V_A = 80\,\text{kts}$, $\dot{\psi}_A = 0.1\,\text{rad/s}$, $\gamma_{FP} = 0.1\,\text{rad}$. For the 3rd example, the OVC, which was designed for the redesigned model linearized around $V_A = 1\,\text{kt}$, $\dot{\psi}_A = 0\,\text{rad/s}$, $\gamma_{FP} = 0\,\text{rad}$ (hover), is evaluated for the redesigned model linearized around $V_A = 40\,\text{kts}$, $\dot{\psi}_A = 0\,\text{rad/s}$, $\gamma_{FP} = 0\,\text{rad}$ (straight level flight). For all of these examples, plant and measurement noises were considered with nondimensionalized intensities of $W = 10^{-7}I_{25}$, $V = 10^{-7}I_9$.
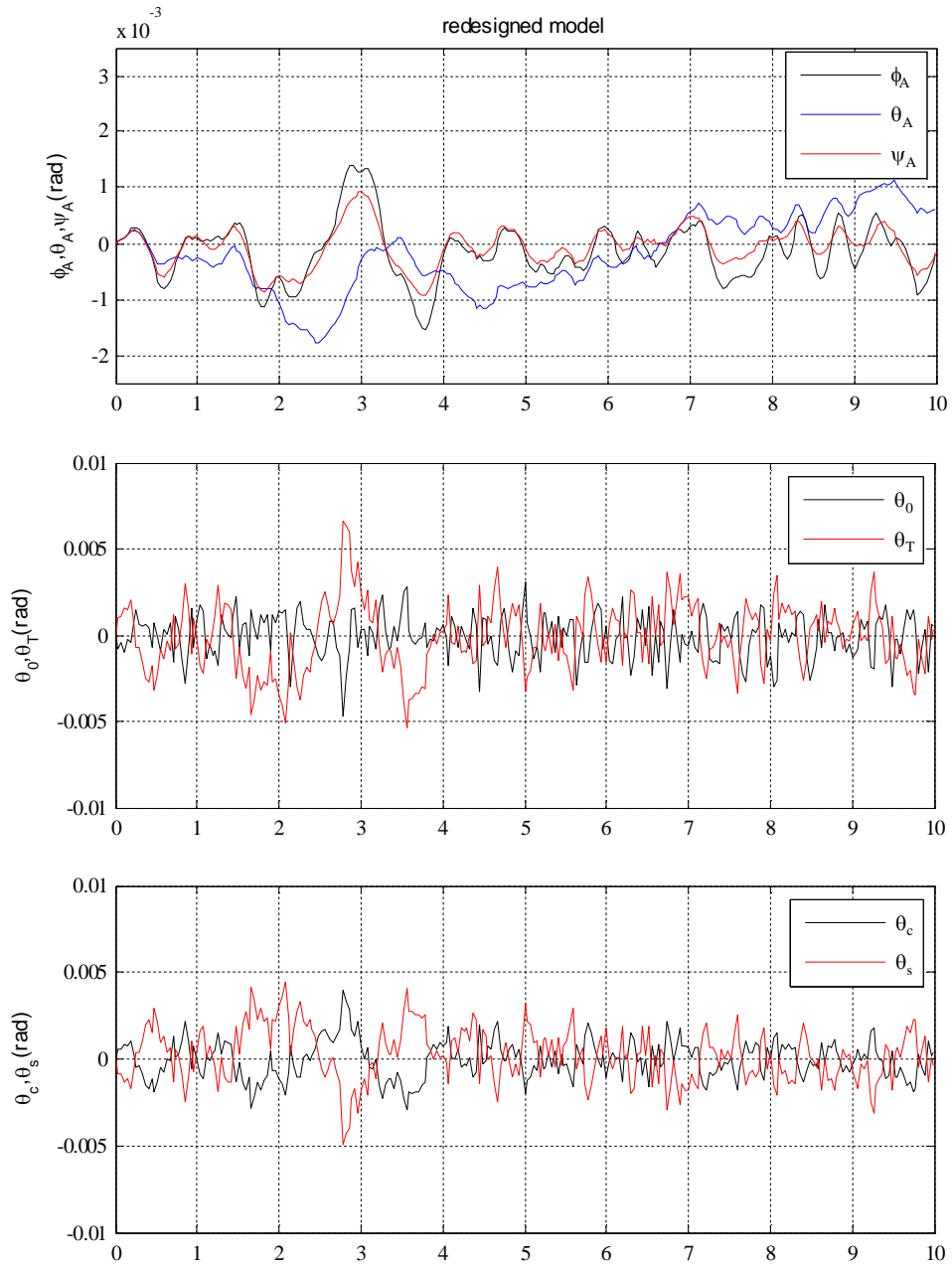
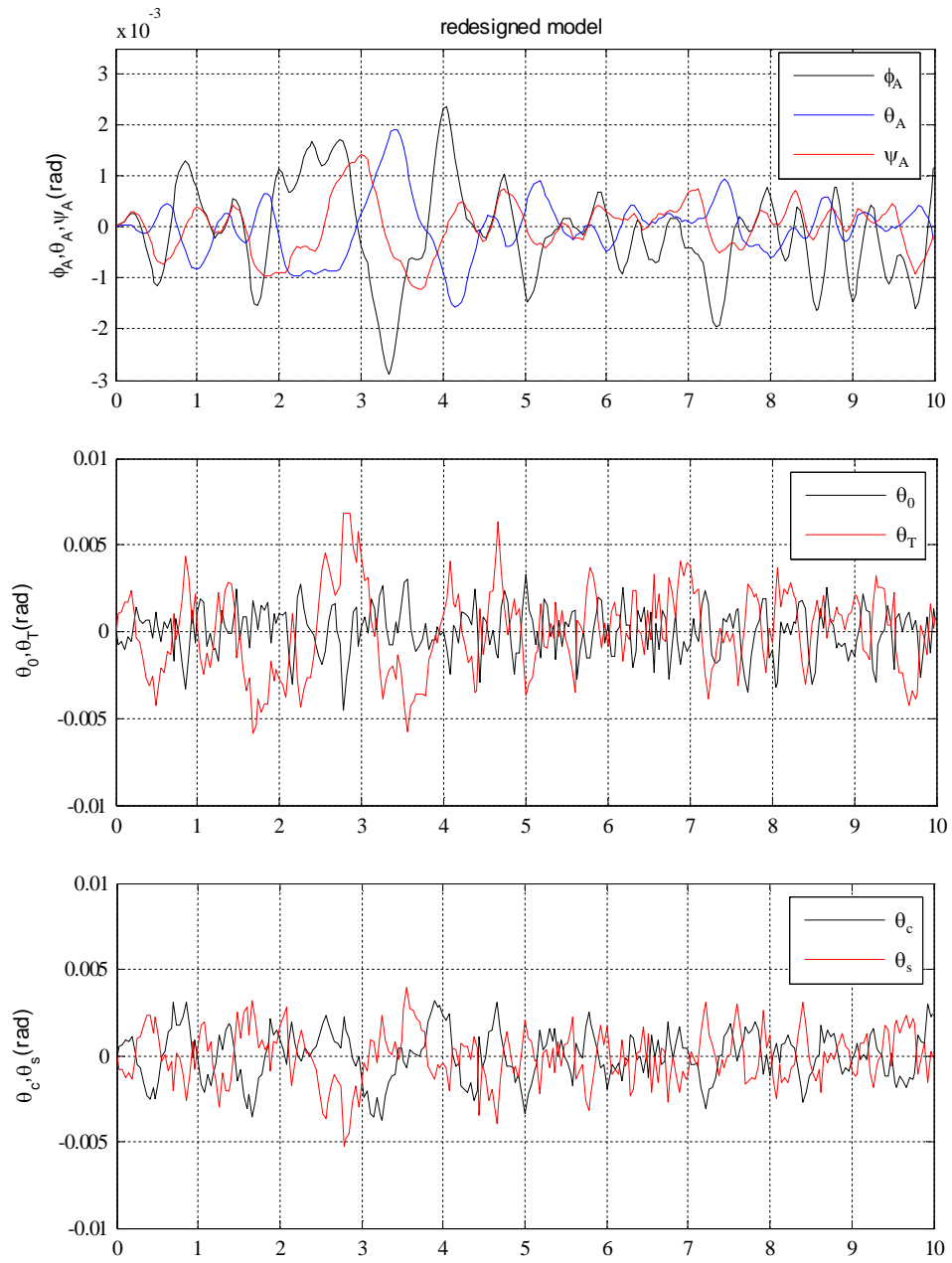**Figure H.9: 1st Additional Robustness Example for Redesigned Helicopter**

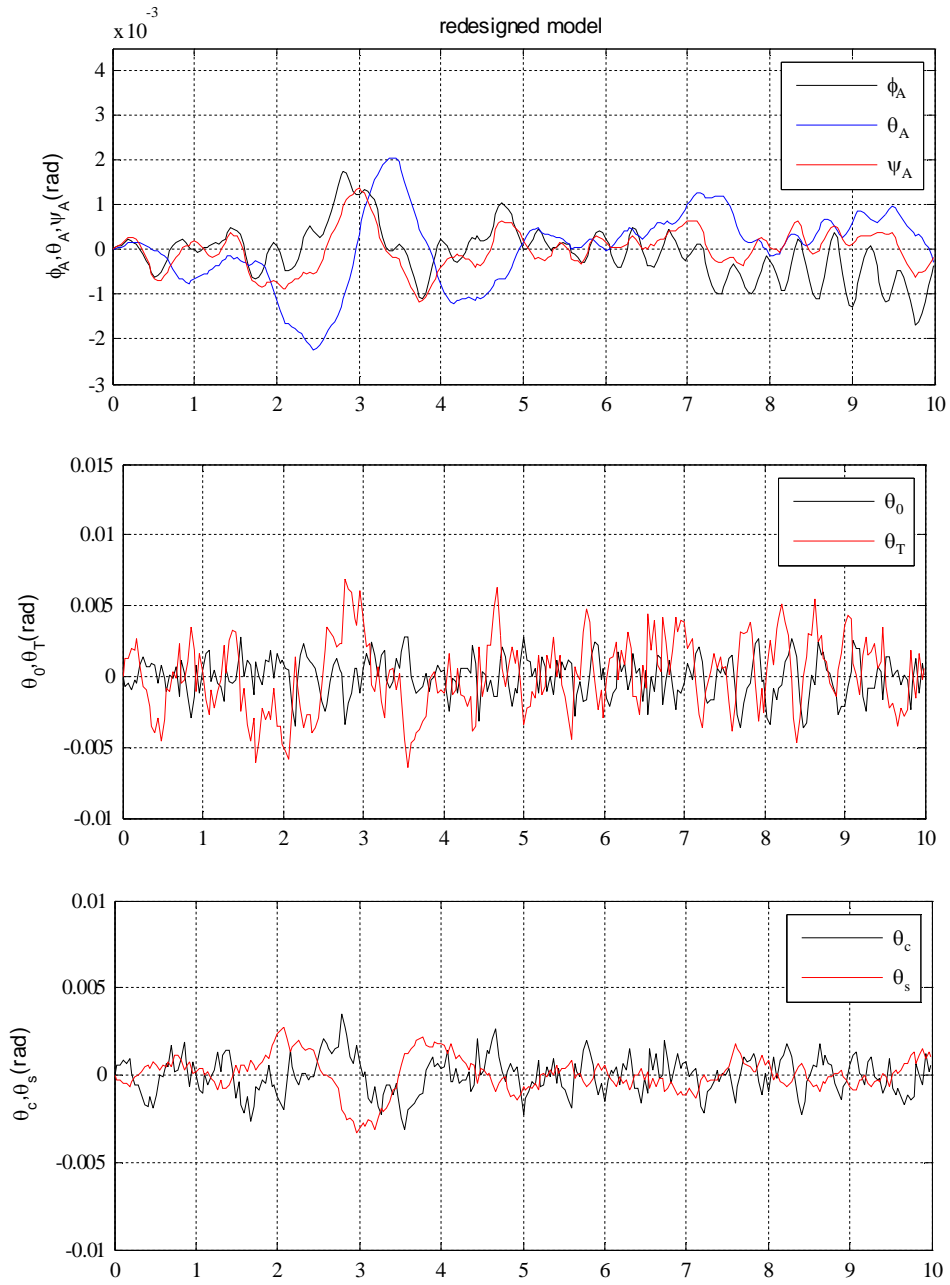**Figure H.10: 2nd Additional Robustness Example for Redesigned Helicopter**

Figure H.11: 3rd Additional Robustness Example for Redesigned Helicopter